University of Bath

PHD

Synthesis and study of porous and photocatalytic metal oxide foams for environmental remediation

(Alternative Format Thesis)

Warren, Zachary

Award date:
2023

Awarding institution:
University of Bath

Link to publication

Alternative formats
If you require this document in an alternative format, please contact:
openaccess@bath.ac.uk

Copyright of this thesis rests with the author. Access is subject to the above licence, if given. If no licence is specified above, original content in this thesis is licensed under the terms of the Creative Commons Attribution-NonCommercial 4.0 International (CC BY-NC-ND 4.0) Licence (https://creativecommons.org/licenses/by-nc-nd/4.0/). Any third-party copyright material present remains the property of its respective owner(s) and is licensed under its existing terms.

Take down policy
If you consider content within Bath's Research Portal to be in breach of UK law, please contact: openaccess@bath.ac.uk with the details. Your claim will be investigated and, where appropriate, the item will be removed from public view as soon as possible.

Download date: 07. Oct. 2023

Synthesis and study of porous and photocatalytic metal oxide foams for environmental remediation

Zachary Warren

A thesis submitted for the degree of Doctor of Philosophy

University of Bath

Department of Chemical Engineering

September 2022

COPYRIGHT

Attention is drawn to the fact that copyright of this thesis rests with its author. A copy of this thesis has been supplied on the condition that anyone who consults it is understood to recognise that its copyright rests with its author and that they must not copy it or use material from its except as permitted by law or with the consent of the author.

This thesis may be made available for consultation within the University Library and may be photocopied or lent to other libraries for the purposes of consultation.

Signature of Author . . . . . .

Declaration

This thesis contains original work carried out by the stated author with any collaboration stated and acknowledged within the corresponding text.

X-ray diffraction (XRD) spectra were produced by Dr Gabriele Kociok-Kohn, X-ray photoelectron spectroscopy (XPS) spectra were produced by Dr Mark Isaacs Harwell, and inductively coupled plasma mass spectrometry (ICP-MS) was produced by Dr J. Andy Milton, University of Southampton.

Abstract

Current wastewater treatment methods are not able to effectively remove organic micropollutants, present in low concentrations. This group of compounds includes a wide range of biologically active substances from a range of human sources, including pharmaceuticals, pesticides, drugs, and caffeine that are found in concentrations of ng L^{-1} to µg L^{-1} in domestic wastewater. Photocatalysis is an advanced oxidation technique that can be applied as a tertiary treatment step after conventional treatment, utilising semiconductor materials activated by UV irradiation to degrade these compounds. Currently, most examples of photocatalysis focus on either nanoparticles slurries or immobilised catalyst systems. Slurry systems require post-treatment downstream removal, while immobilised systems have lower surface areas and show lower activities than slurry systems. Recently, more interest has been paid to immobilising photocatalysts onto porous supports, however a remaining issue with this approach is the potential leaching of catalyst and loss of nanoparticles from the support surface due to weak surface-catalyst interactions. Focusing on ZnO, the aim of this thesis was to develop a novel method to produce porous structures made entirely of ZnO, thus removing the surface-catalyst interactions and removing the need for downstream removal, while combining the high surface areas of a slurry system.

Novel foam-like structures were produced via direct air incorporation into a sol-gel reaction of zinc acetylacetonate and oxalic acid leading to the formation of macroscale zinc oxalate foams. These proto foams were then sintered to form ZnO foams, consisting of a continuous structure, free from discrete crystals or particles. The resulting structures were termed molecular foams or MolFoams. Control of the pore size was found to be possible by tuning the concentration of surfactant present in the gel, resulting in foams of smaller pore sizes and unique crystal morphologies, both of which proved to be beneficial to the photocatalytic activity of the foams. To analyse the photocatalytic activity of the foams, a bespoke recirculating batch reactor was developed to utilise the foams while making best use of the porous, hierarchical structure, consisting of a range of interconnected pores of different sizes. These foams were able to surpass the performance of slurry and supported

photocatalyst systems for the removal of carbamazepine, with reaction rate constant of 5.43 $x10^{-3}$ min^{-1} along with high electrical energy efficiencies and quantum efficiencies.

ZnO is a widely used photocatalyst but is hindered by its low resistance to photocorrosion, and its large band gap means that it is unsuitable for solar applications. While research into doping of ZnO exists, it is focused on nanoparticles and films, with the few publications that report negative results failing to provide significant characterisation or interpretation to discern the cause of the reduced photocatalytic activity. The ZnO MolFoam synthetic method was modified for the incorporation of transition metal dopants into the structure to reduce the band gap of the material, such that it could be used under solar or visible light irradiation and to increase the resistance to photocorrosion that hinders wider usage. After initial testing revealed doping metal into the structure to have been successful at significantly reducing the photocorrosion of ZnO, with a 60-85 % reduction in Zn^{2+} leaching after irradiation but resulted in decreases in photocatalytic activity, focus was shifted towards analytical characterisation of the materials, including x-ray photoelectron spectroscopy and ultra-violet photoelectron spectroscopy, to identify the cause of this decrease in activity as the shifting of band edge positions.

Also in this thesis is a meta-review of foams used in photocatalysis, which proposes an expansion of the terminology and literature surrounding porous materials, building upon the existing IUPAC terminology, and expanding it to include categorisation of foams and porous objects. This work also describes categorisation of foam materials with definitions based on synthesis method and includes a systematic analysis based on this categorisation, while also providing a semi-quantitative comparison of the literature surrounding foams and photocatalysis, considering the wide range of parameters involved in the publications in this area. Finally, this work highlights the relevance of using multiple figures of merit in photocatalysis and proposes a short list of common best practices for the field.

To conclude, this work has placed a primary focus on the development and adaptation of the MolFoam synthesis, leading to the production of wholly photocatalytic foams of ZnO, demonstrating good photocatalytic activity and high

efficiencies. The pore size of these foams was shown to be a key parameter for the photocatalytic activity, with smaller pores leading to a higher reaction rate constant due to decreased distance required for pollutant to diffuse to the catalyst surface, and could be controlled using surfactant, CTAB.

Doping of these foams with transition metals was shown to significantly increase the resistance to photocorrosion, with higher dopant concentrations leading to significantly reduced Zn^{2+} leaching post irradiation, however the doping process was found to lead to shifting of the band edge positions of the material, such that the photocatalyst lacked the ability to produce hydroxyl radicals required to degrade carbamazepine.

The research presented in this thesis has led to three published papers and future work would be to refine the doping process for the ZnO foams, such that the resulting foams do not see the reduction in photocatalytic activity shown by the initial doping process. Additionally, it is of interest to examine the effect of doping of non-metal dopants such as nitrogen, assessing the impact on photocatalytic activity and stability, when compared to metal doped foams. The photocatalytic activity of these foams would also be investigated under visible light irradiation, in comparison to the UV irradiation described herein.

Acknowledgements

Well, it's been an interesting few years to say the least and times like these make one realise how lucky they are to be surrounded by such a supportive group. I would like to give thanks to everyone mentioned below (and more).

First and foremost, thanks must be given to my supervisors, Professor Davide Mattia and Dr Jannis Wenk, for their invaluable advice, constant support and endless patience. They have guided me through this, often tumultuous, process and helped me grow, while pushing me to refine my skills as a researcher for which I am incredibly grateful.

To my Mum, Brothers and Sister, thank you for always having my back and for putting up with my stress/coffee fuelled rants about, water, lamps or "the literature", and for always being there to listen while I talk about photocatalysis or water treatment and nodding encouragingly before politely asking me to stop.

To my non-PhD friends, James, Mark and Roz. Thank you for constantly reminding me there is a world outside of the PhD and for being generally wonderful people.

To the chemists from Southampton, thank you for constantly providing me with laughs and life updates that occasionally made me feel better about my situation.

I have spent more hours in 9W over the last years than I care to count. I appreciate all the support that the technical staff have provided me and for being incredibly helpful throughout my PhD. I also owe so much to university staff from across multiple departments for their time and assistance, particularly Dr Shaun Reeksting, Dr Philip Fletcher, Dr Gabriele Kociok-Kohn, Diana Lednitzky and Clare Ball.

I consider myself very lucky to have worked with all members of the Mattia group over the last few years and alongside others from multiple groups working in 4.01, 4.04 and 1.02.

Particular thanks must be given to Dr Thais Tasso Guaraldo, for being there for me from day one and always having the time to sit down with me to discuss some results or a theory about experiments. Her patience and willingness to talk and

listen have helped get me through some of the more stressful periods of this PhD while her help and guidance has helped make me a better researcher.

My thanks are also extended to the EPSRC for providing the funding and allowing me the opportunity to undertake this PhD.

My final thanks are to the rest of the 2018 cohort, whom it has been a pleasure to take this journey alongside. Thanks in particular Viviane Runa and Scott Allan, for making the regular weekends in the lab much more bearable. Best of luck in your future endeavours.

In memory of Brian Grover. The best man I ever knew.

Papa, I wish you could have seen this.

Dissemination

Publications

Warren, Z., et al. (2022). "Synthesis of photocatalytic pore size-tuned ZnO molecular foams." Journal of Materials Chemistry A **10**(21): 11542-11552.

Warren, Z., et al. (2023). "Photocatalytic foams for water treatment: A systematic review and meta-analysis." Journal of Environmental Chemical Engineering **11**(1).

Warren, Z., et al. (2023). "Increased photocorrosion resistance of ZnO foams via transition metal doping." RSC Advances **13**(4): 2438-2450.

Conferences

January 2021	RSC Materials Chemistry Division Poster Symposium. Poster Presentation.
April 2021	American Chemistry Society, Spring Meeting 2021. Oral Presentation.
April 2021	Materials Research Society, Spring Meeting 2021. Oral Presentation.
July 2021	15th International conference on materials chemistry (MC15). Oral Presentation.
May 2022	Water Innovation Research Centre Poster Day. Poster Presentation.

Honours & Awards

January 2021	Poster Award - Judges' Selection RSC Materials Chemistry Division Poster Symposium 2021 for poster titled "ZnO Molecular foams for micropollutant removal"

Table of Contents

List of Equations

List of Figures

List of Tables

List of symbols

a_{vs}	Surface Area : Volume ratio [cm^{-1}]
A	Cross-sectional area of foam [m^2]
c	Speed of light [m s^{-1}]
C_0	Initial concentration of pollutant
C_t	Concentration of pollutant at time, t
D	Diffusion Coefficient [m^2 s^{-1}]
D_u	Density of Water [g cm^{-3}]
D_f	Density of ZnO [g cm^{-3}]
d_p	Pore Diameter [mm]
D_p	Pore Diameter [mm]
E	Band gap energy [eV]
E_p	Photon energy [J]
E_{qf}	Photon flux [Einstein s^{-1}]
E_{EO}	Electrical energy per order [kWh m^{-3}]
e^-	Electron
F	Flow rate [m^3 hr^{-1}]
h	Planck's Constant [6.63 x 10^{-34} m^2 kg s^{-1}]
h^+	Charge hole
$I_{\alpha\lambda}$	Attenuated irradiance of light [mW cm^{-2}]
k	Rate constant [min^{-1}]
k'	Molar rate of degradation [mol s^{-1}]
k_ϵ	Normalised kinetic constant [M cm min^{-1}]
L	Foam length [m]
N_A	Avagadro's number [mol^{-1}]
N_p	Number of Photons [-]
R	Reflectance
Re	Reynolds number [-]
P	Power [kW]
Pe	Peclet number [-]
Q	Volumetric flow rate [m^3 s^{-1}]

QE	Quantum Efficiency
S	Irradiated surface area [m^2]
Sc	Schmidt number [-]
Sh	Sherwood number [-]
T	Transmittance
t	Reaction time
u	Flow velocity [m s^{-1}]
V_I	Volume illuminated [L]
V_o	Volume receiving UV dose per second [mL s^{-1}]
V_R	Total reaction solution [mL]
W	Work function [eV]
ε	Molar absorption coefficient [M^{-1} cm^{-1}]
ε	Porosity [%]
Φ	Quantum yield [-]
λ	Wavelength [nm]
ν	Frequency [Hz]
τ	Irradiation time [s] (UV dose)
τ	Average crystallite size (XRD)
ρ	Fluid density
μ	Dynamic viscosity of fluid [kg m^{-1} s^{-1}]
θ	Diffraction angle

List of Abbreviations

AO	Atomic orbitals
AOP	Advanced oxidation processes
BET	Brunauer-Emmet-Teller
BOD	Biological oxygen demand
BPA	Bisphenol A
CAFO	Concentrated animal feeding operation
CB	Conduction band
CBZ	Carbamazepine
CPS	Chlorpyrifos
CTAB	Cetrimonium bromide
CVD	Chemical vapour deposition
EDC	Endocrine disrupting chemical
ES	Endosulfan
EtOH	Ethanol
EDX	Energy Dispersive X-ray spectroscopy
FESEM	Field emission scanning electron microscopy
FWHM	Full width at half maximum
HPLC	High performance liquid chromatography
ICP-MS	Inductively coupled plasma mass spectrometry
ID	Inner diameter
LCAO	Linear combination of atomic orbitals
LED	Light emitting diode
MAC	Molar absorption coefficient
MDMA	Methylenedioxymethamphetamine
MO	Molecular orbital
MB	Methylene Blue
MP	Methyl parathion
OD	Outer diameter
PA	Parathion
PAH	Polyaromatic hydrocarbon

PEG	Poly-ethylene glycol
PMR	Photocatalytic membrane reactor
PPCP	Pharmaceuticals and personal care products
PTFE	Poly-tetrafluoroethylene
QE	Quantum Efficiency
RGO	Reduced graphene oxide
SCE	Standard calomel electrode
sCO_2	Supercritical carbon dioxide
SHE	Standard hydrogen electrode
SI	Supplementary information
STY	Space-time yield
TCCP	Tris(chloropropyl)phosphate
TCEP	Tris(2-chloroethyl) phosphate
TiO_2	Titanium dioxide
TSS	Total suspended solids
UPS	Ultraviolet photoelectron spectroscopy
UV	Ultraviolet
UV-Vis	Ultraviolet-Visible
VB	Valence band
XANES	X-ray Absorption Near Edge Structure
XPS	X-ray photoelectron spectroscopy
(P)XRD	(Powder) X-ray diffraction
ZnO	Zinc oxide

Thesis outline

This doctoral thesis investigates the development of highly porous ZnO monoliths, or foams, including the use of a novel method for the formation of solid foams with the ability to include metal dopants into the foams. The photocatalytic activity of these foams was studied to assess their potential for use in wastewater treatment.

This thesis consists of six chapters

Chapter 1 provides a literature review of organic micropollutants, advanced oxidation processes and photocatalysis, in addition to the synthesis of pure and doped ZnO and its application as a photocatalyst in water treatment.

Chapter 2 consists of a literature review paper, focussing of the use of foams as photocatalysts, while also expanding on literature definitions and the use of specific figures of merit. Based on work in *Warren, Z., et al. (2023). "Photocatalytic foams for water treatment: A systematic review and meta-analysis." Journal of Environmental Chemical Engineering 11(1).*

Chapter 3 summarises and supplements methods, materials and experimental procedures used through this thesis, including discussions on the fundamental theories behind characterisation techniques used.

Chapter 4 covers the development of ZnO MolFoams and the discussion on the impact of pore size on photocatalytic activity of foams. Based on work published in *Warren, Z., et al. (2022). "Synthesis of photocatalytic pore size-tuned ZnO molecular foams." Journal of Materials Chemistry A 10(21): 11542-11552.*

Chapter 5 covers the modification to the synthetic method for the production of MolFoams presented in the preceding chapter to incorporate dopant metals into the foams. Based on work in Warren, Z., et al. (2023). "Increased photocorrosion resistance of ZnO foams via transition metal doping." RSC Advances **13**(4): 2438-2450.

Chapter 6 includes general conclusions of the presented research as well as an outlook for future work and research.

Chapter 1

Literature Review

Literature Review

1.1. Wastewater Treatment & Micropollutants

Access to clean water is one of the greatest challenges facing modern society, caused by deep imbalances between availability and demand, with scarcity expected to rise within countries deemed "water rich" and those without.[1] The risks associated with consumption of clean water are well known, with over 1 billion people lacking access to safe drinking water and the annual death toll due to waterborne disease in the millions.[2] Compounding this issue, is an increasing global population as well as the impact that it will have on existing water supplies due to increased usage and increased pollution through human interaction.[3]

Wastewater treatment processes have seen use for over a century, primarily driven by outbreaks of waterborne diseases such as cholera and typhoid in high-income countries caused by contamination of drinking waters with the pathogens present in wastewater with the goal of preventing further outbreaks.[4] A typical wastewater treatment plant, consists of three treatment steps, as seen in Figure 1.1. Wastewater is a complex matrix, consisting of multiple compounds present at the same time. Typical wastewater has a biological oxygen demand (BOD) of 100 to 300 mg L^{-1}, a salt content of 30- to 100 mg L^{-1} in addition to nutrients such as nitrogen and phosphorus present at levels > 100 mg L^{-1}.[5]

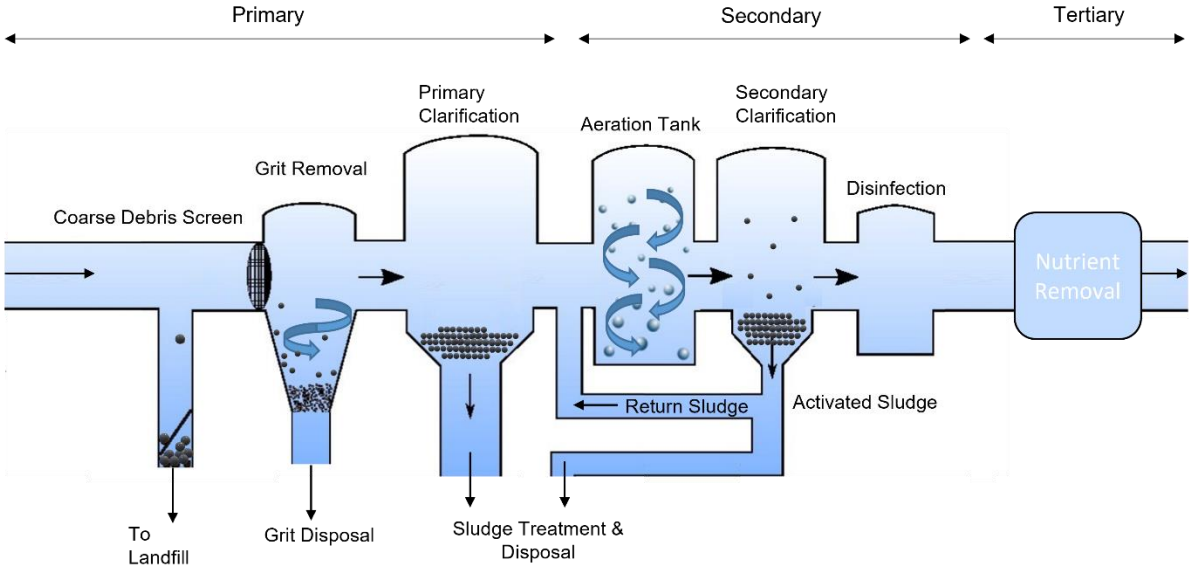

Figure 1.1: An example diagram of the three steps in wastewater treatment including an optional disinfection step. Image adapted from ref [6]

The primary treatment step is used to facilitate separation processes of grit and particulate matter using physical processes such as size separation and sedimentation with the aim to remove total suspended solids (TSS) and reduce the BOD via removal of sludge. A coarse screen is used to remove larger solid matter such as leaves, from the effluent. From here, grit and smaller particulates along with oils and fats are removed, separated by density relative to water, with the former undergoing sedimentation to form sludge and the latter being skimmed off the surface.[7]

Secondary treatment consists of biological processes to further reduce BOD from the influent via biochemical decomposition of organic solids via oxidation by aerobic microbial species.[8] This process typically involves aeration of the solution, via bubbling of compressed air, to promote the growth of aerobic microorganisms which are responsible for the degradation of organic compounds and reduction of BOD. As these microorganisms grow to a sufficient size, they form flocs, which sink and form sediment at the bottom of the tank, forming activated sludge, allowing for them to be removed and either returned to the aeration tank to provide seeded microorganisms, or treated before further use in agriculture as fertilizers.[9] The tertiary step, which was added to many wastewater treatment plants in the 1960s and 70s in water treatment involves the reclamation of nutrients, such as nitrogen and phosphorus, using a wide range of methods including filtration and chemical treatment,[10] as their presence has been linked to eutrophication of surface waters.[4] A summary of a range of water treatment processes can be seen below in Figure 1.2.

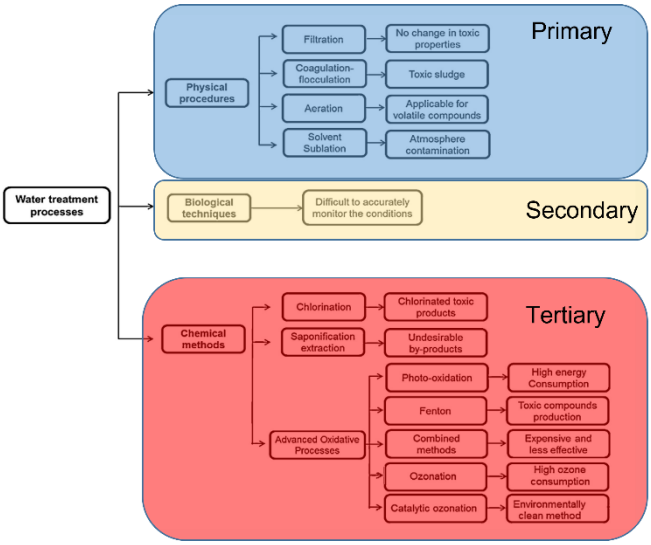

Figure 1.2: Various methods of water treatment processes for removal of organic compounds. Adapted from ref [11]

While wastewater treatment plants are capable of removing macropollutants, including particulates, total suspended solids and BOD, the low concentration of micropollutants (µg L^{-1} to ng L^{-1}) coupled with the often-persistent nature of the compounds means that these compounds are able to pass through treatment plants with little to no change in concentration and be released into the wider environment.[12, 13]

Pharmaceutical usage is estimated to be around 15 g per capita as a worldwide average, increasing to 50-150 g per capita in industrialised countries. [14] However disparities in water treatment technologies leads to higher concentrations of pharmaceutical micropollutants in water supplies in low to middle income

countries, compared with higher income ones,[15] as shown in Figure 1.3.

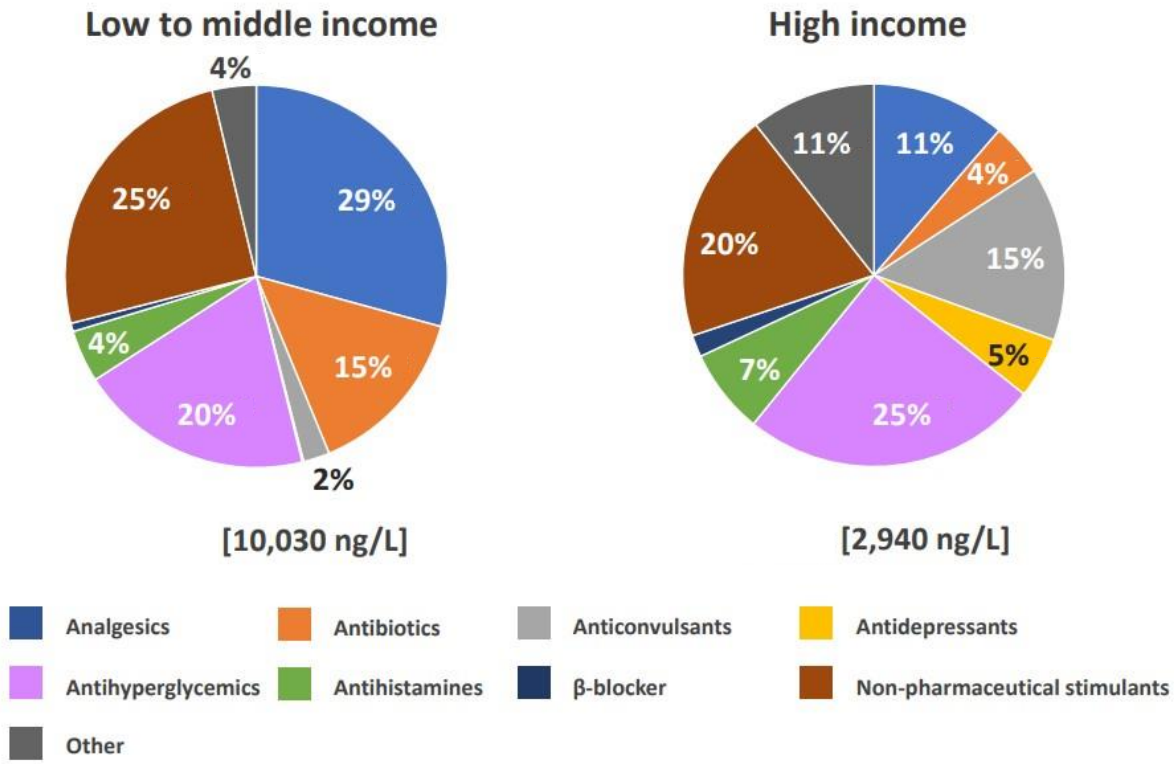

Figure 1.3: Composition of pharmaceutical micropollutants by therapeutic class across low- to middle- and high-income countries. Brackets contain mean cumulative pharmaceutical concentration. Image adapted from reference [15].

A growing concern of developed countries is the accumulation of, often organic, pollutant compounds in water supplies present in low concentrations in water at the µg L^{-1} or ng L^{-1} scale,[16] which are identified as micropollutants. Micropollutants can be roughly categorised into drugs, both pharmaceutical and illicit, personal care products and cosmetics, pesticides and industrial compounds, as shown in Table 1.1.[17]

Table 1.1: Table of micropollutants and their common uses, along with their main sources of pollution. [18-23]

Category	Compound	Use	Common Sources
Pharmaceutical	Carbamazepine	Anti-convulsant	Domestic wastewater, landfill leachate Hospital effluent, CAFO runoff.
	Diclofenac	Anti-inflammatory	
	Azithromycin	Anti-bacterial	
	Estrone (E1)	Steroid hormone	
	Estradiol (E2)		
	Fluoxitine	Anti-depressant	
Illicit drugs	MDMA	Hallucinogen	Domestic wastewater, landfill leachate
	Methamphetamine	Stimulant	
	Cocaine		
Personal Care Products (PCP)	Parabens	Preservative	Domestic wastewater, landfill leachate
	Triclosan	Disinfectant	
	1-Benzophenone	Sunscreen UV filter	
	Galaxolide	Fragrance	
Pesticides	Atrazine	Herbicide	Agricultural runoff
	Diuron	Herbicide	
	Diazinon	Insecticide	
Industrial compounds	Perfluorinated compounds	Coatings	Industrial wastewater, manufacturing discharges, landfill leachate.
	Bisphenol A (BPS)	Plasticiser	
	Tris(2-chloroethyl) phosphate (TCEP)	Flame retardants	
	Tris(chloropropyl)phosphate (TCCP)		

While present in low concentrations, these compounds are still of concern as they can have wide reaching effects to both health and the ecosystem while also bioaccumulating in living organisms, with the potential to make their way up the food chain. Many of the compounds that are considered to be micropollutants, particularly pharmaceuticals, show toxicological effects,[24] particularly endocrine

disrupting effects, given that these organic pollutants tend to be highly lipophilic and as such are able to accumulate inside fatty tissues.[25, 26] This process referred to as bioconcentration[27] or bioaccumulation, leads to increased exposure via dietary intake and thus can impact human health. [28] These endocrine disrupting chemicals (EDCs) can affect the endocrine system in three ways, either directly mimicking or antagonising the effects of hormones, altering the synthesis or metabolism of hormones within the body, or by altering the levels of hormone receptors within the body.[29] The impact of endocrine disruption on the body has widespread effects, including: infertility, altered sexual behaviours, increased incidence of specific cancers and birth defects.[30] Furthermore the impacts of the EDCs are not specific to humans nor mammals. It is widely reported the impact that these chemicals have had on a wide variety of fauna, e.g. the since banned pesticide DDT and it's metabolite DDE have been linked to the thinning of avian egg shells and the related decrease in population of raptors in the UK and USA.[31]

Carbamazepine is a pharmaceutical product used as an anti-convulsant for the treatment of conditions such as epilepsy,[32] with an estimated annual consumption in excess of 1,000 tonnes worldwide. [33] It is also a micropollutant frequently detected in municipal waterways [22] and rivers.[15] A recent worldwide study found carbamazepine to be one of the most prevalent micropollutants in aquatic systems worldwide: In a study consisting of over 1,000 sampling sites across 104 countries, carbamazepine was detected in water at over 60% of sampling sites with an average concentration of 75 ng L^{-1}, with upper concentrations detected exceeding 5 µg L^{-1}.[15] The ecotoxic effects of carbamazepine have been widely reported: One study found that exposure of mussels to carbamazepine led to a decrease in filter feeding behaviours, along with a reduction in growth and reproductive behaviours, with potential impacts on long term population stability.[34] Asian clams (*Corbicula fluminea)* exposed to carbamazepine in concentrations ranging from 0.1- to 50 µg L^{-1} over 14 days exhibited inhibition of the neurotransmitter acetylcholine esterase resulting in higher concentrations of acetylcholine and potential disruption to the central nervous system.[35] Zebrafish exposed to carbamazepine showed

greater chance of embryo deformation and abnormalities along with swelling in adult fish, highlighting detrimental issues at all stages of life.[36, 37]

A study into the exposure of swallows feeding on midge larvae exposed to carbamazepine, estimated the exposure rates and daily dosage per body weight at between 0.5- and 49.8 μg kg^{-1},[38] clearly demonstrating the effect of bioaccumulation. Exposure to carbamazepine has been shown to have a range of adverse effects on birds, including deformation of embryos, bone marrow suppression and reduced food competition aggression behaviours. [38]

Of further concern is the polar nature and stability of micropollutants, allowing them to resist the biological and physiochemical treatment steps in typical wastewater treatment plants.[39-42] Furthermore, organic micropollutants can also decrease the effectiveness of biological treatment generally, due to the presence of antibiotic compounds inhibiting the activated sludge bacteria,[20] or through micropollutant sorption into the sludge,[43] leading to micropollutants being released back into the environment as effluent or as fertilizer (Figure 1.4).

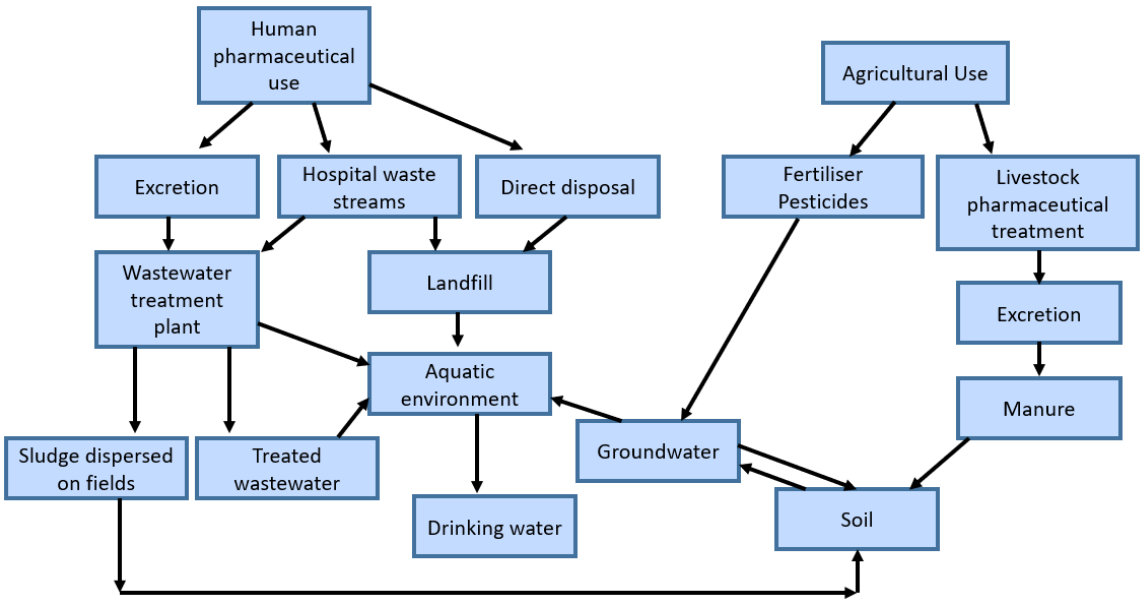

Figure 1.4: Pathways used by micropollutants in water to travel through the environment. Adapted from references [44-46]

Additionally, these compounds come from a wide variety of sources and can travel through the aquatic environment due to their polar nature, leading to delocalisation of pollutant molecules across the water and soil environments, with the eventual occurrence and build up in human food chains and the wider anthroposphere.

As such, in order to prevent the release of micropollutants into the environment, there is a need for improved water treatment processes to remove micropollutants from wastewater.

1.2. Advanced Oxidation Processes (AOP)

Advanced oxidation processes is the name given in the 1980's to the oxidative processes able to generate hydroxyl radicals in the quantities required to purify water,[47] as these hydroxyl radicals are powerful oxidizing agents able to destroy organic pollutants in wastewater.[48] As such, they provide a promising approach for the removal of organic micropollutants from water.[49] AOP is a broad title encompassing a wide variety of reactions, with AOP technologies utilising many different methods for activation and oxidant generation for the formation of hydroxyl radicals and the destruction of organic components. A generic AOP reaction scheme is shown below:

$$Organic\ Pollutant \xrightarrow{Hydroxyl\ Radicals} H_2O + CO_2 + Inorganic\ Ions$$

Equation 1.1: Pollutant mineralisation via hydroxyl radicals.

Hydroxyl radicals are the most reactive oxidising agent used in water treatment, with the oxidation potential between 2.80 – and 1.95 V at pH 0 and 14 respectively, versus SCE (saturated calomel electrode).[7] These radicals, though nonselective, react rapidly with rate constants in the order of 10^8-10^{10} M^{-1} s^{-1}.[50-52] Hydroxyl radicals attack organic compounds in four pathways: radical addition, hydrogen abstraction, electron transfer and radical combination.[53] Compound with regions of high electron density, such as carbon double bonds or aromatic rings are more reactive towards hydroxyl radical attack than saturated molecules, with the reactivity also being proportional to molecular weight and inversely proportional to the oxidation level.[54]

As stated previously, AOP is a broad title, covering physical, chemical, electrochemical and photochemical processes for the formation of hydroxyl radicals, with the most established types being ozone or UV-based, or Fenton type processes as seen in Figure 1.5.

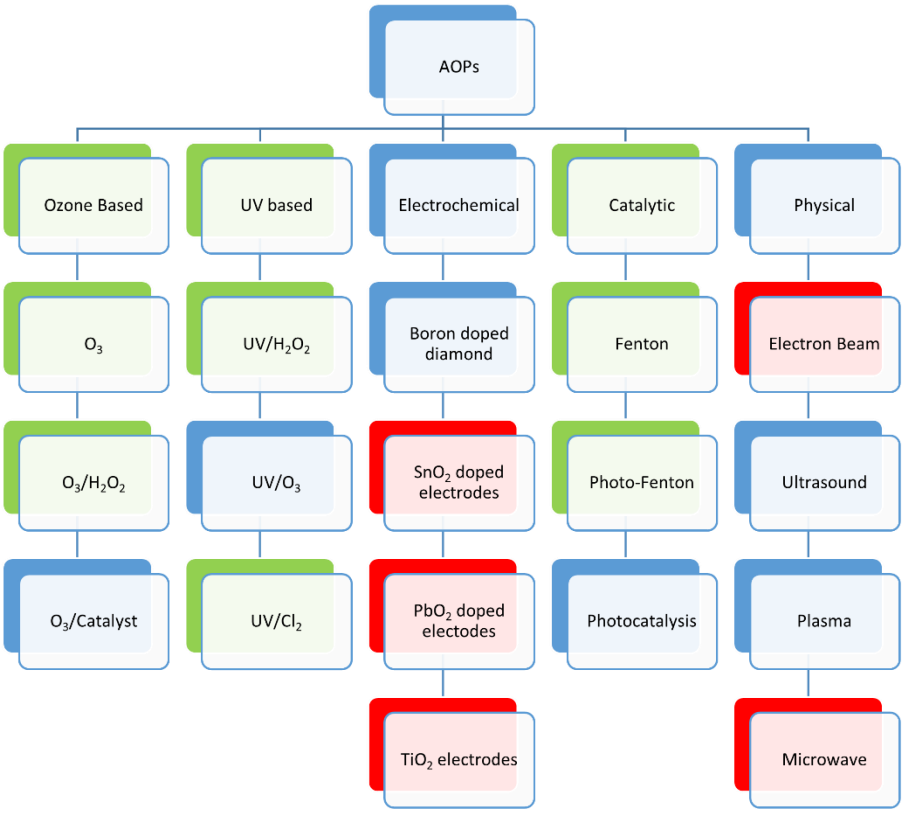

Figure 1.5 Broad overview and classification of AOPs.

Processes marked according to established scale, Red – Lab based, Blue – Pilot scale, Green – Full scale.

Adapted from ref [55]

Ozone-based AOPs have seen widespread usage in water treatment as ozone itself acts directly as an oxidant for organic degradations, albeit a weaker and more selective one compared with hydroxyl radicals.[47] While hydroxyl radicals will react with most organic groups regardless of oxidation state or saturation (although electron dense functional groups are more reactive), ozone reacts with electron rich functional groups such as amines, double bonds, or aromatic rings.[55] In addition to this, in an aquatic environment, ozone decomposition and reaction with water forms hydroxyl radicals to further degrade organic pollutants.[18, 56] This can be enhanced through the addition of H_2O_2 as the process of hydroxyl formation with ozone alone is very slow with formation rates of 70 $M^{-1}s^{-1}$.[57] The increased presence of hydroxyl

radicals further enhances the removal capabilities of ozone based AOPs due as the less selective radicals can remove contaminants deemed recalcitrant to ozonation.

Due to the rapid degradation of ozone however, it has to be generated *in situ* and constantly supplied to the reactor.[58] In addition to this, more widespread use of ozone-based AOPs is hindered due to the formation of degradation by-products such as bromate compounds which pose a hazard to human health.[59] The addition of H_2O_2 to increase the reactivity of ozone-based systems requires an additional treatment step to ensure the H_2O_2 is destroyed prior to release to the environment, increasing the cost of the process.[55]

UV-based processes require a combination of UV irradiation and a suitable oxidant, often ozone or hydrogen peroxide, as the UV irradiation alone is insufficient to induce significant photolysis and removal of micropollutant compounds.[60] Hydrogen peroxide undergoes photolysis to two hydroxyl radicals, while ozone cleavage leads to the formation of highly energetic atomic oxygen which reacts with water to form H_2O_2 which, as before, degrades to form hydroxyl radicals.[61] UV/H_2O_2 systems are limited by their low molar absorption coefficient,[50] requiring high concentrations of H_2O_2, which, in turn, requires removal of the excess peroxide from the effluent.[57] Additionally, photolysis based systems are highly dependent on the UV adsorption of the compound and, as such, micropollutants show low removal efficiencies under UV irradiation, requiring high UV doses, up to an order of magnitude higher than other AOP-based systems.[62] Furthermore, as mentioned previously, the H_2O_2 required to increase the efficiencies must be treated and destroyed prior to release.

Catalytic AOPs fall into two main categories, Fenton related AOPs and photocatalysis. Fenton processes feature hydrogen peroxide decomposed at the surface of an iron catalyst, through the oxidation of Fe^{2+} to Fe^{3+} to form hydroxyl radicals,[47, 63] while photo-Fenton processes improve the efficiency through the use of UV irradiation to couple photolysis with catalytic cleavage of the peroxide molecules, couple with the reduction of Fe^{3+} species back to Fe^{2+} to facilitate peroxide decomposition.[64, 65] The iron complexes used in Fenton processes have two key drawbacks, the generation of hydroxyl radicals is most effective at acidic pH while wastewater treatment plants operate at higher pH, requiring pre-treatment of the influent, thus increasing running

costs. Furthermore, the rate at which the oxidised Fe^{3+} ions are reduced is significantly slower, resulting in the formation of an iron sludge that is non-catalytic and requires separate disposal.[47]

Even with their specific drawbacks, AOPs show advantages over traditional wastewater treatment methods discussed previously, such as higher degradations and non-selectivity due to the hydroxyl radicals. AOPs have been employed for the degradation of antibiotics, such as amoxicillin,[66] and pharmaceuticals including carbamazepine and diclofenac.[67] Physical treatment steps such as adsorption to activated carbon are able to remove micropollutants but have no chemical effect on the structure, leading to the concentration of micropollutant that still needs to be treated. [68]

Furthermore, AOPs are hindered by more complex water matrices, with dissolved organic and inorganic species having multiple inhibitory effects, including acting as hydroxyl scavengers, competing with the targeted organic compound, increasing the light attenuation, and in the case of heterogenous systems, adsorption and other fouling effects. These inhibitory effects are highly variable and matrix dependant but, in all cases, reduce the efficiency and effectiveness of treatment.[69, 70]

As such, further research into AOPs is required.

1.3. Photocatalysis – Fundamental Principles

Regarding the history of photocatalysis, one of the first reported papers on the phenomenon regarded the use of TiO_2 powders for the bleaching of dyes under oxygen and vacuum conditions.[71, 72] The discovery of the water splitting capability of TiO_2 by Fujishima and Honda, wherein exposure to near UV light and a platinum black counter electrode could lead to the formation of gaseous oxygen and hydrogen at the titania and platinum electrodes respectively, and opened the possibility for the production of hydrogen gas as an alternative fuel source,[73] lead to an increased interest for research in the area.[74] Since then, photocatalysis has found use within a wide range of areas including water splitting,[75] self-cleaning surfaces,[76, 77] disinfection,[78-80] and chemical synthesis.[81-84]

In photocatalysts, the band gap corresponds to the energy of the incoming photon of light required to excite electrons from the valence to conduction band, forming an electron-hole (e^-h^+ pair) that are then responsible for the subsequent photochemistry, which will be discussed later.[85]

When predicting and modelling the electronic structures of bulk materials such as semiconductors it is useful to apply Band Theory. This model considers the electronic structure of the bulk material to be derived from a linear combination of atomic orbitals (LCAO) of the individual atoms that make up the crystal. As the two atomic orbitals (AOs) combine they form two molecular orbitals (MOs), a lower energy, stabilised bonding orbital and a higher energy, destabilised antibonding orbital. Increasing the number of AO's in the model to four means that we will form 4 MO's, two bonding and two antibonding. Due to varying degrees of orbital overlap, when dealing with more than two AO's and MO's, the bonding (and antibonding) orbitals are of marginally different but quantised energies and this energy difference decreases as the number of molecular orbitals formed increases. When considering a bulk structure in semiconductors it is convention to consider an infinite number of atomic orbitals and as such there will be an infinite number of molecular orbitals formed each with an infinitely small energy gap between them. At this point the molecular orbitals are no longer considered to be quantised and are instead considered as two continuous bands of energy, with the bonding orbitals forming the valence band and the antibonding orbitals forming the conduction band. A simplified diagram of this is shown below in Figure 1.6 which shows the formation of energy bands within the bulk structure of a semiconductor using based on a 1 electron system.

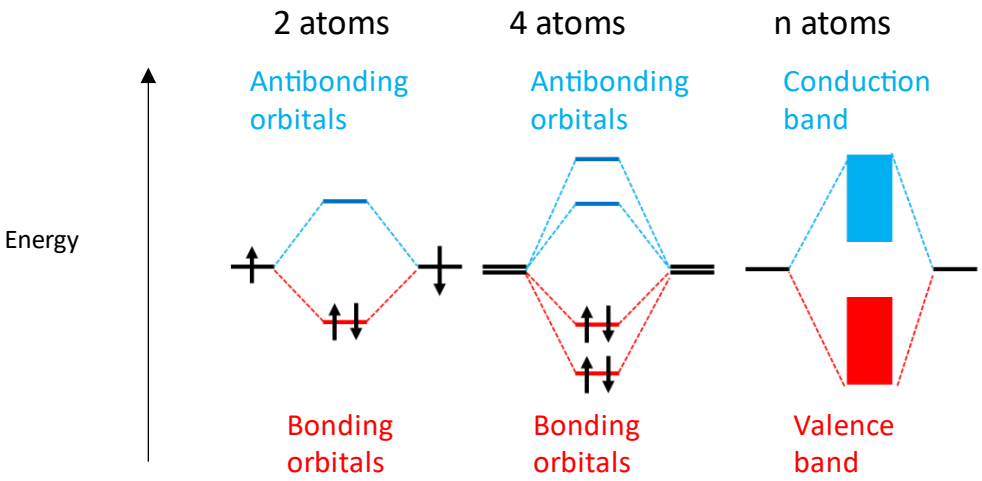

Figure 1.6: A simplified diagram showing the formation of energy bands through combination of multiple atomic orbitals

For more complex binary systems, with a focus on metal oxides, the inherent difference in energy levels between the metal orbitals and oxygen orbitals (although this is also true for other anions including nitrides and sulphides to varying extent) leads to an energy difference in the formed valence and conduction bands with this energy difference referred to as the band gap.

The energy of the band gap determines the materials properties, in particular whether the material acts as a conductor, semiconductor or insulator as shown in Figure 1.7. If the energy difference between the valence and conduction bands is sufficiently large that promotion of an electron from the valence band to the conduction band cannot occur, thus preventing the movement of charge and flow of current, the material shows insulating properties. On the other hand, conductors have continuous energy bands allowing for movement of electrons, and therefore a flow of charge.

Meanwhile, semiconductors have a sufficiently narrow band gap that a only a small addition of energy to the material is required to facilitate promotion of electrons from the filled valence band to the empty conduction band (1.5 - 3.5 eV). This means that the addition of thermal energy is often sufficient to allow a movement of electrons and a flow of charge, resulting in the temperature dependence of semiconductors and their use in electronic devices such as thermistors.

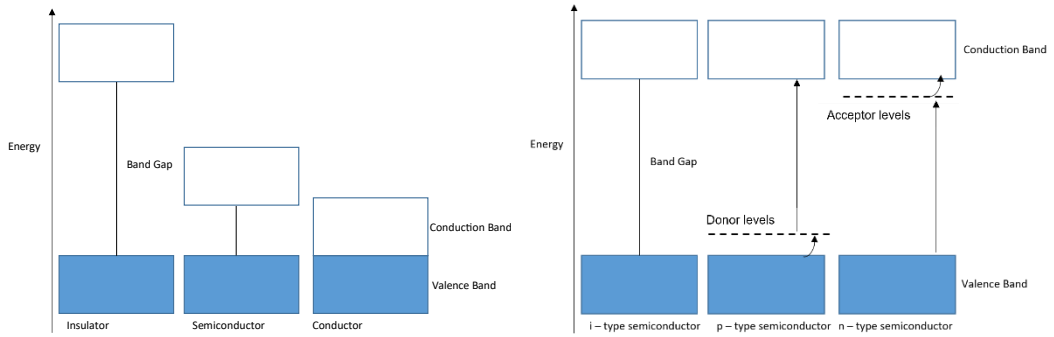

Figure 1.7: (Left) A diagram depicting the band structure of an insulator and a semiconductor material. (Right) A diagram showing the band structure of intrinsic and doped semiconductors and the differences between them. Adapted from reference [86]

Furthermore, semiconductors can be considered either to be intrinsic or extrinsic: Intrinsic, or i-type, semiconductors are formed of a pure, un-doped material, e.g. silicon,[87] while extrinsic semiconductors are those that are made up of multiple elements, either as a binary (or higher order) material or one that contains dopants. The latter can be further categorised depending on the nature of the effect the incorporation of secondary elements has on the band structure, and whether the dopant atoms form acceptor or donor levels, as can be seen in Figure 1.7. Semiconductors made with dopants that are electron deficient relative to the host material are classified as p-type semiconductors.[88] The electron deficiency of the dopant atoms (or the presence of holes) appears as electron acceptor levels below the conduction band. The presence of these acceptor states increases the mobility of the electrons within the valence band as they move up into the acceptor levels, leading to a flow of charge and leaving a partially filled valence band along with an e^- h^+ pair that can be used for photochemical or photocatalytic reactions.

In the case of semiconductor materials where the dopant atoms are more electron-rich than the host, these are referred to as n-type semiconductors and the increased electron density of the dopant atoms appear as electron donor levels above the valence band. Flow of charge occurs in this case as the electrons move from the donor level to the conduction band, once again forming an electron-hole pair.[88]

In order to classify a semiconductor as a photocatalyst it must have two main properties: Firstly, the band gap of the semiconductor must correspond to the energy levels of photons found in solar rays, in particular visible and UV photons, to allow

for excitation of electrons from the valence band to the conduction band under irradiation. Secondly, the energy levels of the valence and conduction bands must lie either side of the redox potential of the desired redox products so as to enable the desired reactions to proceed.

Considering the reduction of oxygen into superoxide radicals and the oxidation of water into hydroxyl radicals, as shown in Figure 1.8, the redox potentials of these reactions are -0.28 V Vs Standard Hydrogen Electrode (SHE) and +2.27 V Vs SHE respectively,[89] which leads to an overall minimum band gap of 2.55 eV required to effectively promote this reaction.

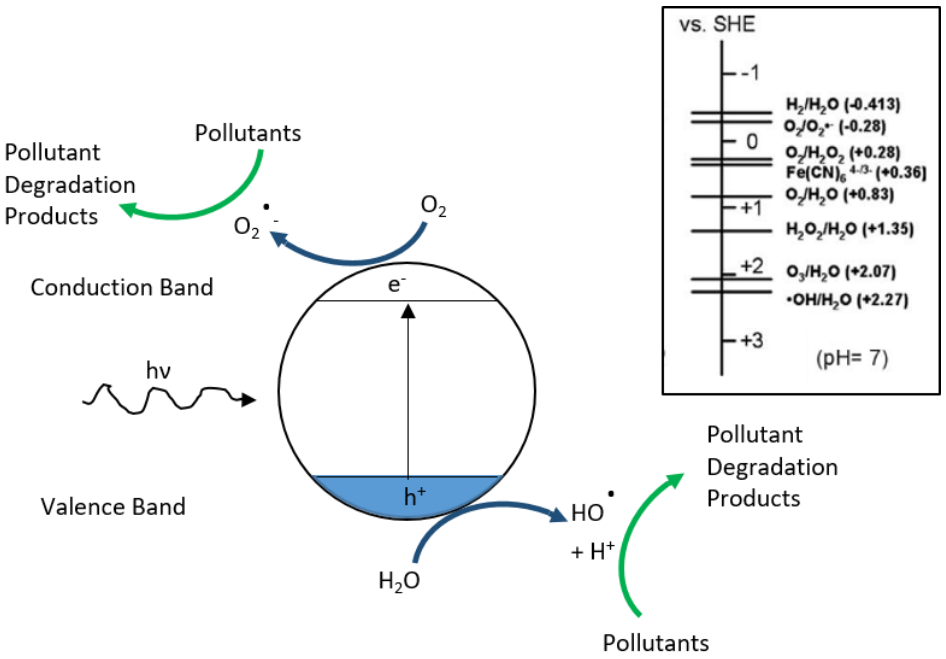

Figure 1.8: A diagram showing the formation of charge carriers and photocatalytic breakdown of pollutants with the potentials of redox processes that occur. Adapted from references [89, 90]

Photocatalysts exposed to a suitably high energy light source and an oxidant such as air or oxygen can cause organic pollutants to undergo breakdown. Absorption of photons of light with energy greater than the band gap of the material leads to the formation of an electron-hole pair in the conduction and valence bands, respectively.[91] The positive hole formed in the valence band oxidises water to produce the hydroxyl radical (•OH) or oxidises organic pollutant adsorbed to the photocatalyst surface directly, and the electron in the conduction band reduces

oxygen molecules in the water, or is adsorbed on the surface of the material to form superoxide radicals that then undergo sequential reduction to water molecules.[92] This can be represented by the following reactions:[93]

Activation of photocatalyst:

$$\text{Photocatalyst} + h\nu\ (E \geq E_g) \rightarrow e^- + h^+$$

$$e^- + O_2 \rightarrow O_2^{-\bullet}$$

Photo-oxidation reactions:

$$h^+ + \text{pollutant} \rightarrow \text{degradation products} \rightarrow H_2O + CO_2$$

$$h^+ + H_2O \rightarrow {}^{\bullet}OH + H^+$$

$${}^{\bullet}OH + \text{pollutant} \rightarrow \text{degradation products} \rightarrow H_2O + CO_2$$

Photo-reduction reactions:

$$O_2^{-\bullet} \rightarrow H_2O_2 \rightarrow {}^{\bullet}OH \rightarrow H_2O$$

Equation 1.2 Photo-redox reactions for the photocatalytic degradation of organic compounds.

These advanced oxidation processes take place within the reactant solution but can be further classified depending on the state of the oxidant or catalyst relative to the reactants:

Homogenous photocatalysis refers to systems where the reactant and catalyst or oxidant are in the same physical state and include systems that use dissolved hydrogen peroxide and its subsequent decomposition to form •OH radicals, that then go on to degrade pollutants as shown in equation 1.2 above.[93] UV/Ozone systems are another alternative to facilitate homogenous photo degradation of pollutants as the dissolved ozone radicals decompose in water under UV irradiation to form the hydroxyl radicals required for the degradation.[54]

Heterogeneous catalysis on the other hand is used to describe a system where the catalyst or oxidant are in a different physical state to the reactant, e.g. often a solid, supported catalyst or as a slurry. In these systems, oxidation can occur either directly, where the micropollutant adsorbs onto the surface of the catalyst and is oxidised by holes at the catalyst surface, or is oxidised indirectly, where the hydroxyl radicals react and lead to the decomposition, as discussed earlier. In systems using direct oxidation, the process of the reagent reaching the catalyst surface has to be taken

into consideration as the rate at which the reagents are brought into contact with the active surface can have an effect on the overall rate of the reaction.[1]

Shown in Figure 1.9 are the steps involved in a reaction occurring at a catalyst surface: Step 1 involves the transport of a reagent molecule (either organic pollutant or water) to the catalyst surface; step 2 is the adsorption of the reagent to the surface; step 3 in is the photocatalytic reaction in which reagents, R, are converted to products, P; followed by desorption from the surface and transfer away from the surface and into the bulk, steps 4 and 5, respectively.[94]

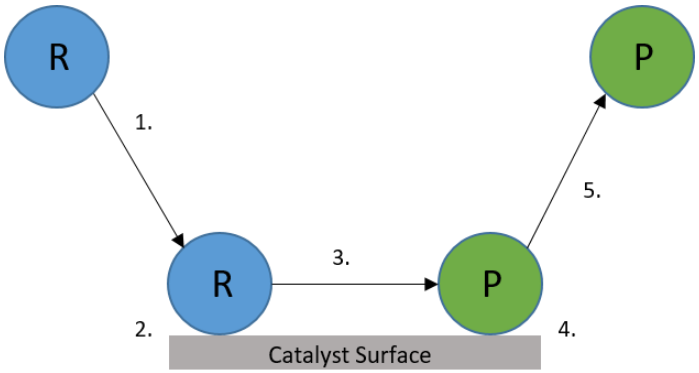

Figure 1.9: Schematic depicting the steps occurring during advanced oxidation processes at a catalyst surface. Adapted from reference [94]

Given this complex process the overall rate of a reaction is considered to be equivalent to the slowest step. When the rates at which reactants are brought to the surface and products are removed from the surface (steps 1 and 5) are fast in comparison to the reaction step, they are not considered to be rate limiting and as such are not considered when determining the reaction rate.[94]

For a photocatalyst to be applied in water treatment, the material choice must fulfil certain specifications, such as being photocatalytically active, chemically and photochemically stable (resistant/immune to photocorrosion), insoluble in wastewater at a range of pH, non-toxic and economically viable.[95] A range of materials have been used as photocatalysts, including ZnO, TiO_2, SnO_2, WO_3, CdS, Fe_3O_4 and Cu_2O,[96, 97] as well as carbon based and metal-free photocatalysts including graphitic carbon nitride (g-C_3N_4).[98-101] Tungsten oxide (WO_3), tin oxide (SnO_2) and copper oxide (Cu_2O) are limited by their poor stability and high rates of electron-hole

pair recombination.[102-104] CdS exhibits photocorrosion in water to Cd^{2+} and sulphate ions (SO_4^{2-}),[105] and the toxicity of Cd limits its use in water treatment applications.[106, 107] Carbon-based photocatalysts are hindered by high production costs, limiting their wider adoption.[108] Zinc oxide (ZnO) and titanium dioxide (TiO_2) are the predominant materials used for photocatalysis at present, due to their relatively low cost, similar degradation mechanisms and capability for use as disinfectants, in addition to photocatalysts.[97] ZnO and TiO_2 are examples of large band gap semiconductors, with band gaps in excess of 3.0 eV, requiring illumination by UV irradiation (λ <400 nm) accounting for less than 5% of the solar spectrum as shown in Figure 1.10.[109]

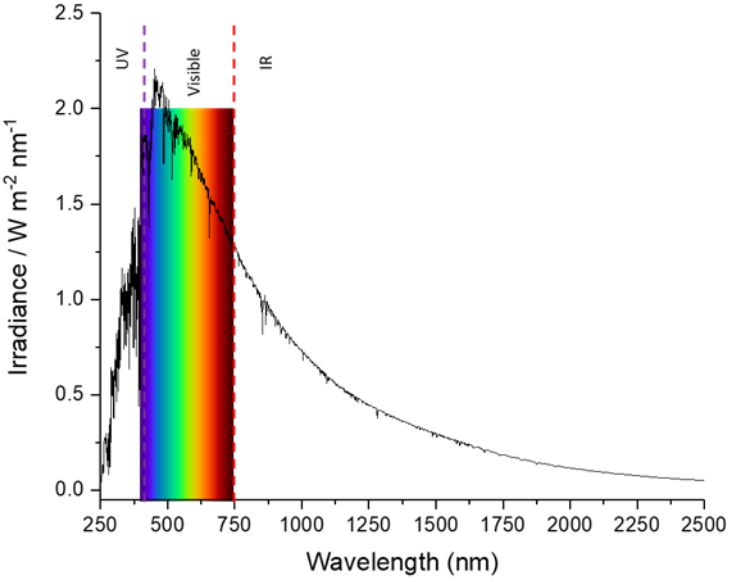

Figure 1.10: Solar spectrum showing UV, visible and infra-red regions. Adapted from reference [109]

As such, solar irradiation is not suitable for promotion of electrons to the conduction bands of the photocatalyst, meaning dedicated UV sources are required, increasing the cost of these systems.[55] Doping of the catalyst surface is one potential method for reducing the band gap and increasing the range of wavelengths absorbed into the visible spectrum, as well as reducing the rate of electron-hole pair recombination. This will be discussed in greater depth in section 1.6.

Photocatalysis is promising as a method of water treatment as it can mineralise organic pollutants, rather than transferring them to an alternate phase, e.g. activated carbon, which the requires further containment, treatment or disposal. Furthermore

photocatalysis does not require the addition of hazardous materials such as ozone or peroxide.[110] To this end, pilot scale testing of photocatalysis for water treatment has been demonstrated effective for the removal of pharmaceuticals from wastewater,[111-113] the treatment of water from agricultural and concentrated animal feeding operations (CAFO),[114-116] as well as treatment of wastewater from textile industries.[117-119] However issues remain as UV/photocatalytic systems are more energy intensive than other AOPs,[55] and while this may be abated by the use of more efficient UV LEDs, at present, more research is required into improving the efficiency of these systems.

1.4. Photocatalytic Reactor Design

While extensive research into photocatalyst materials has been conducted, less vigour has been applied to the study of photocatalytic reactor design, an equally important area of study. The design of the reactor will impact the efficiency and suitability for scaled up applications and therefore needs to be taken into consideration when creating a photocatalytic set up.

While multiple reactor designs exist - a recent review discussed 28 different reactor designs[120] - the current state of the art focusses on 4 different design types: slurry, immobilised, membrane and fluidised bed reactors,[121] as shown in Figure 1.11, with foam based reactors, the focus of this work, emerging as a 5th main type.

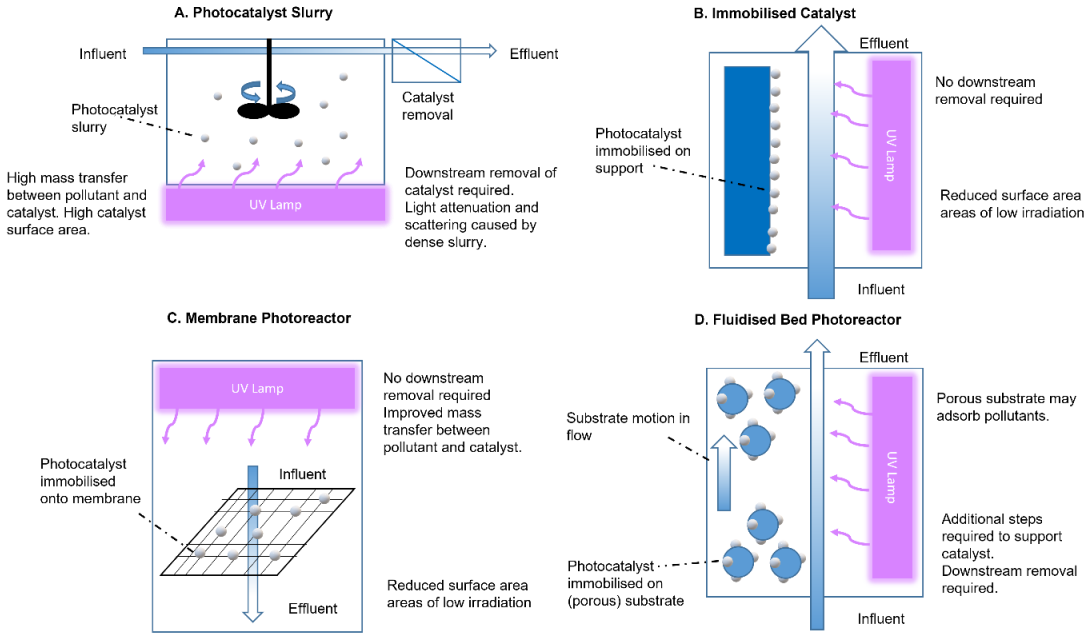

Figure 1.11: Graphical summary of the 4 main photocatalytic reactor designs. Modified from reference [121].

Slurry-type reactors are the most highly researched type of photocatalytic reactor used in a laboratory setting. These reactors use a suspension of photocatalyst particles, usually in the nanometre range, within the reaction solution allowing for utilisation of the photocatalysts' high surface area to be in contact with the reaction solution,[97, 122] thus providing (i) a larger area for the adsorption of reagents to the photocatalyst,[123, 124] and therefore, potentially higher rates of degradation; and (ii) a larger surface area to receive photons to promote the formation of the electron hole pairs required for the reaction to proceed.[125, 126]

The large contact area between the photocatalyst and the pollutant solution when suspended, assuming adequate mixing or agitation occurs, means that the distance between the catalyst and reactants (or products) is minimised and, as such, the diffusion to and from the catalyst surface increases. This leads to a decrease in the time required for reactants in the flow to diffuse to the catalyst, resulting in faster reaction kinetics. By increasing the rate at which the mass transfer occurs, such that it is occurring much quicker than the reactions at the surface, mass transfer steps are not considered to be rate limiting and therefore do not affect the overall rate of reaction,[94] as was shown in Figure 1.9.

The main drawback of slurry systems is that they require downstream removal of the catalyst which will result in increased cost and complexity of the reactor system.[127] Considerations need also to be paid to the potential negative impacts of the release of nanoparticles into the environment. Similar to micropollutants, when released into the environment, nanoparticles are able to bioaccumulate within marine animals and eventually make their way into the anthroposphere, while also showing the potential to accumulate within plant cells as well as mammalian ones.[128] Furthermore, it has been shown that there is the potential for synergic interactions between catalyst nanoparticles and pollutants present in the environment, such that the toxicity of both compounds is amplified.[128] Additionally, particular care needs to be taken regarding the concentration of the photocatalyst in the slurry as it has a negative impact on the light penetration into the slurry, and therefore on the photocatalytic activity.[125] A recent study into the degradation of chlorpyrifos (CPS) and endosulfan (ES), found that in both cases a twofold increase in the concentration of TiO_2 particles in the slurry led to a ten percent decrease in the rate constant of the degradation of both pesticides.[129] Similar findings were also reported using slurries of nano-ZnO as a photocatalyst in the degradation of two more pesticides, parathion (PA) and methyl parathion (MP), reporting a decrease in the rate constant and the overall reaction rate in both cases over a range of concentrations.[130]

Conversely to slurry reactors, immobilised (or fixed bed) photocatalyst reactors use photocatalysts that are fixed within the reactor and the reaction solution is flowed over, across or through the surface.[131] One basic design involves the coating of the inner wall of the reactor with photocatalyst usually through repeated dip coating into suspensions of photocatalyst, followed by calcination, to form highly crystalline films and improve adherence to the support.[132] Similarly, a fixed bed reactor using glass beads or rings that have been coated in photocatalyst has also been reported,[125] with a schematic representation of these shown in Figure 1.12. Immobilised catalyst reactors have also made use of fibre optic cables,[133, 134] and metallic meshes,[135, 136] as supports for photocatalysts. The material used as a support is required to be heat- and UV-resistant, while also resisting oxidative treatment and environments, in order to be suitable for catalyst immobilisation and operation, respectively.[137] A range of

substrates have been used as supports, including glass,[138-140] quartz,[141, 142] carbon nanotubes, [143] and concrete.[144]

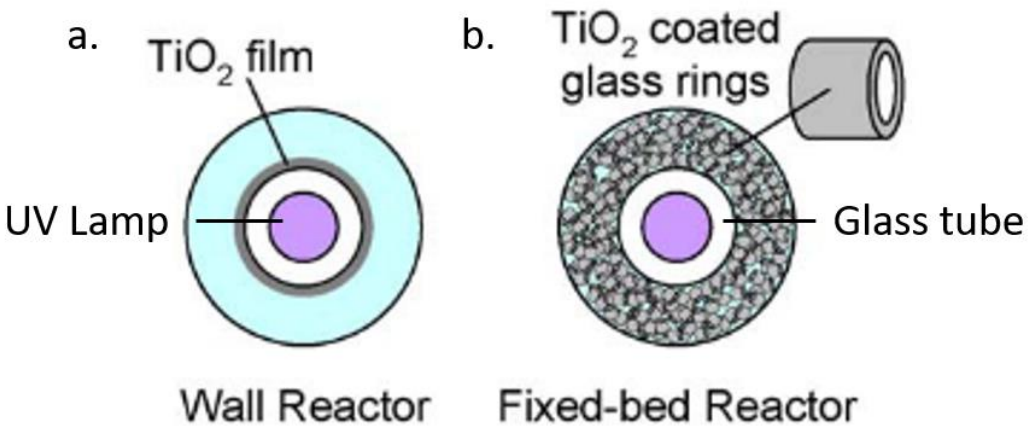

Figure 1.12: Schematic to show two methods of photocatalyst immobilisation in reactors.

Adapted from reference [132]

The primary advantage of immobilised catalyst reactors over slurry reactors is the removal of the catalyst recovery step during the process, eliminating any downtime in the reaction process. In addition to this, supported photocatalysts on a support that is inherently a suitable adsorbent for reactants can improve the removal of organic matter from the flow, allowing for increased reaction rates as the reagent and catalyst are brought into contact with each other at a greater rate.[127, 145]

A major drawback of immobilised catalysts is that these reactors suffer from a lower surface area in contact with the eluent stream which leads to lower rates of reaction and efficiencies.[126] Another disadvantage of the immobilised catalyst is that of light scattering and absorption of radiation by external media: The photocatalyst must be irradiated before it is able to catalyse any reactions and immobilisation onto a support can prevent this, if the support is not entirely transparent to the light required to activate the photocatalyst, thereby reducing or blocking entirely the number of photons activating the catalyst.[146, 147] This is also an issue for porous photocatalysts and those on porous supports, with the catalyst within the pores receiving less irradiation as the support or the photocatalyst itself on the outside of the pores will absorb the light and prevent it from reaching the catalyst.[131, 146]

Furthermore, over time the photocatalyst can become detached from the support and leach into the stream. The impact of this is that the catalyst is no longer acting as an immobilised entity and as such any reactor design around this may no longer be suitable: For example, if no downstream separation is in place, there is the risk that the photocatalyst will be lost or released into the wider environment, ending up with the same limits of slurry-based systems but not their advantages.[148-150]

Another drawback of immobilised catalyst reactors is the distance between catalyst and pollutant, leading to long diffusion times resulting in low kinetics as the pollutant must first reach the surface of the photocatalyst before they are able to adsorb and then be degraded as shown in Figure 1.9. They must then desorb and travel away from the surface. It is the diffusion steps of this process that limit the reaction as compared to the transfer of electrons between the activated photocatalyst and the pollutant.[94] This is most evident in the case of batch reactors where insufficient perturbation of the solution can lead to the formation of concentration gradients which can lead to mass transfer limitations.[94, 151] On the other hand, when the photocatalytic reactors are run as flow reactors or with a recirculating system, it is possible to reduce the mass transfer limitations to negligible levels by ensuring that the flow is sufficiently turbulent, and the flow rate is sufficiently high.[151, 152]

An area of interest is the combination of membrane separation with AOPs, particularly photocatalysis. These hybrid systems, known as photocatalytic membrane reactors (PMR), involve immobilising photocatalyst onto or within a porous membrane which influent is passed across,[153] leading to the removal of pollutants and simultaneous separation of photocatalyst, eliminating the need for downstream removal. An alternative operating configuration is the use of a catalyst slurry with membrane separation as part of the reactor, rather than as part of downstream removal.[154] These are shown in Figure 1.13. In addition to this, control over the pore size, and thus filtration type (micro-,[155, 156] ultra-,[157] or nanofiltration[158]), allows for greater control over the removal and quality of the permeate.[1]

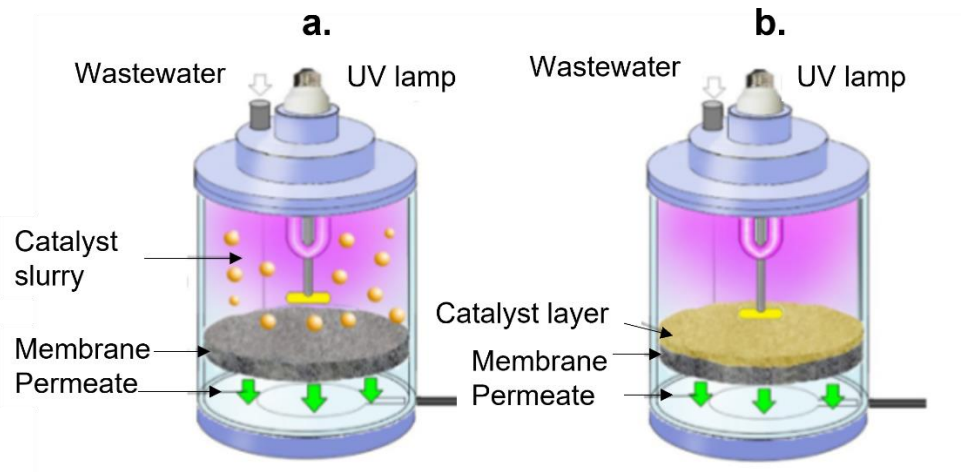

Figure 1.13 Configurations of PMRs where the photocatalyst is a) suspended as a slurry, b) immobilised onto membrane. Adapted from reference [159]

As a hybrid technology, PMRs bring a range of advantages from the separate techniques that make them up, as well as potentially mitigating some of the drawbacks. One key advantage is the removal of any downstream removal requirements, similar to immobilised reactors. PMRs that use a photocatalyst slurry also benefit from the high surface areas of catalyst present that are associated with slurry reactors. Furthermore, traditional micro- and ultrafiltration membranes are unable to remove micropollutants and, as such, are restricted to use as a pre-treatment for the removal of natural organic matter.[160] Combining these membranes with photocatalytic material, allows the use of lower levels of filtration, compared with nanofiltration or reverse osmosis, which have significantly higher running costs.[161] Additionally, the combination of photocatalyst with membranes leads to a reduction in the rate of membrane fouling, as the presence of photocatalyst leads to a breakdown of the foulant at the membrane surface.[159, 162]

As a hybrid technology, PMRs are also hindered by the drawbacks of its constituent parts. As with all photocatalyst systems, loss of catalyst needs to be monitored as, after extensive use, PMRs can show loss of activity, either through material from the slurry passing through the membrane into the permeate or from loss of adherence from within the membrane.[159] Secondly, while the presence of the photocatalyst may lead to the degradation of pollutants in the system, they are not 100% effective at reducing fouling and, in the case of slurry systems, can cause or even exacerbate fouling of the membrane as particles become caught in the pores of the membranes,

causing blockage.[162] Furthermore, when immobilising photocatalyst onto a membrane, care needs to be given to the membrane material, due to the exposure to UV and oxidising species that will be present during operation. Polymeric membranes may be less suitable for use in these reactors due to the potential for damage to occur after exposure to UV and hydroxyl radicals.[162]

A fourth type of reactor design – fluidised bed reactors involve the use of photocatalytic particles immobilised onto a solid support, which when fluid or air flow is applied, becomes suspended and thus acts like a slurry system.[163] The inert supports used frequently tend to be beads of similar materials used for immobilised photoreactors, such as glass, due to the ease of adhering the photocatalyst.[164, 165]

The advantages of fluidised bed reactors are the low pressure drop within the system, reducing any inhibitory effects on flow through the system which may impact diffusion times of pollutant and subsequently lower the kinetics of the system.[110] Additionally, owing to the upward stream required to "fluidise" the catalyst, these reactors are often operated as recirculatory or flow systems leading to higher throughput of the reactor.[166] Additionally, the porous nature of the supports allows for large surface areas to be coated in catalyst and can lead to removal of pollutant via adsorption.[167] The benefits of high surface area are further enhanced by the fluidisation of the reactor, leading to a "slurry like" system with the benefits of surface area of slurries discussed previously.

Similar to slurry reactors, the disadvantages of fluidised bed reactors are the need for downstream removal of any support material and catalyst that may be lost during operation, as well as the potential for excess catalyst presence, leading to light attenuation and reduction in activity.[164]

As mentioned briefly, foam-based photocatalysts show promise as a potential new reactor design. These systems make use of a highly porous, monolithic structure to provide high surface areas, similar to slurry systems while providing the stability of immobilised catalysts, thus removing the need for downstream removal. This foam structure tends to be produced in one of three ways: Use of a porous substrate, usually mechanically stable and non-photocatalyst, to which photocatalyst is

adhered. Use of a sacrificial porous structure which is coated in catalyst before being removed, to leave a porous structure of photocatalyst. Finally, foams produced without a substrate, through the use of liquid templating or sol-gel synthesis. These shall be discussed in greater depth later in Chapter 2

Multiple comparisons between different reactor types have already been made discussing the photocatalytic efficiencies. One review compared the activity of TiO_2 as a slurry or immobilised as a film or fixed bed for the photocatalytic disinfection of E.Coli,[132] within an annular reactor (Figure 1.14).

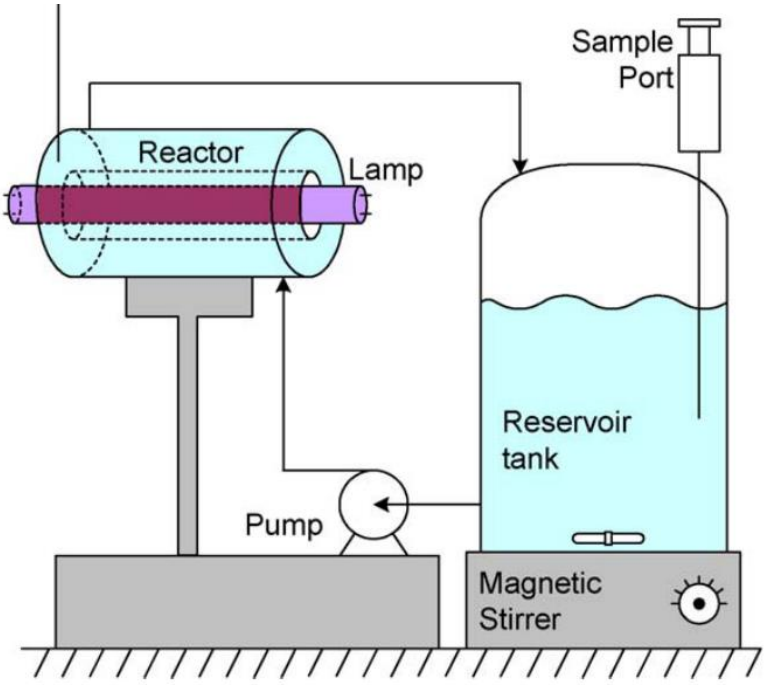

Figure 1.14: Schematic representation of reactor used to study photocatalytic disinfection of E.Coli. Abstracted from reference [132]

It was found that while the supported TiO_2 showed lower removal rates than an equivalent mass of slurry, they also showed less inhibition due to dissolved organic content, and thus showed comparable activity when applied with a more complex matrix. Additionally, it was shown that the immobilised catalyst was stable and able to be applied in continuous systems.

A complementary study into the efficiency of TiO_2 for the removal of the pharmaceutical clofibric acid,[125] this time using an experimental set up with UV lamp positioned perpendicular to the reactor and photocatalyst. Similarly, TiO_2 was used

as a slurry and immobilised, this time onto the reactor window and glass beads (Figure 1.15).

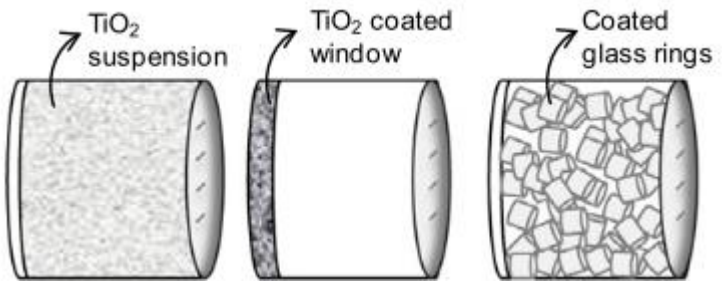

Figure 1.15: Schematic representation of the reactor configurations used for the degradation of clofibric acid. Abstracted from reference [125]

The results of this study found that the slurry system showed the highest kinetics and quantum efficiencies, although the slight decrease shown by the fixed bed set up relative to the slurry was deemed highly promising for applications, with the efficiency increased with thicker TiO_2 films on the beads.

Both studies showed an inherent drawback of slurry systems, the need for catalyst separation after degradation. In both studies, prior to analysis, the solutions were centrifuged and filtered through either a 0.02- or 0.22 μm filter, a process that is both time and cost intensive.

Other reviews have shown a wide variance in types of photocatalytic reactor as well as the multiple operating parameters that can be assessed, including:[120]

- Space-Time Yield (STY) which considers the processing volume of a reactor relative to the volume of the reservoir and how much pollutant can be processed from 100 mM to 0.1 mM.[168]
- Electrical energy per Order (E_{EO}) which considers the electrical energy required to reduce the concentration of a pollutant by an order of magnitude (90%) in 1 cubic metre of water. [169]
- Quantum Yield/Efficiency which considers the ratio of degradation of pollutant per photon absorbed by the system, often calculated using the ratio of the rate constant of the system and the photon flux.[170] The usage of quantum efficiency is preferred over quantum yield as the former requires incident irradiation as opposed to attenuated irradiation, allowing for ease of

comparison between systems using different pollutants, while the latter requires information on the number of absorbed photons and often assumes negligible scattering, which is not applicable to heterogenous photocatalysis as solid particles (suspended or immobilised) will lead to photon scattering.[171]

Reactor design is a key factor in photocatalytic efficiency and the optimisation of the reactor will lead to enhanced performance of the photocatalyst. As such, reactor design will be a key area of investigation in this thesis.

1.5. ZnO

ZnO is a highly researched material both within and without the field of photocatalysis,[172] with its properties highly dependent on its structure, including morphology and crystal size.[172] ZnO shows ideal properties for photocatalysis including a UV active and direct band gap of 3.2 eV,[173] similar to TiO_2 . In addition it is able to absorb a greater fraction of the solar spectrum than TiO_2,[174, 175] between 470 and 350 nm while TiO_2 absorbs in the much narrower range of 420 to 400 nm.[176] ZnO also shows greater electron mobility,[177] and longer electron lifetimes than TiO_2 photocatalysts.[178] Additionally ZnO is a markedly cheaper a material, having production costs of around 25% of that of TiO_2 when comparing the cost of production of metal oxide nanoparticles.[179]

ZnO, like most other II-VI binary compounds, shows two main crystal phases, hexagonal closed packed wurtzite structure and a cubic close packed zinc blende structure. Both wurtzite and zinc blende crystal structures show AB stacking of alternating Zn^{2+} and O^{2-} ions in a tetrahedral coordination as shown in Figure 1.16:

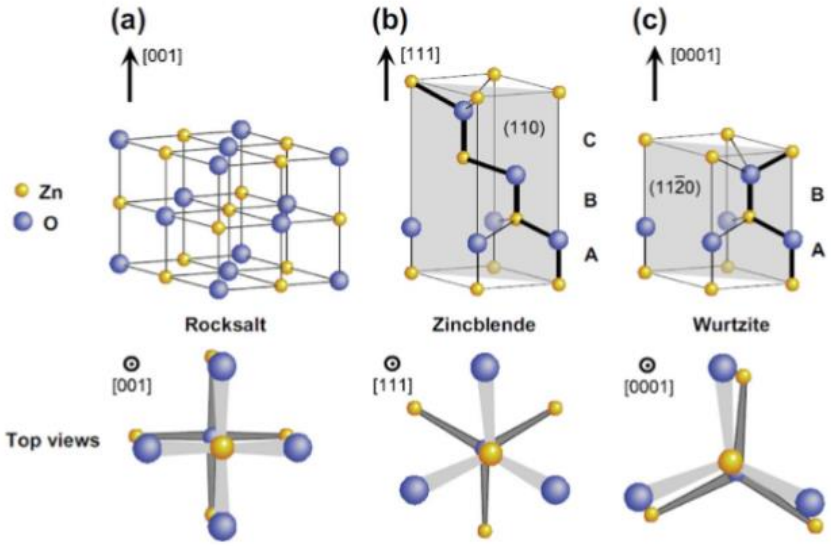

Figure 1.16: Crystal structures of a) rocksalt, b) zinc blende and c) wurtzite ZnO. Adapted from reference [179]

Wurtzite is the thermodynamically stable crystalline phase of zinc oxide with lattice parameters of a = b = 3.25 Å and c = 5.21 Å,[180] while the zinc blende phase is metastable and requires growth on a cubic substrate to stabilise it and prevent the formation of the wurtzite phase.[172, 181] A third, rock salt phase for zinc oxide has also been reported but requires very high pressures.[182]

However, a key issue for ZnO and its use as a photocatalyst is that, like other II-VI semiconductors, it suffers from photocorrosion in aqueous solutions under UV irradiation.[183] This is due to instability of the photogenerated holes at the surface of the ZnO interacting with surface oxygen atoms leading to the release of O_2 and the dissolution of Zn^{2+} as shown Equation 1.3.[105] Additionally, the solubility of ZnO in water is high, 8.59 mg L^{-1} and is increased at acidic pH and when using nanomaterials compared to bulk ZnO.[184]

Reactions at the surface:

$$O^{2-}_{Surface} + h^{+} \xrightarrow{oxidation} O^{-}_{Surface}$$

$$O^{-}_{Surface} + 3O^{2-} + 3h^{+} \xrightarrow{oxidation} 2(O - O^{2-})$$

$$(O - O^{2-}) + 2h^{+} \xrightarrow{oxidation} O_2$$

$$2Zn^{2+} \xrightarrow{Dissolution} 2Zn^{2+}_{(aq)}$$

$$O_2 + 4e^{-} + 2H^{+} \xrightarrow{Reduction} 2OH^{-}$$

Overall reaction for the photocorrosion of ZnO

$$2ZnO + 4h^{+} \xrightarrow{Photocorrosion} 2Zn^{2+} + O_2$$

Equation 1.3 Overall reactions for the photocorrosion of ZnO.

Synthesis and photocatalysis

Within the literature, ZnO shows a remarkably wide range of synthesis methodologies, such as chemical or vapour phase deposition (CVD/PVD),[185] hydrothermal processes, as well as electrochemical methods such as anodisation,[186] each with their own resultant morphologies and size ranges. Vapour deposition covers all methods where a solid material is deposited from the gas phase onto a surface and uses zinc or zinc salts as precursors, which react with oxygen or decompose to form ZnO.[187] Hydrothermal synthesis involves the reaction of zinc salts (often acetates or nitrates) under elevated temperatures and pressures within an autoclave. The key experimental parameters for this synthesis are ratio of reagents,[188] time of reaction, [189] pH of solution,[189] and the presence of a templating agent such as CTAB.[190, 191] Dip coating or spin coating the gels onto FTO glass is often used to form thin films of ZnO.[192] Similarly to immobilised photocatalysts, these syntheses require suitable substrates for the deposition of ZnO, due to the need for the support to have high surface areas, strong immobilisation between support and ZnO as well as being resistant to oxidising environments.[137] Suitable substrates that have been used include glass, quartz,[193] and activated carbon.[194]

The novel synthetic methodology for ZnO monoliths reported in this thesis is based on the sol-gel synthesis, a soft chemical approach that involves the formation of a sol and its subsequent gelation into a gel. A sol is defined as a suspension of colloidal

solids, either particles or polymers within a liquid, usually a solvent. Gelation occurs leading to the formation of a continuous solid phase within and around the liquid phase, leading to a 3D porous network.[195]

Degradation of multiple pharmaceutical and pesticides, both groups of compounds commonly labelled as micropollutants, using ZnO slurries has also been reported: Progesterone, ibuprofen and naproxen were degraded under UV irradiation using a loading of ZnO of 0.50 g L^{-1} leading to calculated rate constants of 65.0 X 10^{-3} min^{-1} , 39.1 X 10^{-3} min^{-1} and 110.0 X 10^{-3} min^{-1} respectively,[196] and common pesticide pentachlorophenol was degraded under natural solar light over ZnO nanoparticles with a loading of 1.00 g L^{-1} with a rate constant of 52.0 X 10^{-3} min^{-1}.[197] Porous ZnO nanostructures led to 70 % degredation of the dye Methyl Orange in 60 minutes with a rate constant of 18.9 X 10^{-3} min^{-1} under UV irradiation in a slurry reactor with a catalyst loading of 1.25 g L^{-1}.[198]

Immobilised photocatalysis utilising ZnO, often as films, have also been reported. Thin films of plasma sputtered ZnO have been shown to lead to the degradation of 2-chlorophenol with rate constant of 16.6 X 10^{-3} min^{-1}.[199] Films of ZnO nanoplates, electrodeposited onto indium tin oxide (ITO) glass slides have been applied for the degradation of methyl orange with 80% removal in 60 minutes and a rate constant of 24.4 X 10^{-3} min^{-1}. When the morphology of this material is altered to include a hierarchical structure of nanowires on nanoplates, the removal within 60 minutes increases to >95% with an increased rate constant of 65.3 X 10^{-3} min^{-1},[200] highlighting the impact morphology has on the photocatalytic ability of ZnO. Of note is the disparity between compounds used to assess the photocatalytic ability of materials. This, and the issues associated with it are addressed later in chapter 2.

1.6. Bandgap Engineering of ZnO

As discussed previously, ZnO is a wide band gap material that is hindered by photocorrosion, limiting its potential use in water treatment. While the latter alone can be abated through the use of operating reactors under oxygen rich environments,[201] band gap engineering shows promise as a solution for both issues

simultaneously. Engineering the band gap and tuning the properties tends to be done via introduction of defects,[202] coupling of co-catalysts or doping.

Defect engineering involves the use of interstitial atoms and atomic vacancies and are responsible for the electrical conductivity intrinsic to oxide materials.[203] Much like a dopant atom, these defects lead to the formation of energy bands between the valence and conduction bands as shown in Figure 1.17, reducing the energy required to promote electrons from the valence band to the conduction band. For example, it has been shown that in undoped ZnO films on a Si substrate the presence of anti-site oxygen atoms (oxygen substituting zinc in the crystal lattice) lead to green emission in the photoluminescence spectrum.[204]

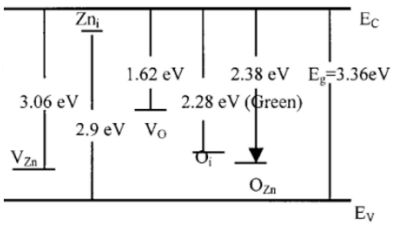

Figure 1.17: Energy levels of defects within ZnO. V denotes a vacancy while I denotes interstitial atoms. O_{Zn} shows the energy level of an antisite oxygen atom. Abstracted from ref [204].

Coupled, or composite semiconductor systems use two semiconductor materials with different band gaps in a single photocatalytic system, typically one with a large band gap coupled to another with a smaller one with a higher energy conduction band.[205] Thus, when the system is irradiated, electrons are transferred from the conduction band of the smaller band gap photocatalyst into that of the larger band gap catalyst, facilitating charge transfer separation. Alternatively, as shown in Figure 1.18, if the irradiation is of sufficient energy to activate both photocatalysts, electrons from the conduction band of the larger band gap catalyst can transfer to the valence band of the smaller where they combine with the holes present there, while the electron and hole that remain on either catalyst are significantly separated, leading to longer charge species lifetimes.[206]

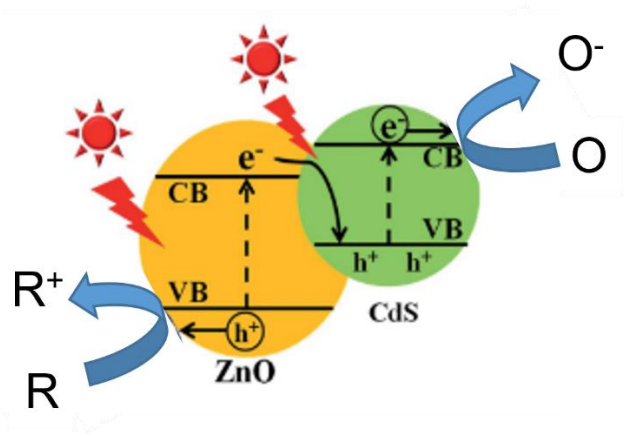

Figure 1.18: Schematic of band structure and charge separation of a ZnO/CdS coupled photocatalyst system. Adapted from ref [206]

Doping is another modification of photocatalysts that enhance the photocatalytic activity through the addition of a foreign element into the bulk crystal structure of a photocatalyst either partially or entirely replacing one of the elements in the original structure. Both metals and non-metals can be doped into a semiconductor and each type will have a unique impact on the lattice structure of the photocatalyst.[205]

Dopants increase the photocatalytic activity by reducing the band gap to allow for visible light utilisation as well as altering the band gap structure to reduce recombination of electron-hole pairs, thus increasing the lifetime of the charged species required for photocatalysis.[207] Similar to structure defects, dopant atoms can occupy a number of sites within the lattice, such as interstitial atoms where the dopant occupies space within the crystal lattice, or substituted atoms, where the dopant replaces an atom within the structure, with cationic dopants such as Cu^{2+},[208] replacing metal atoms, and anionic dopants such as N^{3-},[209] or S^{2-},[210] replacing oxygen atoms within metal oxide structures as seen in Figure 1.19.

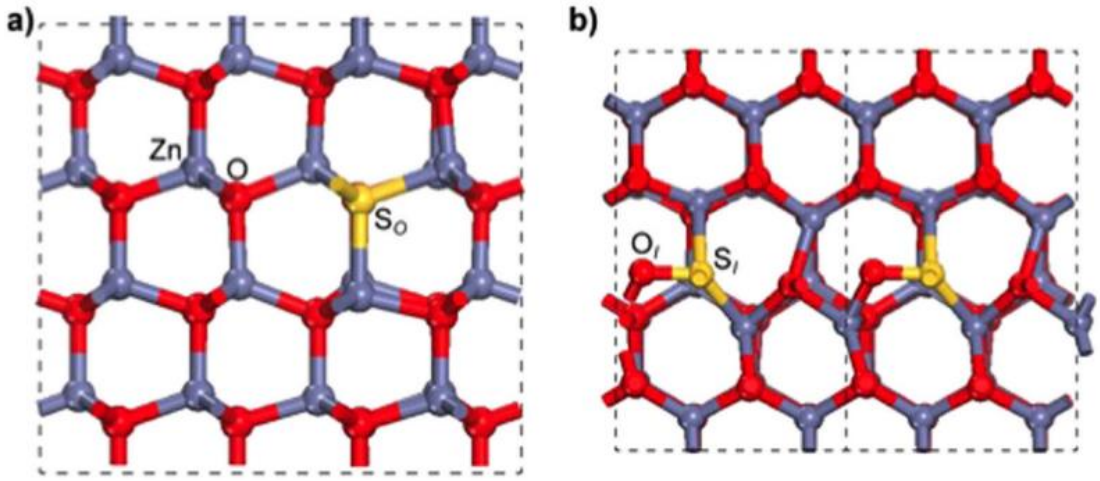

Figure 1.19: Depiction of S-doping of ZnO. A) shows oxygen substituted with sulphur while b) show interstitial sulphur and oxygen atoms. Abstracted from ref [210]

Use of metal substitutes of the same valency as the host metal leads to shrinkage of the band gap, due to a lowering of conduction band energy, while lower valency metals lead to an increase, however this has also been shown to lead to oxygen vacancies which lead to a smaller band gap.[211] As shown in Figure 1.20 metal dopants lower the band gap through the formation of acceptor and donor levels between the conduction and valence bands, non-metal doping leads to hybridisation of the dopant orbitals with the $2p_{Zn}$ and $2p_O$ orbitals leads to the formation of a new valence band, of higher energy, thus lowering the band gap.[212]

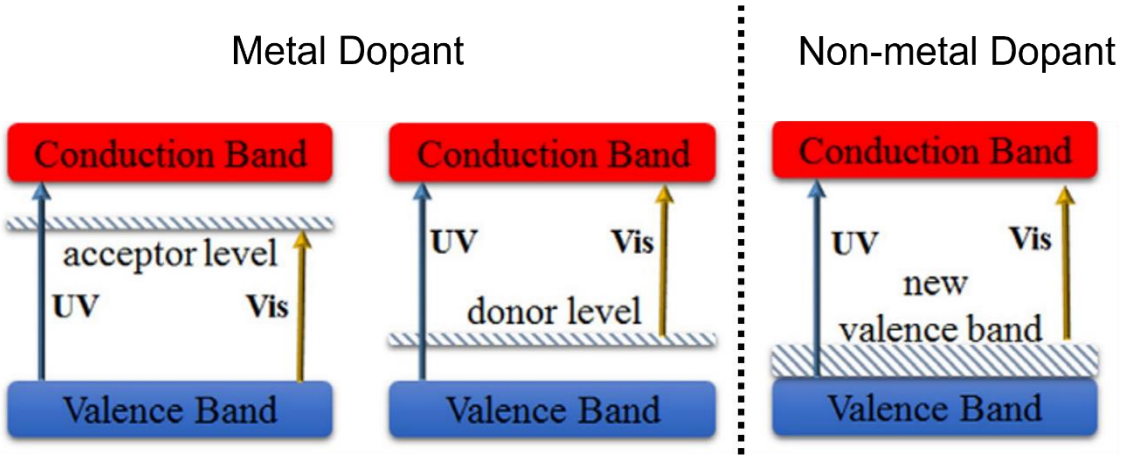

Figure 1.20: Schematic representation of doped ZnO energy levels using metal and non-metal dopants. Adapted from ref [90]

As an n-type semiconductor, ZnO shows great promise as a host for dopant atoms with a range of dopants reported in the literature, both metal and non-metal including N,[213] C,[214] and S,[215] as well as Cu,[216] Co,[217] Fe,[218] in addition to precious metals such as Ag.[219]

As a non-metal dopant, nitrogen sees widespread use as a dopant in metal oxides due to the similarity between its atomic radii and that of oxygen and is able to form stable centres in the octahedral holes of the wurtzite lattice.[220] The similar lattice size and valences also make 3d transition metals such as Mn, Fe, Co, Ni and Cu attractive dopants for ZnO.[221]

The wide range of potential dopants for ZnO allows for an equally wide range of synthetic methods to produce doped ZnO. N-doped ZnO has been produced via solvothermal treatment of ZnO powders with HNO_3 leading to a 10 fold increase in the degradation of Rhodamine 6G dye under visible light irradiation.[222] Post-synthesis N-doping of ZnO is also possible. Flowing nitrogen gas at high temperature over sol-gel synthesised ZnO was shown to allow for increased photocatalytic degradation of methylene blue dye under visible light compared to pristine ZnO.[223]

Transition metal doping of ZnO is frequently achieved through solvothermal or sol gel methods. The former was used to produce ZnO doped with 3 mol% of either Mn, Fe, Co, Ni or Cu, all of which showed smaller band gap and superior degradation of methylene blue than undoped material.[221] The latter has been used to produce ZnO nanoparticles doped with Mn or Co of dopant concentrations between 1-5% and reported Co replacing Zn atoms in the lattice with Mn decorating the surface of the lattice. Conversely, in both cases the degradation of rhodamine B was reduced when compared to undoped ZnO at all concentrations of dopant with the Mn leading to the lower reduction in activity.[224]

This highlights the need for further study into the efficacy of transition metal doping of ZnO as it shows promise for improving the photocatalytic properties of the material, such that it may see wider application as a potential method for water treatment.

1.7. Summary of Literature and Thesis Aims.

This chapter has introduced photocatalysis and the potential for its use in wastewater treatment. The first section discussed an overview of wastewater treatment and the inability of these processes to remove micropollutants, with advanced oxidation processes being discussed as a potential solution. The next section discussed photocatalysis, its fundamental principles as well as design of photocatalytic reactors, including the advantages and disadvantages of each type. ZnO, the photocatalyst studied within this thesis, was also discussed, as well as the synthetic methods used to produce it. Finally, band gap engineering of ZnO was discussed as a closing section, focusing on potential methods for overcoming the drawbacks of ZnO while highlighting disparity between the efficacy of doping ZnO nanoparticles.

This chapter has highlighted some questions and areas of novel research which are addressed in this thesis:

- The vast majority of photocatalytic degradations involve the use of either slurry systems or immobilised catalysts. Slurries require downstream removal while immobilised systems have lower surface areas. The use of a 3D porous structure could be an effective alternative. The majority of publications on foam reactors utilise nanoparticles immobilised on a support material, thereby not addressing the possible loss of catalyst into the effluent stream and, if applied as a potential wastewater treatment method, requiring monitoring and downstream removal as for slurries. The design of a foam formed entirely of photocatalyst without the support material could potentially be beneficial as it could sidestep these issues.
- ZnO doping has been previously discussed, but the literature has focused on films and nanoparticles, and also fails to reach a consensus on the suitability of transition metals as dopants. Further investigation into this, along with study of doped foam materials would provide greater understanding into this area. Furthermore, the doping of ZnO could potentially be utilised to improve the stability towards photocorrosion that has hindered the use of ZnO. While papers discuss the decrease in band gap and changes in catalytic activity,

they do not discuss the implications of increased photostability, as potentially an unreported benefit of doping.

- Comparison between photocatalyst systems remains difficult, due to the range of parameters involved, all of which impact the efficiency and activity of the system. While comparisons can be drawn between systems utilising identical conditions such as target pollutant, the literature is far from homogenous in this respect, making comparison difficult. As such, many arguments are resolved using the kinetic constant of the system, although this is an imperfect solution.

The aim of this thesis was to answer these questions and address gaps in the literature by providing a deeper understanding of porous photocatalytic materials, their applications in water treatment as well as seeking to provide a sound methodology for the normalisation of reported values in literature to allow for more accurate comparison between currently disparate systems.

1.8. References

1. M. N. Chong, B. Jin, C. W. Chow and C. Saint, *Water Res*, 2010, **44**, 2997-3027.
2. S. Malato, P. Fernández-Ibáñez, M. I. Maldonado, J. Blanco and W. Gernjak, *Catalysis Today*, 2009, **147**, 1-59.
3. S. L. Zubaidi, S. Ortega-Martorell, P. Kot, R. M. Alkhaddar, M. Abdellatif, S. K. Gharghan, M. S. Ahmed and K. Hashim, *Water Resources Management*, 2020, **34**, 1265-1279.
4. C. Prasse, D. Stalter, U. Schulte-Oehlmann, J. Oehlmann and T. A. Ternes, *Water Res*, 2015, **87**, 237-270.
5. S. J. Masten, in *Principles of environmental engineering and science*, eds. M. Davis and M. L. Davis, New York : McGraw-Hill Education, New York, 4th edition edn., 2020.
6. L. A. Hamilton, L. A. Tremblay, G. L. Northcott, M. Boake and R. P. Lim, *Sci Total Environ*, 2016, **560-561**, 101-109.
7. E. Metcalf, *Wastewater Engineering: Treatment and Resource Recovery : Treatment and Resource Recovery*, McGraw-Hill US Higher Ed USE Legacy, New York, 2013.

8. P. Singh, V. K. Singh, R. Singh, A. Borthakur, S. Madhav, A. Ahamad, A. Kumar, D. B. Pal, D. Tiwary and P. K. Mishra, in *Abatement of Environmental Pollutants*, eds. P. Singh, A. Kumar and A. Borthakur, Elsevier, 2020, pp. 1-23.
9. I. V. Muralikrishna and V. Manickam, in *Environmental Management*, 2017, pp. 249-293.
10. J. Illueca-Muñoz, J. A. Mendoza-Roca, A. Iborra-Clar, A. Bes-Piá, V. Fajardo-Montañana, F. J. Martínez-Francisco and I. Bernácer-Bonora, *Desalination*, 2008, **222**, 222-229.
11. D. Shahidi, R. Roy and A. Azzouz, *Applied Catalysis B: Environmental*, 2015, **174-175**, 277-292.
12. M. A. Launay, U. Dittmer and H. Steinmetz, *Water Res*, 2016, **104**, 82-92.
13. R. Troger, P. Klockner, L. Ahrens and K. Wiberg, *Sci Total Environ*, 2018, **627**, 1404-1432.
14. Y. Zhang, S. U. Geissen and C. Gal, *Chemosphere*, 2008, **73**, 1151-1161.
15. J. L. Wilkinson, A. B. A. Boxall, D. W. Kolpin, K. M. Y. Leung , *Proc Natl Acad Sci U S A*, 2022, **119**.
16. J. Virkutyte, R. S. Varma and V. Jegatheesan, *Treatment of Micropollutants in Water and Wastewater*, IWA Publishing, 2010.
17. A. Jurado, M. Walther and M. S. Díaz-Cruz, in *Emerging Contaminants Vol. 1: Occurrence and Impact*, eds. N. Morin-Crini, E. Lichtfouse and G. Crini, Springer International Publishing, Cham, 2021, pp. 113-163.
18. Y. Luo, W. Guo, H. H. Ngo, L. D. Nghiem, F. I. Hai, J. Zhang, S. Liang and X. C. Wang, *Sci Total Environ*, 2014, **473-474**, 619-641.
19. B. Petrie, R. Barden and B. Kasprzyk-Hordern, *Water Res*, 2015, **72**, 3-27.
20. Y. Yang, Y. S. Ok, K. H. Kim, E. E. Kwon and Y. F. Tsang, *Sci Total Environ*, 2017, **596-597**, 303-320.
21. J. O. Tijani, O. O. Fatoba, O. O. Babajide and L. F. Petrik, *Environmental Chemistry Letters*, 2015, **14**, 27-49.
22. K. Osenbruck, H. R. Glaser, K. Knoller, S. M. Weise, M. Moder, R. Wennrich, M. Schirmer, F. Reinstorf, W. Busch and G. Strauch, *Water Res*, 2007, **41**, 3259-3270.

23. J. Gasperi, C. Sebastian, V. Ruban, M. Delamain, S. Percot, L. Wiest, C. Mirande, E. Caupos, D. Demare, M. D. Kessoo, M. Saad, J. J. Schwartz, P. Dubois, C. Fratta, H. Wolff, R. Moilleron, G. Chebbo, C. Cren, M. Millet, S. Barraud and M. C. Gromaire, *Environ Sci Pollut Res Int*, 2014, **21**, 5267-5281.
24. K. Fent, A. A. Weston and D. Caminada, *Aquat Toxicol*, 2006, **76**, 122-159.
25. G. Buttiglieri and T. P. Knepper, in *Emerging Contaminants from Industrial and Municipal Waste*, 2008, ch. Chapter 98, pp. 1-35.
26. C. Vogelsang, M. Grung, T. G. Jantsch, K. E. Tollefsen and H. Liltved, *Water Res*, 2006, **40**, 3559-3570.
27. D. Mackay and A. Fraser, *Environ Pollut*, 2000, **110**, 375-391.
28. K. Chojnacka, *Environ Int*, 2010, **36**, 299-307.
29. F. A. Caliman and M. Gavrilescu, *CLEAN - Soil, Air, Water*, 2009, **37**, 277-303.
30. S. M. Dickerson and A. C. Gore, *Rev Endocr Metab Disord*, 2007, **8**, 143-159.
31. J. G. Vos, E. Dybing, H. A. Greim, O. Ladefoged, C. Lambre, J. V. Tarazona, I. Brandt and A. D. Vethaak, *Crit Rev Toxicol*, 2000, **30**, 71-133.
32. M. Gavrilescu, K. Demnerova, J. Aamand, S. Agathos and F. Fava, *N Biotechnol*, 2015, **32**, 147-156.
33. H. Baali and C. Cosio, *Environ Sci Process Impacts*, 2022, **24**, 209-220.
34. P. Oliveira, A. Almeida, V. Calisto, V. I. Esteves, R. J. Schneider, F. J. Wrona, A. Soares, E. Figueira and R. Freitas, *Water Res*, 2017, **117**, 102-114.
35. G. V. Aguirre-Martinez, T. A. DelValls and M. L. Martin-Diaz, *Ecotoxicol Environ Saf*, 2016, **124**, 18-31.
36. M. Galus, J. Jeyaranjaan, E. Smith, H. Li, C. Metcalfe and J. Y. Wilson, *Aquat Toxicol*, 2013, **132-133**, 212-222.
37. M. Galus, S. Rangarajan, A. Lai, L. Shaya, S. Balshine and J. Y. Wilson, *Aquat Toxicol*, 2014, **151**, 124-134.
38. A. J. Wicht, K. Heye, A. Schmidt, J. Oehlmann and C. Huhn, *Anal Bioanal Chem*, 2022, **414**, 4909-4917.
39. A. Joss, S. Zabczynski, A. Gobel, B. Hoffmann, D. Loffler, C. S. McArdell, T. A. Ternes, A. Thomsen and H. Siegrist, *Water Res*, 2006, **40**, 1686-1696.
40. M. J. Bueno, M. J. Gomez, S. Herrera, M. D. Hernando, A. Aguera and A. R. Fernandez-Alba, *Environ Pollut*, 2012, **164**, 267-273.

41. T. Reemtsma, S. Weiss, J. Mueller, M. Petrovic, S. Gonzalez, D. Barcelo, F. Ventura and T. P. Knepper, *Environ Sci Technol*, 2006, **40**, 5451-5458.
42. R. Loos, B. M. Gawlik, G. Locoro, E. Rimaviciute, S. Contini and G. Bidoglio, *Environ Pollut*, 2009, **157**, 561-568.
43. D. Patureau, R. Mailler, N. Delgenes, A. Danel, E. Vulliet, S. Deshayes, R. Moilleron, V. Rocher and J. Gasperi, *Waste Manag*, 2021, **125**, 122-131.
44. J. B. Ellis, *Environ Pollut*, 2006, **144**, 184-189.
45. N. M. Kumar, M. C. Sudha, T. Damodharam and S. Varjani, in *Current Developments in Biotechnology and Bioengineering*, eds. S. Varjani, A. Pandey, R. D. Tyagi, H. H. Ngo and C. Larroche, Elsevier, 2020,
46. S. O. Ganiyu, E. D. van Hullebusch, M. Cretin, G. Esposito and M. A. Oturan, *Separation and Purification Technology*, 2015, **156**, 891-914.
47. Y. Deng and R. Zhao, *Current Pollution Reports*, 2015, **1**, 167-176.
48. R. Andreozzi, *Catalysis Today*, 1999, **53**, 51-59.
49. S.-W. Nam, Y. Yoon, S. Chae, J.-H. Kang and K.-D. Zoh, *Environmental Engineering Science*, 2017, **34**, 752-761.
50. G. V. Buxton, C. L. Greenstock, W. P. Helman and A. B. Ross, *Journal of Physical and Chemical Reference Data*, 1988, **17**, 513-886.
51. M. Cheng, G. Zeng, D. Huang, C. Lai, P. Xu, C. Zhang and Y. Liu, *Chemical Engineering Journal*, 2016, **284**, 582-598.
52. J. Wang and R. Zhuan, *Sci Total Environ*, 2020, **701**, 135023.
53. S. E. Systems, *The UV/oxidation Handbook*, Solarchem Environmental Systems, 1994.
54. G. Boczkaj and A. Fernandes, *Chemical Engineering Journal*, 2017, **320**, 608-633.
55. D. B. Miklos, C. Remy, M. Jekel, K. G. Linden, J. E. Drewes and U. Hubner, *Water Res*, 2018, **139**, 118-131.
56. W. H. Glaze, *Environ Sci Technol*, 1987, **21**, 224-230.
57. M. Jekel, I. Zucker and U. Hübner, *Journal of Water Reuse and Desalination*, 2015, **5**, 8-16.
58. M. Pera-Titus, V. García-Molina, M. A. Baños, J. Giménez and S. Esplugas, *Applied Catalysis B: Environmental*, 2004, **47**, 219-256.

59. U. von Gunten and J. Hoigné, *Environmental Science and Technology*, 1994, **28**, 1234-1242.

60. S. Luo, Z. Wei, R. Spinney, Z. Zhang, D. D. Dionysiou, L. Gao, L. Chai, D. Wang and R. Xiao, *J Hazard Mater*, 2018, **343**, 132-139.

61. Z. Shu, J. R. Bolton, M. Belosevic and M. G. El Din, *Water Res*, 2013, **47**, 2881-2889.

62. I. Kim, N. Yamashita and H. Tanaka, *J Hazard Mater*, 2009, **166**, 1134-1140.

63. J. J. Pignatello, E. Oliveros and A. MacKay, *Critical Reviews in Environmental Science and Technology*, 2006, **36**, 1-84.

64. M. Punzi, B. Mattiasson and M. Jonstrup, *Journal of Photochemistry and Photobiology A: Chemistry*, 2012, **248**, 30-35.

65. S. Rahim Pouran, A. R. Abdul Aziz and W. M. A. Wan Daud, *Journal of Industrial and Engineering Chemistry*, 2015, **21**, 53-69.

66. E. Elmolla and M. Chaudhuri, *J Hazard Mater*, 2009, **170**, 666-672.

67. S. K. Alharbi, W. E. Price, J. Kang, T. Fujioka and L. D. Nghiem, *Desalination and Water Treatment*, 2016, **57**, 29340-29351.

68. J. Margot, C. Kienle, A. Magnet, M. Weil, L. Rossi, L. F. de Alencastro, C. Abegglen, D. Thonney, N. Chevre, M. Scharer and D. A. Barry, *Sci Total Environ*, 2013, **461-462**, 480-498.

69. A. R. Lado Ribeiro, N. F. F. Moreira, G. Li Puma and A. M. T. Silva, *Chemical Engineering Journal*, 2019, **363**, 155-173.

70. J. Choi, H. Lee, Y. Choi, S. Kim, S. Lee, S. Lee, W. Choi and J. Lee, *Applied Catalysis B: Environmental*, 2014, **147**, 8-16.

71. K. Hashimoto, H. Irie and A. Fujishima, *Japanese Journal of Applied Physics*, 2005, **44**, 8269-8285.

72. C. F. Goodeve and J. A. Kitchener, *Transactions of the Faraday Society*, 1938, **34**, 902-908.

73. A. Fujishima and K. Honda, *Nature*, 1972, **238**, 37-38.

74. J. M. Coronado, F. Fresno, M. D. Hernández-Alonso and R. Portela, *Design of Advanced Photocatalytic Materials for Energy and Environmental Applications*, Springer London, 2013.

75. L. Yuan, C. Han, M.-Q. Yang and Y.-J. Xu, *International Reviews in Physical Chemistry*, 2016, **35**, 1-36.
76. I. P. Parkin and R. G. Palgrave, *Journal of Materials Chemistry*, 2005, **15**.
77. S. Banerjee, D. D. Dionysiou and S. C. Pillai, *Applied Catalysis B: Environmental*, 2015, **176-177**, 396-428.
78. H. A. Foster, I. B. Ditta, S. Varghese and A. Steele, *Appl Microbiol Biotechnol*, 2011, **90**, 1847-1868.
79. A. Sirelkhatim, S. Mahmud, A. Seeni, N. H. M. Kaus, L. C. Ann, S. K. M. Bakhori, H. Hasan and D. Mohamad, *Nanomicro Lett*, 2015, **7**, 219-242.
80. O. Akhavan and E. Ghaderi, *The Journal of Physical Chemistry C*, 2009, **113**, 20214-20220.
81. Y. Wang, X. Wang and M. Antonietti, *Angew Chem Int Ed Engl*, 2012, **51**, 68-89.
82. C. K. Prier, D. A. Rankic and D. W. MacMillan, *Chem Rev*, 2013, **113**, 5322-5363.
83. M. H. Shaw, J. Twilton and D. W. MacMillan, *J Org Chem*, 2016, **81**, 6898-6926.
84. T. P. Yoon, M. A. Ischay and J. Du, *Nat Chem*, 2010, **2**, 527-532.
85. J. Zhang, B. Tian, L. Wang, M. Xing and J. Lei, *Photocatalysis*, Springer Singapore, Singapore, 2018.
86. E. S. Yang, *Fundamentals of semiconductor devices*, McGraw-Hill, New York London, 1978.
87. F. Fresno, R. Portela, S. Suárez and J. M. Coronado, *J. Mater. Chem. A*, 2014, **2**, 2863-2884.
88. G. Parker, *Introductory Semiconductor Device Physics*, CRC Press, Boca Raton, 2004.
89. A. Fujishima and X. Zhang, *Comptes Rendus Chimie*, 2006, **9**, 750-760.
90. M. Samadi, M. Zirak, A. Naseri, E. Khorashadizade and A. Z. Moshfegh, *Thin Solid Films*, 2016, **605**, 2-19.
91. C. Sushma and S. Girish Kumar, *Chemical Papers*, 2017, **71**, 2023-2042.
92. I. J. Ani, U. G. Akpan, M. A. Olutoye and B. H. Hameed, *Journal of Cleaner Production*, 2018, **205**, 930-954.

93. F. Saadati, N. Keramati and M. M. Ghazi, *Critical Reviews in Environmental Science and Technology*, 2016, **46**, 757-782.

94. H. S. Fogler, *Elements of chemical reaction engineering*, Upper Saddle River, N.J., Upper Saddle River, N.J., 3rd ed. edn., 1999.

95. D. G. Rao, R. Senthilkumar, J. A. Byrne and S. Feroz, in *Wastewater Treatment: Advanced Processes and Technologies*, CRC Press, London New York, 2012, pp. 37-60.

96. K. Rajeshwar, M. E. Osugi, W. Chanmanee, C. R. Chenthamarakshan, M. V. B. Zanoni, P. Kajitvichyanukul and R. Krishnan-Ayer, *Journal of Photochemistry and Photobiology C: Photochemistry Reviews*, 2008, **9**, 171-192.

97. S. N. Ahmed and W. Haider, *Nanotechnology*, 2018, **29**, 342001.

98. F. Dong, Z. Wang, Y. Li, W. K. Ho and S. C. Lee, *Environ Sci Technol*, 2014, **48**, 10345-10353.

99. P. Murugesan, J. A. Moses and C. Anandharamakrishnan, *Journal of Materials Science*, 2019, **54**, 12206-12235.

100. X. Wang, S. Blechert and M. Antonietti, *ACS Catalysis*, 2012, **2**, 1596-1606.

101. G. Liao, S. Chen, X. Quan, H. Yu and H. Zhao, *J. Mater. Chem.*, 2012, **22**, 2721-2726.

102. W. Zou, L. Zhang, L. Liu, X. Wang, J. Sun, S. Wu, Y. Deng, C. Tang, F. Gao and L. Dong, *Applied Catalysis B: Environmental*, 2016, **181**, 495-503.

103. N. O. Balayeva, M. Fleisch and D. W. Bahnemann, *Catalysis Today*, 2018, **313**, 63-71.

104. C. Karthikeyan, P. Arunachalam, K. Ramachandran, A. M. Al-Mayouf and S. Karuppuchamy, *Journal of Alloys and Compounds*, 2020, **828**.

105. B. Weng, M.-Y. Qi, C. Han, Z.-R. Tang and Y.-J. Xu, *ACS Catalysis*, 2019, **9**, 4642-4687.

106. R. A. Lemen, J. S. Lee, J. K. Wagoner and H. P. Blejer, *Annals of the New York Academy of Sciences*, 1976, **271**, 273-279.

107. S. T. Hossain and S. K. Mukherjee, *Journal of Hazardous Materials*, 2013, **260**, 1073-1082.

108. M. Zhang, Y. Yang, X. An and L.-a. Hou, *Chemical Engineering Journal*, 2021, **412**.

109. C. A. Gueymard, *Solar Energy*, 2004, **76**, 423-453.
110. C. McCullagh, N. Skillen, M. Adams and P. K. J. Robertson, *Journal of Chemical Technology & Biotechnology*, 2011, **86**, 1002-1017.
111. M. J. Benotti, B. D. Stanford, E. C. Wert and S. A. Snyder, *Water Res*, 2009, **43**, 1513-1522.
112. D. Maffessoni, I. C. Grazziotin, C. R. Klauck, T. Benvenuti, S. W. da Silva and A. Meneguzzi, *J Environ Manage*, 2021, **297**, 113296.
113. M. Antonopoulou, C. Kosma, T. Albanis and I. Konstantinou, *Sci Total Environ*, 2021, **765**, 144163.
114. M. Aliste, I. Garrido, P. Flores, P. Hellin, G. Perez-Lucas, S. Navarro and J. Fenoll, *J Hazard Mater*, 2021, **414**, 125603.
115. I. Garrido, J. Fenoll, P. Flores, P. Hellin, G. Perez-Lucas and S. Navarro, *Environ Sci Pollut Res Int*, 2021, **28**, 23647-23656.
116. E. Domingues, E. Fernandes, J. Gomes and R. C. Martins, *Science of The Total Environment*, 2021, **776**.
117. M. K. Bouchareb, M. Berkani, S. Merouani and M. Bouhelassa, *Water Sci Technol*, 2020, **82**, 1393-1403.
118. N. Bahadur and N. Bhargava, *Journal of Water Process Engineering*, 2019, **32**.
119. T. G. Ambaye and K. Hagos, *Nanotechnology for Environmental Engineering*, 2020, **5**.
120. K. P. Sundar and S. Kanmani, *Chemical Engineering Research and Design*, 2020, **154**, 135-150.
121. S. K. Loeb, P. J. J. Alvarez, J. A. Brame, E. L. Cates, W. Choi, J. Crittenden, D. D. Dionysiou, Q. Li, G. Li-Puma, X. Quan, D. L. Sedlak, T. David Waite, P. Westerhoff and J. H. Kim, *Environ Sci Technol*, 2019, **53**, 2937-2947.
122. C. Yu, W. Zhou, H. Liu, Y. Liu and D. D. Dionysiou, *Chemical Engineering Journal*, 2016, **287**, 117-129.
123. L. Xiong, Y. Yang, J. Mai, W. Sun, C. Zhang, D. Wei, Q. Chen and J. Ni, *Chemical Engineering Journal*, 2010, **156**, 313-320.
124. D. S. Kim, S. J. Han and S. Y. Kwak, *J Colloid Interface Sci*, 2007, **316**, 85-91.
125. A. Manassero, M. L. Satuf and O. M. Alfano, *Chemical Engineering Journal*, 2017, **326**, 29-36.

126. M. F. J. Dijkstra, A. Michorius, H. Buwalda, H. J. Panneman, J. G. M. Winkelman and A. A. C. M. Beenackers, *Catalysis Today*, 2001, **66**, 487-494.

127. H. d. Lasa, *Photocatalytic Reaction Engineering*, Springer US : Imprint: Springer, Boston, MA, 2005.

128. B. Nowack and T. D. Bucheli, *Environ Pollut*, 2007, **150**, 5-22.

129. K. Sivagami, B. Vikraman, R. R. Krishna and T. Swaminathan, *Ecotoxicol Environ Saf*, 2016, **134**, 327-331.

130. A. K. Sharma, R. K. Tiwari and M. S. Gaur, *Arabian Journal of Chemistry*, 2016, **9**, S1755-S1764.

131. M. F. J. Dijkstra, H. Buwalda, A. W. F. de Jong, A. Michorius, J. G. M. Winkelman and A. A. C. M. Beenackers, *Chemical Engineering Science*, 2001, **56**, 547-555.

132. R. van Grieken, J. Marugán, C. Sordo and C. Pablos, *Catalysis Today*, 2009, **144**, 48-54.

133. L. Ling, H. Tugaoen, J. Brame, S. Sinha, C. Li, J. Schoepf, K. Hristovski, J.-H. Kim, C. Shang and P. Westerhoff, *Environmental Science & Technology*, 2017, **51**, 13319-13326.

134. G. Odling and N. Robertson, *Catalysis Science & Technology*, 2019, **9**, 533-545.

135. S. Ramasundaram, M. G. Seid, H. E. Kim, A. Son, C. Lee, E. J. Kim and S. W. Hong, *J Hazard Mater*, 2018, **360**, 62-70.

136. S. Murgolo, S. Franz, H. Arab, M. Bestetti, E. Falletta and G. Mascolo, *Water Res*, 2019, **164**, 114920.

137. B. Srikanth, R. Goutham, R. Badri Narayan, A. Ramprasath, K. P. Gopinath and A. R. Sankaranarayanan, *J Environ Manage*, 2017, **200**, 60-78.

138. R. D. Suryavanshi, S. V. Mohite, A. A. Bagade, S. K. Shaikh, J. B. Thorat and K. Y. Rajpure, *Materials Research Bulletin*, 2018, **101**, 324-333.

139. T. Saidani, M. Zaabat, M. S. Aida, R. Barille, M. Rasheed and Y. Almohamed, *Journal of Materials Science: Materials in Electronics*, 2017, **28**, 9252-9257.

140. N. S. Portillo-Vélez, A. Hernández-Gordillo and M. Bizarro, *Catalysis Today*, 2017, **287**, 106-112.

141. V. Vaiano, G. Iervolino, D. Sannino, L. Rizzo and G. Sarno, *Chemical Engineering Research and Design*, 2016, **109**, 190-199.

142. D. Tekin, H. Kiziltas and H. Ungan, *Journal of Molecular Liquids*, 2020, **306**.

143. Y. Dong, D. Tang and C. Li, *Applied Surface Science*, 2014, **296**, 1-7.

144. H. Z. Malayeri, B. Ayati and H. Ganjidoust, *Water Environ Res*, 2014, **86**, 771-778.

145. F. Cao, T. Wang and X. Ji, *Applied Surface Science*, 2019, **471**, 417-424.

146. M. Bideau, B. Claudel, C. Dubien, L. Faure and H. Kazouan, *Journal of Photochemistry and Photobiology A: Chemistry*, 1995, **91**, 137-144.

147. R. J. Braham and A. T. Harris, *Industrial & Engineering Chemistry Research*, 2009, **48**, 8890-8905.

148. R. Hardman, *Environ Health Perspect*, 2006, **114**, 165-172.

149. C. Marambio-Jones and E. M. V. Hoek, *Journal of Nanoparticle Research*, 2010, **12**, 1531-1551.

150. C. Buzea, Pacheco, II and K. Robbie, *Biointerphases*, 2007, **2**, MR17-71.

151. M. d. l. M. Ballari, R. Brandi, O. Alfano and A. Cassano, *Chemical Engineering Journal*, 2008, **136**, 50-65.

152. D. Chen, F. Li and A. K. Ray, *AIChE Journal*, 2000, **46**, 1034-1045.

153. P. Argurio, E. Fontananova, R. Molinari and E. Drioli, *Processes*, 2018, **6**, 162-162.

154. R. Molinari, C. Grande, E. Drioli, L. Palmisano and M. Schiavello, *Catalysis Today*, 2001, **67**, 273-279.

155. K. H. Choo, D. I. Chang, K. W. Park and M. H. Kim, *J Hazard Mater*, 2008, **152**, 183-190.

156. S. S. Chin, T. M. Lim, K. Chiang and A. G. Fane, *Chemical Engineering Journal*, 2007, **130**, 53-63.

157. S. K. Papageorgiou, F. K. Katsaros, E. P. Favvas, G. E. Romanos, C. P. Athanasekou, K. G. Beltsios, O. I. Tzialla and P. Falaras, *Water Res*, 2012, **46**, 1858-1872.

158. L. Erdei, N. Arecrachakul and S. Vigneswaran, *Separation and Purification Technology*, 2008, **62**, 382-388.

159. N. Nasrollahi, L. Ghalamchi, V. Vatanpour and A. Khataee, *Journal of Industrial and Engineering Chemistry*, 2021, **93**, 101-116.

160. S. A. Snyder, S. Adham, A. M. Redding, F. S. Cannon, J. DeCarolis, J. Oppenheimer, E. C. Wert and Y. Yoon, *Desalination*, 2007, **202**, 156-181.

161. S. S. Yoo, K. H. Chu, I. H. Choi, J. S. Mang and K. B. Ko, *J Environ Manage*, 2018, **206**, 1126-1134.

162. W. Zhang, L. Ding, J. Luo, M. Y. Jaffrin and B. Tang, *Chemical Engineering Journal*, 2016, **302**, 446-458.

163. T. Van Gerven, G. Mul, J. Moulijn and A. Stankiewicz, *Chemical Engineering and Processing: Process Intensification*, 2007, **46**, 781-789.

164. E. Vaisman, M. F. Kabir, A. Kantzas and C. H. Langford, *Journal of Applied Electrochemistry*, 2005, **35**, 675-681.

165. W. Qiu and Y. Zheng, *Applied Catalysis B: Environmental*, 2007, **71**, 151-162.

166. T. H. Lim and S. D. Kim, *Chemosphere*, 2004, **54**, 305-312.

167. J. H. Pan, H. Dou, Z. Xiong, C. Xu, J. Ma and X. S. Zhao, *Journal of Materials Chemistry*, 2010, **20**.

168. M. E. Leblebici, B. Van den Bogaert, G. D. Stefanidis and T. Van Gerven, *Chemical Engineering Journal*, 2017, **310**, 240-248.

169. J. R. Bolton, K. G. Bircher, W. Tumas and C. A. Tolman, *Pure and Applied Chemistry*, 2001, **73**, 627-637.

170. S. E. Braslavsky, *Pure and Applied Chemistry*, 2007, **79**, 293-465.

171. B. Ohtani, *Journal of Photochemistry and Photobiology C: Photochemistry Reviews*, 2010, **11**, 157-178.

172. Ü. Özgür, Y. I. Alivov, C. Liu, A. Teke, M. A. Reshchikov, S. Doğan, V. Avrutin, S. J. Cho and H. Morkoç, *Journal of Applied Physics*, 2005, **98**, 1-103.

173. H. Tong, S. Ouyang, Y. Bi, N. Umezawa, M. Oshikiri and J. Ye, *Adv Mater*, 2012, **24**, 229-251.

174. N. Jiang, Y. Du, X. Lv, K. Yang, M. Du, Y. Feng and Y. Liu, *Materials Research Express*, 2018, **5**.

175. R. Qiu, D. Zhang, Y. Mo, L. Song, E. Brewer, X. Huang and Y. Xiong, *J Hazard Mater*, 2008, **156**, 80-85.

176. S. Sakthivel, B. Neppolian, M. V. Shankar, B. Arabindoo, M. Palanichamy and V. Murugesan, *Solar Energy Materials and Solar Cells*, 2003, **77**, 65-82.

177. J. S. Chang, J. Strunk, M. N. Chong, P. E. Poh and J. D. Ocon, *J Hazard Mater*, 2020, **381**, 120958.
178. N. M. Gupta, *Renewable and Sustainable Energy Reviews*, 2017, **71**, 585-601.
179. C. B. Ong, L. Y. Ng and A. W. Mohammad, *Renewable and Sustainable Energy Reviews*, 2018, **81**, 536-551.
180. C. W. Bunn, *Proceedings of the Physical Society*, 1935, **47**, 835-842.
181. A. B. M. A. Ashrafi, A. Ueta, A. Avramescu, H. Kumano, I. Suemune, Y.-W. Ok and T.-Y. Seong, *Applied Physics Letters*, 2000, **76**, 550-552.
182. A. Janotti and C. G. Van de Walle, *Reports on Progress in Physics*, 2009, **72**.
183. K. M. Lee, C. W. Lai, K. S. Ngai and J. C. Juan, *Water Res*, 2016, **88**, 428-448.
184. M. L. Avramescu, P. E. Rasmussen, M. Chenier and H. D. Gardner, *Environ Sci Pollut Res Int*, 2017, **24**, 1553-1564.
185. J. L. Gomez and O. Tigli, *Journal of Materials Science*, 2012, **48**, 612-624.
186. A. Ramirez-Canon, M. Medina-Llamas, M. Vezzoli and D. Mattia, *Phys Chem Chem Phys*, 2018, **20**, 6648-6656.
187. K. Black, A. C. Jones, I. Alexandrou, P. N. Heys and P. R. Chalker, *Nanotechnology*, 2010, **21**, 045701.
188. M. Podlogar, A. Rečnik, G. Yilmazoglu, I. Ö. Özer, M. Mazaj, E. Suvaci and S. Bernik, *Ceramics International*, 2016, **42**, 15358-15366.
189. K. Govender, D. S. Boyle, P. B. Kenway and P. O'Brien, *J. Mater. Chem.*, 2004, **14**, 2575-2591.
190. Y.-H. Ni, X.-W. Wei, X. Ma and J.-M. Hong, *Journal of Crystal Growth*, 2005, **283**, 48-56.
191. S. Baruah and J. Dutta, *Sci Technol Adv Mater*, 2009, **10**, 013001.
192. M. Ohyama, H. Kouzuka and T. Yoko, *Thin Solid Films*, 1997, **306**, 78-85.
193. J. Herrmann, H. Tahiri, Y. Aitichou, G. Lassaletta, A. Gonzalezelipe and A. Fernandez, *Applied Catalysis B: Environmental*, 1997, **13**, 219-228.
194. C. H. Ao and S. C. Lee, *Chemical Engineering Science*, 2005, **60**, 103-109.
195. U. Schubert and N. Husing, *Synthesis of Inorganic Materials*, Wiley-VCH, Weinheim ; Chichester, 1989.
196. R. Sabouni and H. Gomaa, *Environ Sci Pollut Res Int*, 2019, **26**, 5372-5380.

197. M. M. Ba-Abbad, M. S. Takriff, M. Said, A. Benamor, M. S. Nasser and A. W. Mohammad, *International Journal of Environmental Research*, 2017, **11**, 461-473.

198. Z. Jia, D. Ren, L. Xu and R. Zhu, *Materials Science in Semiconductor Processing*, 2012, **15**, 270-276.

199. N. Salah, A. Hameed, M. Aslam, M. S. Abdel-wahab, S. S. Babkair and F. S. Bahabri, *Chemical Engineering Journal*, 2016, **291**, 115-127.

200. F. Xu, Y. Shen, L. Sun, H. Zeng and Y. Lu, *Nanoscale*, 2011, **3**.

201. C. M. Taylor, A. Ramirez-Canon, J. Wenk and D. Mattia, *J Hazard Mater*, 2019, **378**, 120799.

202. A. M. Smith and S. Nie, *Acc Chem Res*, 2010, **43**, 190-200.

203. V. C. Anitha, A. N. Banerjee and S. W. Joo, *Journal of Materials Science*, 2015, **50**, 7495-7536.

204. B. Lin, Z. Fu and Y. Jia, *Applied Physics Letters*, 2001, **79**, 943-945.

205. R. Ameta, M. S. Solanki, S. Benjamin and S. C. Ameta, in *Advanced Oxidation Processes for Waste Water Treatment*, 2018, pp. 135-175.

206. X. Li, J. Yu, J. Low, Y. Fang, J. Xiao and X. Chen, *Journal of Materials Chemistry A*, 2015, **3**, 2485-2534.

207. E. Fosso-Kankeu, S. Pandey and S. Sinha Ray, in *Photocatalysts in Advanced Oxidation Processes for Wastewater Treatment*, John Wiley & Sons, Hoboken, 2020

208. F. Rasouli, A. Rouhollahi and F. Ghahramanifard, *Superlattices and Microstructures*, 2019, **125**, 177-189.

209. D. Zhang, J. Gong, J. Ma, G. Han and Z. Tong, *Dalton Trans*, 2013, **42**, 16556-16561.

210. F. Fabbri, L. Nasi, P. Fedeli, P. Ferro, G. Salviati, R. Mosca, A. Calzolari and A. Catellani, *Sci Rep*, 2016, **6**, 27948.

211. F. Wang, C. Di Valentin and G. Pacchioni, *The Journal of Physical Chemistry C*, 2012, **116**, 8901-8909.

212. X. Chen, S. Shen, L. Guo and S. S. Mao, *Chem Rev*, 2010, **110**, 6503-6570.

213. J. J. Macias-Sanchez, L. Hinojosa-Reyes, A. Caballero-Quintero, W. de la Cruz, E. Ruiz-Ruiz, A. Hernandez-Ramirez and J. L. Guzman-Mar, *Photochem Photobiol Sci*, 2015, **14**, 536-542.

214. M. Samadi, H. A. Shivaee, M. Zanetti, A. Pourjavadi and A. Moshfegh, *Journal of Molecular Catalysis A: Chemical*, 2012, **359**, 42-48.

215. S. Y. Bae, H. W. Seo and J. Park, *The Journal of Physical Chemistry B*, 2004, **108**, 5206-5210.

216. M. Mittal, M. Sharma and O. P. Pandey, *Solar Energy*, 2014, **110**, 386-397.

217. S. Kuriakose, B. Satpati and S. Mohapatra, *Phys Chem Chem Phys*, 2014, **16**, 12741-12749.

218. S. Yi, J. Cui, S. Li, L. Zhang, D. Wang and Y. Lin, *Applied Surface Science*, 2014, **319**, 230-236.

219. P. Amornpitoksuk, S. Suwanboon, S. Sangkanu, A. Sukhoom, N. Muensit and J. Baltrusaitis, *Powder Technology*, 2012, **219**, 158-164.

220. C. Di Valentin and G. Pacchioni, *Acc Chem Res*, 2014, **47**, 3233-3241.

221. K. Qi, X. Xing, A. Zada, M. Li, Q. Wang, S.-y. Liu, H. Lin and G. Wang, *Ceramics International*, 2020, **46**, 1494-1502.

222. C. Wu, Y. C. Zhang and Q. Huang, *Materials Letters*, 2014, **119**, 104-106.

223. B. M. Rajbongshi, A. Ramchiary and S. K. Samdarshi, *Materials Letters*, 2014, **134**, 111-114.

224. R. He, R. K. Hocking and T. Tsuzuki, *Journal of Materials Science*, 2011, **47**, 3150-3158.

Chapter 2

Photocatalytic Foams For Water Treatment: A Systematic Review And Meta-Analysis

The work presented in this chapter has been published to Journal of Environmental Chemical Engineering in January 2023

Warren, Z., et al. (2023). "Photocatalytic foams for water treatment: A systematic review and meta-analysis." Journal of Environmental Chemical Engineering **11**(1).

Chapter 2: Photocatalytic Foams For Water Treatment: A Systematic Review And Meta-Analysis

This declaration concerns the article entitled:			
Photocatalytic Foams For Water Treatment: A Systematic Review And Meta-Analysis			
Publication status (tick one) **Draft manuscript** ☐ **Submitted** ☐ **In review** ☐ **Accepted** ☐ **Published** X			
Publication details (reference)	Warren, Z., et al. (2023). "Photocatalytic foams for water treatment: A systematic review and meta-analysis." Journal of Environmental Chemical Engineering 11(1).		
Copyright status (tick the appropriate statement) The material has been published with a CC-BY license ☐ The publisher has granted permission to replicate the material included here ☐			
Candidate's contribution to the paper (provide details, and also indicate as a percentage)	The candidate contributed to / considerably contributed to / predominantly executed the… Formulation of ideas: 60% Project initially conceived by DM. The candidate and co-authors TTG and ASM were responsible for planning of the project. Design of methodology: 70% The candidate designed the methodology for the literature, data analysis and calculations under supervision of DM and JW. Experimental work: 70% The candidate collected and analysed raw data from the literature, provided in part by co-authors TTG and ASM. Presentation of data in journal format: 75% The candidate wrote the majority of the manuscript, with contributions from co-authors TTG and ASM, which were edited by the candidate. The candidate also prepared the graphs and tables within the manuscript.		
Statement from Candidate	This paper reports on original research I conducted during the period of my Higher Degree by Research candidature.		
Signed	Zachary Warren	**Date**	21/09/2022

PHOTOCATALYTIC FOAMS FOR WATER TREATMENT: A SYSTEMATIC REVIEW AND META-ANALYSIS

*Zachary Warren, Thais Tasso Guaraldo, Alysson Stefan Martins, Jannis Wenk, and Davide Mattia**

Department of Chemical Engineering, University of Bath, BA2 7AY, UK.

e-mail: d.mattia@bath.ac.uk

Keywords: foams, photocatalysts, photocatalysis, water treatment

Highlights

- Describes photocatalytic foams as the third generation of catalysts.
- Proposes classification according to pore size.
- Describes a systematic analysis according to synthesis methods.
- Highlights the relevance of describing figures of merit in photocatalysis.

Graphical Abstract

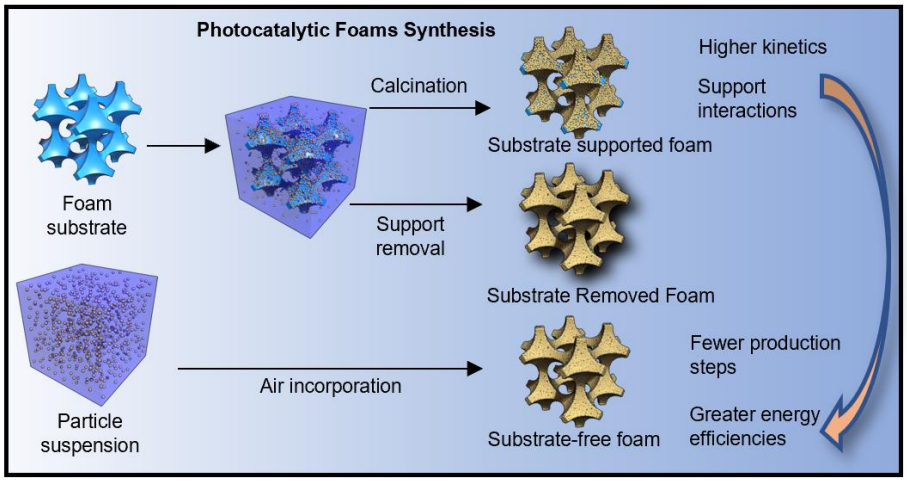

Abstract

Photocatalysis has proven to be highly effective for the removal of recalcitrant organic micropollutants at the lab scale. However, drawbacks such as the need for downstream removal of nanoparticle slurries and low surface areas of immobilised catalyst have, so far, hindered large-scale application. Photocatalytic foams have the potential to address these issues and advance the field towards large scale deployment. This review offers the first comprehensive overview of the state-of-the-art in this growing research field while simultaneously addressing two key issues which are slowing down further progress: The lack of classification nomenclature for foams, particularly regarding pore size and production method, and the use of kinetics as the defining feature of a photocatalyst, when alternate figures of merit, such electrical and quantum efficiencies, may be more appropriate. These were particular evident from a semi-quantitative comparison of the literature reported here, which highlighted the need for standardisation of experimental methods within the field. Finally future perspectives and best practices are discussed and recommended.

Photocatalytic Foams For Water Treatment: A Systematic Review And Meta-Analysis

2.1. General overview

Photocatalysis has been extensively investigated for the degradation and mineralisation of organic micropollutants in water [1, 2]. The effectiveness of photocatalysts results from a complex combination of materials properties, e.g. charge carrier separation and the formation of oxidative species [3], and process parameters, e.g. light irradiation and mass transfer resistances [4]. Despite the promise, the industrial deployment of photocatalytic systems has been, so far, limited [5]. Nanoparticle slurries, also known as first generation photocatalysts (Figure 2.1), show great photocatalytic efficiency given the high surface area in direct contact with water and irradiation [6]. However, evidence that nanoparticle release into water bodies increases the risk of exposure to humans, animals and plants [7], and that nanoparticles can leach from wastewater treatment plants [8], limits their use in wide spread treatment applications at larger scales due to requiring costly removal steps to prevent loss to the environment [9]. Immobilised, or second-generation, catalysts were developed to address the removal problem, but suffer from low efficiency due their lower photocatalytic active surface area [10, 11]. Macroporous materials, commonly referred as foams, have been developed as an attempt to address the limitations of the previous two generations of photocatalysts [5, 12].

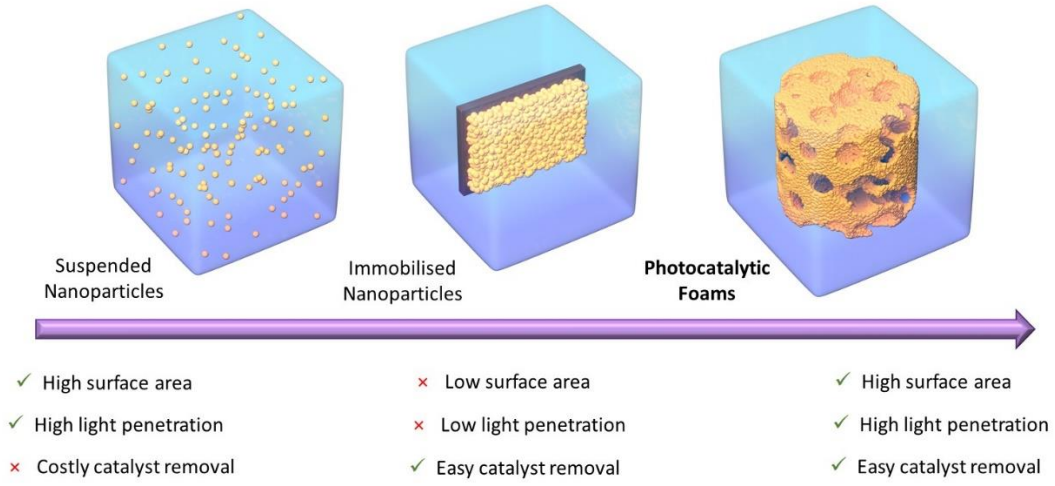

Figure 2.1: First, second and third generations of photocatalysts.

Photocatalytic foams offer great potential in terms of efficiency, activity and, crucially, in scalability. Materials with two distinct levels of porosity, macroporous and microporous, can efficiently convert irradiated light into oxidative species to promote the degradation of micropollutants with significant advantage over flat substrates given higher surface area. The porosity, pore size and shape will also impact the transport of molecules inside the foams as the hierarchical pore structure leads to a tortuous flow [13].

While these foams have been produced in a wide range of forms and shapes, using a range of diverse approaches, they are not without drawbacks, in some instances not providing meaningful advantages over slurries and immobilised photocatalyst. Although superior photocatalytic performance is reported for foams relative to the equivalent slurries [13, 14], including the removal of organic pollutants and mineralisation [15, 16], most reports refer to nanoparticles grafted onto commercial foams. Despite reports of good adherence and stability of the coatings, the potential leak of nanoparticles into the environment remains an issue, limiting their practical use. The use of foams has also generated novel fundamental questions, e.g. about the different relevance of total and illuminated (or active) surface areas in microporous objects as opposed to nanoparticle slurries, or the need to revisit IUPAC nomenclature for porosity to include large porous objects [17].

Photocatalytic foams are a growing area of fundamental and applied research, and this review is the first to systematically analyse the field, not just discussing the state-of-the-art, but also attempting to provide a novel classification based on key characteristics of their structure, how foams are synthesised and their photocatalytic application and providing recommendations on how to further advance this area of research. In this review, foams are divided into three main categories according to the synthesis approach used, as summarized schematically in Figure 2.2. *Supported foams* refer to nanoparticles, mostly TiO_2, ZnO and CuO, immobilised onto a 3D macroporous structure. *Substrate-removed foams* refer to those where the foam is used as a sacrificial template to obtain carbon-based 3D structures. *Substrate-free foams* refer to those produced via direct foaming of particle suspensions with subsequent calcination or sintering.

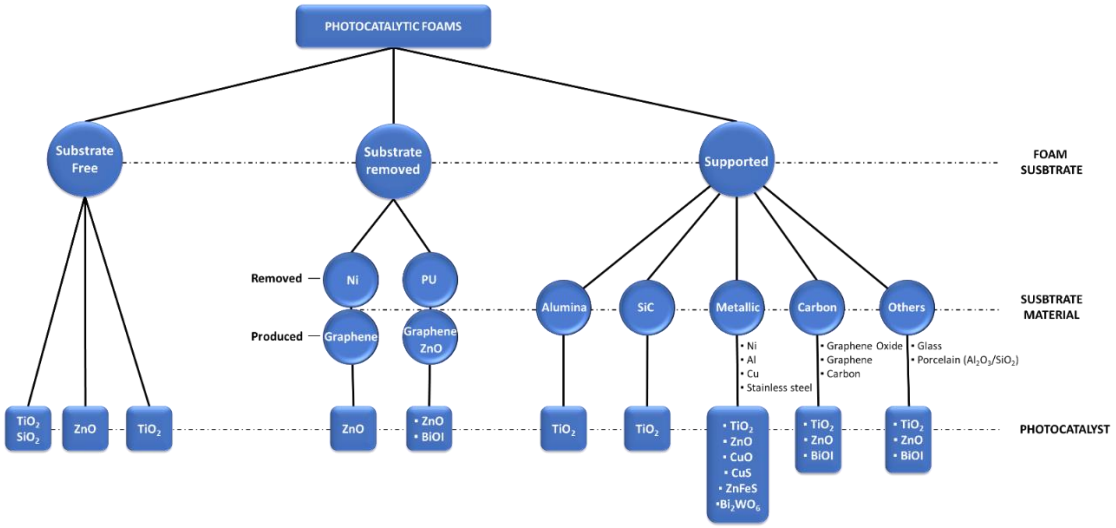

Figure 2.2: Structure of photocatalytic foams for water/wastewater treatment.

2.2. Methods to produce inorganic foams: general aspects

The synthesis of a solid inorganic foam was first reported in 1965 [18]. Since then, macroporous inorganic foams of controlled porosity have been produced using a wide range of methods, such as replica, sacrificial template, or direct foaming with average pore sizes ranging from 1 to 1000 µm [19]. The first report on the use of foams for photocatalytic applications dates to 2004 [20].

The replica technique is based on the impregnation of a suspension or precursor solution onto a cellular structure to produce a macroporous material presenting the same morphology as the original porous structure [19]. In contrast to the replica technique, the sacrificial template method involves the preparation of a biphasic composite composed of a homogeneously dispersed sacrificial phase in a continuous phase of precursors or particles which forms a negative porous microstructure after template removal [21]. The direct foaming technique is based on the incorporation of air into a suspension or liquid phase with subsequent set and drying to maintain the air bubbles within the structure. The material is usually sintered to improve strength of the final porous material [22]. Porosity and pore size are determined by the template and sintering conditions in the replica and sacrificial template methods. The porous object is the negative replica of the original sacrificial template while the replica techniques produces a positive porous structure [19]. The replica method and direct foaming either with surfactants or particles forms objects with higher average porosity (ranging from 40 to 95%), while the sacrificial template method results in

objects with a lower average porosity with reported porosities over a much wider range (2-90%) [19]. The overall porosity is relative to the amount of gas incorporated into the suspension while the stability of the liquid template before setting determines the pore size [19]. Other methods to fabricate inorganic foams such as liquid templating [23, 24, 25], cast moulding and freeze drying [14], microfluidic [24] and 3D printing [26] were also reported either in combination or alone. With understanding and control of the synthesis of foams, particularly replica/template structure, volume and rate of gas incorporation and surfactant concentration [27], properties as porosity, pore size morphology and distribution can be fine-tuned [24, 25].

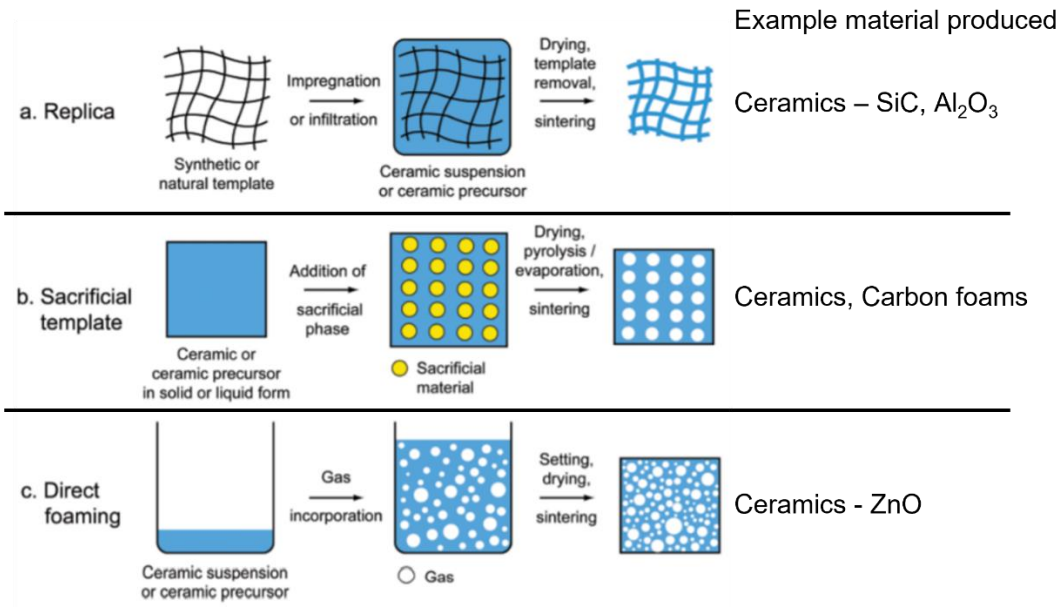

Figure 2.3: Possible processing routes for macroporous foams (a) replica, (b) sacrificial template and (c) direct foaming (adapted from reference [19]).

Commercial foam supports can be divided into four main groups as metallic (such as Ni, Cu and stainless steel), metal oxide (such as Al_2O_3), semiconductor (such as SiC) [28-32] and polymeric (such as polyurethane-PU) [33, 34]. Metallic and polymeric foam supports were used as sacrificial templates to produce carbon-based foams mainly composed of graphene [35] and reduced graphene oxide. [36] A few reports include other supports such as glass [37] and porcelain clay foams [38]. Immobilisation of nanoparticles onto foam supports has been the most common strategy to produce photocatalytic foams. Typical immobilisation techniques include dip coating [3, 39] and impregnation. [40, 41]

2.3. Key definitions

As often happens in a rapidly developing field, the existing literature uses a very wide range of different, often contradicting, language to describe how foams have been produced, what a foam is and how they perform as photocatalyst. This hinders comparison of results and, ultimately, further progress in the area. This review provides the first attempt to provide a comprehensive framework to define, characterise and assess the performance of photocatalytic foams.

2.3.1. Definition of foams and porosity

Within the literature, a wide variety of material structures have been referred to as "foams", from natural sponge-type structures to highly porous powder samples [42, 43]. For this review, to discuss different types of foams and to systematise the available literature, a foam is defined as *"a macroscopic object that is highly porous, with porosity in excess of 80%, and free standing".* From this definition, the authors further suggest classifying foams into three distinct categories according to their macroscopic structure (Figure 2.4).

(A) Foam substrates – systems where the porous structure is both extrinsic to the photocatalyst, and present in the system. These include reticulated foams of ceramic or metal materials, to which catalyst is added, leading to supported catalyst on the foam material. These systems benefit from the mechanical stability of the support material. However, a key drawback of these systems is the presence of adhered particulate at the support surface. The weak particle-support interaction may lead to catalyst leaching, impacting both the activity of the system and posing potential toxicological and environmental concerns due to catalyst loss, requiring downstream removal to prevent this.

(B) Foams formed via substrate removal – Systems where the porous structure is extrinsic to the photocatalytic material, but the support providing the structure is not present in the system. These include photocatalyst foams formed via a templating methodology onto a polymer foam, which is then pyrolised to leave only a porous inorganic photocatalyst, or systems grown on a metallic foam which is then etched. These systems often make use of graphene, graphene oxide or reduced graphene oxide and benefit from the high electron mobility provided by these materials.

Similar to substrate-supported foam catalysts, the presence of particles at the foam surface gives rise to the potential for leaching.

(C) Substrate-free foams – systems with intrinsic porosity to the photocatalyst, and no support is present at any point in the system. These include foams produced via liquid templating or sol gel reactions. A key benefit of these systems is the lack of particle-support interactions, lowering the risk of photocatalyst loss and the need for downstream removal to prevent this. The drawback of these systems is that, as the complete structure is made of the photocatalyst materials and therefore these foams may lack the relative mechanical stability that is present when using a substrate foam as a support for photocatalyst, specifically for the mechanical stability. Furthermore, particularly in the case of ZnO foams, these systems are vulnerable to photocorrosion and methods of mitigation need to be considered in the design of reactors incorporating these foams [44].

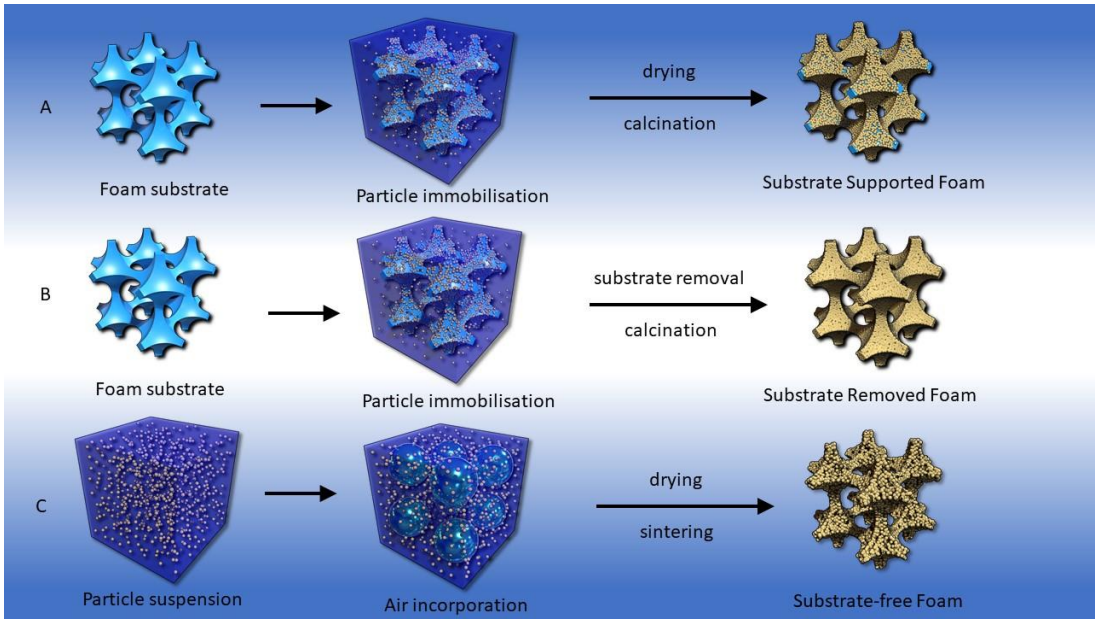

Figure 2.4: Schematic representation of photocatalytic foams: (a) foams with substrates produced via catalyst immobilisation (b) foams formed via substrate removal and (c) substrate-free foams formed via direct foaming.

2.3.2. Classification of pore size for foams – expanding upon IUPAC

Historically, the classification of pore size and pore size distribution has followed definitions set out by IUPAC [17]: Micropore – to describe a pore width below 2 nm, mesopore - to describe pore widths of between 2 and 50 nm, and macropore - to describe pores with a width greater than 50 nm.

However, this system is not without faults, especially when applied to materials at the macroscale, including ceramic foams. Firstly, the IUPAC classification is based on the process of physisorption, which is affected by a wide range of factors including: pore shape, properties of the adsorptive and interactions between the adsorbate – adsorbent [45]. As a result, a distinction needs to be drawn between the porosity of the catalyst material and that of the substrate, particularly when applied to foams for photocatalysis. Both porosity of the catalyst and the substrate have different effects, and can impact catalytic activity differently, with the latter being of greater importance. Material pore size, frequently derived from Brunauer-Emmett-Teller (BET) theory, when applied to photocatalysts, has the greatest impact on the surface area of the material, with smaller pores in the material surface providing higher surface areas for, during BET, nitrogen to adsorb and during photocatalysis, reactions to occur at. It is well reported that, particularly for slurry and immobilised systems, these larger surface areas provide an increase in photocatalytic activity that [46, 47].

Conversely, the porosity and pore size of the foam support impact the hydrodynamics of the eluent flow through the structure, including generating a pressure and inducing turbulence in the flow [48-50]. Furthermore, the pore size has a range of impacts on the photocatalytic activity of the reactor system, with no consensus yet as to which provides the greatest benefit. Larger pore sizes offer less resistance to flow of solutions and potentially allow for greater light penetration [51-53], while smaller pores provide higher surface areas for reactions to occur at, as well as reducing the diffusion times between surface and bulk pollutants leading to greater kinetics [54, 55].

As such, it is proposed that this classification be expanded to include characterisation of the pore size of objects as well as the material's properties to allow for discussions around optimal pore size of foams to occur with greater ease and frequency.

Like the traditional IUPAC method, the authors propose a three-category system for the classification of foam pore size (Figure 2.5).

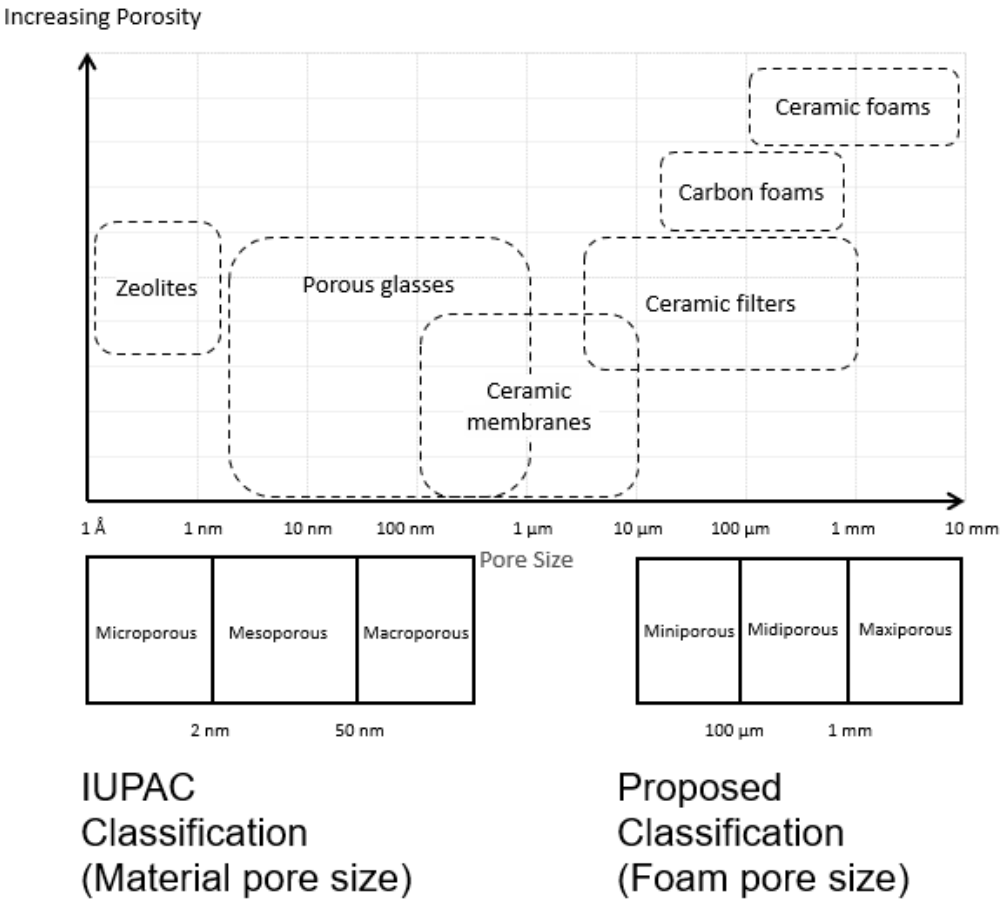

Figure 2.5: Proposed pore size characterisation scheme for foams and porous ceramics. Figure adapted from ref [56].

Foams with the average macropore size of less than 100 µm fall into the category of mini-porous foams, containing the smallest pore sizes but allowing for characterisation when these structures are expanded to macroscale objects. Most foams discussed in this review fall into the next category of midi-porous foams, foams with an average macropore size of between 100 µm and 1 mm. Finally, foams with pore sizes beyond 1 mm are categorised as maxi-porous structures.

This expansion of the classification allows for greater clarity and scope of research in both porous materials and objects (Table 2.1).

Table 2.1: Classification of foams according to the 3D macroscopic structure (foam pore size) and material microporosity (material pore size).

IUPAC Classification (Material pore size)	Expanded Classification (Foam pore size)
Microporous (≤2 nm)	Miniporous (≤100 µm)
Mesoporous (2-50 nm)	Midiporous (100 µm – 1 mm)
Macroporous (≥50 nm)	Maxiporous (≥1 mm)

Most of the literature on foams as photocatalysts reports either the porosity of the substrate material, here referred as the macroporous 3D structure, or the porosity of deposited photocatalytic nanoparticles, here referred as microporosity. As both levels of porosity are intrinsically correlated to the photocatalytic activity of the overall foam structure, reporting both levels allow for better understanding of properties and comparisons. Therefore, the authors propose reporting catalyst material properties, followed by support properties, for example *mesoporous TiO_2 nanopowders supported on a midiporous SiC foam.*

2.3.3. Methodology

To facilitate a systematic review, data was collected in the following way: Concurrent data searches were performed via Scopus using search terms “foam AND water treatment AND photocataly-” and “reticulated AND water treatment AND photocataly-” to provide an initial pool of data. From this pool, entries which were duplicates, irrelevant, e.g. those using “foam” to describe a porous powder as discussed earlier, and showing no photocatalytic application or applied to gas phase photocatalysis, were removed. From this dataset, entries were assessed and those that did not report the E_{EO} or quantum efficiency or the parameters required to calculate them were excluded. This process was reiterated quarterly over the course of 18 months to ensure the data was up to date. After this process, out of the 81 initial entries, 32 publications were analysed with a total number of 43 data points, accounting for publications testing multiple pollutants.

Given the wide range of data, spanning orders of magnitude, logarithmic scales were applied on all figures to allow visualisation of the complete dataset. To compare and assess performances of the catalytic systems, figures are separated into quartiles, to statistically relate the performance of a particular system, within the wider dataset.

Owing to the complex nature of photocatalytic reactions, compounded by the variety of reactor set ups (e.g. batch, recirculating, continuous) and process parameters (e.g. light source, light intensity, reservoir volume, pollutant, concentration, etc.), adopting an integrated analytical framework is made difficult as each of these factors impacts the effectiveness and efficiency of the overall system.

Of particular difficulty is comparing systems using degradation kinetics alone, the most frequently used metric to assess the suitability of a photocatalyst. First, many researchers continue to use dyes for degradation studies, despite well-known limitations of this approach [57], and several key articles and editorials in the literature stating that the degradation rate and kinetics of dyes systems are not truly indicative of the activity of photocatalysts [58].

This issue becomes significant, as research moves towards using more suitable target pollutants, including probe or model compounds that are more resistant toward direct photolysis, with these systems showing slower kinetics due to the absence of secondary degradations [14]. As such, a system assessed using a more photo-resistant pollutant, probe or model compound may exhibit much lower kinetics than if a dye was used, skewing the impact of research towards those that use dyes for the resulting higher kinetics, even though these may not be truly indicative of the actual performance of the system.

An approximate comparative approach is used here, using the terminology defined in the IUPAC glossary [59], allowing for a rough comparison between different systems. For different compounds used across different studies, normalised kinetics k_{ε}, wherein the kinetic rate constant min^{-1} has been normalised by the molar absorption coefficient (MAC) of the compound, M^{-1} cm^{-1} were determined. This allowed accounting for the absorption and attenuation of light, thus enabling comparison between dyes, which have high MAC values, and other pollutants which have lower values.

The authors recognise the limitations of this approach, but adopted it as the only way to provide a semi-quantitative comparison of the literature, with its wide range of pollutants, photocatalysts, reactor configuration, light sources, etc. It also further highlights the need for standardization in how experiments are conducted, and data reported, which is one of the key aims of this review.

2.3.4. Figures of merit in photocatalysis

In terms of the energy efficiency of the system, this review makes use of the Electrical energy per order (E_{EO}), defined as the kilowatt hours of electrical energy needed to decrease the concentration of pollutants by an order of magnitude (90%) in one cubic metre of solution [60], and assessed using the following equations for batch and flow systems, respectively:

$$E_{EO} = \frac{P * t * 1000}{(V)(log\ {}^{C_0}/_{C_t})}$$
$$E_{EO} = \frac{P}{(F)(log\ {}^{C_0}/_{C_t})}$$

Equation 2.1: Electrical energy per order of 1) batch and 2) flow reactors

Where P is the total power output of the light source in kW, t is the irradiation time in hours, V is volume in L, F is flow rate in $m^3\ hr^{-1}$ and C_0 and C_t are initial and final concentrations, respectively.

E_{EO} allows for an analysis of the energy consumption of a reactor system, as well as allowing for assessment of scale up potential. $1/E_{EO}$ is reported herein, for ease of understanding. The more energy efficient systems will thus have a higher $1/E_{EO}$ value.

The quantum efficiency allows for an assessment of the photon efficiency, assessing the number of pollutant molecules undergoing degradation relative to the number of photons reaching the catalyst surface [61]. Based on the definitions contained in the IUPAC glossary, the following equations are proposed to calculate the quantum efficiency of photocatalytic foams:

$$k' = (k)(C_0)(V_{Illuminated})\ \ (mol\ s^{-1})$$

$$N_P = \frac{I_{0\lambda} * S * t}{E_P}\ (-)$$

$$q_{n,p} = \left(\frac{N_P}{t}\right)\frac{1}{N_A}\ (mol\ s^{-1})$$

$$QE = \frac{k'}{q_{n,p}}\ (-)$$

Equation 2.2: Quantum efficiency of photocatalysts

where, k' is the rate of pollutant degradation (mol s^{-1}), k is the kinetic constant (s^{-1}), C_o is the initial pollutant concentration (mol L^{-1}), $V_{Illuminated}$ is the total volume of pollutant irradiated.

The number of photons can be calculated using Equation 2.2, where $I_{0\lambda}$ is the incident irradiance of the light source (W m^{-2}), S is the surface of the sample onto which the light impinges (m^2) and t is the time under irradiation. $E_p = \frac{h*c}{\lambda}\ (J)$ is the photon energy at the wavelength emitted by the lamps, where h is Planck's constant, c is the speed of light and λ is the wavelength of light (m) from the lamps. The photon flux is the numbers of photons during irradiation of a mol of photons, where N_A is Avogadro's number (equation 2.2). Finally, the quantum efficiency is calculated using equation 2.2.

2.4. Photocatalytic activity for different foam structures

The wide range of materials, supports, reactor design and testing conditions reported in the literature for photocatalytic foams makes a direct comparison between different results challenging. An extensive survey of the literature, reported in Tables S2.1-S2.3 in Appendix 1, is discussed below, and based on the kinetics of the system, the electrical energy per order and quantum efficiencies, broken down by type of foam and substrate material, highlighting the advantages and disadvantages of each system. Examples of each type of foam, along with synthetic methods, advantages, and disadvantages of each can be found in sections 2.4.2 – 2.4.4.

2.4.1. Performance comparison

Figure 2.6 shows a breakdown of the data compiled in this meta-analysis, highlighting the disparity between the kinetic constant of a photocatalytic system, and its suitability for large scale adoption, shown here by the inverse electrical energy per order ($1/E_{EO}$) and quantum efficiency. With one exception [30], photocatalytic systems that show very high kinetics (above the 75th percentile), show neither $1/E_{EO}$ nor quantum efficiency values above the 75th percentile. Even when considering data points above the 50th percentile, only a very small proportion of reported systems show equally high values of k_ε and either $1/E_{EO}$ or quantum efficiency.

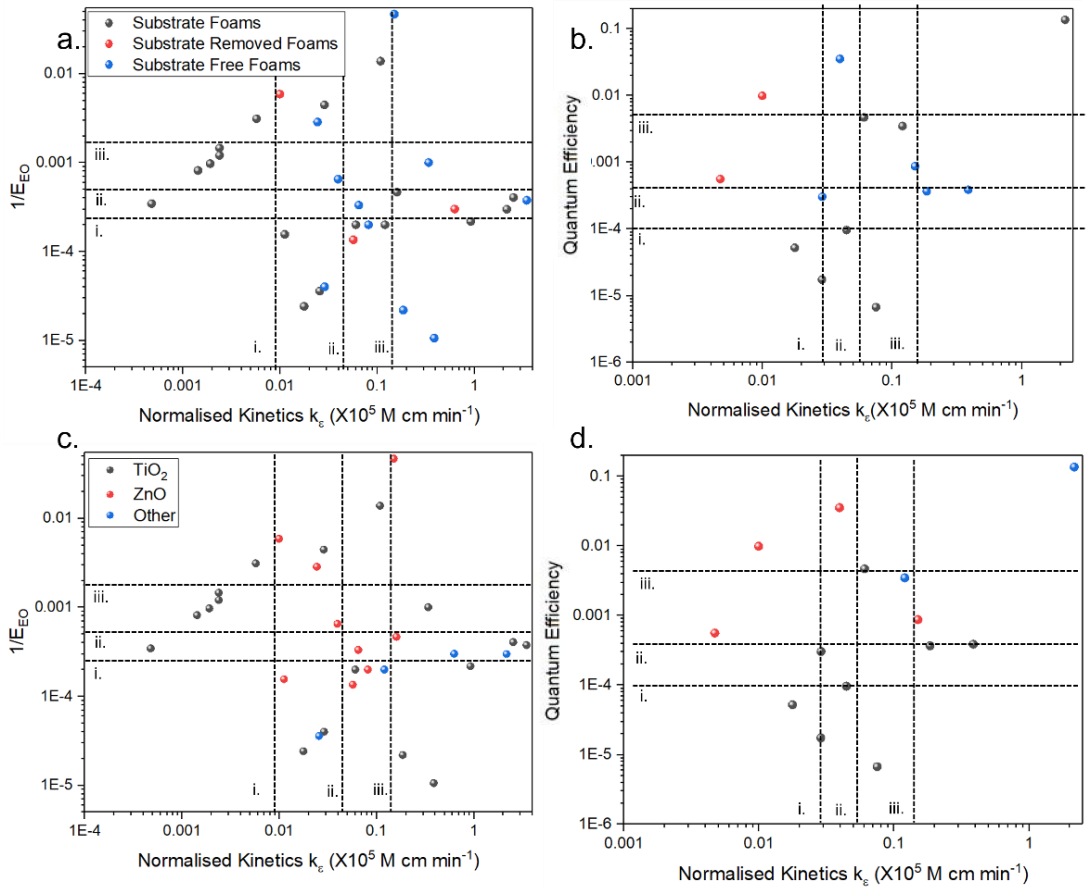

Figure 2.6: Plots of left) 1/EEO and right) Photocatalyst quantum efficiency, against normalised kinetics, kε, for foam based photocatalytic systems showing a breakdown by: (a,b type of foam and (c,d) photocatalyst material. Lines I, ii and iii represent the 25th, 50th and 75th percentile respectively. The legend in graphs a and c, also apply to graphs b and d, respectively.

Due to the initial research in the field being based on substrate supported foams, it is unsurprising that most of the data reported is based on these foams, and as such, these reports show the widest ranges, with data points falling in all four quartiles for all parameters. While these supported foams show high kinetics, when evaluating for both $1/E_{EO}$ and quantum efficiency, both parameters had ~50% of the data points falling below the 50th percentile. This means, while the 3D structure of foams has been shown to be beneficial for photocatalysis due to the higher surface areas and surface area to volume ratios, this is countered by the fact that the supports are inert, i.e. non-photocatalytic, thereby limiting the effective use of the incoming light from the irradiation source, resulting in lower quantum efficiencies [62].

Figure 2.6 shows that the substrate-free foams have some of the highest values for k_ε, $1/E_{EO}$ and quantum efficiency. These can be attributed to multiple factors: The substrate removed foams show very high porosities (>90%), and particularly open

porosity, resulting in high surface areas that can be reached by both pollutant and photons, providing area for degradation reactions to occur at. This allows for greater utilisation of light, increased electrical efficiency and thus better performance.

Discussion on the impact of substrate removed foams is partially hindered by the low number of data points. Note, that the data available comes from systems involving reduced graphene oxide (rGO) within the foam. rGO is not inherently photocatalytic, but finds use within photocatalytic systems due to its excellent charge transfer properties resulting in longer electron/hole pair lifetimes [63, 64]. This means that its inclusion likely leads to increased quantum efficiency of the system for a wide range of photocatalyst materials [65].

The impact of photocatalyst material on figures of merit is of particular interest. Considering quantum efficiency of the photocatalytic systems, foams with highest quantum efficiency are those made of ZnO or Zn based photocatalysts, with one exception. Foams made of TiO_2 show low quantum efficiency irrespective of foam type. This is because ZnO to absorbs over wider range of wavelengths compared to TiO_2, allowing for greater utilisation of available photons [66]. While the majority of publications assess TiO_2 and ZnO foams, the use of more complex catalysts has been reported in a few cases, Including copper oxide-based catalysts, [32, 67] and bismuth tungstate, [68] or oxoiodide catalyst. [69] The latter two provide photocatalytic activity in the visible light spectrum and may be therefore useful in solar-driven photocatalytic systems.

As one would expect, as more time is dedicated to research into the field, coupled with technological advances, the results published show an upward trajectory in terms of performance. This can be seen in Figure 2.7 a and b, where > 85% of the data points from papers published between 2009 and 2014 show kinetics below the 50th percentile for kinetics, contrasted with 50 % from 2015-2019 and 33% from those published since 2020, respectively.

As shown in Figure 2.7 c and d, the research conducted between 2009 and 2014 primarily used TiO_2 supported on foam substrates, likely due to the widespread usage of TiO_2 nanoparticles for slurry systems and the relative simplicity of production of ceramic and metallic foams [12, 70, 71], as discussed previously. After 2015, publications appear to split into distinct camps: those continuing to focus on supported TiO_2 with reports of greater electrical efficiencies but with little change in quantum efficiency, along with higher kinetics. This suggests main improvements were made in reactor design and photocatalysts preparation, leading to faster degradation kinetics and associated shorter times to do so, thus reducing the

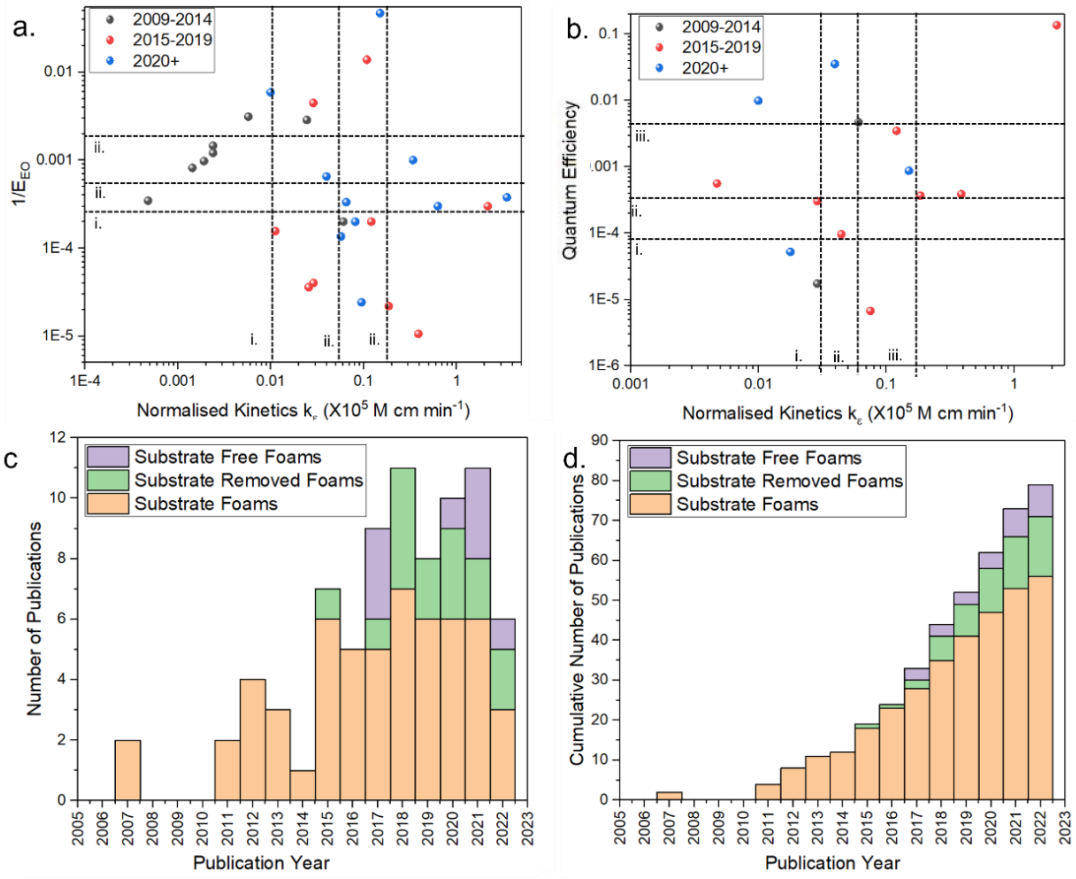

Figure 2.7: Plots of a) 1/EEO and b) Photocatalyst quantum efficiency, against normalised kinetics, kε, for foam based photocatalytic systems showing a breakdown by year of publication. Lines I, ii and iii represent the 25th, 50th and 75th percentile, respectively; c,d) Plots of c) annual and d) cumulative number of publications related to photocatalytic foams for water treatment broken down by type of foam used.

electrical energy per order [15]. The other camp is represented by publications focusing on Zn-based catalysts, containing ZnO and ZnFeS catalysts on substrates [41, 72]. The first use of substrate-free foams as photocatalysts was reported in 2017 [14]. From here, moving into the 2020s, the field undergoes further expansion: More research

has been conducted into TiO_2 supported foams, with reporting of higher kinetics, but with limited improvements to the electrical efficiency [38, 73, 74]. Zn-based catalysts have also been used on substrate-removed foams, by removing the metal substrate while retaining the underlying porous structure [75]. These foams show improvements in electrical efficiency and quantum efficiency, compared to the earlier supported Zn-based catalysts. The higher efficiency can be attributed to improvements in reactor design, particularly regarding use of more energy efficient light sources. Substrate-free ZnO foams show higher electrical efficiencies, quantum efficiency and kinetics, which can be attributed to improvements from TiO_2 as discussed previously, development of reactors and the increased efficiencies that come with a foam that is entirely photocatalytic [55, 76]. A graphical depiction of this development pathway is shown below in Figure 2.8.

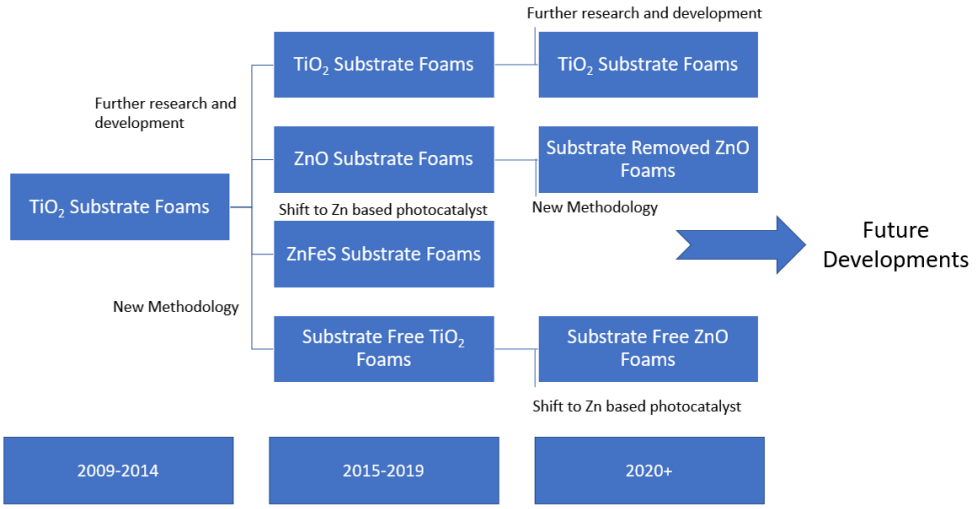

Figure 2.8: Flow chart showing the development of foam based photocatalysts over time.

2.4.2. Substrate supported foams – effect of substrate materials.

For use as porous supports for photocatalysts, materials fall into three major categories: Metallic foams, alumina-based foams, and silica / silicon carbide-based foams. TiO_2 and ZnO are the most common materials grafted, coated, or deposited onto foams substrates. Other catalysts successfully coated onto foam substrates include multi-walled carbon nanotubes [75], BiOI [77], ZnFeS [41], as well as binary [68, 78, 79] and ternary [32] photocatalysts. The methods for the deposition usually lead to good adhesion of the catalyst on the substrate, preserving the open porosity and, therefore, the high surface area of the foams. The main reported methods of

deposition include spray coating [13], dip coating [13, 28, 74], and growth during hydrothermal synthesis [32, 78, 80].

Metallic foams see widespread use across multiple areas, from aerospace engineering to biomedicine applications [81], to electrochemistry [82] to catalysis [83]. Metallic foams can be synthesised in a multitude of ways with techniques including casting within a resin mould, [84], use of a sacrificial template such as a polymer, [85] or use of a foaming agent [70] .

In photocatalysis, the mechanical strength of metal foams represents their key benefit, allowing for applications in flow or recirculating systems [86]. Their high surface area also provides for high catalyst loading [70]. The conductive nature of metals has benefits when applied as supports for photocatalysts. Nickel foams have been shown to significantly increase the photocatalytic activity of supported catalyst [30]. As strong electron acceptors, the metal foams facilitate greater charge pair separation, thus increasing the lifetime of charged species at the photocatalyst surface that degrade pollutant molecules [72]. Research using $Zn_{0.9}Fe_{0.1}S$ supported on Ni foam, showed a 6-fold increase in degradation of the fluoroquinolone antibiotic norfloxacin, when compared with an equivalence of unsupported catalyst [72] shown below in Figure 2.9.

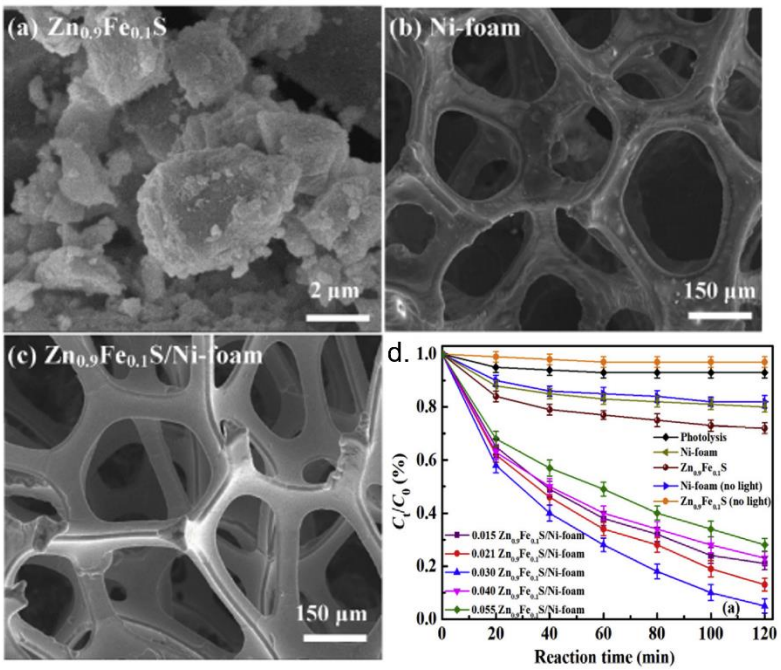

Figure 2.9: SEM micrographs of a) unsupported $Zn_{0.9}Fe_{0.1}S$, b) Ni foam, c) $Zn_{0.9}Fe_{0.1}S$, supported on Ni foam. D) Removal rates of norfloxacin using $Zn_{0.9}Fe_{0.1}S$ photocatalysts. Adapted from reference [72].

Similar findings were obtained using Fe-ZnS on Ni foams for the degradation of bisphenol A [41]. The increase in activity is attributed to the 3D structure of the foam and the high surface area that it provides, while also acting as an electron sink, leading to increased charge pair lifetimes. In addition, the substrate may increase the stability of the supported catalyst by reducing water-surface interaction, with both Zn^{2+} and Fe^{2+} at half the concentration leaching into solution compared with the unsupported catalyst. This, coupled with charge separation of electrons away from the catalyst surface provides a promising approach for to mitigate photo-corrosion of certain photocatalysts especially Zn-based [87].

Another beneficial effect of the use of metallic foams is the formation of interstitial oxide layers at the catalyst-substrate interface, arising as part of a heat treatment step. The metal oxide layer, particularly NiO from Ni foams, leads to the formation of a heterojunction at the surface, providing an additional route towards charge pair separation and enhanced photocatalytic activity [68, 88, 89].

Porous ceramic materials exhibiting high porosities currently find use in a wide range of applications including architectural infrastructure and in the biomedical sector [90], with their widescale adoption due to multiple beneficial properties including: high surface areas and permeability as well as significant mechanical, thermal and chemical stability [91]. These properties are also conducive to their use in photocatalytic flow reactors and in the decoration and coating of photocatalyst nanoparticles onto the support, as this frequently requires high temperature sintering to ensure adherence to the surface and formation of desired crystal phases of photocatalyst [92]. The synthesis of these supports generally follows a replica-type methodology, wherein a slurry of particles is soaked into an easily pyrolised template material, e.g. PU foams, and dried prior to heat treatment to remove the template and leave the sintered ceramic support behind [12, 52, 93].

Alternatively, as a metal oxide, alumina aerogel foams have been produced via a sol-gel reaction using gas evolution from the decomposition of the reactants to generate porosity [94-96] [97]. Interestingly, the surface structure of some alumina foams, particularly γ-Al_2O_3 and η-Al_2O_3, are themselves catalytic, due to the high proportion of oxygen rich groups and hydroxyl groups [98, 99]. These regions provide active sites

for the deposition of photocatalysts, providing strong chemical bonds and adherence to the surface of the foam [100]. With a band gap > 7 eV [101, 102], Al_2O_3 is an insulating material and as such, unlike other support materials such as Ni or SiC which benefit from high electron mobility or the formation of a p-n heterojunction, its use as a support cannot provide electronic effects to promote photocatalytic degradation. Instead, alumina supports provide high surface areas for anchoring of photocatalyst nanoparticles. This gives significant performance improvement over slurries, for which it is well reported that increasing the concentration of particles in solution leads to a decrease in photocatalytic activity due to higher turbidity of the solution, negatively impacting light penetration and subsequently activation of catalyst particles [6, 103, 104]. For example, increasing titania nanoparticle slurry loading from 10 % to 12 % saw a decrease in kinetic constant of ~ 48 %, whereas the same catalyst loading increase onto a reticulated Al_2O_3 led to a ~ 450 % increase in a pilot-scale photocatalytic oxidation reactor under UV irradiation for the degradation of tertiary amine (DBU) [13]. Similarly, complete mineralisation of phenol was achieved using TiO_2/Al_2O_3 foams with around 75% higher photocatalytic activity than the corresponding slurry dispersion [16].

B-Silicon carbide (β-SiC) foams are highly suited towards use as foams due to their ease of synthesis, from a range of precursors, e.g. via chemical vapour deposition method (CVD) using silicon chloride and methane [105, 106]. Alternatively, open cell foams of self-bonded SiC materials have been synthesised through the replica method using a polyurethane (PU) foam as template, onto which a sol containing elemental silicon and carbon black particles were deposited, followed by high temperature reaction and pyrolysis of the support [71] as shown in Figure 2.10.

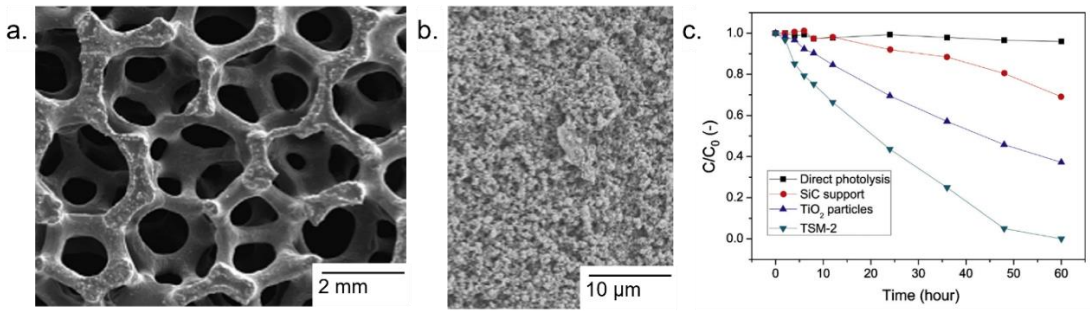

Figure 2.10: SEM micrographs of a) SiC foam, b) Supported TiO_2 on foam and c) removal rates of 4-ABS using supported TiO_2 photocatalysts. Adapted from reference [107]

The high thermal stability of SiC has proved beneficial for the synthesis of composite materials, e.g. TiO_2/SiC where oxidation at high temperature has allowed tuning TiO_2 crystal structure, in particular the anatase/ rutile crystal ratio, with no change observed in the carbide support [71]. Furthermore, this stability may allow for the regeneration of deactivated catalyst, through thermal or chemical treatment, without risks of compromising the support material [91].

A particular advantage of SiC foams as supports for photocatalysis is a high density of superficial oxygenated groups, providing multiple sites for anchoring metal oxide photocatalysts to the foam [28], resulting in higher catalyst loadings than reported for other ceramic foams [13, 107, 108]. A widely reported phenomena is the synergic effect between p-type β-SiC and n-type TiO_2 due to β-silicon carbides' semiconductor nature, thus allowing for coupling between the two materials to form a p-n heterojunction in the structure. [109] This results in greater charge separation, with the electrons promoted to the conduction band of the SiC moving across the heterojunction to the TiO_2 conduction band and the holes in the TiO_2 valence band moving to the valence band of the SiC [110]. This separation of charges increases the lifetime of the charged species such that the charge species have a greater chance to be involved in reduction or oxidation reaction [111]. This can clearly be seen in cases where a catalyst-free, reticulated SiC foam was shown to have low photocatalytic activity towards 4-ABS under UV irradiation with a removal of ~ 30% after 60 hours, compared with ~60% removal using TiO_2 particles alone [107]. After immobilising an equivalent mass of TiO_2 catalyst onto the SiC foams, ~100% removal over the same time scale was achieved [107, 110]. Additionally, the photocatalytic removal of the herbicide paraquat was performed using TiO_2/SiC foams, with 90% TOC removal achieved in a flow reactor using UV irradiation [15].

2.4.3. Substrate removed foams

Foams in this group are generally obtained from coating, primarily with conductive carbon materials of a sacrificial substrate, which is subsequently removed. Commonly employed supports include metal-organic frameworks (MOFs), prepared as a template via calcination of solid architectures, obtaining clean and smooth skeleton foams, with a lightweight and interconnected highly porous structure [112].

These were subsequently coated with graphene oxide (GO) and porous ZnO nanocages, providing a superior photocatalytic activity. Similar foams were also synthesized via carbonization of starch and polyvinyl pyrrolidone (PVP). The resulting foam produced a semi-graphitized structure with high porosity where, after addition of ZnO nanorods as photocatalyst and effectively decomposed more than 98% of rhodamine B under both visible and UV light [113].

A further example is the use of nickel-based skeletons as foam templates to generate graphene 3D structures, providing an inert and resistant substrate as shown in Figure 2.11. Using commercial nickel foams consisting of a surrounded uniform close-packed macropores over the structure, a highly porous graphene foam was obtained with pores in the micrometre range and a large specific surface area [36].

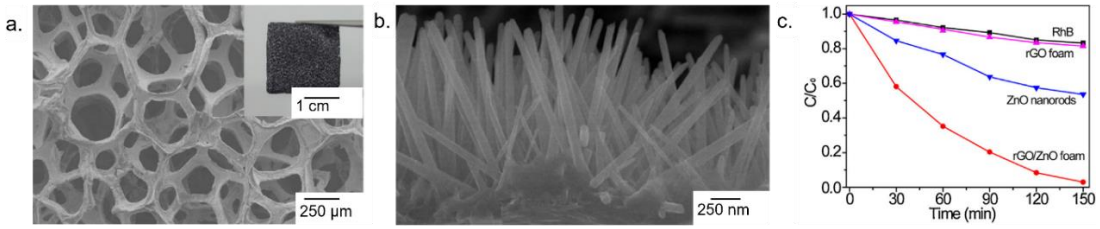

Figure 2.11: SEM micrographs of a) ZnO/rGO foam (inset is the photograph of free-standing ZnO/rGO foam), b) ZnO nanorods on the ZnO/rGO foam scaffold and c) removal rates of RhB using ZnO/rGO foam. Adapted from reference [36].

The removal of the Ni scaffold from the graphene foam structure played an important role on the photocatalytic processes, with 2.5 times higher photoactivity compared to the graphene foam still incorporating the nickel substrate. This enhanced performance was attributed to the higher electron mobility of graphene and its interaction with the catalyst (ZnO). The dissolution of Ni template also increased the illumination sites on the 3D sample, improving the overall photocatalytic efficiency [114].

Furthermore, the combination of the 3D structures and the conductive properties of graphene foams can ameliorate photocatalytic processes: Reduced graphene oxide (rGO) foams grown on nickel templates showed a superior photocatalytic performance thank flat films, related to the higher surface of the structure with a more effective contact between the reaction solution and the active sites [79]. The 3D structure of GO foams allowed more target molecules to be absorbed onto the

surface, reducing the light scatter by the internal pores [36]. The thickness of graphene foams can also affect the photocatalytic activity, with thicker layers of graphene compromising the mobility and electron acceptability of the foam structure, negatively affecting the photocatalytic properties of the ZnO semiconductor used as a modifier [35]. In the study, few-layers graphene was more appropriate in comparison to multi-layers, reaching a higher photocatalytic degradation of methylene blue solution under visible light illumination.

2.4.4. Substrate-free photocatalytic foams

A recent development in the field of photocatalytic foams is the formation of foam structures from the photocatalytic material itself, thus forming substrate-free foams. These substrate-free foams can be produced in multiple ways, including the formation of TiO_2-SiO_2 aerogels [115], hydrogel formation [116], freeze drying followed by template removal [14] as shown in Figure 2.12, liquid templating followed by sintering of metal oxide particles [76] and direct foaming of sol-gel syntheses [55]. When compared with synthesis methods for other types of foams, which involve the use of high temperatures (e.g. for metallic foams, [70]), or the use of highly caustic reagents (e.g. for the removal of Ni foams for substrate removal, [35, 79]), these synthetic methods require milder conditions and reagents for foam production.

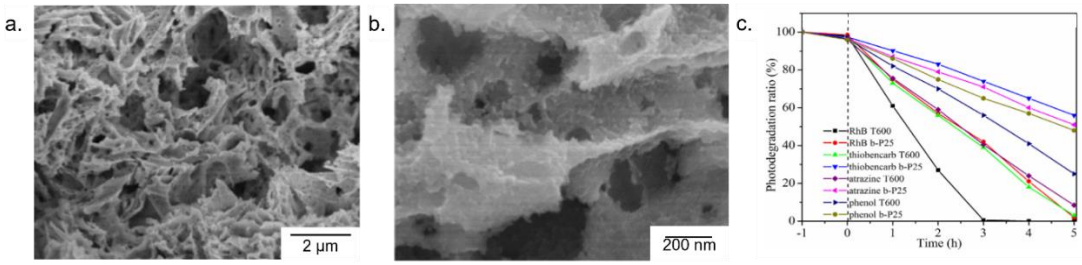

Figure 2.12: a,b) SEM micrographs of TiO_2 foam and c) removal rates of multiple target pollutants using TiO_2 photocatalysts. Adapted from reference [14].

Furthermore, the very low densities and high porosities of these foams (> 90%) cause these foams to show buoyancy and as such are easy to replace and remove from reactors. The formation of low density, floating black-TiO_2 foams, has been reported, with the freeze drying synthesis forming a structure of both open and closed pores, with the buoyancy attributed to the latter [14]. While too many closed pores are less desirable due to the catalyst surface being inaccessible, the reported foams still showed excellent removal performance for the degradation of a range of organic

pollutants including hexadecane, phenol, atrazine, rhodamine B and thiobencarb. The foams demonstrated better removal performance for all substances than the P25 TiO_2 powder reference [12]. Substrate-free ZnO foams synthesised by liquid templating and sol gel methods, applied for the photocatalytic degradation of carbamazepine show better quantum efficiency and energy efficiency than immobilised and slurry systems, further highlighting the benefits of the 3D foam structure [55, 76].

2.5. Use of photocatalytic foams in reactors

The design of photocatalytic foams is intrinsically linked to the configuration of the reactors they are used in, with different designs of the latter used to make full use of the former's physical properties, particularly their 3D structure and high surface areas. Photocatalytic reactor design challenges include: (1) increasing mass transfer between the aqueous medium and the photocatalyst surface for greater kinetics; (2) maximising light efficiency and irradiation of the entire foam, due to the structural complexity of the foams, while maximising the illuminated (or active) surface area; (3) increasing long-term stability of the photocatalyst on the substrate/template foam for use at scale, avoiding leaching and, in view of potential use, with minimal downtime caused by replacement or repair [117, 118].

There is a wide range of foams photoreactors designed for water treatment, their configuration comprising continuous, batch and semi-continuous systems. The vast majority consist of simple batch systems, with the foam located in a single tank reactor with the aqueous solution being continuously stirred. However, this configuration does not take advantage of the high porosity and interconnected 3D structure of foams, which are better suited for flow reactors, where the liquid phase can permeate through the pores into the internal structure of the foam [28]. In this case, the flow can operate in a re-circulating or single pass mode with uniform mixing, with the contaminant in close contact with the foams' surface. Moreover, the flow through the tortuous structure can generate turbulence improving mixing, thereby improving the mass transfer by decreasing the external diffusion layer [13]. In a typical flow reactor, a glass tube (quartz or borosilicate) is filled with a photocatalytic foam and surrounded by UV/visible lamps, where the liquid can flow through the foams by

a circulation mode using an external pump. In terms of configuration, a recirculating flow reactor is considered a versatile system for evaluation of the photocatalyst, reactor geometry, irradiation source, and fluid residence time, which can provide a simpler solution than slurry reactors [118, 119]. Furthermore, it allows for the catalyst to be applied under conditions like what would be used at scale, in this case single pass flow systems. Operating under recirculating conditions allows for evaluation of catalyst performance at varying flow rates and assessment of mechanical stability.

Most of the foams applied in flow systems so far have been prepared using alumina or SiC [120], which have a miniporous reticulated structure, usually at the micrometre range, and are considerably more resistant than polymer or carbon foams. The latter show lower mechanical stability and are less suitable at present for use within a flow reactor. Alumina- and SiC-based foam can be adapted to different geometries to maximise flow rate without significant increases in pressure, which would negatively affect the energy efficiency of the reactors. Metallic foams also exhibit a highly resistant structure which make them suitable for use in flow reactor systems, but the cost to generate an open cell monolith is still considerably higher than for ceramic foams [121].

The main challenge in the design of photoreactors remains light efficiency, specifically the difficulty of providing a uniform light distribution over the whole 3D structure of the foam with sufficient light penetration to its internal core [122, 123].

To overcome this challenge, different configurations have been developed, including an annular reactor, wherein the irradiation source is internal and central to the foam, positioned between the light source and the internal wall of the reactor [13]. These reactors ensure that the core of the foam is irradiated, as it is closest to the light source, but therefore, the exterior surfaces now require additional irradiation. A clever alternative has been to use a reflector, a screen made of highly reflective material such as aluminium, wrapped around the outer wall of the reactor [124], reflecting photons that passed through the foam back into the reactor and foam structure, increasing the quantum efficiency of the reactor.

An alternative strategy for the configuration of the reactor was to allocate the irradiation source through the foam, internal but not centrally. This allows for multiple irradiation sources to be included within the foam, enabling greater light coverage and higher illuminated surface areas, while providing for lamps of smaller diameters to be included, thus maximizing the illumination area and reducing the dimensions in a tubular configuration [125]. The decentralization of irradiation means that, with design and simulation, an optimal number of irradiation sources can be applied throughout the foam structure to allow for high illuminated surface areas [126].

A third strategy is to position the catalyst inside of a tubular quartz tube surrounded by the light source(s) placed externally. This methodology warrants the greatest control over irradiation, light intensity, and power usage of the reactor, through designing the reactor for light sources to be placed outside the tube at varied distance from the tube [108]. However, as it the only design with an external irradiation source, the use of a reflector is more complex and less effective, reducing the efficiency of the irradiation. Examples of reactor designs can be seen in Figure 2.13.

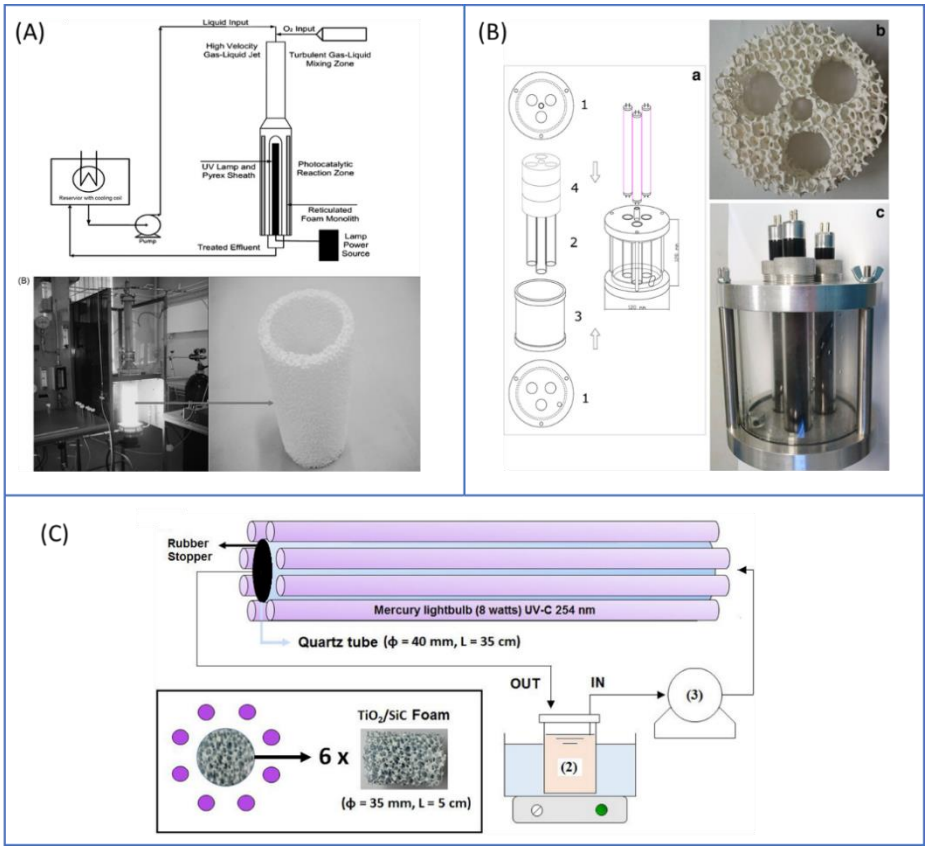

Figure 2.13: Single-pass reactor configurations for photocatalytic foams: (A) the irradiation source is allocated internally and centrally, surrounded by a photocatalytic foam [13]; (B) designed foams allowing the presence of

multiple illuminating points internally to the structure [125]; and (C) a foam centrally allocated with UV lamps externally surrounding it [108].

The source of irradiation and how the catalyst is allocated are critical parameters that can impact the design and geometry of photocatalytic reactors for immobilized catalysts [119]. In the case of photocatalytic foams, their complex, 3D shape must also be taken into consideration as it directly affects mass and radiation transfer limitations when considering scale-up.

2.6. Future perspectives on development of photocatalytic foams

As shown in Figure 2.7, the field of photocatalytic foams has been constantly developing, from supported TiO_2 foams to the variety of foams discussed herein, and this is likely to continue. While development thus far has focused on new methodologies for foam production, or improving the activity of photocatalysis, future developments could be expanded to include technological advancements as well.

2.6.1. Technological advances.

Of particular interest is the application of UV-LED lamp technology that may provide significantly improved energy efficiency of photocatalysis, offer new reactor designs given the small size of LEDs compared to traditional mercury (Hg) lamps, and more sustainable lamp disposal as LEDs do not contain toxic materials as illumination source and lower energy consumption (potentially lower E_{EO}). [127] [128]. While not the focus of this review, it is worth noting that these advances will bring these benefits all light driven advanced oxidation processes as well as water treatment.

2.6.2. Novel foam materials

Alongside the technological development, material developments will likely continue, expanding into two new fields, increasing the number of photocatalyst materials applied as foams and the use of doping materials: While most materials used currently are large band gap semiconductors, requiring UV irradiation, a common method for band gap engineering of nanoparticles is doping and has shown promise in allowing for visible light utilisation of ZnO and TiO_2 [129-131]. Non-metal dopants such as nitrogen have been shown to allow for visible light (or solar) photocatalysis of both ZnO [132] and TiO_2 [133, 134], along with metal dopants such as copper [135], allowing for utilisation of photocatalysts under visible light. However, thus

far these developments have been limited to modification of nanoparticle or film based photocatalysts and not been applied to foam photocatalysts in any form.

Graphitic carbon nitride (g-C_3N_4), has shown good visible light activity for degradation of pollutants [136, 137], and is therefore a possible candidate for photocatalysts used for water treatment. Photocatalytic systems that utilise g-C_3N_4 thus far use it in a slurry system. Immobilisation of g-C_3N_4 onto a foam or production of a foamed variant of g-C_3N_4 would prove to be a system of interest. Furthermore, the photocatalytic activity of g-C_3N_4 systems can be tuned via doping [138].

As previously discussed, the use of substrate-free foams shows great promise for practical application and the synthetic procedures to make these foams (e.g., sol-gel, direct foaming) have potential for incorporation of dopants into the foam structure, via control of the molar % of dopant in the foam formulation.

2.6.3. Foam reactor development

As discussed briefly previously, the application of foam based photocatalysts in reactors requires particular care be taken with the positioning of irradiation sources as well as accounting for the 3D structure of the foam, such as pore size and illuminated surface area. As the field develops and the use of these reactors become more widespread, it is likely that these parameters will be more easily controlled leading to increased performance of the reactor, in terms of photocatalytic activity, energy efficiency and quantum efficiency, due to maximised illuminated surface areas of photocatalyst.

3D printing of photocatalytic foams [139, 140], coupled with computational modelling [141],shows potential in this area, as design of the structures to be printed provides opportunity to increase the surface area which will be illuminated, allowing for bespoke foams to be printed to maximised the efficiency of the reactors. At present, while substrates can be printed with hierarchical foam structures [139], attempts to print substrate free foams are currently limited to simplistic structures. [142, 143]

2.7. Conclusions

This review of the available literature shows the that photocatalytic foams have the potential to address the limitations of slurries and immobilized catalysts which have, so far, hindered more widespread industrial adoption of photocatalysis for the

degradation of organic pollutants in water. Furthermore, studies on their use in continuous flow reactors provide a clear path towards practical adoption. The high performance of foams can be attributed to the combination of favourable physical, e.g. high porosity and surface area, and structural parameters, e.g. mechanical resistance. However, some fundamental gaps still exist, particularly in relation to linking materials' properties to foam performance in photocatalytic flow reactors. The authors encourage the community to focus on key challenges, including:

- Shift the focus from the assessment of surface area, which is relevant for slurries, towards methods to reliably evaluate the active surface, i.e. open porosity which can be reached by the external light source. Characterisation methods like computed tomography (CT) and BET can support these efforts.

- Develop methods to combine the design of the irradiation source and of the foam structure to maximize the active surface, including estimating how deep the irradiation source can penetrate.

- Include assessments of catalyst reusability and long-term performance in scientific publications to facilitate scale-up considerations, including cost.

Furthermore, the field suffers from a lack of common best practices and nomenclature, which makes it challenging comparing performance across different materials, geometries, and process conditions. To address this, the authors have suggested the adoption of:

A clear and simple nomenclature to classify foams based on average pore size and manufacturing process.

The routine use of key figures of merit, including photocatalyst quantum efficiency and electrical energy per order to compare the performance of different foams under different conditions, moving beyond the mere reporting of degradation rates.

Finally, the authors would like to re-iterate the often-repeated advice that whenever practical or possible, researchers should move away from using dyes, and using HPLC rather than UV-Vis, to determine photocatalytic activity and degradation kinetics.

2.8. CrediT authorship contribution statement

Zachary Warren: Conceptualisation, Investigation, Methodology, Visualisation, Writing – original draft. **Thais Tasso Guaraldo:** Conceptualisation, Investigation, Writing – review & editing. **Alysson Stefan Martins:** Conceptualisation, Investigation, Writing – review & editing. **Jannis Wenk:** Conceptualisation, Supervision, Writing – review & editing. **Davide Mattia:** Conceptualisation, Funding acquisition, Project administration, Supervision, Writing – review & editing.

Acknowledgments

The authors are grateful for EPSRC for funding support (Grant No. EP/P031382/1).

ZW acknowledges The University of Bath for funding his PhD.

The authors also acknowledge Dr Daniel F Segura for artwork support.

2.9. Appendix

Table S2.1: Foams as substrate

Material	Catalyst loading	Degradation conditions	$[Pollutant]_0$	ε / M^{-1} cm^{-1}	porosity	Pore size /µm	k X 10^{-3} /min^{-1}	1/Eeo	QE	k^{t} (k/ε) X10^{5} /M cm min^{-1}	Ref
ZnO/Ni Foam	No details provided on foams	Batch reactor 70 mL volume Lamp Xe 300 W	Rhodamine B 15 mg L^{-1} 30.0 µmol L^{-1}	40300 (524 nm) [144]	-	750	64.3	46.67 X10^{-5}	-	1.60 X10^{-1}	[80]
Zn0.9Fe0.1S/Ni-foam	11.7 g L^{-1} foam	Batch rector 300 mL volume Lamp Xe 500 W, 6.1 W cm-2 Visible light	Norflaxin 5.0 mg L^{-1} 15.0 µmol L^{-1}	15400 (254 nm) [145]	97%	400	18.5	20.00 X10^{-5}	3.49 X 10^{-3}	1.20 X10^{-1}	[72]
Bi_2WO_6-TiO_2/Ni foam	1.0 g L^{-1} foam	Batch reactor 100 mL volume Solar irradiation used 2 hrs	Rhodamine B 5.0 mg L^{-1} 10.0 µmol L^{-1}	40300 (524 nm) [144]	-	-	12.1	-	-	3.00 X10^{-2}	[68]
ZnFeS/Ni-foam	11.7 g L^{-1} foam	Batch rector 300 mL volume Lamp Xe 500 W, 6.1 W cm-2 Visible light	Bisphenol A 0.2 mg L^{-1} 1.0 mmol L^{-1}	750 (254 nm) [145]	97%	500	16.2	30.00 X10^{-5}	1.37 X 10^{-1}	2.16	[41]
TiO_2-SiO_2 / Al foam	2.34 g L^{-1} foam	Recirculating batch reactor, reservoir V 1 L, reactor volume 35 mL. Reflector (solar compound parabolic collector) UV lamp, 365 nm 35 W cm-2	Pyrimethanil 10.0 mg L^{-1} 50.0 µmol L^{-1}	13200 (254 nm) [146]	95%	-	9.9	-	6.72 X 10^{-6}	7.50 X10^{-2}	[124]
CuO-CuS-ZnO/Cu foam	No details provided on foams	Batch reactor, 10 mL volume Lamp – 300 W Xe lamp 420 nm cut off filter	Rhodamine B 5 mg L^{-1} 10.0 µmol L^{-1}	40300 (524 nm) [144]	-	-	10.3	3.5915 X10^{-5}	-	2.56 X10^{-2}	[67]
TiO_2 /Alumina foam	12 % wt 21.78 g L-1	Recirculating reactor 15 L volume, Irradiated volume 4 L 1 KW lamp UVA 365 nm	DBU 100.0 mg L^{-1} 655.0 µmol L^{-1}			1200	65.9	0.03	-	-	[13]
TiO_2/Alumina foam	No details provided on foams	Batch reactor 250 mL volume Lamp 400W λ>300nm	Phenol 28.2 mg L^{-1} 300.0 µmol L^{-1}	750 (254 nm) [145]		2000		-	-	-	[52]
TiO_2 /Alumina foam	No details provided on foams	Batch reactor 250 mL volume Lamp 400W λmax = 365nm	Phenol 47.0 mg L^{-1} 500.0 µmol L^{-1}	750 (254 nm) [145]		500	11.5	40.66 X10^{-5}	-	1.53	[12]
TiO_2 /Alumina foam	40 g L^{-1}	Batch reactor, 500 mL Lamps, 6 X 8W lamps 254 nm, 3.54 mW cm-2.	RO16 20.0 mg L^{-1} 32.3 µmol L^{-1}	-	92%	836	23.9	6.78 X10^{-3}	8.94 X 10^{-1}	-	[93]
TiO_2 / β-SiC	9.5 g TiO2 on 52 g foam 9.5 g L-1	Recirculating batch reactor, 1 L volume, flow rate 60 – 1680 mL min^{-1} 4 X 8W UV-A lamp intensity 14 W m-2	Diuron 10 mg L^{-1} 42.9 µmol L^{-1}	16400 (254 nm) [145]	91	-	4.7	4.46 X10^{-3}	1.74 X 10^{-5}	2.87 X10^{-2}	[147]

Material	Catalyst loading	Degradation conditions	[Pollutant]	ε / M^{-1} cm^{-1}	porosity	Pore size µm	k X 10^{-3}	1/Eeo	QY	k' (k/ε) X10^{5} M cm min^{-1}	Ref
TiO_2 / β -SiC	No details provided on foams	Batch reactor volume 50 mL Lamp, 125 W Hg lamp, 365 nm, 130 W m-2	Diuron 10 mg L^{-1} 42.9 µmol L^{-1}	16400 (254 nm) [145]	91	-	9.9	0.20 X10^{-3}	4.69 X 10^{-3}	6.04 X10^{-2}	[5]
P25 TiO2 / SiC	6 foams, 35 mm diameter, 5 cm L. 16 wt% TiO2	Recirculating batch reactor 1L, flow rate 30 mL min-1 Lamps, 6 X 8W Hg bulbs, 254 nm	Paraquat 20 mg L^{-1} 77.7 µmol L^{-1}	20,600 (265 nm) [148]	-	4000	22.3	13.89 X10^{-3}	-	1.08 X10^{-1}	[108]
TiO_2 / β -SiC	No details provided on foams	Batch reactor volume 100 mL Solar simulator 1700 W, (300-800nm),250 W m^{-2}	Diuron 10 mg L^{-1} 42.9 µmol L^{-1}	16400 (254 nm) [145]	94	2400	2.9	2.42 X10^{-5}	5.23 X 10^{-5}	1.77 X10^{-2}	[74]
ZnO/SiO_2 (foamed glass)	Foams produced using ZnO 170 mg L-1	Batch reactor volume 200 mL 160 W Hg lamp, 380 nm	Rhodamine B 50 mg L^{-1} 100.0 µmol L^{-1}	40300 (524 nm) [144]	-	100	4.5	0.16 X10^{-3}	-	1.12 X10^{-2}	[37]
P90 TiO_2 /Alumina foam	7.2 g L^{-1}	Recirculating batch reactor, 1 L min-1. Reactor volume 690 mL Lamps, 3 X 4W Black light UV lamps 4 mW cm-2 intensity 365 nm Reflector made of polished Al and wrapped around reactor 3 hr experiments	Reactive Blue 19 25.0 mg L^{-1} 40.0 µmol L^{-1}	5625 (585 nm) [149]	-	-	25	-	9.67 X 10^{-5}	4.44 X10^{-2}	[125]
			LAS 32.0 mg L^{-1} 180.0 µmol L^{-1}	-			22.5	-	3.87 X 10^{-4}	-	
			PBIS 4.0 mg L^{-1} 15.0 µmol L^{-1}	-			30	-	4.24 X 10^{-5}	-	
TiO_2 /α-SiC	No details provided on foams	Batch reactor, volume 750 mL Lamps 8W, 365 nm	4-ABS 20 mg L^{-1} 100 µmol L^{-1}	21000 (217nm) [150]	70	1300	0.3	0.82 X10^{-3}	-	1.43 X10^{-3}	[151]
TiO_2 /α-SiC-SiO_2							1.2	0.31 X10^{-3}	-	5.71 X10^{-3}	
TiO_2 / β -SiC							0.1	0.35 X10^{-3}	-	4.76 X10^{-4}	
TiO_2 /α-SiC	No details provided on foams	Batch reactor, volume 750 mL Lamps 8W, 365 nm	4-ABS 20 mg L^{-1} 100 µmol L^{-1}	21000 (217nm) [150]	70	1000	0.4	0.98 X10^{-3}	-	2.38 X10^{-3}	[107]
TiO_2 /β-SiC						1300	0.5	1.4 X10^{-3}	-	2.38 X10^{-3}	
TiO_2 / SiC						2500	0.5	1.21 X10^{-3}	-	2.38 X10^{-3}	
TiO_2/Porcelain clay	14 pieces of TiO2-coated alveolar clay foams (about 28 mm in height and 22 mm in diameter per piece)	Recirculating batch reactor, 400 mL volume, 40 mL min-1 12 X 18 W UV-A lamp tubes (Actinic BL TL-D, Philip).	CHP 2,000 mg L-1 13.1 mmol L^{-1}	-		1260	11.5	0.60 X10^{-3}	-	-	[38]
						2590	-	-	-	-	

Table S2.2: Foams formed via substrate removal

Material	Catalyst loading	Degradation conditions	[Pollutant]$_0$	ε / M^{-1} cm^{-1}	porosity	Pore size /µm	k X 10^{-3} /min^{-1}	1/Eeo	QE	k' (k/ε) X10^5 /M cm min^{-1}	Ref
BiOI/GO foam	3.3 g L^{-1} foam	Batch reactor, 15 mL volume Lamp 60 W LED lamp (>400 nm)	Phenol 100 mg L^{-1} 1.0 mmol L^{-1}	750 (254 nm) [145]	-		4.7	0.30 X10^{-3}	-	6.27 X10^{-1}	[69]
Au/ZnO/rGO foam	No details provided on foams	200-780 nm	Rhodamine B	40300 (524 nm) [144]	-	500	12.8	-	-	3.18 X10^{-2}	[79]
ZnO/rGO	0.2 g L^{-1} foam	Batch reactor, 25 mL Lamp, solar simulator 100 mW cm-2	Rhodamine B 5 mg L-1 10.0 µmol L^{-1}	40300 (524 nm) [144]	87	100	1.9	-	5.61 X 10^{-4}	4.71 X10^{-3}	[36]
ZnO/graphene	0.5*0.5*0.5 cm^3 sample	Batch reactor, 3.4 mL cuvette as reactor, 85 mW LED lamp, 365 nm, 0.48 mW cm^{-2}	Rhodamine B 1 mg L-1 2.0 µmol L^{-1}	40300 (524 nm) [144]	87	-	4.0	5.91 X10^{-3}	9.90 X 10^{-3}	9.93 X10^{-3}	[114]
ZnO/rGO	0.5 g L^{-1} foam	Batch reactor, 100 mL Lamps, 300 W Xe lamp, 200 mW cm-2	Rhodamine B 10 mg L-1 20.0 µmol L^{-1}	40300 (524 nm) [144]	87	20	22.9	0.14 X10^{-3}		5.68 X10^{-2}	[112]

Table S2.3: Substrate-free foams

Material	Catalyst loading	Degradation conditions	[Pollutant]$_0$	ε / M^{-1} cm^{-1}	porosity	Pore size /μm	k X 10^{-3} /min^{-1}	1/Eeo	QE	k' (k/ε) X10^5 /M cm min^{-1}	Ref
TiO_2 – SiO_2	Annular foams. H = 9 cm, OD = 4.5 cm, ID = 3 cm	Batch reactor, 500 mL volume Lamp 16 W UV lamp (254 nm)	Glyphosate 20 mg L^{-1} 118.3 μmol L^{-1}	-	-	15.00	3.3	3.14 X10^{-3}	-	-	115
TiO_2	12.5 g L^{-1} foam	Batch reactor, 40 mL volume 300 W Xe lamp, 100 mW cm-2 1.5 AM	Rhodamine B 1 mg L^{-1} 2.0 μmol L^{-1}	40300 (524 nm) 144	91	500	11.6	4.01 X10^{-5}	3.04 X 10^{-4}	2.88 X10^{-2}	14
			Thiobencarb 1 mg L^{-1} 4.0 μmol L^{-1}		91		6.3	2.33 X10^{-5}	3.08 X 10^{-4}	-	
			Atrazine 1 mg L^{-1} 4.5 μmol L^{-1}	3400 (254 nm) 145	91		6.3	2.19 X10^{-5}	3.68 X 10^{-4}	1.85 X10^{-1}	
			Phenol 1 mg L^{-1} 10.0 μmol L^{-1}	750 (254 nm) 145	91		2.9	1.06 X10^{-5}	3.87 X 10^{-4}	3.87 X10^{-1}	
ZnO	0.5 g L^{-1} foam	Batch reactor 250 mL volume Lamp – UV lamp (5 W, 6.2 mW cm-2 254 nm)	Carbamazepine 2.4 mg L^{-1} 10.0 μmol L^{-1}	6070 (254 nm) 145	900 °C= 94-95% 1000 °C= 91-93%	300	2.4	0.65 X10^{-3}	3.56 3.08 X 10^{-2}	3.95 X10^{-2}	76
ZnO/Carbon foam	Nanorod loaded foam 1 g L-1 foam	Batch reactor, 100 mL volume Visible light – 300 W Xe lamp 420 nm cut off.	Rhodamine B 10 mg L-1 20.0 μmol L^{-1}	40300 (524 nm) 144	88% at 600 °C	35.00	26.1	0.33 X10^{-3}	-	6.48 X10^{-2}	113
		Batch reactor, 100 mL volume UV lamp – 500 W 365 nm			92% at 1000 °C		32.7	0.20 X10^{-3}	-	8.11 X10^{-2}	
ZnO	1.5 g L^{-1} foam	Recirculating reactor, flow rate 250 mL min-1, 500 mL volume Lamps (3 X 5 W, 10.3 mW cm-2, 254 nm)	Carbamazepine 2.4 mg L^{-1} 10.0 μmol L^{-1}	6070 (254 nm) 145	94-96%	690	9.1	46.86 X10^{-3}	2.63 X 10^{-3}	1.50 X10^{-1}	55
ZnO	10 g L^{-1} foams	Batch reactor, 500 mL Lamps, 6 X 8W lamps 254 nm, 3.54 mW cm-2.	Rhodamine B 50 mg L-1 100.0 μmol L^{-1}	40300 (524 nm) 144	91.5% ± 0.02 36 ppi	903	9.8	2.86 X10^{-3}		2.43 X10^{-2}	33, 34
TiO_2/graphene	3 g L^{-1} foam	100 mL batch reactor 250 W Hg lamp	Methyl Orange 20 mg L^{-1} 61.1 μmol L^{-1}	25100 (466.5 nm) 152	-	-	85	1.00 X10^{-3}	-	3.39 X10^{-1}	153
			Phenol 10.0 mg L-1 100.0 μmol L^{-1}	750 (254 nm) 145			26	0.38 X10^{-3}	-	3.47	

2.10. References

1. M. N. Chong, B. Jin, C. W. Chow and C. Saint, *Water Res*, 2010, **44**, 2997-3027.
2. S. K. Loeb, P. J. J. Alvarez, J. A. Brame, E. L. Cates, W. Choi, J. Crittenden, D. D. Dionysiou, Q. Li, G. Li-Puma, X. Quan, D. L. Sedlak, T. David Waite, P. Westerhoff and J. H. Kim, *Environ Sci Technol*, 2019, **53**, 2937-2947.
3. C. B. D. Marien, M. Le, A. Azaïs, I. Christian, M. Bra, P. Drogui, A. Dirany and D. Robert, *Journal of Hazardous Materials*, 2019, **370**, 164-171.
4. H. d. Lasa, *Photocatalytic Reaction Engineering*, Springer US Boston, MA, 2005.
5. N. A. Kouamé, D. Robert, V. Keller, N. Keller, C. Pham and P. Nguyen, *Catalysis Today*, 2011, **161**, 3-7.
6. A. Manassero, M. L. Satuf and O. M. Alfano, *Chemical Engineering Journal*, 2017, **326**, 29-36.
7. S. Horikoshi and N. Serpone, *Catalysis Today*, 2020, **340**, 334-346.
8. V. L. Colvin, *Nature Biotechnology*, 2004, **22**, 760-760.
9. M. A. Kiser, P. Westerhoff, T. Benn, Y. Wang, J. Perez-Rivera and K. Hristovski, *Environ Sci Technol*, 2009, **43**, 6757-6763.
10. M. F. J. Dijkstra, H. Buwalda, A. W. F. de Jong, A. Michorius, J. G. M. Winkelman and A. A. C. M. Beenackers, *Chemical Engineering Science*, 2001, **56**, 547-555.
11. M. F. J. Dijkstra, A. Michorius, H. Buwalda, H. J. Panneman, J. G. M. Winkelman and A. A. C. M. Beenackers, *Catalysis Today*, 2001, **66**, 487-494.
12. M. Vargová, G. Plesch, U. F. Vogt, M. Zahoran, M. Gorbár and K. Jesenák, *Applied Surface Science*, 2011, **257**, 4678-4684.
13. I. J. Ochuma, O. O. Osibo, R. P. Fishwick, S. Pollington, A. Wagland, J. Wood and J. M. Winterbottom, *Catalysis Today*, 2007, **128**, 100-107.
14. K. Zhang, W. Zhou, X. Zhang, B. Sun, L. Wang, K. Pan, B. Jiang, G. Tian and H. Fu, *Applied Catalysis B: Environmental*, 2017, **206**, 336-343.
15. C. B. D. Marien, M. Le Pivert, A. Azaïs, I. C. M'Bra, P. Drogui, A. Dirany and D. Robert, *Journal of Hazardous Materials*, 2019, **370**, 164-171.
16. M. Vargová, G. Plesch, U. F. Vogt, M. Zahoran, M. Gorbár and K. Jesenák, *Applied Surface Science*, 2011, **257**, 4678-4684.

17. K. S. W. Sing, *Pure and Applied Chemistry*, 1985, **57**, 603-619.
18. R. A. Shaw and T. Ogawa, *Journal of Polymer Science Part A: General Papers*, 1965, **3**, 3343-3351.
19. A. R. Studart, U. T. Gonzenbach, E. Tervoort and L. J. Gauckler, *Journal of the American Ceramic Society*, 2006, **89**, 1771-1789.
20. A. Yamamoto and H. Imai, *Journal of Catalysis*, 2004, **226**, 462-465.
21. A. Feinle, M. S. Elsaesser and N. Husing, *Chem Soc Rev*, 2016, **45**, 3377-3399.
22. H. Maekawa, J. Esquena, S. Bishop, C. Solans and B. F. Chmelka, *Advanced Materials*, 2003, **15**, 591-596.
23. D. Zabiegaj, M. T. Buscaglia, D. Giuranno, L. Liggieri and F. Ravera, *Microporous and Mesoporous Materials*, 2017, **239**, 45-53.
24. S. Andrieux, W. Drenckhan and C. Stubenrauch, *Polymer (United Kingdom)*, 2017, **126**, 425-431.
25. D. Zabiegaj, E. Santini, E. Guzmán, M. Ferrari, L. Liggieri, V. Buscaglia, M. T. Buscaglia, G. Battilana and F. Ravera, *Colloids and Surfaces A: Physicochemical and Engineering Aspects*, 2013, **438**, 132-140.
26. M. Costantini, J. Jaroszewicz, Ł. Kozoń, K. Szlązak, W. Święszkowski, P. Garstecki, C. Stubenrauch, A. Barbetta and J. Guzowski, *Angewandte Chemie - International Edition*, 2019, **58**, 7620-7625.
27. C. Vakifahmetoglu, D. Zeydanli and P. Colombo, *Materials Science and Engineering: R: Reports*, 2016, **106**, 1-30.
28. A. N. Kouamé, R. Masson, D. Robert, N. Keller and V. Keller, *Catalysis Today*, 2013, **209**, 13-20.
29. S. W. da Silva, J. P. Bortolozzi, E. D. Banús, A. M. Bernardes and M. A. Ulla, *Chemical Engineering Journal*, 2016, **283**, 1264-1272.
30. Y. Xue, R. Su, G. Zhang, Q. Wang, P. Wang, W. Zhang and Z. Wang, *RSC Advances*, 2016, **6**, 93370-93373.
31. M. Kete, O. Pliekhova, L. Matoh and U. L. Štangar, *Environmental Science and Pollution Research*, 2018, **25**, 20453-20465.
32. F. Cao, Z. Pan and X. Ji, *New Journal of Chemistry*, 2019, **43**, 11342-11347.
33. A. Kocakuşakoğlu, M. Dağlar, M. Konyar, H. C. Yatmaz and K. Öztürk, *Journal of the European Ceramic Society*, 2015, **35**, 2845-2853.

34. M. Konyar, T. Yildiz, M. Aksoy, H. C. Yatmaz and K. Öztürk, *Chemical Engineering Communications*, 2017, **204**, 705-710.

35. N. Karimizadeh, M. Babamoradi, R. Azimirad and M. Khajeh, *Journal of Electronic Materials*, 2018, **47**, 5452-5457.

36. X. Men, H. Chen, K. Chang, X. Fang, C. Wu, W. Qin and S. Yin, *Applied Catalysis B: Environmental*, 2016, **187**, 367-374.

37. E. M. Rangel, C. C. N. d. Melo and F. M. Machado, *Boletín de la Sociedad Española de Cerámica y Vidrio*, 2019, **58**, 134-140.

38. K. Pinato, K. Suttiponparnit, S. Jinawath and D. P. Kashima, *Journal of Materials Science*, 2020, **55**, 1451-1463.

39. K. Elatmani, N. B. oujji, G. Plantara, V. Goetz and I. A. ichou, *Materials Research Bulletin*, 2018, **101**, 6-11.

40. S. Qiu, S. Xu, G. Li and J. Yang, *Materials*, 2016, **9**.

41. Y. Xue, R. Su, G. Zhang, Q. Wang, P. Wang, W. Zhang and Z. Wang, *RSC Advances*, 2016, **6**, 93370-93373.

42. M. Du, B. Qiu, Q. Zhu, M. Xing and J. Zhang, *Catalysis Today*, 2019, **327**, 340-346.

43. D. Ding, W. Lan, Z. Yang, X. Zhao, Y. Chen, J. Wang, X. Zhang, Y. Zhang, Q. Su and E. Xie, *Materials Science in Semiconductor Processing*, 2016, **47**, 25-31.

44. C. M. Taylor, A. Ramirez-Canon, J. Wenk and D. Mattia, *J Hazard Mater*, 2019, **378**, 120799.

45. K. S. W. Sing, *Colloids and Surfaces*, 1989, **38**, 113-124.

46. J. Yu and X. Yu, *Environ Sci Technol*, 2008, **42**, 4902-4907.

47. T. Peng, D. Zhao, K. Dai, W. Shi and K. Hirao, *J Phys Chem B*, 2005, **109**, 4947-4952.

48. J. G. Fourie and J. P. Du Plessis, *Chemical Engineering Science*, 2002, **57**, 2781-2789.

49. P. Dechadilok and W. M. Deen, *Industrial & Engineering Chemistry Research*, 2006, **45**, 6953-6959.

50. S. A. M. Karimian and A. G. Straatman, *International Journal of Heat and Fluid Flow*, 2008, **29**, 292-305.

51. S. Josset, S. Hajiesmaili, D. Begin, D. Edouard, C. Pham-Huu, M. C. Lett, N. Keller and V. Keller, *J Hazard Mater*, 2010, **175**, 372-381.

52. G. Plesch, M. Gorbár, U. F. Vogt, K. Jesenák and M. Vargová, *Materials Letters*, 2009, **63**, 461-463.

53. G. Plesch, M. Vargová, U. F. Vogt, M. Gorbár and K. Jesenák, *Materials Research Bulletin*, 2012, **47**, 1680-1686.

54. H. S. Fogler, *Elements of chemical reaction engineering*, Pearson, Upper Saddle River, N.J., 3rd ed. edn., 1999.

55. Z. Warren, T. T. Guaraldo, J. Wenk and D. Mattia, *Journal of Materials Chemistry A*, 2022, **10**, 11542-11552.

56. K. Okada, T. Isobe, K. I. Katsumata, Y. Kameshima, A. Nakajima and K. J. MacKenzie, *Sci Technol Adv Mater*, 2011, **12**, 064701.

57. X. Yan, T. Ohno, K. Nishijima, R. Abe and B. Ohtani, *Chemical Physics Letters*, 2006, **429**, 606-610.

58. J. M. Buriak, P. V. Kamat and K. S. Schanze, *ACS Appl Mater Interfaces*, 2014, **6**, 11815-11816.

59. S. E. Braslavsky, *Pure and Applied Chemistry*, 2007, **79**, 293-465.

60. J. R. Bolton, K. G. Bircher, W. Tumas and C. A. Tolman, *Pure and Applied Chemistry*, 2001, **73**, 627-637.

61. N. Serpone and A. Salinaro, *Pure and Applied Chemistry*, 1999, **71**, 303-320.

62. A. Ramirez-Canon, M. Medina-Llamas, M. Vezzoli and D. Mattia, *Phys Chem Chem Phys*, 2018, **20**, 6648-6656.

63. N. M. Julkapli and S. Bagheri, *International Journal of Hydrogen Energy*, 2015, **40**, 948-979.

64. F. Li, X. Jiang, J. Zhao and S. Zhang, *Nano Energy*, 2015, **16**, 488-515.

65. P. V. Kamat, *J Phys Chem Lett*, 2012, **3**, 663-672.

66. R. Qiu, D. Zhang, Y. Mo, L. Song, E. Brewer, X. Huang and Y. Xiong, *J Hazard Mater*, 2008, **156**, 80-85.

67. F. Cao, T. Wang and X. Ji, *Applied Surface Science*, 2019, **471**, 417-424.

68. Q. Tong, Y.-M. Dong, X.-J. Wang, P. Yan and D.-N. He, *Nano*, 2015, **10**.

69. R. He, Z. Lou, J. Gui, B. Tang and D. Xu, *Applied Surface Science*, 2020, **504**, 144370.

70. M. F. Ashby, *Metal foams : a design guide*, Butterworth-Heinemann, Boston Oxford, 2000.
71. P. Nguyen and C. Pham, *Applied Catalysis A: General*, 2011, **391**, 443-454.
72. G. Zhang, Y. Xue, Q. Wang, P. Wang, H. Yao, W. Zhang, J. Zhao and Y. Li, *Chemosphere*, 2019, **230**, 406-415.
73. M. Rico-Santacruz, P. García-Muñoz, V. Keller, N. Batail, C. Pham, D. Robert and N. Keller, *Catalysis Today*, 2019, **328**, 235-242.
74. M. Rico-Santacruz, P. García-Muñoz, C. Marchal, N. Batail, C. Pham, D. Robert and N. Keller, *RSC Advances*, 2020, **10**, 3817-3825.
75. W. Wang, Z. Li, M. Zhang and C. Sun, *Sci Total Environ*, 2020, **702**, 135006.
76. T. Tasso Guaraldo, J. Wenk and D. Mattia, *Advanced Sustainable Systems*, 2021, **5**.
77. R. He, Z. Lou, J. Gui, B. Tang and D. Xu, *Applied Surface Science*, 2020, **504**.
78. Y. Zhang, L. Liu, B. Van der Bruggen, M. K. H. Leung and F. Yang, *Chemical Engineering Journal*, 2019, **373**, 179-191.
79. P. She, S. Yin, Q. He, X. Zhang, K. Xu, Y. Shang, X. Men, S. Zeng, H. Sun and Z. Liu, *Electrochimica Acta*, 2017, **246**, 35-42.
80. Y. F. Zhu, L. Zhou and Q. S. Jiang, *Ceramics International*, 2020, **46**, 1158-1163.
81. S. Wu, X. Liu, K. W. K. Yeung, C. Liu and X. Yang, *Materials Science and Engineering: R: Reports*, 2014, **80**, 1-36.
82. J. Banhart, *Progress in Materials Science*, 2001, **46**, 559-632.
83. P. Zhu and Y. Zhao, *Advanced Engineering Materials*, 2017, **19**.
84. Y. Yamada, K. Shimojima, Y. Sakaguchi, M. Mabuchi, M. Nakamura, T. Asahina, T. Mukai, H. Kanahashi and K. Higashi, *Advanced Engineering Materials*, 2000, **2**, 184-187.
85. E. Solórzano, M. A. Rodriguez-Perez and J. A. de Saja, *Advanced Engineering Materials*, 2008, **10**, 596-602.
86. G. Plantard, F. Correia and V. Goetz, *Journal of Photochemistry and Photobiology A: Chemistry*, 2011, **222**, 111-116.
87. Y. Xue, P. Shao, Y. Yuan, W. Shi, Y. Guo, B. Zhang, X. Bao and F. Cui, *Chemical Engineering Journal*, 2021, **418**.
88. Z. Zeng, D. Jing and L. Guo, *Energy*, 2021, **228**.

89. C. Luo, D. Li, W. Wu, Y. Zhang and C. Pan, *RSC Adv.*, 2014, **4**, 3090-3095.

90. E. C. Hammel, O. L. R. Ighodaro and O. I. Okoli, *Ceramics International*, 2014, **40**, 15351-15370.

91. B. L. Krasnyi, V. P. Tarasovskii, E. V. Rakhmanova and V. V. Bondar, *Glass and Ceramics*, 2004, **61**, 337-339.

92. H. Cheng, J. Wang, Y. Zhao and X. Han, *RSC Adv.*, 2014, **4**, 47031-47038.

93. T. Yildiz, H. C. Yatmaz and K. Öztürk, *Ceramics International*, 2020, **46**, 8651-8657.

94. J. F. Poco, J. H. Satcher and L. W. Hrubesh, *Journal of Non-Crystalline Solids*, 2001, **285**, 57-63.

95. K. Prabhakaran, N. M. Gokhale, S. C. Sharma and R. Lal, *Journal of the American Ceramic Society*, 2005, **88**, 2600-2603.

96. G. Zu, J. Shen, X. Wei, X. Ni, Z. Zhang, J. Wang and G. Liu, *Journal of Non-Crystalline Solids*, 2011, **357**, 2903-2906.

97. T. F. Baumann, A. E. Gash, S. C. Chinn, A. M. Sawvel, R. S. Maxwell and J. H. Satcher, *Chemistry of Materials*, 2004, **17**, 395-401.

98. J. B. Peri and R. B. Hannan, *The Journal of Physical Chemistry*, 2002, **64**, 1526-1530.

99. D. Maciver, *Journal of Catalysis*, 1964, **3**, 502-511.

100. J. Reardon, A. K. Datye and A. G. Sault, *Journal of Catalysis*, 1998, **173**, 145-156.

101. J. Cañas, J. C. Piñero, F. Lloret, M. Gutierrez, T. Pham, J. Pernot and D. Araujo, *Applied Surface Science*, 2018, **461**, 93-97.

102. E. O. Filatova and A. S. Konashuk, *The Journal of Physical Chemistry C*, 2015, **119**, 20755-20761.

103. K. Sivagami, B. Vikraman, R. R. Krishna and T. Swaminathan, *Ecotoxicol Environ Saf*, 2016, **134**, 327-331.

104. A. K. Sharma, R. K. Tiwari and M. S. Gaur, *Arabian Journal of Chemistry*, 2016, **9**, S1755-S1764.

105. R. Moene, H. T. Boon, J. Schoonman, M. Makkee and J. A. Moulijn, *Carbon*, 1996, **34**, 567-579.

106. R. Moene, L. F. Kramer, J. Schoonman, M. Makkee and J. A. Moulijn, in *Studies in Surface Science and Catalysis*, eds. G. Poncelet, J. Martens, B. Delmon, P. A. Jacobs and P. Grange, Elsevier, 1995, vol. 91, pp. 371-380.

107. D. Hao, Z. Yang, C. Jiang and J. Zhang, *Applied Catalysis B: Environmental*, 2014, **144**, 196-202.

108. C. B. D. Marien, M. Le Pivert, A. Azais, I. C. M'Bra, P. Drogui, A. Dirany and D. Robert, *J Hazard Mater*, 2019, **370**, 164-171.

109. T. Zou, C. Xie, Y. Liu, S. Zhang, Z. Zou and S. Zhang, *Journal of Alloys and Compounds*, 2013, **552**, 504-510.

110. C. Gomez-Solis, I. Juarez-Ramirez, E. Moctezuma and L. M. Torres-Martinez, *J Hazard Mater*, 2012, **217-218**, 194-199.

111. V. Keller and F. Garin, *Catalysis Communications*, 2003, **4**, 377-383.

112. Y. Su, S. Li, D. He, D. Yu, F. Liu, N. Shao and Z. Zhang, *ACS Sustainable Chemistry & Engineering*, 2018, **6**, 11989-11998.

113. T. Wang, C. Zhu, L. Song, P. Du, Y. Yang and J. Xiong, *Materials Research Bulletin*, 2020, **122**.

114. M. M. Messina, M. E. Coustet, J. Ubogui, R. Ruiz, F. D. Saccone, P. C. Dos Santos Claro and F. J. Ibanez, *Langmuir*, 2020, **36**, 2231-2239.

115. T. Long, Y. Xu, X. Lv, J. Ran, S. Yang and L. Xu, *Materials & Design*, 2018, **159**, 195-200.

116. A. Yamamoto, *Journal of Catalysis*, 2004, **226**, 462-465.

117. K. P. Sundar and S. Kanmani, *Chemical Engineering Research and Design*, 2020, **154**, 135-150.

118. Y. Abdel-Maksoud, E. Imam and A. Ramadan, *Catalysts*, 2016, **6**.

119. D. Wang, M. A. Mueses, J. A. C. Marquez, F. Machuca-Martinez, I. Grcic, R. Peralta Muniz Moreira and G. Li Puma, *Water Res*, 2021, **202**, 117421.

120. P. H. Allé, P. Garcia-Muñoz, K. Adouby, N. Keller and D. Robert, *Environmental Chemistry Letters*, 2020, **19**, 1803-1808.

121. K. Elatmani, N. B. oujji, G. Plantara, V. Goetz and I. A. ichou, *Materials Research Bulletin*, 2018, **101**, 6-11.

122. Y. Li, Y. Jiang, Z. Ruan, K. Lin, Z. Yu, Z. Zheng, X. Xu and Y. Yuan, *J. Mater. Chem. A*, 2017, **5**, 21300-21312.

123. Y. Li, Z. Ruan, Y. He, J. Li, K. Li, Y. Jiang, X. Xu, Y. Yuan and K. Lin, *Applied Catalysis B: Environmental*, 2018, **236**, 64-75.

124. K. Elatmani, N. B. oujji, G. Plantara, V. Goetz and I. A. ichou, *Materials Research Bulletin*, 2018, **101**, 6-11.

125. M. Kete, O. Pliekhova, L. Matoh and U. L. Stangar, *Environ Sci Pollut Res Int*, 2018, **25**, 20453-20465.

126. M. E. Leblebici, J. Rongé, J. A. Martens, G. D. Stefanidis and T. Van Gerven, *Chemical Engineering Journal*, 2015, **264**, 962-970.

127. D. Bertagna Silva, G. Buttiglieri, T. Babić, L. Ćurković and S. Babić, *Process Safety and Environmental Protection*, 2021, **153**, 94-106.

128. D. Bertagna Silva, G. Buttiglieri and S. Babic, *Environ Sci Pollut Res Int*, 2021, **28**, 103-120.

129. M. M. Khan, S. A. Ansari, D. Pradhan, M. O. Ansari, D. H. Han, J. Lee and M. H. Cho, *J. Mater. Chem. A*, 2014, **2**, 637-644.

130. F. Achouri, S. Corbel, L. Balan, K. Mozet, E. Girot, G. Medjahdi, M. B. Said, A. Ghrabi and R. Schneider, *Materials & Design*, 2016, **101**, 309-316.

131. I. N. Reddy, C. V. Reddy, J. Shim, B. Akkinepally, M. Cho, K. Yoo and D. Kim, *Catalysis Today*, 2020, **340**, 277-285.

132. B. M. Rajbongshi, A. Ramchiary and S. K. Samdarshi, *Materials Letters*, 2014, **134**, 111-114.

133. M. B. Fisher, D. A. Keane, P. Fernández-Ibáñez, J. Colreavy, S. J. Hinder, K. G. McGuigan and S. C. Pillai, *Applied Catalysis B: Environmental*, 2013, **130-131**, 8-13.

134. D. A. Keane, K. G. McGuigan, P. F. Ibáñez, M. I. Polo-López, J. A. Byrne, P. S. M. Dunlop, K. O'Shea, D. D. Dionysiou and S. C. Pillai, *Catal. Sci. Technol.*, 2014, **4**, 1211-1226.

135. A. Ghosh and A. Mondal, *Materials Letters*, 2016, **164**, 221-224.

136. Y. Li, C. Zhang, D. Shuai, S. Naraginti, D. Wang and W. Zhang, *Water Res*, 2016, **106**, 249-258.

137. J. Xu, Z. Wang and Y. Zhu, *ACS Appl Mater Interfaces*, 2017, **9**, 27727-27735.

138. Q. Zheng, D. P. Durkin, J. E. Elenewski, Y. Sun, N. A. Banek, L. Hua, H. Chen, M. J. Wagner, W. Zhang and D. Shuai, *Environ Sci Technol*, 2016, **50**, 12938-12948.

139. Y. de Rancourt de Mimerand, K. Li and J. Guo, *ACS Appl Mater Interfaces*, 2019, **11**, 24771-24781.

140. D. Friedmann, A. F. Lee, K. Wilson, R. Jalili and R. A. Caruso, *Journal of Materials Chemistry A*, 2019, **7**, 10858-10878.

141. E. Lee, J. Pruvost, X. He, R. Munipalli and L. Pilon, *Chemical Engineering Science*, 2014, **106**, 18-29.

142. S. Son, P. H. Jung, J. Park, D. Chae, D. Huh, M. Byun, S. Ju and H. Lee, *Nanoscale*, 2018, **10**, 21696-21702.

143. M. J. Martín de Vidales, A. Nieto-Márquez, D. Morcuende, E. Atanes, F. Blaya, E. Soriano and F. Fernández-Martínez, *Catalysis Today*, 2019, **328**, 157-163.

144. N. O. McHedlov-Petrosyan and Y. V. Kholin, *Russian Journal of Applied Chemistry*, 2004, **77**, 414-422.

145. B. A. Wols and C. H. M. Hofman-Caris, *Water Research*, 2012, **46**, 2815-2827.

146. V. Feigenbrugel, S. Le Calve and P. Mirabel, *Spectrochim Acta A Mol Biomol Spectrosc*, 2006, **63**, 103-110.

147. N. A. Kouame, D. Robert, V. Keller, N. Keller, C. Pham and P. Nguyen, *Environ Sci Pollut Res Int*, 2012, **19**, 3727-3734.

148. K. Minakata, O. Suzuki, S. Saito and N. Harada, *International Journal of Legal Medicine*, 2000, **114**, 1-5.

149. M. Siddique, R. Farooq, Z. M. Khan, Z. Khan and S. F. Shaukat, *Ultrason Sonochem*, 2011, **18**, 190-196.

150. R. Ramani and C. Ranganathaiah, *Polymer Degradation and Stability*, 2000, **69**, 347-354.

151. D. Hao, Z. Yang, C. Jiang and J. Zhang, *Journal of Materials Science & Technology*, 2013, **29**, 1074-1078.

152. M. Taniguchi and J. S. Lindsey, *Photochem Photobiol*, 2018, **94**, 290-327.

153. L. Chen, S. Yang, Q. Zhang, J. Zhu and P. Zhao, *Separation and purification technology*, 2021, **265**, 118444.

Chapter 3

Materials and Methods

Methodology and Materials

3.1. Context

This chapter provides a detailed overview of the methods used to synthesize novel photocatalysts and characterise their properties and performance, including information in excess of that provided in the submitted manuscripts. This chapter is broken down into sections as follows: the development of the synthetic method for production of photocatalytic foams (Section 3.2); the theoretical background to the characterisation methods (Section 2.3.); and the design of the recirculating reactor for the use of foams as photocatalysts.

Once synthesised, the foams were characterised using a wide range of analytical methods to elucidate key chemical and physical parameters including crystal structure, morphology and surface chemistry, along with photocatalytic testing to study the activity for the degradation of organic micropollutants. Figure 3.1 shows the steps involved in the synthesis, characterisation and testing of the photocatalyst foams presented here. This involves the preparation of the reagent solutions, with or without dopants, the simultaneous gelation and aeration to form the highly porous intermediate oxalate foams, drying and sintering to form the metal oxide foams before finally testing the foams within a recirculating photoreactor. The non-essential steps in the process, such as doping and characterisation are shown perpendicular to the process in the diagram.

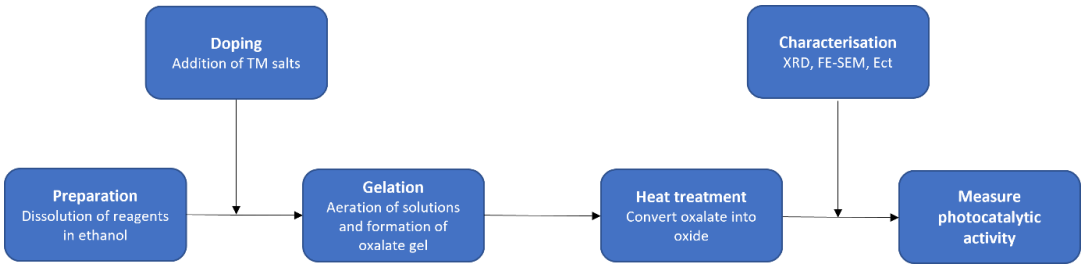

Figure 3.1: Schematic diagram of the process of synthesising, characterising and testing the photocatalytic foams.

3.2. Experimental Procedure

3.2.1. Reagents

Zinc acetylacetonate (Zn $(AcAc)_2$; ≥95.0 %, 25% Zn) and Ethanol (Absolute, 99.8%) were purchased from Fischer Scientific and used as provided. Cobalt (II) acetylacetonate (≥99.0%), Copper(II) acetylacetonate ≥99.9% trace metals basis, Nickel(II) acetylacetonate (for synthesis) Oxalic acid anhydrous (≥99.9 %), Hexadecyltrimethylammonium bromide (CTAB; ≥99.9 %), Polyethylene glycol (PEG; 10,000), Carbamazepine and Methylene Blue were all purchased from Sigma Aldrich and used as provided. Jacketed, fritted funnels were purchased from Chemglass Lifesciences and fitted with PTFE sheets (Zwanzer). Desiccant from a Drierite™ gas-drying unit (Sigma Aldrich) was used as provided by the manufacturer but transferred to a smaller tube.

3.2.2. Foam synthesis

Synthesis of FOAMM

Synthetic method – ZnO Foams

To a 25 mL Pyrex beaker was added, 15.0 mmol (3.9541 g) $Zn(AcAc)_2$ (≥95.0 %). CTAB was dissolved in 15 mL ethanol and added to the beaker such that the final concentration in the reaction mixture was 5, 10, 15 or 20 mM. To a separate beaker was added 15.0 mmol (1.3500 g) Oxalic acid (≥99.9 %) and 40 µmol (0.4000 g) PEG10,000. Both solutions were set to stir vigorously at 60 °C for 1 hour to ensure homogenous solutions.

After stirring, the solutions were sequentially added to the Teflon lined jacketed fritted filter funnel set at 60 °C through the use of a recirculating bath and aerated with compressed air with an upward flow rate of 0.1 sL min^{-1}. An image and schematic diagram of this can be seen in Figure 3.2.

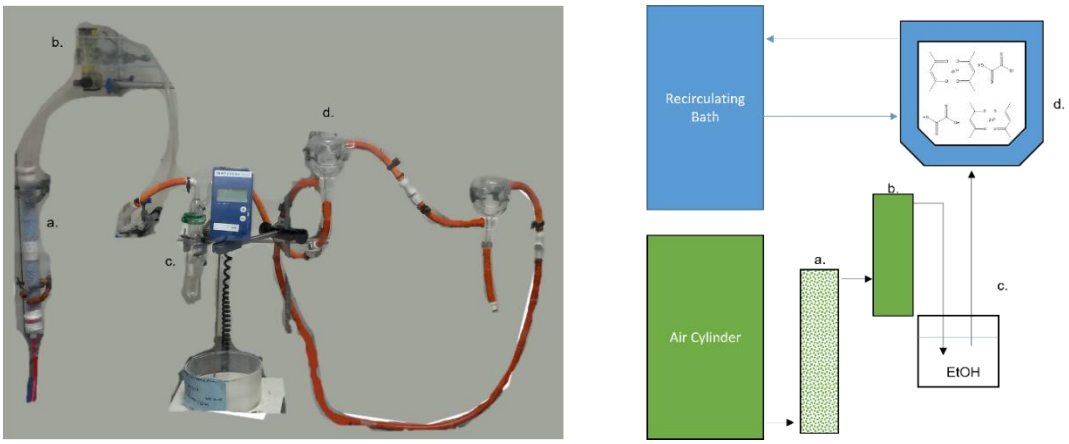

Figure 3.2: Left) Front view of the final set up used in the synthesis of the foams. Right) Schematic diagram of set up used. a) drying column; b) rotameter; c) ethanol bubbler; d) fritted jacketed funnel. Black arrows indicate air flow whilst blue arrows indicate water flow.

Finally, the ZnO foam was sintered using a furnace (Carbolite) heated to 1,000 °C with a ramp rate of 5 °C min^{-1}, then held at temperature for 0.5 hours before cooling to 900 °C and holding for an additional 20 hours, leading to sintering of the crystallites and an increase in the physical stability of the samples as well as leading to the formation of faceted crystallites needed for photocatalysis. This is shown below in Figure 3.3.

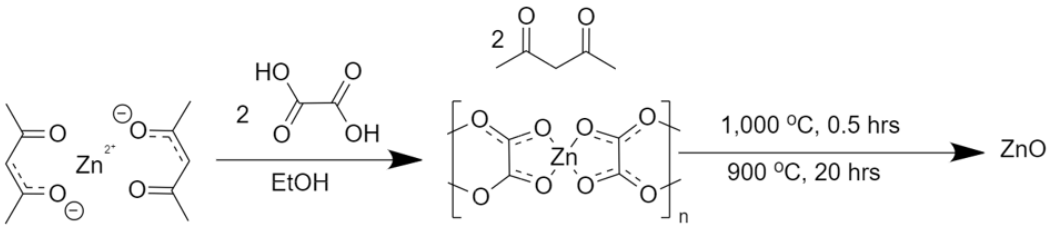

Figure 3.3: Reaction mechanism for the synthesis of ZnO MolFoams.

Synthetic method – Doped ZnO Foams

Transition metal doped foams were produced in the same manner as described earlier, with the difference between the syntheses being the presence of dopant metal salt present in the solutions. Table 3.1 shows the mass used of each dopant metal salt and $Zn(AcAc)_2$ used in each solution, to ensure that a total of 15.0 mmol of metal acetylacetonate was used.

Table 3.1: Mass of dopant salts used to produce doped ZnO MolFoams.

	Metal salt	$Co(AcAc)_2$	$Ni(AcAc)_2$	$Cu(AcAc)_2$	$Zn(AcAc)_2$
Dopant %		Dopant Mass /g			Mass /g
0.5		0.0193	0.0193	0.0196	3.9344
1		0.0386	0.0385	0.0393	3.9147
2		0.0771	0.0771	0.0785	3.8751

The mixture of solutions was aerated for 3 hours leading to the formation of a gel, white for undoped foams, and pink, green or blue for those doped with Co, Ni or Cu, respectively. The gel was then transferred to a pre-weighed ceramic crucible and placed in a preheated oven and dried at 80 °C for 12 hours resulting in a zinc oxalate foam which was stored under ambient conditions.

3.3. Material Characterisation

This section includes and explanation and description of the methodology used to characterise the photocatalysts described in this thesis and the fundamental principles behind them. The techniques employed include structural analysis, microscopy and analysis of the photocatalytic activity of the ZnO photocatalysts.

3.3.1. Structural Analysis

2.3.1.1. Powder X-ray Diffraction (PXRD)

X-ray diffraction allows for the identification of crystal phases within a sample of crystallites. When the sample is irradiated with x-rays, the interatomic distances between the atoms are small enough to cause the incoming x-rays to diffract and become scattered. The scattered x-rays can then interfere with each other either constructively or destructively as predicted by Bragg's Law:[1]

$$n\lambda = 2d\ sin\theta$$

Equation 3.1: Bragg's Law

where *n* is the order of reflection (and usually taken to equal 1), λ is the wavelength of the incident x-rays, taken to be 1.54 Å using x-rays generated from the Cu $_{k\alpha 1}$ transition, *d* is the interatomic spacing and θ is the incident angle of the x-ray beam.

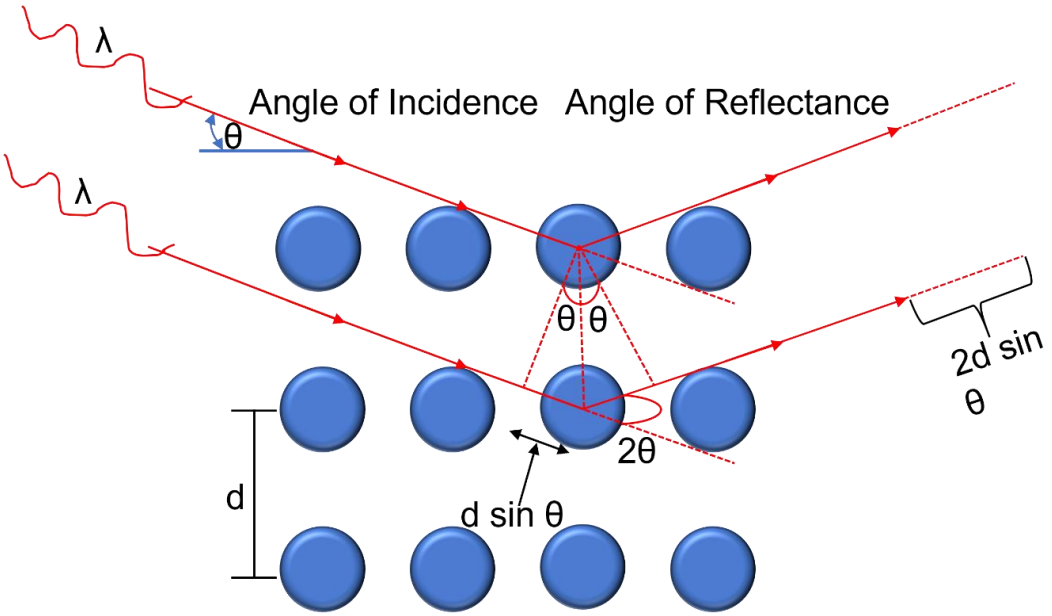

Figure 3.4: Schematic diagram of x-ray diffraction and the relationship to Bragg's Law. Modified from Ref. [2]

A smaller interatomic distance or larger wavelength of light leads to a larger diffraction angle. A typical diffraction pattern plots the intensity of the scattered x-rays against the diffraction angle, 2θ, to allow for material characterisation based on peak height (or intensity) and peak position.

Additionally the x-ray diffraction pattern allows for the average crystallite size to be calculated using the Scherer equation:[3]

$$\tau = \frac{K\lambda}{\beta \cos\theta}$$

Equation 3.2: Scherer Equation.

Where τ is the average crystallite size, *K* is the Scherer shape factor, λ is the wavelength of the incident x-rays, β is the peak broadening factor, the full width at half maximum of the peak (FWHM), and θ is the incident angle of the beam.

XRD was used in this thesis to characterise the ZnO photocatalysts and the effect of changes to sintering conditions, CTAB concentrations and doping. It was used to show crystallinity of the samples as well was calculate the crystallite size. The XRD data used to produce the spectra used in this thesis were collected by Dr Gabriele Kociok-Köhn (Department of Chemistry, University of Bath) using a STOE STADI P dual

powder transmission x-ray diffractometer using a scanning range of 2θ = 20 – 90 and a scan time of 20 minutes.

3.3.1.2. X-ray Microtomography

X-ray microtomography (Micro CT) imaging works using the same principles as CT (Computed Tomography) scanning, using x-ray imaging to image cross sections of a sample. The sample is mounted onto a turntable that can be rotated as well as shifted vertically by motors allowing for scanning at multiple points through the sample. An x-ray source is mono-chromated and projected through the sample, with the beam passing through, with the beam interacting with solid material and the pores within to different extents with the solid material leading to greater absorbance and attenuation of the beam than the voids. The beam then interacts with a fluorescent scintillator plate that emits visible light, converting the x-rays into visible light, towards a lens and detector. This data is a single slice of the material and through repeated measurement of the sample at various height and angular increments, followed by the use of computational reconstruction a three-dimensional image of the original sample can be produced.[4]

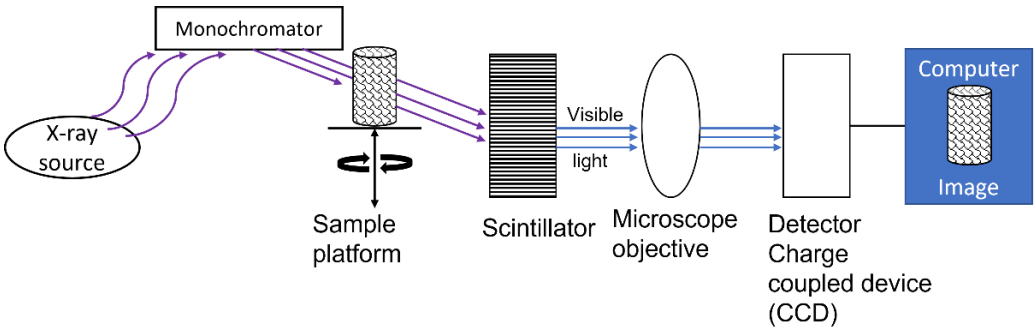

Figure 3.5: Schematic of an x-ray microtomography device.[5]

The images were collected by Mrs Clare Ball (Department of Mechanical Engineering, University of Bath) using a Nikon XT H 225 ST using a 178 kV x-ray source and 0.708 second exposure time, 3141 projections and 4 frames per projection with a resolution of 25 µm and analysed using Thermo Scientific Avizo Software 9 3D data visualisation software.

3.3.1.3. Gravimetric porosity measurement

Owing to the different types of porosity: closed-, open-, through- pores, it was essential to qualitatively assess the nature of the pores within the photocatalyst, as closed pores would be ineffective and unsuited to use within a recirculating reactor. To this end, a bespoke dyeing apparatus was developed. A schematic of this can be found below. Briefly, a solution of Methylene Blue (MB) was flowed through a tube (ID = 22 mm, OD = 25 mm) containing a MolFoam on a plastic support platform using a peristaltic pump (Masterflex L/S, pump head model 77200-62) operating at a flow rate of 50 mL min^{-1} for 120 minutes. After drying, the MolFoam was cut open showing sections dyed blue, indicative of open porosity, whereas sections left undyed would-be indicative of closed pores.

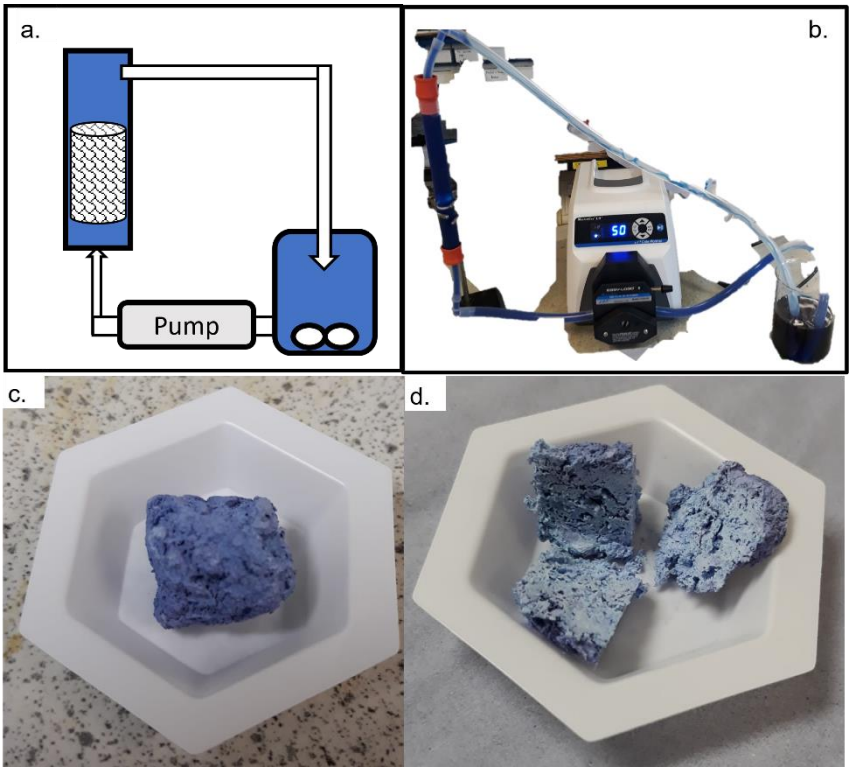

Figure 3.6: schematic diagram of bespoke dyeing rig to test dye uptake into MolFoam pores. B) photograph of dyeing rig in operation. C, d) A dyed MolFoam before and after being cut open.

In order to measure the open porosity of the foams, a gravimetric analysis method was conducted. Using a modified literature method,[6] a known mass of ZnO foam was submerged in ultra-pure deionised water. After 4 hours the sample was removed,

and the wet mass of the foam was recorded and the porosity calculated using the following equation:

$$\varepsilon = \frac{\frac{\omega_1 - \omega_2}{D_u}}{\frac{\omega_1 - \omega_2}{D_u} + \frac{\omega_2}{D_f}}$$

Equation 3.3:Gravimetric porosity.

Where ε is the porosity of the foam, ω_1 is the mass of the wet foam, ω_2 is the mass of the dry foam, D_u is the density of the ultrapure water and D_f is the density of ZnO. The change in mass was attributed to the open pores of the material holding water and from this, using the density of water, the volume of water in the material ($\omega_1 - \omega_2 / D_u$) which is equivalent to the volume of the pores could be calculated.

From this, the porosity was calculated using the volume of the pores divided by the total volume of the material and expressed as a percentage.

Gravimetric porosity measurements were used in this thesis in place of porosity calculated via MicroCT due to the resolution of the latter allowing for reconstruction and analysis of micropore structure only, rather than the complete hierarchical structure of the photocatalysts, leading to porosities significantly lower than were present. As higher resolution scans, or NanoCT were not available, gravimetric porosity from the Archimedes principal was reported as the open porosity of the foams had been qualitatively shown via the dye uptake into the pore in a flow system.

3.3.1.4. Photoelectron Spectroscopy (XPS) and (UPS)

X-ray photoelectron spectroscopy is a surface sensitive spectroscopic technique allowing for characterisation of the chemical composition of a materials surface through measurement of the characteristic binding energies of the elements. Analysis is conducted under vacuum conditions, wherein x-ray photons are used to induce emission of electrons from the surface, described as the photoelectric effect. The kinetic energy of the emitted electrons is measured and allows for calculation of the binding energy of the emitted electron. As the binding energy is unique, it allows for identification of the element, as well as the bonding environment it originated from as shown below:[7]

$$E_{Binding} = E_{Xr} - (E_{Kinetic} + \Phi)$$

Equation 3.4: Binding energy of a photon.

Where E_{Xr} is the energy of the x-ray photons, $E_{kinetic}$ is the measured kinetic energy of the -emitted electron and Φ is the spectrometer work function. E_{Bindng} is the binding energy of the electron, which is specific to the elements and the bonding present in the sample.

Ultraviolet photoelectron spectroscopy is a variation on XPS analysis, designed to provide information on the band structure of a sample allowing for elucidation of the band gap and band edge positions of a material, key parameters when discussing a photocatalyst. Whereas XPS uses a high energy x-ray photon to induce a photoelectric effect, UPS uses much lower energy photons, emitted from a He gas source. With these lower energy photons, the photoelectric effect producing an emitted electron is limited to the outermost electron shells, the valence band electrons compared to core level emissions analysed in XPS. By probing the valence band, the band edge can be elucidated.[8]

XPS was used in this thesis to identify the elemental make-up of the photocatalyst and to determine the extent of transition metal doping within the foams, while UPS was used to measure the band edge positions which, when coupled with measurement of the band gap using UV-Vis allowed for understanding of the band structure of the photocatalysts. Both XPS and UPS were acquired by Dr Mark Isaacs at HarwellXPS using a Kratos Axis SUPRA using monochromated Al kα (1486.69 eV) X-rays at 15 mA emission and 12 kV HT (180W) and a spot size/analysis area of 700 x 300 µm and a He(I) UV lamp running at 20 mA emission. The instrument was calibrated to gold metal Au 4f (83.95 eV) and dispersion adjusted give a BE of 932.6 eV for the Cu 2p3/2 line of metallic copper. Ag 3d5/2 line FWHM at 10 eV pass energy was 0.544 eV. Source resolution for monochromatic Al Kα X-rays is ~0.3 eV. The instrumental resolution was determined to be 0.29 eV at 10 eV pass energy using the Fermi edge of the valence band for metallic silver. Resolution with charge compensation system on <1.33 eV FWHM on PTFE. High resolution spectra were obtained using a pass energy of 20 eV, step size of 0.1 eV and sweep time of 60s,

resulting in a line width of 0.696 eV for Au 4f7/2. Survey spectra were obtained using a pass energy of 160 eV. Charge neutralisation was achieved using an electron flood gun with filament current = 0.4 A, charge balance = 2 V, filament bias = 4.2 V. Successful neutralisation was adjudged by analysing the C 1s region wherein a sharp peak with no lower BE structure was obtained. Spectra have been charge corrected to the main line of the carbon 1s spectrum (adventitious carbon) set to 284.8 eV. All data was recorded at a base pressure of below 9 x 10-9 Torr and a room temperature of 294 K. Data was analysed using CasaXPS v2.3.19PR1.0. Peaks were fit with a Shirley background prior to component analysis.

3.3.1.5. XANES X-ray Absorption Spectroscopy

X-ray Absorption Near Edge Structure (XANES) is a spectroscopic technique used to examine the oxidation state of elements (often metals) within a sample. This is done by exposing sample to monochromatic x-rays and scanned over a range of energies above and below the absorption edge of the target element.[9] This process uses the absorption within the target element of an x-ray photon with specific energy corresponding to the ionisation energy of a core electron. At this energy, the absorption spectra shows a significant rise in absorption coefficient which is termed the “absorption edge” which corresponds to a specific type of core electrons, i.e. 1s electrons of Zn.[10] These absorption edges are names according to the principle quantum number of the excited electron: K edge for n = 1, L for n = 2, M for n = 3 and N for n =4.

XANES is particularly useful as it can be used to elucidate oxidation state of the target element. This is because, as the oxidation state of the absorption site increases, energy of the absorption edge increases as well, due to the higher oxidation state of the element requiring more energy to excite the electron due to it being less shielded from the nucleus and having a higher effective charge.[11]

XANES was used in this thesis in conjunction with XPS to analyse the make up of the photocatalyst, in particular to assess the oxidation state of zinc and the dopant metals within the photocatalyst.

XANES analysis was performed on an easyXAFS 300+ spectrometer, with Ag or Mo X-rays operating at 40 mA and 15 kV emission and silicon spherical bent crystal analysers.

3.3.1.6. RAMAN

Raman spectroscopy is a spectroscopic technique used to determine the vibrational mode of molecules derived from inelastic scattering of photons. During RAMAN spectroscopy, the sample is irradiated with a laser, with energy in the UV-Vis region, with light scattered perpendicular to the beam and consisting of two types of photons: Rayleigh and Raman scattered photons.[12] Rayleigh photons account for the majority of the scattered light and are elastically scattered, that is to say, undergo no change in energy or frequency. Of more interest are the Raman scattered photons which are of a frequency equal to that of the incident beam, plus-minus the vibrational frequency of the molecule or chemical group present. As this scattering occurs inelastically, the photons are deemed as "Stokes shifted" if they have lower energy than the initial photon, or "Antistokes shifted" if they have higher energy. It is possible to attribute the energy ranges in which RAMAN scattering occurs to frequencies characteristic to chemical groups, thus allowing for identification of particular groups present within a sample.[13]

RAMAN spectroscopy was used in this thesis to characterise the surface chemistry of the photocatalysts as well as identify any changes in surface structure induced through doping with transition metals. RAMAN spectra used in this thesis were collected using a Renishaw InVia Confocal Raman microscope, Excitation laser wavelength 532nm, 100% laser power at 74 mW on the sample with 2.6 s exposure times, a diffraction grating of size 1,800 l/mm with slit opening of 65 µm. Detector used was a 1040 x 256 pixel CCD camera.

3.3.1.7. Nitrogen Adsorption and Brunauer – Emmett – Teller Theory

Nitrogen adsorption is a methodology routinely employed in the evaluation of the surface area of powders and porous materials. Through measurement of gas adsorption (usually N_2) against relative pressure of the system, an isotherm can be

produced. This is achieved through the condensation of a known volume of the adsorpant gas onto the surface of a known mass of adsorbate while measuring the change in pressure, relative to the initial pressure. Examples of these isotherms are shown below in Figure 3.7.[14]

These isotherms take into account the total volume of gas adsorbed as a multilayer (gas molecules stacking on gas molecules rather than adsorbate surface) which makes calculation of surface area difficult. To address this, the Brunauer – Emmett – Teller (BET) theory is applied to the isotherm. This theory expands the Langmuir theory of monolayer adsorption of gas to account for multilayer adsorption processes. In BET plots, as seen in Figure 3.6, plotting relative pressure (P/P_0) as φ against $1/v_{ads}$ ($\varphi\,[1-\varphi\,]^{-1}$) allows for the calculation of the volume of a monolayer of gas and then the surface area required for the volume to adsorb onto, providing a measurement of surface area of the sample.[15]

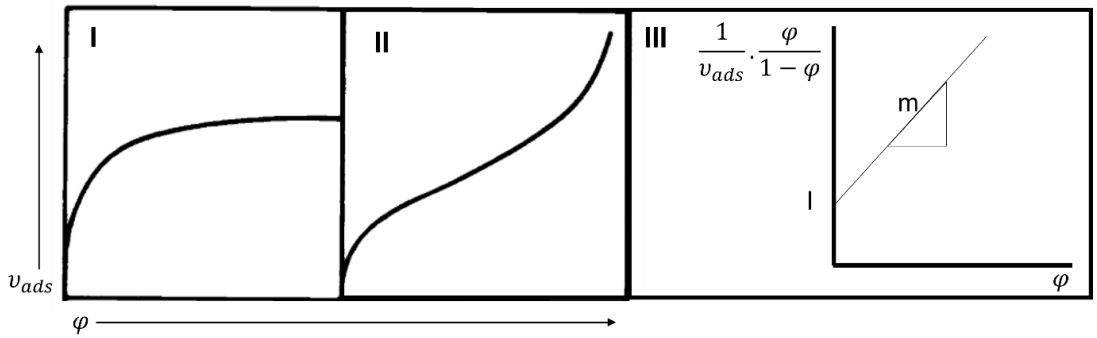

Figure 3.7: Adsorption isotherm of: I. a microporous material, II. a microporous material. III. an example of a BET plot derived from an isotherm. The gradient, m, and intercept, I, allow for the calculation of the monolayer volume. Adapted from ref [14]

N_2 adsorption and BET were used in this thesis to calculate the surface area of the photocatalysts and to allow for description of the type of porosity of the samples. Isotherms were collected via N_2 adsorption using a Autosorb- iQ-C by Quantachrome Anton Paar at 77 K, after degassing under vacuum at 130 ^{o}C for 120 minutes. BET plots and surface area analysis conducted using a multi-step BET method on AsiQwin by Quantachrome.

3.3.2. Microscopy

3.3.2.1. Field Emission Scanning Electron Microscopy

While a traditional microscope uses photons of visible light to generate an image, scanning electron microscopy uses a beam of electrons, defined in terms of the technique as primary electrons.[16] These are used to penetrate the surface of the sample to a depth of a few micrometers, with the depth dependant on the acceleration voltage of the microscope and the material density. The resulting secondary electrons, electrons generated due to ionisation of the sample resulting in electron energies specific to a particular element, are scattered and collected by a charged detector. SEM and FESEM use the same principles as a traditional light based microscope, with the difference being in the wavelengths of electrons being smaller than those of the photons of light, allowing for an image of the surface of the sample to be collected that is much higher in resolution than would be possible with a light microscope.[17]

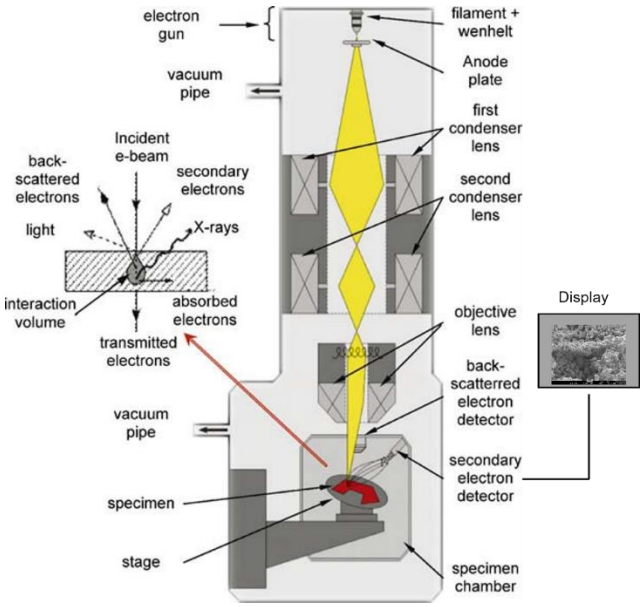

Figure 3.8: Schematic diagram of field emission scanning electron microscope (FE-SEM). Adapted from ref [18]

FESEM micrographs were used in this thesis to conduct qualitative and quantitative analysis of the ZnO morphology and structure, as well as the effect of photocatalysis upon the photocatalyst. The samples synthesised in this work were analysed using a

Jeol JSM-7900F FESEM with Oxford Instruments 100mm² Ultim Extreme EDX attachment. Prior to imaging, samples were coated with 20 nm Cr.

3.3.2.2. Energy Dispersive X-ray spectroscopy (EDX)

Conducted alongside electron microscopy, EDX provides information regarding the chemical composition of a sample. As it is bombarded with high energy x-rays, electrons within the core, often the 1^s (or K) shell are excited to the extent where they have the energy to be removed from the atomic structure, leaving behind a high energy hole. [16] Outer shell electrons then drop down into the vacancy, leading to the release of energy as an x-ray photon. Owing to the quantisation of electron energy levels, the photon energy is characteristic to the unique energy difference in the electron shells allowing for identification of the element from which it was emitted.[17]

The samples synthesised in this work were analysed using a Jeol JSM-7900F FESEM with Oxford Instruments 100mm² Ultim Extreme EDX attachment.

3.3.3. Photocatalysis analysis

3.3.3.1. High Performance Liquid Chromatography (HPLC)

HPLC is a form of liquid chromatography, where the separation of compounds in a mixture occurs between the mobile phase, in this case a solvent, and a stationary phase, the packing column. The analyte sample is injected into the mobile phase and transported through the column where the individual solute components of the sample will separate out into individual peaks or bands, dependant on their chemical composition and its interaction with the stationary phase. This is controlled by solvophobic and silanophilic interactions between the solute and the mobile and stationary phases respectively. These interactions affect the time for the solute to pass through the system, referred to as “retention time” and is a measure of time spent within the column, with compounds that are more strongly attracted to the stationary phase having higher retention times than those that are less strongly attracted.[19] After the column, the solutes are detected by UV absorbance which provides the solute with a quantifiable peak with the absorbance being proportional to the concentration of the sample, as per the Beer – Lambert Law:[20]

$$A = \log\left(\frac{I_0}{I}\right) = \varepsilon bc$$

Equation 3.5: Beer-Lambert Law.

where *A* is the absorbance of the sample, I_0 is the incident light intensity, *I* is the transmitted light intensity, Ɛ is the molar absorptivity (or molar extinction) coefficient, *b* is the cell path length and *c* is sample concentration.

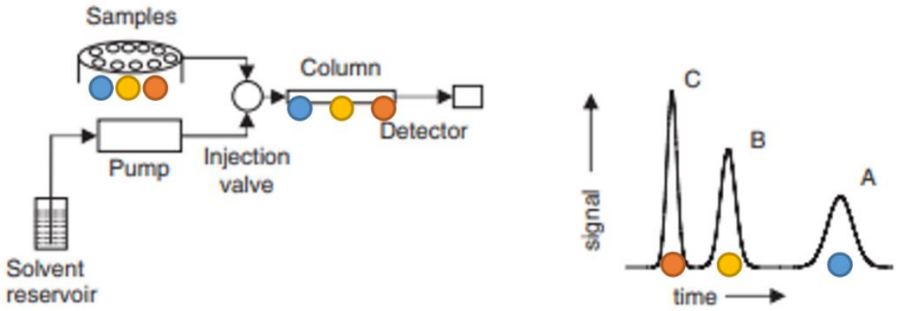

Figure 3.9. Schematic of HPLC. Modified from reference [21]

The absorption peak and the retention time of the solute allows for characterisation of the compounds from the column.

In this thesis, HPLC was used to monitor the degradation of the micropollutant carbamazepine, to examine and assess the photocatalytic activity of the photocatalysts produced. Degradation of micropollutant was calculated using the equation below:

$$Degradation\ \% = \frac{C_t}{C_0}\ X\ 100$$

Equation 3.6: Micropollutant degradation.

where C_t is the peak area from the chromatogram of carbamazepine (CBZ), from the sample taken at time t, and C_0 is the peak area of the initial concentration of carbamazepine before the reaction (time = 0 minutes).

For all photocatalysis experiments, CBZ removal was monitored from 1 mL aliquots collected during sampling every 15 minutes for the first hour and every 30 minutes thereafter, such that the total volume removed was less than 10% of the starting reservoir volume, using high performance liquid chromatography (HPLC).

All experiments were repeated in triplicate. HPLC analysis of CBZ was performed on a Thermo Scientific Ultimate 3000 liquid chromatograph with a UV detector. CBZ analysis used a Thermo Scientific Acclaim 120 C18 column (3.0 X 75.0 mm, particle size 3.0 µm) and a Thermo Scientific Acclaim 120 C18 guard column I 120 C18 (3.0 X 10.0 mm, particle size 5.0 µm) The mobile phase was made up using 5.0 mM phosphoric acid and acetonitrile 70:30 (v:v) with a flow rate of 0.8 mL min^{-1}, injection volume of 20 µL and detection wavelength of 285 nm. Degradation of carbamazepine was measured via plotting (C_t/C_0) Vs time where C_0 is the initial concentration of CBZ and Ct is the concentration of CBZ at a given time. The pseudo first order degradation kinetics (k) was calculated via linear regression of a plot of Ln(C_t/C_0) Vs time.

3.3.3.2. UV-Vis Reflectance Spectroscopy

Ultraviolet – visible spectroscopy is often used to quantitatively measure the optical properties of both materials and solutions. A sample is irradiated with light of wavelengths between 200 and 900 nm and the intensity of the light reaching the detector is measured.

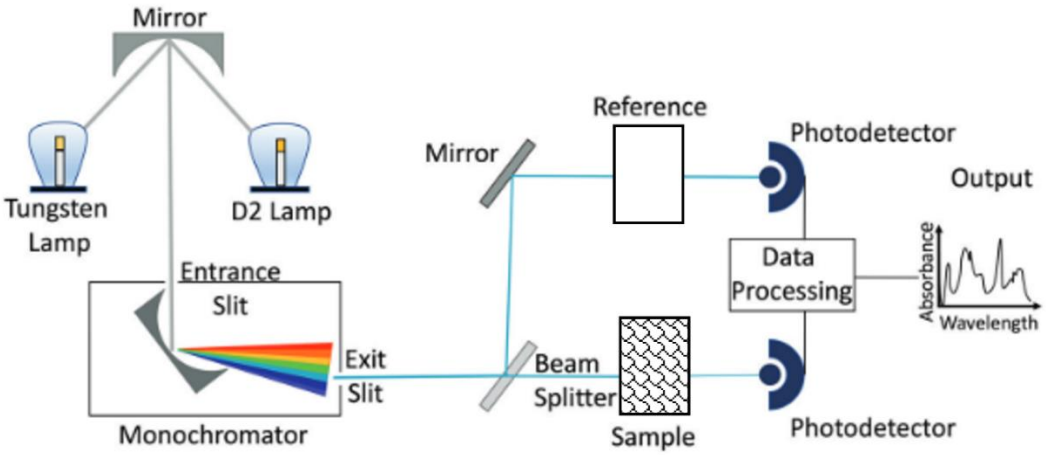

Figure 3.10: Schematic diagram of UV-Vis spectrometer. Adapted from ref [22]

An analysis of the UV-Vis reflectance data using the Kubelka – Munk method allows for a calculation of the band gap of the semiconductor material in a graphical method similar to that conducted for a Tauc plot using the following equations:[23]

$$F(R) = \frac{(1-R)^2}{2R})$$

$$(F(R).(h\upsilon))^2 = A(h\upsilon - E_g)$$

Equation 3.7: Kubelka-Munk method for Tauc plots.

where FI is the Kubelka – Munk function, R is the reflectance, E is the energy of the incoming photon, A is a proportionality constant, h is Planck's constant, v is the frequency of the photons and E_g is the band gap energy of the material.

Plotting $(FI.(hv))^2$ vs hv, the band gap (E_g) can be extracted via extrapolation of the linear region of the plot.

Ultraviolet – Visible (Uv-Vis) spectroscopy was used in this thesis to characterise the band gap of the photocatalytic materials. UV-Vis spectroscopy was conducted using a PerkinElmer LAMBDA 650s series spectrometer. The reflectance of the doped and undoped ZnO produced in this work and the data gathered to conduct the band gap analysis was collected using a UV/Vis/NIR spectrometer with an integrating sphere.

3.3.3.3. Inductively coupled plasma mass spectrometry (ICP-MS)

Inductively coupled plasma mass spectrometry (ICP-MS) is an analytical technique used to measure trace metals in samples with very high sensitivity, up to parts per billion (ppb) scale. Solution based samples are vaporised and injected into a high temperature plasma, usually argon, which atomises and ionises the sample, allowing for detection by mass spectrometry. The mass spectrometer separates the ions according to the mass/charge ratio and the beam of ions then passes through an electron multiplier before reaching a detector which records the charge or current of an ion passing, which is proportional to the concentration of that quantified ion. Concentration of the sample can then be elucidated using calibration curve or known reference material for comparison.[24]

In this thesis, ICP-MS was used to measure the chemical stability of the ZnO foams in water under UV and to assess the extent of photocorrosion that occurred during the photocatalytic degradation experiments, to assess their suitability for use, considering limitations placed on Zn^{2+} ion levels by The World Health Organisation.[25]

The ICP-MS data presented in this thesis was recorded by Dr J. A. Milton at the National Oceanography Centre, Southampton using a Thermo Fisher Scientific X-Series II instrument. All samples, standards and blanks, were spiked with internal standard elements Be, In, and Re. The Zn concentration was calibrated using six synthetic standards prepared from a 1000 ppm Inorganic Ventures (VA, USA) standard. The associated error was typically lower than 1.0%.

3.4. Reactor

The photocatalytic reactor used in this work is a recirculating batch reactor with a tubular design, which allows for greater UV irradiation of the photocatalyst and mass transfer of organic micropollutant from the reaction solution to the catalyst surface, as well as making best use of the hierarchical porosity of the foam structures by flowing the solution through the catalyst compared with batch reactor systems.[26] This system allows for photocatalytic foams to be placed within a quartz tube, surrounded by three equidistant UV-C lamps and the pollutant solution to be repeatedly flowed through the catalyst and back into the reservoir.

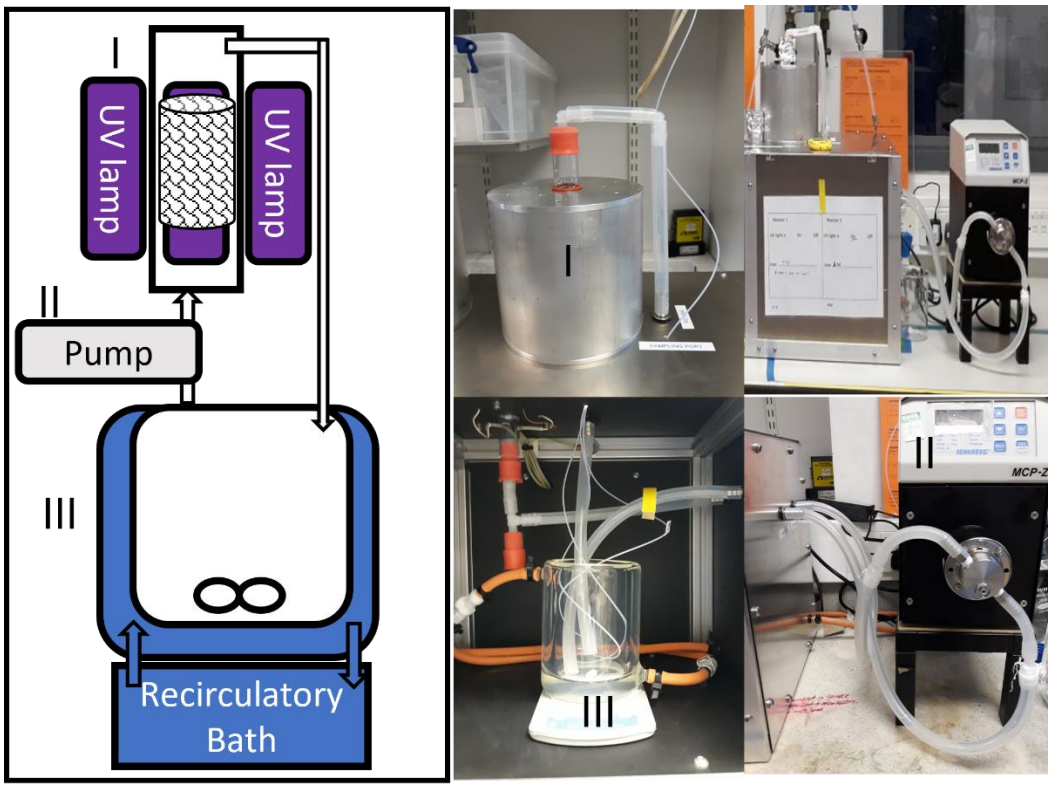

Figure 3.11: Schematic diagram for recirculating photocatalytic reactors. Labelled are I) quartz tube containing foam surrounded by UV lamps, II) gear pump Ismatec, MCP-Z with a pump head Model GBS.P23.JVS.A-B1, III) reservoir 500 mL)

The reactor was developed based on a previous reactor designed by Taylor et al.[27] The length of the quartz tube was 25 cm, with a length of lamp of 8 cm and a distance between the lamp and the quartz tube of 3 cm. Inner diameter of the quartz tube was 2.2 cm and outer diameter was 2.5 cm.

Conditions were kept constant, for all photocatalytic experiments, unless stated otherwise elsewhere: Reservoir temperature maintained at 10 °C, flow rate of 250 mL min^{-1}, 500 mL of 10 µM carbamazepine solution used, oxygen saturation time 40 minutes, irradiation time 120 minutes. After each experiment, the reactor was washed through with 500 mL of ultrapure water at a flow rate of 500 mL min^{-1}. The degradation of carbamazepine was monitored using HPLC (Section 2.3.3.1.).

Carbamazepine was selected as a model micropollutant for photocatalytic activity (PCA) studies, due to its high UV stability,[28] and known degradation pathways, [29] as well as it's prevalence as a pharmaceutical pollutant in waterways. [30] Furthermore, it

has been shown that the photodegradation pathway of carbamazepine is photocatalysis, rather than photosensitisation,[31, 32] the latter of which does not require band gap activation of the photocatalyst.[31]

3.5. References

1. W. L. Bragg, *Proceedings of the Royal Society of London. Series A, Containing Papers of a Mathematical and Physical Character*, 1997, **89**, 248-277.
2. B. Fultz, *Transmission Electron Microscopy and Diffractometry of Materials*, Springer, Berlin, Heidelberg, Berlin, Heidelberg :, 3rd ed. 2008. edn., 2008.
3. B. Cullity, *Readings, MA*, 1978, 102.
4. P. Ruegsegger, B. Koller and R. Muller, *Calcif Tissue Int*, 1996, **58**, 24-29.
5. B. P. Flannery, H. W. Deckman, W. G. Roberge and K. L. D'Amico, *Science*, 1987, **237**, 1439-1444.
6. Y. Liao, R. Wang, M. Tian, C. Qiu and A. G. Fane, *Journal of Membrane Science*, 2013, **425-426**, 30-39.
7. D. Briggs, *Handbook of X-ray and ultraviolet photoelectron spectroscopy*, 1977.
8. D. P. Woodruff, *Modern techniques of surface science*, Cambridge : Cambridge University Press, Cambridge, 1986.
9. P. Chaurand, J. Rose, V. Briois, L. Olivi, J. L. Hazemann, O. Proux, J. Domas and J. Y. Bottero, *J Hazard Mater*, 2007, **139**, 537-542.
10. S. P. Cramer, *X-ray spectroscopy with synchrotron radiation : fundamentals and applications*, Cham, Switzerland : Springer, Cham, Switzerland, 1st ed. 2020. edn., 2020.
11. M. D. Hall, G. J. Foran, M. Zhang, P. J. Beale and T. W. Hambley, *J Am Chem Soc*, 2003, **125**, 7524-7525.
12. J. R. Ferraro, *Introductory Raman spectroscopy*, Academic Press, Amsterdam Boston, 2nd ed. edn., 2003.
13. E. Smith and G. Dent, *Modern Raman Spectroscopy: A Practical Approach*, Wiley, 2019.
14. K. S. W. Sing, *Pure and Applied Chemistry*, 1985, **57**, 603-619.

15. F. Rouquerol, *Adsorption by powders and porous solids : principles, methodology and applications*, Kidlington, Oxford : Academic Press, Kidlington, Oxford, Second edition. edn., 2014.
16. K. C. A. Smith and C. W. Oatley, *British Journal of Applied Physics*, 1955, **6**, 391-399.
17. H. Seiler, *Journal of Applied Physics*, 1983, **54**, R1-R18.
18. M. A. Sutton, N. Li, D. C. Joy, A. P. Reynolds and X. Li, *Experimental Mechanics*, 2007, **47**, 775-787.
19. L. R. Snyder, J. J. Kirkland and J. W. Dolan, *Introduction to Modern Liquid Chromatography*, Hoboken, N.J. : Wiley, Hoboken, N.J., 3rd ed. edn., 2009.
20. J. M. Parnis and K. B. Oldham, *Journal of Photochemistry and Photobiology A: Chemistry*, 2013, **267**, 6-10.
21. M. T. Gilbert, *High performance liquid chromatography*, Bristol : Wright, Bristol, 1987.
22. F. S. Rocha, A. J. Gomes, C. N. Lunardi, S. Kaliaguine and G. S. Patience, *The Canadian Journal of Chemical Engineering*, 2018, **96**, 2512-2517.
23. A. Escobedo Morales, E. Sánchez Mora and U. Pal, *Revista Mexicana de Fisica Supplement*, 2007, **53**, 18-22.
24. F. Adams, R. Gijbels and R. v. Grieken, *Inorganic mass spectrometry / Wiley*, 1988.
25. W. a. UNICEF, WHOUNICEF-Joint-Monitoring-Program-for-Water-Supply-Sanitation-and-Hygiene-JMP, https://www.unwater.org/publications/whounicef-joint-monitoring-program-water-supply-sanitation-hygiene-jmp-2017-update-sdg-baselines/).
26. T. Tasso Guaraldo, J. Wenk and D. Mattia, *Advanced Sustainable Systems*, 2021, **5**.
27. C. M. Taylor, A. Ramirez-Canon, J. Wenk and D. Mattia, *J Hazard Mater*, 2019, **378**, 120799.
28. F. Ali, J. A. Khan, N. S. Shah, M. Sayed and H. M. Khan, *Process Safety and Environmental Protection*, 2018, **117**, 307-314.

29. J. Zhai, Q. Wang, Q. Li, B. Shang, M. H. Rahaman, J. Liang, J. Ji and W. Liu, *Sci Total Environ*, 2018, **640-641**, 981-988.

30. J. L. Wilkinson, A. B. A. Boxall, D. W. Kolpin, K. M. Y. Leung, *Proc Natl Acad Sci U S A*, 2022, **119**.

31. J. Liang, W. Zhang, Z. Zhao, W. Liu, J. Ye, M. Tong and Y. Li, *Journal of Hazardous Materials*, 2021, **416**.

32. E. De Laurentiis, S. Chiron, S. Kouras-Hadef, C. Richard, M. Minella, V. Maurino, C. Minero and D. Vione, *Environmental Science & Technology*, 2012, **46**, 8164-8173.

Chapter 4

Synthesis of Photocatalytic Pore Size-Tuned ZnO Molecular Foams

The work presented in this chapter has been published to Journal Materials Chemistry A in May 2022

Warren, Z., et al. (2022). "Synthesis of photocatalytic pore size-tuned ZnO molecular foams." Journal of Materials Chemistry A **10**(21): 11542-11552.

This declaration concerns the article entitled:			
Synthesis of photocatalytic pore size-tuned ZnO molecular foams.			
Publication status (tick one) **Draft manuscript** [ ] **Submitted** [ ] **In review** [ ] **Accepted** [ ] **Published** [X]			
Publication details (reference)	Warren, Z., et al. (2022). "Synthesis of photocatalytic pore size-tuned ZnO molecular foams." Journal of Materials Chemistry A **10**(21): 11542-11552.		
Copyright status (tick the appropriate statement) The material has been published with a CC-BY license [X] The publisher has granted permission to replicate the material included here [ ]			
Candidate's contribution to the paper (provide details, and also indicate as a percentage)	The candidate contributed to… Formulation of ideas: 65% The original project was conceived and planned by co-authors DM, TTG and JW before the candidate started his PhD research. The candidate contributed further ideas that became the final project. Design of methodology: 85% The candidate designed the synthetic methodology for the manuscript under the supervision of DM and JW. Input on experimental set up offered by DM. Experimental work: 90% The candidate conducted all experimental procedures including synthesis, characterisation and analysis ICP-MS experiments performed externally but analysed by the candidate and external input was acknowledged. Presentation of data in journal format: 85% The candidate wrote the manuscript and prepared graphs and tables under the supervision of DM and JW. Input was offered by all co-authors		
Statement from Candidate	This paper reports on original research I conducted during the period of my Higher Degree by Research candidature.		
Signed	Zachary Warren	**Date**	21/09/2022

Synthesis of Photocatalytic Pore Size-Tuned ZnO Molecular Foams

Zachary Warren,[a] Thais Tasso Guaraldo, [a] Jannis Wenk,[a] and Davide Mattia*[a]

[a]Department of Chemical Engineering, University of Bath, BA2 7AY, UK

Graphical Abstract

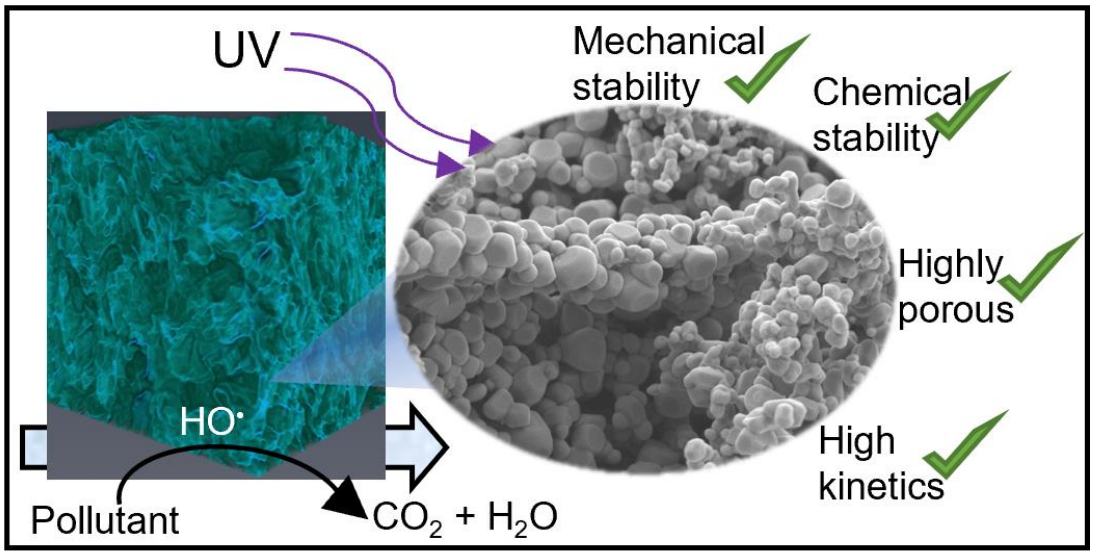

Abstract

The safe and efficient removal of organic micropollutants, such as pharmaceuticals, pesticides or caffeine from wastewater remains a major technological and environmental challenge. Here, the synthesis of self-supporting ZnO foam monoliths by direct incorporation of air into the forming gel is presented for the first time. These foams, labelled as MolFoams, showed a highly porous and interconnected structure, allowing for high solution flow rates and fast degradation kinetics of carbamazepine, a widely used pharmaceutical compound, used here as a model micropollutant. Altering the concentration of CTAB used in the formulation of the gels allowed controlling the size of the macropores of the MolFoam in the of 0.69 – 0.84 mm range. Smaller macropores within the MolFoam structure were highly beneficial for the degradation of carbamazepine with pseudo first-order degradation kinetics of 5.43 $x10^{-3}$ min^{-1} for the MolFoams with the smallest macropore size. The best foams were tested in a recirculating reactor, with an optimal flow rate of 250 mL min^{-1},

resulting in a quantum efficiency of 2.63 X 10^{-3} and an electrical energy per order of 21.34 KWh m^{-3} $order^{-1}$, in addition to high mechanical and chemical stability. These results surpass the performance of photocatalytic slurries and immobilised systems, showing that self-supporting, photocatalytic foams can be an effective solution for the removal of organic micropollutants in wastewater.

Synthesis of Photocatalytic Pore Size-Tuned ZnO Molecular Foams

4.1. Published Manuscript

Introduction

The presence of organic micropollutants at ng L^{-1} to µg L^{-1} concentrations in water bodies poses an emerging threat to public health and aquatic ecosystems.[1,2] Organic micropollutants comprise a wide range of compounds including pesticides, pharmaceutical, personal care products, drugs and hormones.[3] Many organic micropollutants cannot be efficiently removed with the physical, chemical and biological methods applied in conventional wastewater treatment plants.[4] Through wastewater effluent, organic micropollutants are discharged into the aquatic environment, where they exert ecotoxicological effects on aquatic organisms, bioaccumulate and eventually may reach water supplies or enter the human food chain.[5] New technology is required to effectively remove organic micropollutants during wastewater treatment. Advanced oxidation processes (AOPs) are among the most promising approaches for the removal of organic micropollutants in wastewater. AOPs encompass a wide range of different methods that utilize hydroxyl radicals as the main oxidizing species targeting organic micropollutants. [6] Ozone-based AOPs are widely used due to their low cost,[7] but can cause the formation of bromate compounds in water supplies with high concentrations of bromides, posing a risk to human health.[8] UV/H_2O_2 systems are also employed,[9] however the use of peroxide is limited by its low molar absorption coefficient, thereby requiring high concentrations to generate sufficient hydroxyl radicals. [10] Fenton related processes are less common, due to a low efficiency of the iron complexes when operated at the typical pH of wastewater.[6] The photocatalytic degradation of organic micropollutants has the potential to address some of the limitation of other AOPs,[11] but also faces some key challenges which have, so far, limited its large-scale adoption. Currently, photocatalysts are used as slurries or supported catalyst. [12] In slurries, suspensions of photocatalytic nanoparticles are mixed with the pollutant stream ensuring a high

surface area contact between pollutant molecules and photocatalyst,[13] as well as a higher active surface area that can be irradiated. [14] A key drawback of photocatalytic slurries is the requirement for costly downstream separation of the slurry prior to release into waterways. [15] While the benefits of using nanoparticle slurries are significant, considerations need to be paid to the impacts of their release to the environment, with established evidence of bioaccumulation within fish, plants and mammals. [16] Furthermore, it has been shown that there is the potential for synergic interactions between catalyst nanoparticles and pollutants present in the environment, resulting in enhanced toxicity. [16] With supported catalysts downstream removal is not required as for slurries. However, supported catalysis have a lower surface area of catalyst in contact with the pollutant stream resulting in lower treatment efficiencies, [17] [18] as well as issues of "shadowing", where the structure of the support and morphology of the catalyst can lead to areas where light cannot reach the surface, resulting in a reduced reactor efficiency. [18] Reticulated foam materials as supports for photocatalysts can integrate the advantages of supported immobilised catalysts with the higher surface areas of photocatalytic slurries. Synthesis of these generally involve decoration or coating a porous material, often Al_2O_3, [19] Ni [20] or SiC,[21] with photocatalytic nanoparticles, typically TiO_2 [19, 22] or ZnO.[20] While these decorated foams have shown faster degradation kinetics than an equivalent unsupported catalyst, [19] they do not solve the issues associated with the potential leaching of nanoparticles in the treated wastewater. [23]

A further advancement in the use of foams has been to obtain a photocatalytically active porous monolithic structure, obtained from the sintering of ZnO microparticles around an organic template.[24] This approach removes the potential issue of weak adherence of particles to a support observed in decorated foams. However, zero leaching of particles cannot still be guaranteed during continued use. It is therefore advantageous to move away from the use of particles of any size in the synthesis, instead using a solution-based synthesis for the formation of monolithic photocatalysts.

Zinc oxide was selected as the starting metal oxide for this work, as its use as a photocatalyst in water treatment research is well established, [25] due to its UV active band gap of 3.2 eV, high electron mobility and low cost and toxicity. [26] Furthermore it absorbs over a wider range of wavelengths of light compared to TiO_2 allowing for greater utilisation of a light source and more efficient degradation of pollutants,[27] while additionally TiO_2 suffers from high rates of electron hole recombination which limits its effectiveness as a photocatalyst. [28] However ZnO is not without its drawbacks, including photo-corrosion under UV irradiation, [29] leading to the dissolution and formation of Zn^{2+} ions in solution, limiting its use for water treatment. The World Health Organisation limits the maximum concentration of Zn^{2+} in water to 3.0 ppm. [30] The impact of this photo-corrosion can be reduced at high dissolved oxygen concentration that stabilises ZnO. [31]

This work reports the use of a solution-based synthesis of zinc salt and a dicarboxylate linker in a sol-gel synthesis with controlled incorporation of air to form a porous zinc oxalate precursor foam, which is then sintered to form robust metal oxide foam. Synthesis in this manner has many advantages: Firstly, the foams are produced avoiding the use of volatile foaming agents while still retaining the high porosity that that would be expected from their synthetic use. [32, 33] Furthermore, the sintering and conversion of oxalate to oxide results in a porous structure without the presence of discrete particles. Rather, a singular interconnected structure made of metal oxide is formed, thus removing the need for a porous support structure and discrete particles within the structure. As the formation of the porous monolith occurs via a bottom-up approach, using the reaction at a molecular basis, the foams synthesised in this way as called “Molecular Foams” or MolFoams.

Experimental

Materials

Zinc acetylacetonate (Zn $(AcAc)_2$; ≥95.0 %), Oxalic acid anhydrous (≥99.9 %), Hexadecyltrimethylammonium bromide (CTAB; ≥99.9 %), Polyethylene glycol (PEG; 10,000), Ethanol (Absolute) and Methylene Blue were all purchased from Sigma Aldrich and used as provided. Jacketed, fritted funnels were purchased from

Chemglass Lifesciences and fitted with PTFE sheets (Zwanzer). Desiccant from a Drierite™ gas-drying unit (Sigma Aldrich) was used as provided by the manufacturer but transferred to a smaller tube.

Synthesis of ZnO MolFoams

Zinc oxide foams were synthesised by substantially altering a method originally used to make nanoparticles,[34, 35] to form a solid foam monolith. First, Zn $(AcAc)_2$ (15.0 mmol) was added to a 25 mL Pyrex beaker. Subsequently, CTAB was dissolved in 15 mL ethanol and added to the beaker such that the final concentration in the reaction mixture was 5, 10, 15 or 20 mM respectively. Oxalic acid (15.0 mmol) and 40 µmol PEG10000 with 10 mL EtOH mixed in a separate beaker**.** Both solutions were stirred at 60 °C for 60 minutes in an oil bath until homogenous solutions were obtained. The solutions were sequentially added to a PTFE-lined, temperature controlled jacketed filter funnel at 60 °C. The reaction mixture was aerated with compressed air with an upward flow rate of 0.1 Standard Litres per Minute (sL min^{-1}) using a rotameter.

The reaction mixture of the Zn and acid solutions was aerated for 3 hours leading to the formation of a white gel. The gel was then transferred to a pre-weighed ceramic crucible and placed in a preheated muffle furnace (Carbolite CWF 1100) at 80 °C and dried for 12 hours to remove any remaining ethanol resulting in a dry zinc oxalate foam which was stored under ambient conditions.

Conversion of zinc oxalate foam into zinc oxide was achieved using a two-step thermal sintering process: The zinc oxalate foam was sintered using a furnace, heated to 1,000 °C with a ramp rate of 5 °C min^{-1} and held at temperature for 0.5 hours, and then 900 °C with a ramp rate of 5 °C min^{-1} and held at temperature for 20 hours. This resulted in the formation of a mechanically stable ZnO foam. The high temperature sintering was also used to remove any remaining organic components. After sintering, the foams were cylindrical in shape, with an average diameter of 20 ± 1 mm and height of 19 ± 1 mm. Multiple parameters were studied, including sintering times and temperatures, aeration method, flow rate of air and composition of reactant solutions, for the formulation of the foams. (Table S4.1).

Characterisation of ZnO MolFoams

The surface morphology of the zinc oxide foams was studied using a JEOL 6301F FESEM and JEOL JSM-7900F FESEM. Prior to imaging, samples were coated with 20 nm Cr. The crystal structure of the foams was investigated using a STOE STADI P dual powder transmission x-ray diffractometer using a scanning range of 2θ = 20 – 90 degrees and a scan time of 20 minutes.

The chemical stability of the MolFoams was analysed using inductively coupled plasma mass spectrometry (ICP-MS) in a Thermo Fisher Scientific X-Series II instrument. All samples, standards and blanks, were spiked with internal standard elements Be, In, and Re. The Zn concentration was calibrated using six synthetic standards prepared from a 1000 ppm Inorganic Ventures (VA, USA) standard. The associated error was typically lower than 1.0%.

The porosity and internal structure of the MolFoam were determined using a combination of different characterisation methods. First, gravimetric porosity measurements were conducted using the Archimedes principle: [36]

$$\varepsilon = \frac{\frac{\omega_1 - \omega_2}{D_u}}{\frac{\omega_1 - \omega_2}{D_u} + \frac{\omega_2}{D_f}}$$

Equation 4.1 Gravimetric Porosity

where ε is the porosity of the foam, ω_1 is the mass of the wet foam, ω_2 is the mass of the dry foam, D_u is the density of water (deionised, ultrapure) and D_f is the density of ZnO. The porosity and internal structure of the foams were further analysed using microcomputer tomography. The slices were collected using a Nikon XT H 225 ST using a 178 kV x-ray source and 0.708 s exposure time, 4 frames per projection and 3141 projections and analysed using Thermo Scientific AvizoSoftware 9 3D data visualisation software. This data was used to calculate the Surface Area: Volume ratio, a_{vs}: [37]

$$a_{vs} = \frac{8.002\ (1 - 0.833\sqrt{1-\varepsilon}}{d_p\sqrt{1-\varepsilon}}$$

Equation 4.2 Surface Area: Volume ratio

where d_p is the pore diameter and Ɛ is the porosity of the foam.

To probe the microporosity, the MolFoams were broken in smaller pieces and analysed via BET N2 adsorption using a Autosorb- iQ-C by Quantachrome Anton Paar at 77 K, after degassing under vacuum at 130 ^{o}C for 120 minutes, obtaining the specific surface area, SA_{BET}. Samples were loaded carefully avoiding the formation of powders, to avoid characterisation of the porosity of a powdered MolFoam.

Finally, a bespoke dyeing apparatus was developed to qualitatively assess the nature of the pores (open or closed porosity) within the MolFoam. A schematic of this can be found in Figure S4.3. Briefly, a solution of Methylene Blue (MB) was flowed through a tube (ID = 22 mm, OD = 25 mm) containing a MolFoam on a plastic support platform using a peristaltic pump (Masterflex L/S, pump head model 77200-62) operating at a flow rate of 50 mL min^{-1} for 120 minutes. After drying, the MolFoam was cut open showing sections dyed blue, indicative of open porosity, whereas sections left undyed would-be indicative of closed pores.

Photocatalytic reactor setup

For the reciculating photocatalytic experiments, reactor cartridges were made up of a quartz tube (h = 250 mm ,OD = 25 mm , ID = 22 mm) with a 3D printed plastic buffer designed to hold the foams in place and prevent loss of the foam into the tubing and pump, positioned to avoid interference with the light source. A 3D model and a diagram of the reactor can be found in Figures S4.1 and S4.2.

ZnO MolFoams of known mass (0.7 g) were placed inside the cartridge and secured using subaseal fittings, connected to a gear pump (Ismatec, MCP-Z with a pump head Model GBS.P23.JVS.A-B1, Cole Parmer) connected to a jacketed beaker of 500 mL (acting as the reservoir) with a magnetic stirrer, where the temperature was maintained using a water-cooled bath (RC-10 Digital Chiller, VWR) with three UV lamps (Aquatix pond UV lamp, λ = 254 nm, 5W) positioned equidistant around the quartz tube reactor containing the ZnO MolFoam at a distance of 3 cm served as the light source.

Photocatalytic activity (PCA) experiments

PCA experiments were conducted using 10 µM solutions of carbamazepine (CBZ) in 500 mL unbuffered ultrapure water at 10 ± 1 °C. CBZ was selected as a model micropollutant for photocatalytic activity (PCA) studies, due to its high UV stability,[38] and known degradation pathways, [39] allowing for comparison with both slurries and immobilised catalysts.[40, 41] To minimize photocorrosion of ZnO, [31] CBZ solutions were saturated with O_2 for 40 minutes prior to experiments. The recirculating reactors were operated at flow rates between 100 mL min^{-1} and 500 mL min^{-1}. Control experiments were conducted in the absence of MolFoams in the reactor. Adsorption and removal of CBZ under dark conditions were found to be negligible as shown in Figure S4.8.

For all photocatalysis experiments, CBZ removal was monitored from 1 mL aliquots collected during sampling every 15 minutes for the first hour and every 30 minutes thereafter, such that the total volume removed was less than 10% of the starting reservoir volume, using high performance liquid chromatography (HPLC).

All experiments were repeated in triplicate. HPLC analysis of CBZ was performed on a Thermo Scientific Ultimate 3000 liquid chromatograph with a UV detector. CBZ analysis used a Thermo Scientific Acclaim 120 C_{18} column (3.0 X 75.0 mm, particle size 3.0 µm) and a Thermo Scientific Acclaim 120 C_{18} guard column (R) 120 C_{18} (3.0 X 10.0 mm, particle size 5.0 µm) The mobile phase was made up using 5.0 mM phosphoric acid and acetonitrile 70:30 (v:v) with a flow rate of 0.8 mL min^{-1}, injection volume of 20 µL and detection wavelength of 285 nm. Degradation of carbamazepine was measured via plotting (C_t/C_0) Vs time where C_0 is the initial concentration of CBZ and C_t is the concentration of CBZ at a given time. The pseudo first order degradation kinetics (k) was calculated via linear regression of a plot of Ln(C_t/C_0) Vs time.

Photocatalyst quantum efficiency

The quantum efficiency (QE) of a photocatalytic system is defined as the number of molecules of pollutant (carbamazepine) undergoing degradation relative to the number of photons reaching the catalyst surface. [42] The photon flux (E_{qf}) arriving at the surface of the photocatalyst along with the kinetic constant (k') allows calculating the quantum efficiency (QE). Details of the calculations are provided in the SI.

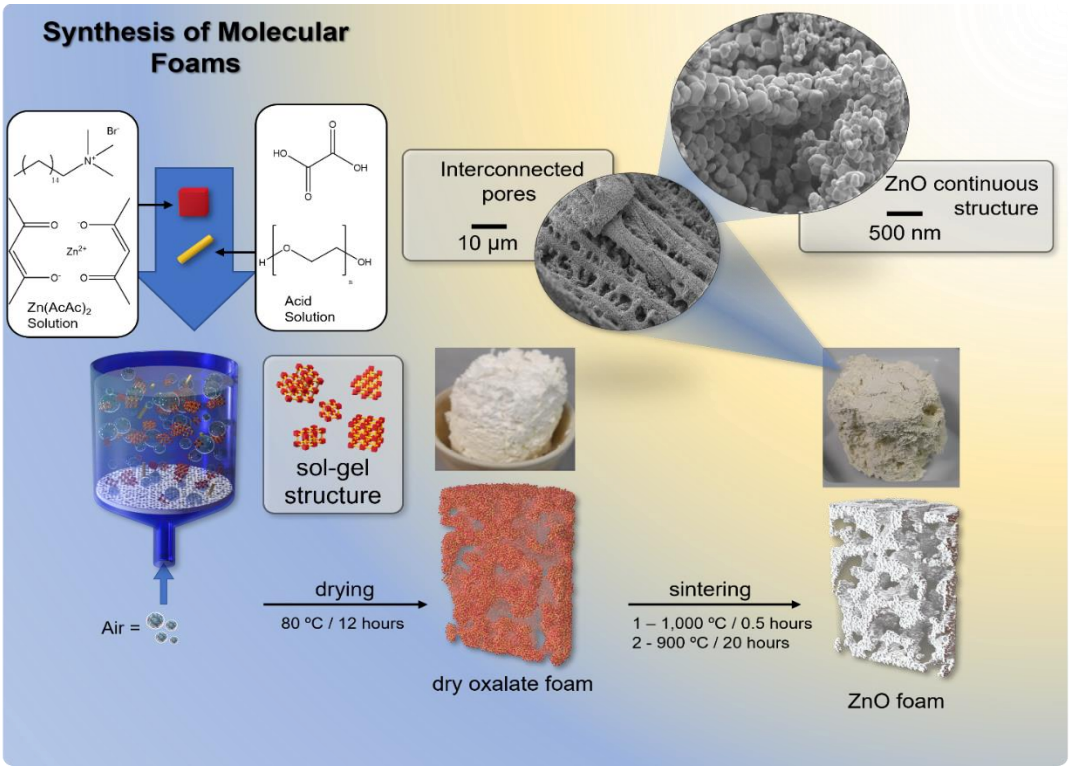

Figure 4.21: Graphical overview of synthetic method of MolFoam production

Electrical Energy Per Order (E_{EO})

To assess the scale up potential of the system, the energy consumption of the reactor was estimated via the electrical energy per order (E_{EO}), defined as the kilowatt hours of electrical energy needed to decrease the concentration of a pollutant by an order of magnitude (90%) in one cubic metre of solution: [43]

$$E_{EO} = \frac{P * t * 1000}{(V)(log\, {C_0}/{C_t})}$$

Equation 4.3 E_{EO}

Where: P is the total power output of the 3 lamps onto the 12 cm long quartz tube, t is time in hours and V is the volume of the reservoir. As the foam occupied only a fraction of the quartz tube, the total power of the lamps was multiplied by the volumetric fraction occupied by the foam, to provide the effective power used for photocatalysis, considering that the contribution of photolysis is negligible. Details of the calculations are provided in the SI.

Results and discussion

ZnO MolFoams characterisation

Upon removal from the funnel, the wet gel monoliths were white in colour, free-standing and plastic via gentle pressure. After drying, the samples became brittle upon application of pressure. The dried monoliths were 28 mm in diameter and 30 mm in height on average. This decreased to 20 ± 1 mm diameter and 19 ± 1 mm height post sintering and could be handled and subjected to flow experiments.

The XRD pattern of the foams (Figure S4.4) shows the formation of hexagonal wurtzite ZnO with lattice parameters of a = b =3.25 Å and c =5.21 Å, sharp peaks indicating the sample is highly crystalline in nature and strongest intensity in the peaks associated with the (100), (002) and (101) crystal phases. All peaks are in agreement with those reported from JCPDS No. 36-1451. [44] The gravimetric porosity of these MolFoams, as measured using the Archimedes principle, [36] was found in all cases to be 95 ± 1 %. This high porosity is required for solution flow through the foams in a flow reactor system. Furthermore, this high porosity is comparable with those reported in the literature for metal oxide aerogels, [45, 46] with the key distinction that this porosity is achieved without the use of volatile foaming agents such as propylene oxide, nor the use of supercritical CO_2 (sCO_2). The FESEM micrographs show the presence of interconnected pores with faceted wall structures within the foam (Figure 4.2). The MicroCT slices and 3D reconstructions (Figure S4.5) show the internal structure of the MolFoams to be comprised of irregularly shaped pores and channels, connecting throughout the MolFoam. The irregularity of the pores can be ascribed to multiple factors: The use of EtOH as a solvent resulted in CTAB concentration well below the critical micelle concentration (CMC) of the CTAB/EtOH

system of 0.24 M,[47] hindering formation of regular micelles compared to an equivalent system using an aqueous solvent; and the densification due to sintering, compounded by the release of CO_2 from the zinc structures during the conversion of the oxalate into the oxide. [34]

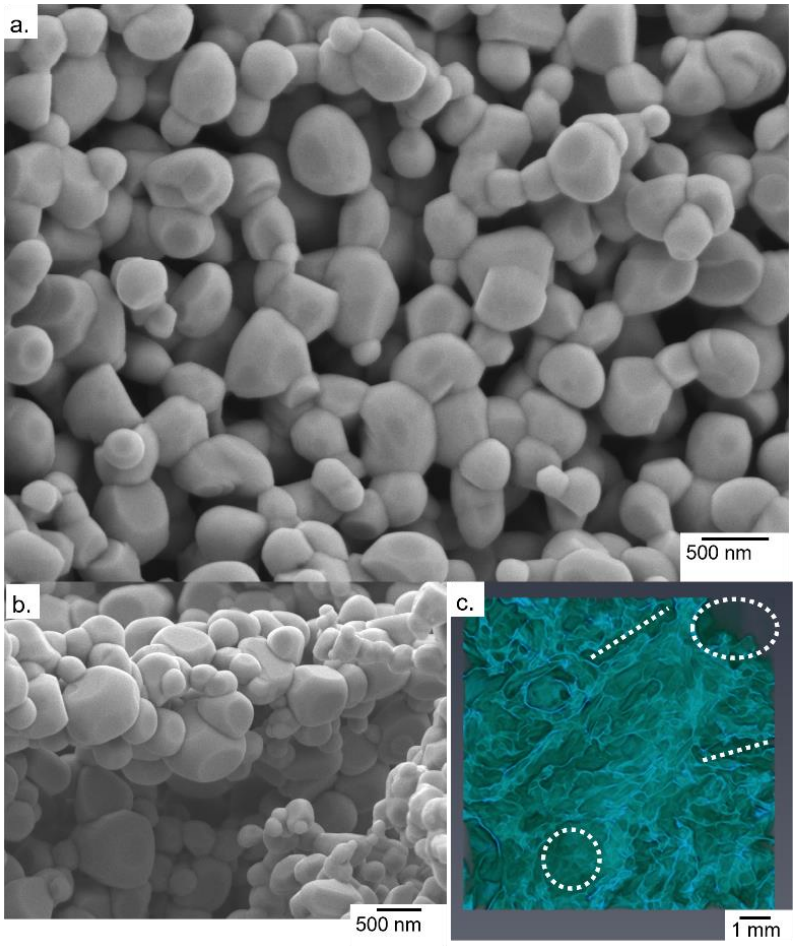

Figure 4.22 FE-SEM micrographs showing the interconnected structure of the MolFoams (a) and the irregular microporous channel structure (b). (c) 3D reconstruction from MicroCT showing the irregular pore and channel structures within the MolFoams. The dashed circles and lines highlight examples of pores and channels, respectively.

Effect of flow rate on photocatalytic activity of MolFoams synthesised using 5 mM CTAB solution.

The photocatalytic activity of the MolFoam was investigated in a recirculating flow reactor. Initially operated at 100 mL min^{-1} in

the absence of a MolFoam, the carbamazepine underwent minimal degradation (9%) within 2 hours due to photolysis alone. When the ZnO MolFoam photocatalyst was added, the degradation increased to 36% after 2

hours (Figure 4.3). Further increases of the flow rate from 100 to 400 mL min^{-1}, led to an increase in the total degradation of CBZ to 57% (Figure 4.3). This increase in CBZ removal, along with a corresponding increase in kinetics reveals that the process is in the mass transfer limited regime, a well reported effect wherein the diffusion of pollutant through the boundary layer at the catalyst/pollutant interface limits the rate of degradation. [48] As the flow rate is increased, this leads to the formation of a thinner boundary layer at the catalyst surface between it and the bulk of solution, reducing the time required for the carbamazepine molecules to diffuse to the surface of the foams.[12] The effect of this can be seen clearly within Figure 4.3, where, as the flow rate is increased, both the degradation of carbamazepine and the kinetics increase, with a significant change in the kinetics between 200 and 300 mL min^{-1}. The change becomes less pronounced as the flow rate is further increased and begins to decrease at flow rates of 500 mL min^{-1}. Comparable phenomena has been observed for the photocatalytic degradation of phenol using ZnO wire.[31] However whether this is indicative that the system is no longer in the mass transfer-limited regime and the adsorption of carbamazepine onto the ZnO is the rate limiting factor is unclear, as it was at this high flow rate that the foams underwent significant mechanical degradation and, hence, were deemed unsuitable for use at these higher flowrates. As such the MolFoams were modified to improve their mechanical stability at higher flow rates.

Furthermore, the quantum efficiencies of these MolFoams ranged from 1.21 X 10^{-3} to 1.79 X 10^{-3} at flow rates of 100 and 400 mL min^{-1}, respectively. While these initial values are higher than for those reported for supported TiO_2,[49, 50] and comparable with ZnO nanoparticle slurries, [41, 51] they are lower than those for other ZnO foams.[24] Further comparisons with quantum efficiencies reported in the literature can be found in Table S4.8.

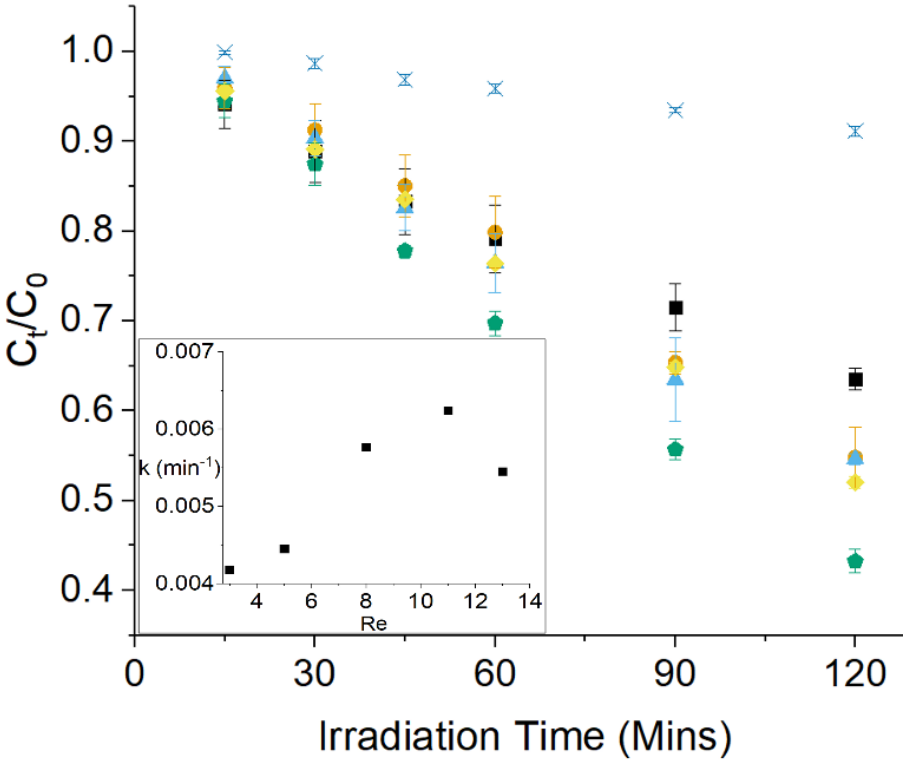

Figure 4.23:Photocatalytic degradation of CBZ using ZnO MolFoams at varying flow rates × photolysis, ■ 100 mL min^{-1} , ● 200 m L min^{-1} , ▲ 300 mL min^{-1} , ⬟ 400 mL min^{-1} , ◆500 mL min^{-1}. Inset shows first order reaction kinetic as a function of flow rate (Reynolds number).

Table 4.1: Correlation between [CTAB], CBZ removal for foams prepared at different CTAB conditions (120 min irradiation time, flow rate 200 mL min-1) and pseudo first order degradation kinetics (k) with the porosity calculated by Archimedes' method (e), macropore diameter and pore Surface Area: Volume ratio (a_{vs}) and BET Surface (SABET). Also tabulated are overall quantum efficiency (QE) and E_{EO} at corresponding CTAB

[CTAB] /mM	C_{120}/C_0	k (x10^{-3}) /min^{-1}	ε /%	Macropore Diameter /mm	a_{vs} / cm^{-1}	SA_{BET} /m^{2}g^{-1}	QE	E_{EO} /KWh m^{-3} order^{-1}
5	0.56 ± 0.03	4.44 ± 0.32	96	0.81 ± 0.02	16.50	34.50	1.30 X 10^{-3}	39.71 ± 3.93
10	0.48 ± 0.02	5.43 ± 0.37	96	0.69 ± 0.01	19.37	35.68	1.56 X 10^{-3}	31.37 ± 1.85
15	0.53 ± 0.03	5.29 ± 0.17	96	0.76 ± 0.01	17.58	28.18	1.53 X 10^{-3}	36.27 ± 3.44
20	0.58 ± 0.02	4.71 ± 0.18	94	0.84 ± 0.02	15.91	39.05	1.36 X 10^{-3}	42.27 ± 2.81
Correlation	0.33	0.18	-0.78	0.32	-0.30	0.17		
	Correlation – Kinetics		0.37	-0.85	0.85	-0.41		
	Correlation - Degradation		-0.65	0.99	-0.99	0.29		

CTAB-modified MolFoams

The concentration of CTAB in the formulation was modified to increase the mechanical stability of the MolFoams at higher flowrates. Initially, CTAB was used as a surfactant solely to stabilise the air bubbles within the gel and increase the porosity of the foams.[52, 53] It was then theorised that by increasing the concentration of the surfactant, the foams would be able to incorporate more air and show both greater porosity and larger pore sizes, as greater stabilisation of the air/EtOH interface occurs. Small increases to the CTAB concentration were made, to achieve final concentrations of CTAB in the foams of either 5, 10, 15 or 20 mM, still well below the CMC. Foams synthesised with the increased CTAB concentrations up to 15 mM showed no change in macroscopic dimensions, while the foams synthesised using 20 mM CTAB were slightly squatter than previous foams. At the microstructural level, on the other hand, there were significant changes: The increased presence of the CTAB led to the formation of more rod-like microstructures within the foam structure (Figure 4.4, S4.6) with a higher proportion of the crystals showing well-defined facets.

This combination has been shown to result in higher photocatalytic activity,[54] due to these facets showing greater potential for adsorption of pollutants to the surface, as well as showing greater trapping of photoexcited electrons and holes at the surface. [55] ZnO nanorods are well reported to have increased charge separation and trapping properties, associated with the higher aspect ratio of the crystals compared with other morphologies as this leads to greater delocalisation of electrons. [56] Furthermore the [002] crystal plane and associated (0001) facet have been shown to be promote adsorption of oxygen species, allowing for the formation of reactive hydroxyl radicals to promoted degradation of pollutant species. [57] The formation of the rod-like structures is attributed to the preferential adsorption of ionic surfactants on the [100] crystal plane or (1010) crystal facet, which, in turn, has an inhibitory effect on the crystal growth in this direction.[58, 59] This then promotes growth of the crystal along the [101] crystal plane of the (1011) facet,[58] and the [002] plane

of the (0001) facet,[60] resulting in the formation of the longer rod-like structures observed here and in the literature. [61]

It is widely reported that particle shape has a significant impact on the photocatalytic activity of ZnO, along with the effect the shape has on the relative intensity of the main ZnO peaks within the XRD,[44] in particular, regarding ZnO nanorods as

Increasing the CTAB concentration from 5 to 10 mM lead to an increase in the relative intensity of the (100), (002) and (101) peaks, suggesting a degree of crystallite anisotropy, [59] while a decrease in relative intensity of the (100)/(101) ratio from 0.70 to 0.65 and (002)/(101) ratio from 0.50 to 0.44 is indicative of an increased presence of 1011 facets typical of those found on ZnO rod-like structures. [54] Further increases in the CTAB concentration did not lead to any further changes in the relative intensities or ratio of the peak intensities, indicating no further changes to the shape of the crystallites, with similar findings reported in the literature. [60]

The degradation of CBZ and the degradation kinetics follow a nonlinear relationship, with the Pearson's r value for the correlations between CTAB concentration and degradation or

kinetics being only 0.33 and 0.18, respectively (Table 4.1). Figure 4.5a shows that the highest kinetics and greatest CBZ removal occurring in MolFoams synthesised using 10 mM CTAB solutions, increasing from 5 mM and then decreasing as the concentration increases further.

This suggests that, while 10 mM is the optimum CTAB concentration, the greater concentration of CTAB is not directly responsible for this increase, nor is it the increased presence of the rod-like crystals that are observed at higher concentrations. It is likely that this increased activity is due to the effect that the CTAB has on the structural properties of the MolFoams. As the CTAB concentration increases, the average diameter of the pores shows a minimum macropore size for 10 mM CTAB, then increasing as the concentration increases, while at minimum pore diameter, the degradation and reaction kinetics are highest (Figure 4.5 b-d). This is further reinforced by the Pearson's r value for the

correlations for macropore size and the related SA/V ratio of the pores with very strong correlation to the degradation of carbamazepine (r = 0.99 and -0.99, respectively) and strong correlation with the pseudo first order kinetics (r = -0.85 and 0.85, respectively) as shown in Table 4.1. The decrease in pore size can be qualitatively

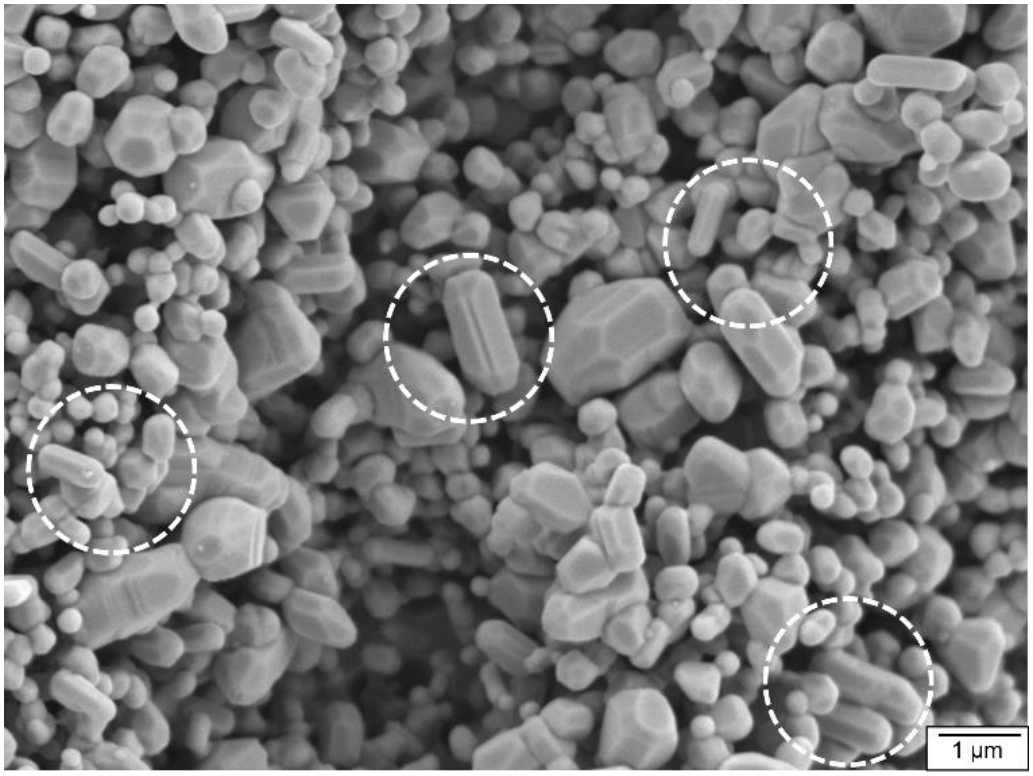

Figure 4.24: FE-SEM micrograph of ZnO MolFoams synthesised using 10 mM CTAB solutions. Encircled regions show highly faceted rod-like structures.

observed in Figures 4.6c and 4.6d, where the 3D reconstruction of the MolFoams shows the formation of smaller pores in the foams synthesised with higher CTAB concentrations. This is of particular interest as opinion within the literature is divided on the impact of pore size on the degradation activities of supported catalysts. One argument is that the smaller the pore size, the higher the surface areas within,[62] resulting in larger reactive catalyst area. This, along

with thinner coatings of catalyst allows for greater light utilisation.[37] A contrasting argument is that the larger the pore size, the greater the light penetration into the foam and thus greater activation of photocatalyst. [63] However, this argument is frequently made of foams of photocatalytically inactive materials such as alumina with thick struts surrounding the pores. [64, 65] Larger pores also offer less resistance to

the flow of the solution through the foam structure.[64] Figure 4.5 shows a clear relationship between CTAB concentration and the pore size of the foams as well as the degradation of CBZ and reaction kinetics, with the smaller pore sizes leading to greater degradations and higher kinetic constants. The improved activity from smaller pores can be explained by the hierarchical pore structure of the foams. The channels within the foam favour fluid flow through the porous material, while the smaller macropores, as observed in the 10 mM CTAB samples, provide greater degradations and higher kinetics, due to pollutant molecules having shorter diffusion times within smaller pores.[48] Reducing the macropore size increases the rate of diffusion, resulting in faster kinetics and higher degradation of CBZ. Smaller pores also provide higher surface areas for the degradation reaction to occur. Furthermore, the reduction of pore size without changes in overall porosity suggests the presence of a greater number of pores within the foam structure with each individual pore having a higher surface area: volume ratio and acting as a site for the adsorption and degradation of pollutant molecules from the eluent stream.

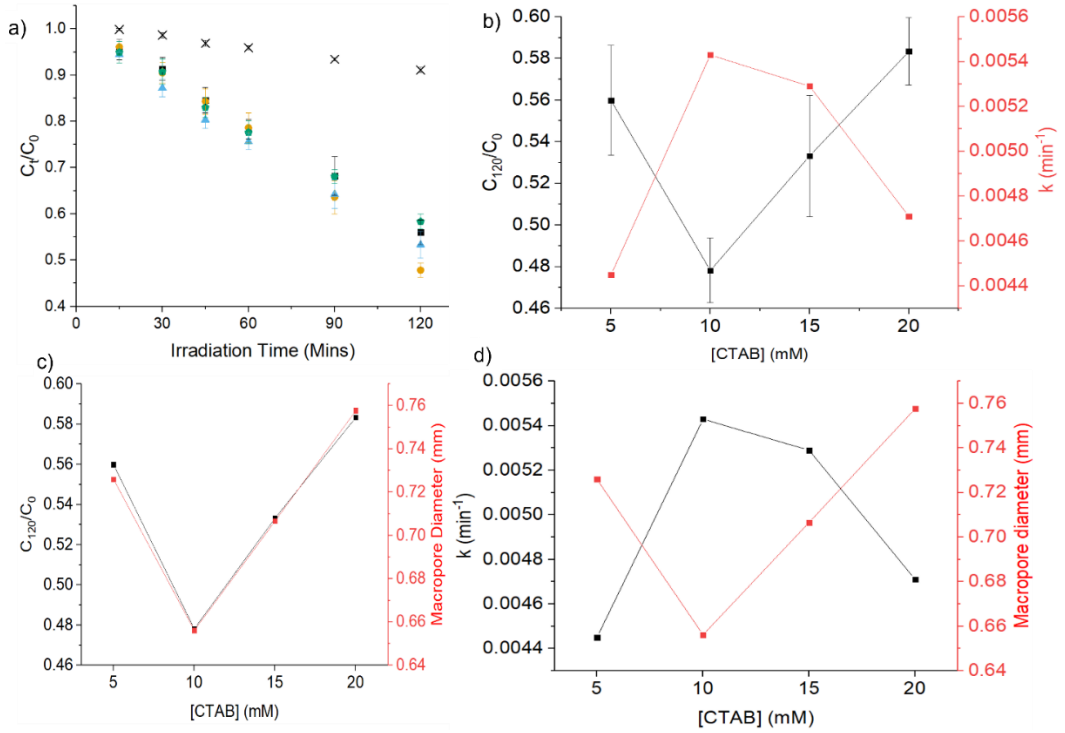

Figure 4.5. a) Photocatalytic degradation of CBZ using ZnO MolFoams synthesised using various CTAB concentrations: × photolysis, ■ 5 mM, ● 10 mM, ▲ 15 mM, ⬟ 20 mM. Relationship between [CTAB] and b) CBZ degradation and the associated pseudo first order kinetics; c) CBZ degradation and the pore diameter of the MolFoams; and d) pseudo first order kinetics and the pore diameter of the MolFoams.

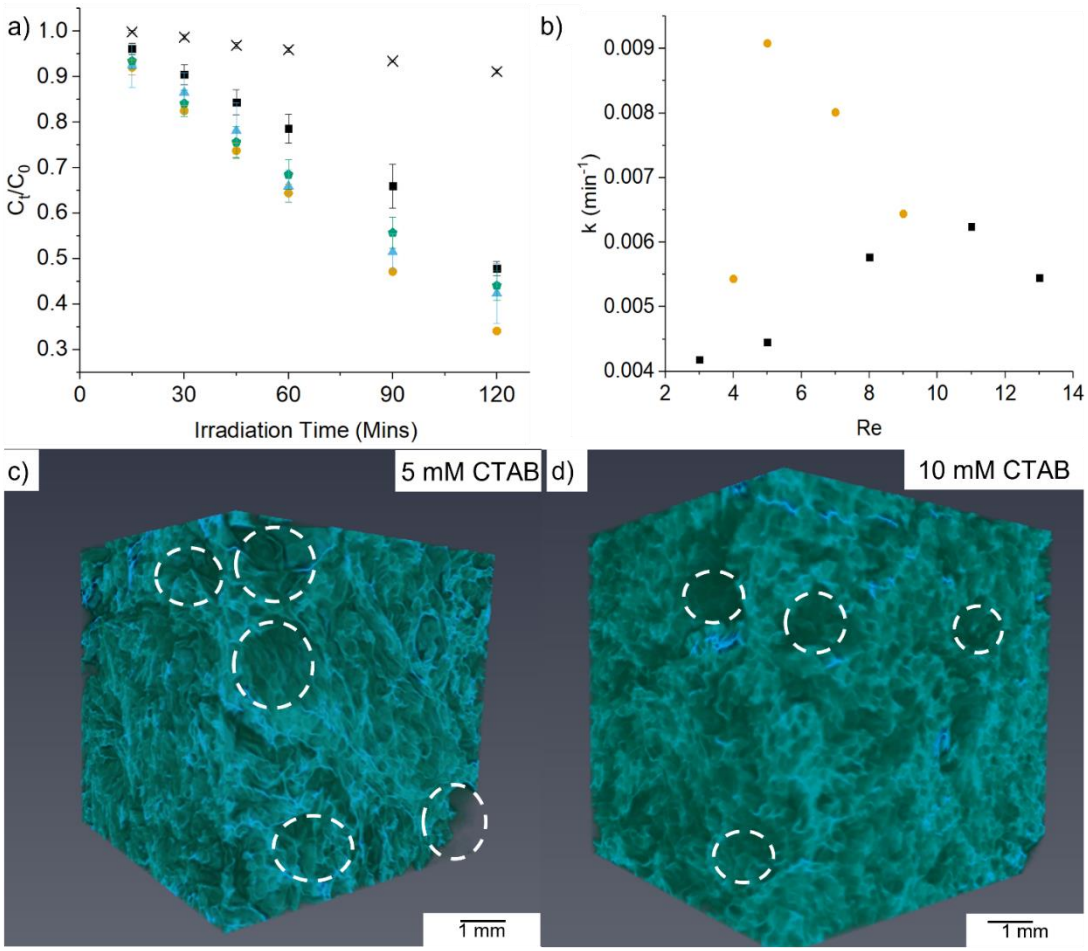

Figure 4.6 a) Photocatalytic degradation of CBZ using MolFoams synthesised using 10 mM CTAB within a recirculating reactor operated at various flow rates [X photolysis ■ 200 mL min^{-1}, ● 250 mL min^{-1}, ▲ 300 mL min^{-1}, ⬟ 400 mL min^{-1}] b) First order kinetic constant for MolFoams synthesised using ■ 5 mM, ● 10 mM CTAB as a function of flow rate (Reynolds Number) c,d) MicroCT 3D reconstructions of MolFoams synthesised using 5 or 10 mM CTAB solutions, respectively. Circled areas highlight the decrease in pore size as CTAB concentration increases.

Effect of flow rate on photocatalytic activity of 10 mM CTAB MolFoams.

As shown in Table S4.4, increasing the flow rate of the reactor leads to an increase in the quantum efficiency of the system. As such, the photocatalytic activity of the 10 mM CTAB synthesised MolFoams was evaluated within the recirculating reactor at flow rates between 200- and 400-mL min^{-1} (Figure 4.6a). The degradation increases as the flow rate is increased, with the highest removal of CBZ occurring at 250 mL min^{-1}. The 10 mM CTAB synthesised foams show faster kinetics than the 5 mM MolFoams operated at the same flow rate (Figure 4.6b). This is attributed to the improvements in activity promoted by the reduction in pore size and larger surface area-to-volume ratio within the pores that occurs with the use of higher CTAB concentrations. Of particular interest is the variation in the profiles in Figure 4.6b,

with the 10 mM CTAB MolFoams showing an optimum flow rate of 250 mL min^{-1} compared to 400 mL min^{-1} for the 5 mM MolFoams. The corresponding kinetics at the optimal flow rate of the 10 mM system are around 150% that of the 5 mM system. Furthermore, changes in the flow rate for the 10 mM MolFoams have a greater effect on the kinetics with the profile showing a much sharper peak for the 10 mM system, compared with the gradual increase and decrease of the kinetics seen in the 5 mM. This suggests that the increase in the flow rate within the 10 mM system and the reduction of the boundary layer thickness has a more pronounced impact on the kinetics. This behaviour can be effectively explained by the presence of more smaller pores, [62] as discussed earlier.

This analysis is further confirmed by hydrodynamic calculations for the reactor system, showing a Peclet number (ratio of convective to diffusional mass transfer) significantly greater than 1, and a more than doubling of the Sherwood number (ratio of convective mass transfer rate to the rate of diffusive mass transfer) from 4 to 9 as the flow rate of the system increases. Both confirm that the higher flow rates used lead to higher rates of convective mass transfer within the reactor,[31] overcoming mass transfer resistances (Table S4.5). The E_{EO} of the foam reactor system is reduced in all cases, when compared to equivalent flow rates using 5 mM CTAB foams (Table S4.4). As can be seen in Figure 4.7, operating the reactor using a 10 mM CTAB foam with the flow rate of 250 mL min^{-1} provides the best overall performance within the range studied in terms of kinetics, zinc concentration and E_{EO}. Furthermore, as tabulated in Table S4.5, the optimisation of both the MolFoams, through control of macropore size via CTAB concentration, and the reactor, through control of the flow rate, leads to an increase of the quantum efficiency from an initial value of 1.56 X 10^{-3} up to a maximum of 2.63 X 10^{-3}, showing a significant increase in photocatalytic efficiency. This, coupled with the electrical energy per order (E_{EO}) of the reactors decreasing by over 50 %, means the optimised foam/reactor system requires less than half the electrical energy relative to those initially tested, showing promise for scale up. Additionally, all zinc concentrations after photocatalytic degradations show levels in the ppb range, significantly lower than the WHO limits of 3.0 ppm. [30] The FE-SEM micrographs in Figure S4.7 show no appreciable change in the morphology at a

range of magnifications of the MolFoams after photocatalytic degradation corroborates this and further reinforces the chemical stability of the MolFoam structure. A comparison with other photocatalytic systems for the degradation of CBZ shows that the MolFoam outperform reported literature in terms of energy requirements, i.e. low E_{EO}, and photocatalytic efficiency, i.e. high quantum efficiency (Figure 4.8 and Table S4.8). This included TiO_2 and ZnO photocatalysts, batch nanoparticle slurries systems,[66,67,68] and supported catalysts in recirculating or flow systems.[40,50,67] In some instances, the catalysts showed higher kinetics but lower overall quantum efficiencies and higher electrical energy per order values, highlighting the advantages of the highly porous and interconnected structure of the MolFoams.

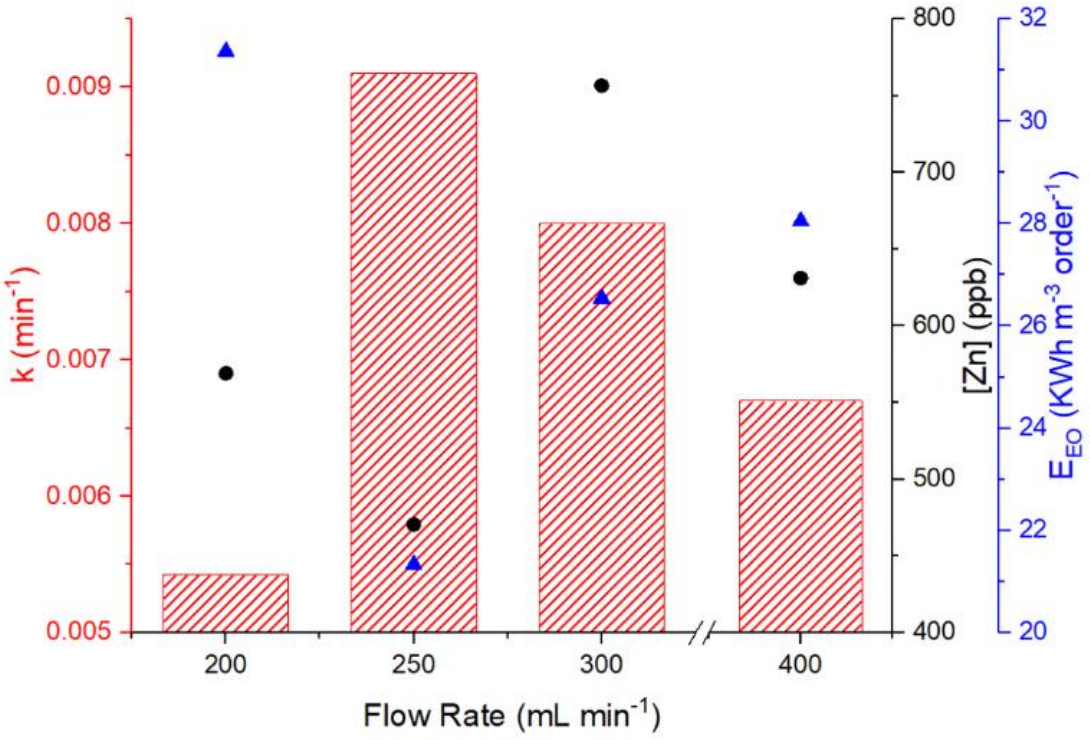

Figure 4.7: Comparison between ● zinc concentration post photocatalytic CBZ degredation after 120 mins, pseudo first order reaction kinetics (bar) and ◢ EEO of MolFoam reactors operating at various flow rates.

It is noted here that while there is a vast literature on the photocatalytic degradation of CBZ, direct comparisons are challenging due to lack of essential details on the quantum efficiency, e.g. light intensity,[69] or energy requirements, despite these being considered best practise for the field.[70] This is often due to a focus on kinetics, which favour nanoparticle slurries,[41,67] whereas quantum efficiency and energy

requirements are more useful when considering the potential practical use of photocatalysts. In this context, a treatment system that makes use of a MolFoam will be able to provide comparable or better photocatalytic activity and removal of pollutants, with greater photocatalytic efficiency and lower energy requirements, while removing the need for the downstream removal required for slurries.

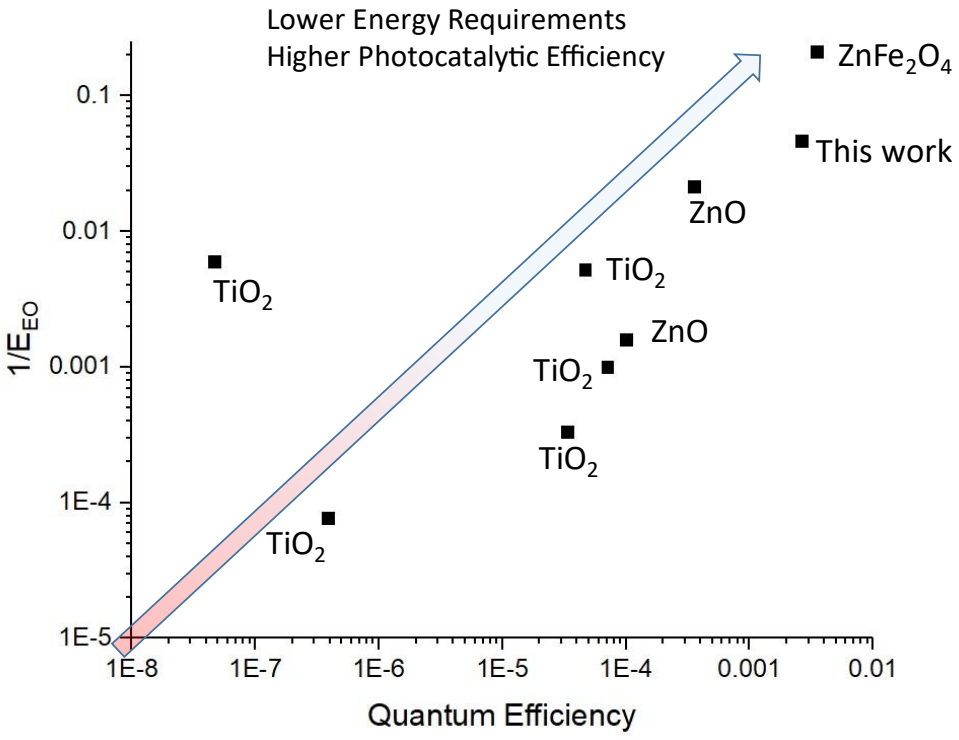

Figure 4.8: Plot mapping quantum efficiency and log of $1/E_{EO}$ of photocatalytic systems for the degradation of CBZ.

Conclusions

Porous ZnO monoliths, defined here as MolFoams, were synthesised through a novel process which results in a continuously interconnected structure with no discrete nano- or micro-particles, a major advancement compared to other foams used for photocatalysis. MolFoams were synthesised using a range of concentrations of CTAB leading to changes in the morphology and pore structure of the foams. While initial MolFoams using 5 mM CTAB lost integrity at the higher flow rates needed to overcome mass transfer resistance, those prepared using 10 mM CTAB showed the greatest degradation of carbamazepine at all flow rates. Changes in the morphology induced by the higher CTAB concentration, with a smaller average macropore size,

resulted in the highest degradation kinetics of 0.009 min^{-1} occurring at a lower flow rate of 250 mL min^{-1}, with high mechanical and chemical stability. Furthermore, when considering the energy requirements and the photocatalytic efficiency, via the electrical energy per order and quantum efficiency, respectively, the MolFoams outperformed both immobilised and slurry systems, in batch and in flow for a variety of photocatalysts. This can be attributed to the highly porous and interconnected structure of the MolFoams which enables high light penetration with short diffusion paths for the pollutant to reach the catalyst surface. All these characteristics show that the MolFoams have the potential to overcome the limits of current photocatalytic systems which have so far limited their practical use, providing a safe and viable method for the removal of organic micropollutants from wastewater.

CRediT authorship contribution statement

Zachary Warren: Conceptualisation, Investigation, Methodology, Validation, Visualisation, Writing – original draft. **Thais Tasso Guaraldo:** Conceptualisation, Writing – review & editing. **Jannis Wenk:** Conceptualisation, Supervision, Writing – review & editing. **Davide Mattia:** Conceptualisation, Funding acquisition, Project administration, Resources, Supervision, Writing – review & editing.

Conflicts of interest

There are no conflicts to declare

Acknowledgements

The authors would like to acknowledge the EPSRC for funding (EP/P031382/1). ZW acknowledges The University of Bath for funding his PhD. ZW would also like to acknowledge R. Castaing, P. Fletcher, D. Lednitzky and S. Reeksting of MC^2 University of Bath analytical facilities, G. Kociok-Köhn of Department of Chemistry and J.A. Milton of The National Oceanography Centre Southampton for support and assistance in collection of the data presented here. The authors also acknowledge D.F.Segura for artwork support.

Data supporting this work is freely accessible in the Bath research data archive system at https://doi.org/10.15125/BATH-01118

References

1. J. K. Fawell, *Water Sci Technol*, 2008, **57**, 183-187.
2. T. Reemtsma, S. Weiss, J. Mueller, M. Petrovic, S. Gonzalez, D. Barcelo, F. Ventura and T. P. Knepper, *Environ Sci Technol*, 2006, **40**, 5451-5458.
3. J. Virkutyte, R. S. Varma and V. Jegatheesan, *Treatment of Micropollutants in Water and Wastewater*, IWA Publishing, 2010.
4. A. Joss, S. Zabczynski, A. Göbel, B. Hoffmann, D. Löffler, C. S. McArdell, T. A. Ternes, A. Thomsen and H. Siegrist, *Water Research*, 2006, **40**, 1686-1696.
5. K. Fent, A. A. Weston and D. Caminada, *Aquat Toxicol*, 2006, **76**, 122-159.
6. Y. Deng and R. Zhao, *Current Pollution Reports*, 2015, **1**, 167-176.
7. Y. Luo, W. Guo, H. H. Ngo, L. D. Nghiem, F. I. Hai, J. Zhang, S. Liang and X. C. Wang, *Sci Total Environ*, 2014, **473-474**, 619-641.
8. U. von Gunten and J. Hoigné, *Environmental Science and Technology*, 1994, **28**, 1234-1242.
9. D. B. Miklos, C. Remy, M. Jekel, K. G. Linden, J. E. Drewes and U. Hubner, *Water Res*, 2018, **139**, 118-131.
10. G. V. Buxton, C. L. Greenstock, W. P. Helman and A. B. Ross, *Journal of Physical and Chemical Reference Data*, 1988, **17**, 513-886.
11. C. Martínez, M. Canle L, M. I. Fernández, J. A. Santaballa and J. Faria, *Applied Catalysis B: Environmental*, 2011, **102**, 563-571.
12. H. d. Lasa, *Photocatalytic Reaction Engineering*, Springer US : Imprint: Springer, Boston, MA, 2005.
13. C. Yu, W. Zhou, H. Liu, Y. Liu and D. D. Dionysiou, *Chemical Engineering Journal*, 2016, **287**, 117-129.
14. A. Manassero, M. L. Satuf and O. M. Alfano, *Chemical Engineering Journal*, 2017, **326**, 29-36.
15. P. Fernández-Ibáñez, S. Malato and F. J. de las Nieves, *Catalysis Today*, 1999, **54**, 195-204.
16. B. Nowack and T. D. Bucheli, *Environ Pollut*, 2007, **150**, 5-22.

17. M. F. J. Dijkstra, A. Michorius, H. Buwalda, H. J. Panneman, J. G. M. Winkelman and A. A. C. M. Beenackers, *Catalysis Today*, 2001, **66**, 487-494.
18. M. Bideau, B. Claudel, C. Dubien, L. Faure and H. Kazouan, *Journal of Photochemistry and Photobiology, A: Chemistry*, 1995, **91**, 137-144.
19. I. J. Ochuma, O. O. Osibo, R. P. Fishwick, S. Pollington, A. Wagland, J. Wood and J. M. Winterbottom, *Catalysis Today*, 2007, **128**, 100-107.
20. Y. F. Zhu, L. Zhou and Q. S. Jiang, *Ceramics International*, 2020, **46**, 1158-1163.
21. N. A. Kouamé, D. Robert, V. Keller, N. Keller, C. Pham and P. Nguyen, *Catalysis Today*, 2011, **161**, 3-7.
22. N. A. Kouame, D. Robert, V. Keller, N. Keller, C. Pham and P. Nguyen, *Environ Sci Pollut Res Int*, 2012, **19**, 3727-3734.
23. C. B. Ong, L. Y. Ng and A. W. Mohammad, *Renewable and Sustainable Energy Reviews*, 2018, **81**, 536-551.
24. T. Tasso Guaraldo, J. Wenk and D. Mattia, *Advanced Sustainable Systems*, 2021, **5**.
25. D. Maučec, A. Šuligoj, A. Ristić, G. Dražić, A. Pintar and N. N. Tušar, *Catalysis Today*, 2018, **310**, 32-41.
26. J. S. Chang, J. Strunk, M. N. Chong, P. E. Poh and J. D. Ocon, *Journal of Hazardous Materials*, 2020, **381**, 120958-120958.
27. R. Qiu, D. Zhang, Y. Mo, L. Song, E. Brewer, X. Huang and Y. Xiong, *Journal of Hazardous Materials*, 2008, **156**, 80-85.
28. N. M. Gupta, *Renewable and Sustainable Energy Reviews*, 2017, **71**, 585-601.
29. K. M. Lee, C. W. Lai, K. S. Ngai and J. C. Juan, *Water Res*, 2016, **88**, 428-448.
30. W. a. UNICEF, WHOUNICEF-Joint-Monitoring-Program-for-Water-Supply-Sanitation-and-Hygiene-JMP, https://www.unwater.org/publications/whounicef-joint-monitoring-program-water-supply-sanitation-hygiene-jmp-2017-update-sdg-baselines/).
31. C. M. Taylor, A. Ramirez-Canon, J. Wenk and D. Mattia, *J Hazard Mater*, 2019, **378**, 120799.
32. X. Lu, K. Kanamori and K. Nakanishi, *New Journal of Chemistry*, 2019, **43**, 11720-11726.

33. O. Durupthy, M. Jaber, N. Steunou, J. Maquet, G. T. Chandrappa and J. Livage, *Chemistry of Materials*, 2005, **17**, 6395-6402.

34. K. G. Kanade, B. B. Kale, R. C. Aiyer and B. K. Das, *Materials Research Bulletin*, 2006, **41**, 590-600.

35. S. Thota, T. Dutta and J. Kumar, *Journal of Physics Condensed Matter*, 2006, **18**, 2473-2486.

36. Y. Liao, R. Wang, M. Tian, C. Qiu and A. G. Fane, *Journal of Membrane Science*, 2013, **425-426**, 30-39.

37. D. Hao, Z. Yang, C. Jiang and J. Zhang, *Applied Catalysis B: Environmental*, 2014, **144**, 196-202.

38. F. Ali, J. A. Khan, N. S. Shah, M. Sayed and H. M. Khan, *Process Safety and Environmental Protection*, 2018, **117**, 307-314.

39. J. Zhai, Q. Wang, Q. Li, B. Shang, M. H. Rahaman, J. Liang, J. Ji and W. Liu, *Sci Total Environ*, 2018, **640-641**, 981-988.

40. V. Rogé, C. Guignard, G. Lamblin, F. Laporte, I. Fechete, F. Garin, A. Dinia and D. Lenoble, *Catalysis Today*, 2018, **306**, 215-222.

41. S. Teixeira, R. Gurke, H. Eckert, K. Kühn, J. Fauler and G. Cuniberti, *Journal of Environmental Chemical Engineering*, 2016, **4**, 287-292.

42. N. Serpone and A. Salinaro, *Pure and Applied Chemistry*, 1999, **71**, 303-320.

43. J. R. Bolton, K. G. Bircher, W. Tumas and C. A. Tolman, *Pure and Applied Chemistry*, 2001, **73**, 627-637.

44. R. Boppella, K. Anjaneyulu, P. Basak and S. V. Manorama, *The Journal of Physical Chemistry C*, 2013, **117**, 4597-4605.

45. B. Chen, X. Wang, S. Zhang, C. Wei and L. Zhang, *Journal of Porous Materials*, 2014, **21**, 1035-1039.

46. A. Benad, F. Jürries, B. Vetter, B. Klemmed, R. Hübner, C. Leyens and A. Eychmüller, *Chemistry of Materials*, 2017, **30**, 145-152.

47. W. Li, M. Zhang, J. Zhang and Y. Han, *Frontiers of Chemistry in China*, 2006, **1**, 438-442.

48. H. S. Fogler, *Elements of chemical reaction engineering*, Upper Saddle River, N.J., Upper Saddle River, N.J., 3rd ed. edn., 1999.

49. Y. He, N. B. Sutton, H. H. H. Rijnaarts and A. A. M. Langenhoff, *Applied Catalysis B: Environmental*, 2016, **182**, 132-141.
50. I. Horovitz, D. Avisar, M. A. Baker, R. Grilli, L. Lozzi, D. Di Camillo and H. Mamane, *J Hazard Mater*, 2016, **310**, 98-107.
51. H. Mohan, V. Ramalingam, A. Adithan, K. Natesan, K. K. Seralathan and T. Shin, *J Hazard Mater*, 2021, **416**, 126209.
52. Q. Sun, Z. Li, J. Wang, S. Li, B. Li, L. Jiang, H. Wang, Q. Lü, C. Zhang and W. Liu, *Colloids and Surfaces A: Physicochemical and Engineering Aspects*, 2015, **471**, 54-64.
53. M. Zhao, R. Wang, C. Dai, X. Wu, Y. Wu, Y. Dai and Y. Wu, *Chemical Engineering Science*, 2019, **206**, 203-211.
54. A. Ramirez-Canon, M. Medina-Llamas, M. Vezzoli and D. Mattia, *Phys Chem Chem Phys*, 2018, **20**, 6648-6656.
55. G. Liu, J. C. Yu, G. Q. Lu and H. M. Cheng, *Chem Commun (Camb)*, 2011, **47**, 6763-6783.
56. H. J. Yun, H. Lee, J. B. Joo, W. Kim and J. Yi, *The Journal of Physical Chemistry C*, 2009, **113**, 3050-3055.
57. A. Leelavathi, G. Madras and N. Ravishankar, *Phys Chem Chem Phys*, 2013, **15**, 10795-10802.
58. M. S. Bakshi, *Crystal Growth & Design*, 2015, **16**, 1104-1133.
59. A. McLaren, T. Valdes-Solis, G. Li and S. C. Tsang, *J Am Chem Soc*, 2009, **131**, 12540-12541.
60. Y.-H. Ni, X.-W. Wei, X. Ma and J.-M. Hong, *Journal of Crystal Growth*, 2005, **283**, 48-56.
61. Y.-X. Wang, J. Sun, X. Fan and X. Yu, *Ceramics International*, 2011, **37**, 3431-3436.
62. R. Chen, W. Jia, D. Lao, S. Li and D. Hei, *Journal of Alloys and Compounds*, 2019, **806**, 596-602.
63. S. Josset, S. Hajiesmaili, D. Begin, D. Edouard, C. Pham-Huu, M. C. Lett, N. Keller and V. Keller, *J Hazard Mater*, 2010, **175**, 372-381.
64. G. Plesch, M. Gorbár, U. F. Vogt, K. Jesenák and M. Vargová, *Materials Letters*, 2009, **63**, 461-463.

65. G. Plesch, M. Vargová, U. F. Vogt, M. Gorbár and K. Jesenák, *Materials Research Bulletin*, 2012, **47**, 1680-1686.

66. N. P. F. Gonçalves, M. A. O. Lourenço, S. R. Baleuri, S. Bianco, P. Jagdale and P. Calza, *Journal of Environmental Chemical Engineering*, 2022, **10**.

67. L. Paredes, S. Murgolo, H. Dzinun, M. H. Dzarfan Othman, A. F. Ismail, M. Carballa and G. Mascolo, *Applied Catalysis B: Environmental*, 2019, **240**, 9-18.

68. A. Surenjan, B. Sambandam, T. Pradeep and L. Philip, *Journal of Environmental Chemical Engineering*, 2017, **5**, 757-767.

69. S. W. da Silva, J. P. Bortolozzi, E. D. Banús, A. M. Bernardes and M. A. Ulla, *Chemical Engineering Journal*, 2016, **283**, 1264-1272.

70. J. M. Buriak, P. V. Kamat and K. S. Schanze, *ACS Appl Mater Interfaces*, 2014, **6**, 11815-11816.

Supplementary Information for

Synthesis of Photocatalytic Pore Size-Tuned ZnO Molecular Foams

Zachary Warren,[a] Thais Tasso Guaraldo, [a] Jannis Wenk [a] and Davide Mattia*[a]

4.2. Supplementary Information

Table S4.1: Table of conditions investigated in research for MolFoam production

Parameter	Initial condition	Preliminary findings	Final condition
Zinc source.	$Zn(Ac)_2$ used as Zn salt.	Issues of solubility and basicity lead to structurally weak foams.	Zn $(AcAc)_2$ selected as alternative Zn salt.
Use of surfactant	No surfactant used.	Foams shorter than reported here, very little porosity seen in MicroCT.	CTAB 5mM added to solution.
Flow rate of air	0.5 sL min^{-1}	Higher flow rates of air (0.5-, 0.25- sL min^{-1}) lead to faster evaporation of EtOH causing poor gelling and fragile foams.	0.1 sL min^{-1}
Calcination step	Foams calcined at 500 ^oC for 3 hours prior to sintering.	Calcining to remove organics unnecessary due to sintering and additional heating/cooling cycle leads to weaker foams	Calcination step removed, 12 hours sintering step only.
Sintering time	12, 15, 18, 20 hours sintering	Batch degradation experiments showed 20 hours sintering at 900 ^oC lead to greatest photocatalytic activity	900 ^oC ,20-hour sintering step
Sintering profile	Single step sintering process	Foams unsuitable for use within recirculating reactor.	Two step sintering condition adopted 1,000 ^oC ,0.5-hour + 900 ^oC ,20-hour
Sintering parameters	Two step sintering condition 1,000 ^oC ,0.5-hour + 900 ^oC ,20-hour	Multiple conditions (1,000 ^oC ,1 -hour + 900 ^oC ,20-hour / 950 ^oC ,0.5 - hour + 900 ^oC ,20-hour/ 950 ^oC ,1.0 - hour + 900 ^oC ,20-hour) analysed using degredation experiments, No significant change in degradation results, but original sintering conditions resulted in larger, more mechanically stable foams.	Two step sintering condition adopted 1,000 ^oC ,0.5-hour + 900 ^oC ,20-hour

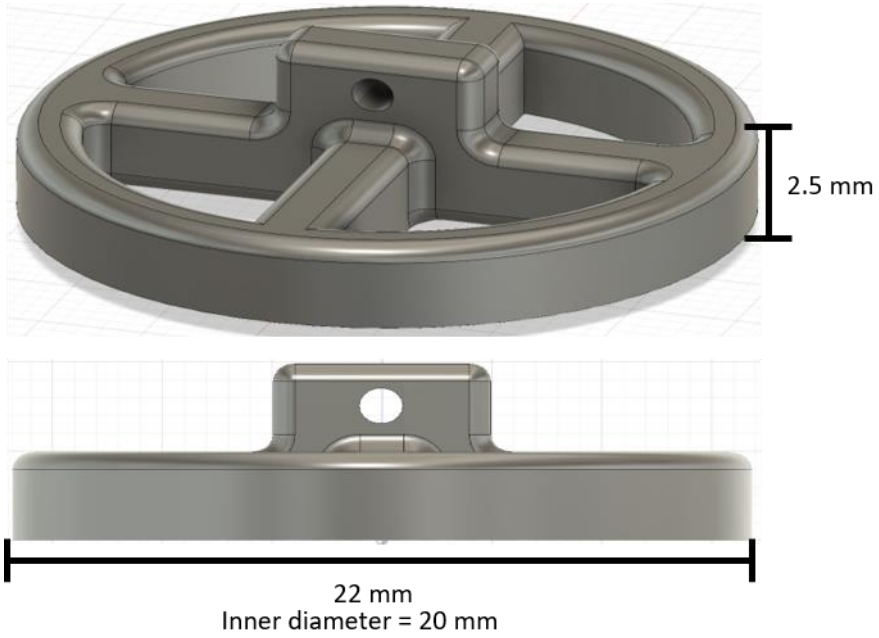

Figure S4.1: 3D model of printed buffer included inside reactor cartridges.

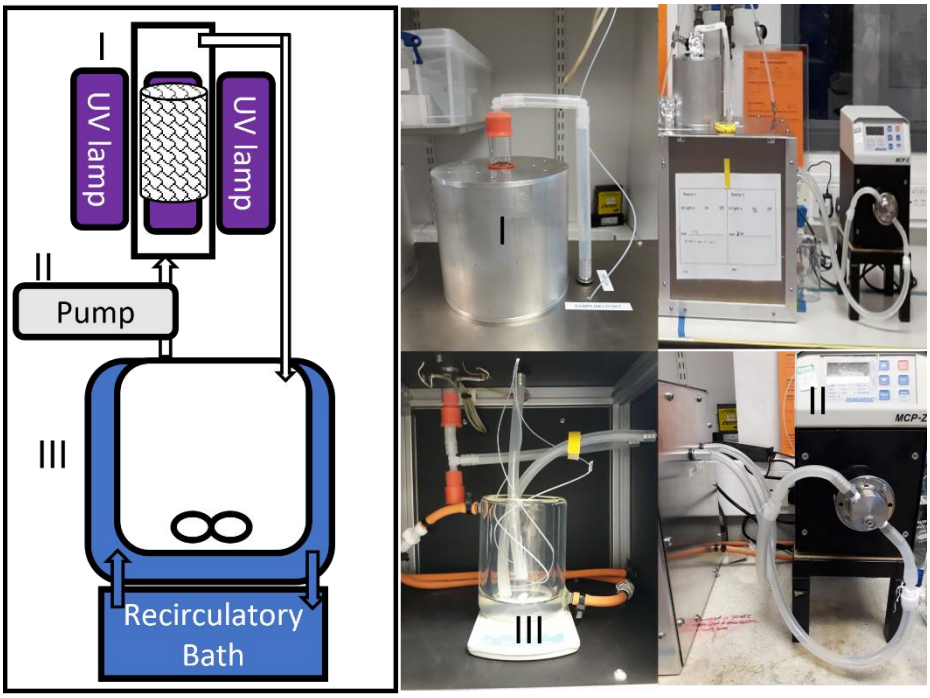

Figure S4.2: Schematic diagrams for recirculating photocatalytic reactors. Labelled are I) quartz tube containing foam surrounded by UV lamps, II) gear pump Ismatec, MCP-Z with a pump head Model GBS.P23.JVS.A-B1 and III) reservoir 500 mL)

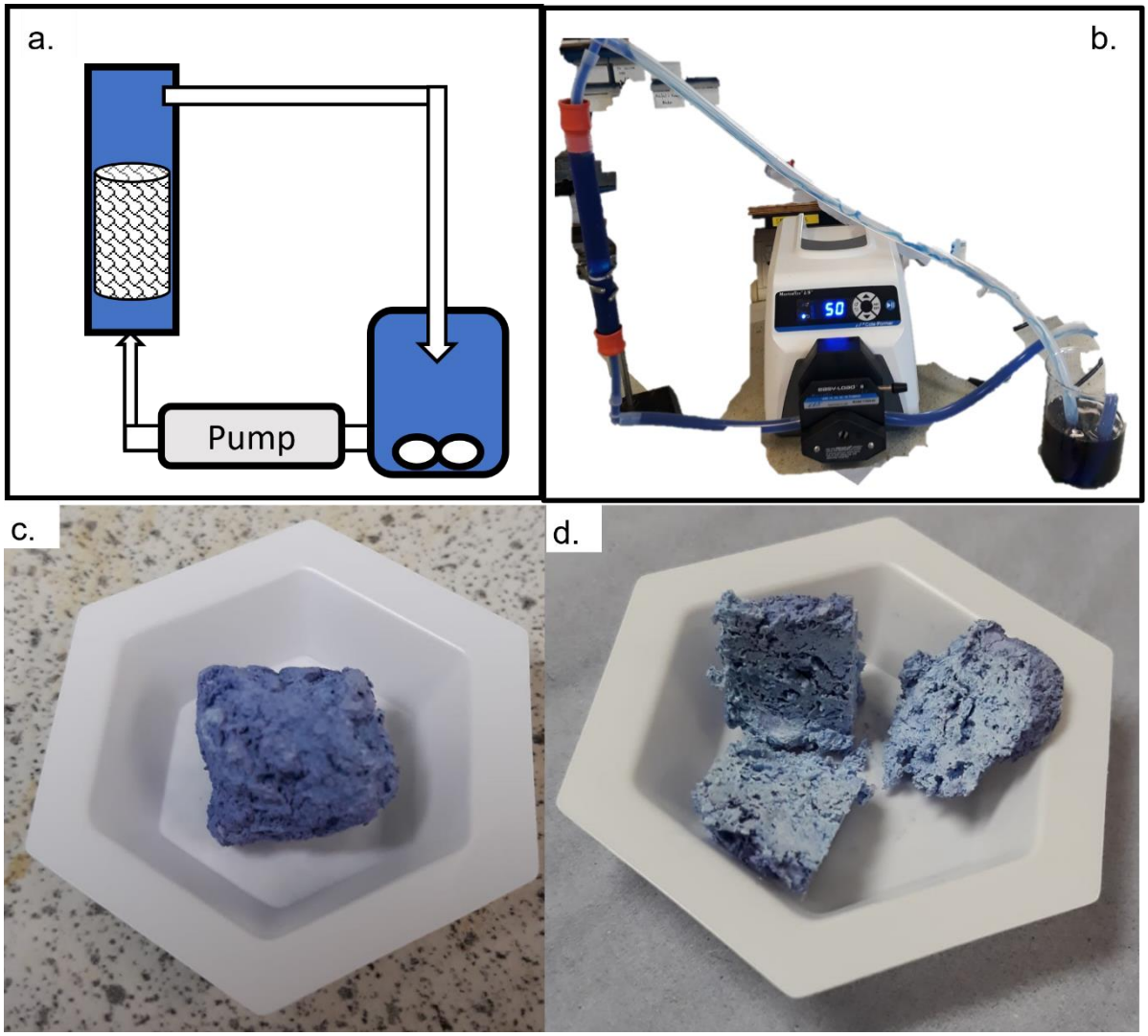

Figure S4.3: a) schematic diagram of bespoke dyeing rig to test dye uptake into MolFoam pores. b) photograph of dyeing rig in operation. c, d) A dyed MolFoam before and after being cut open.

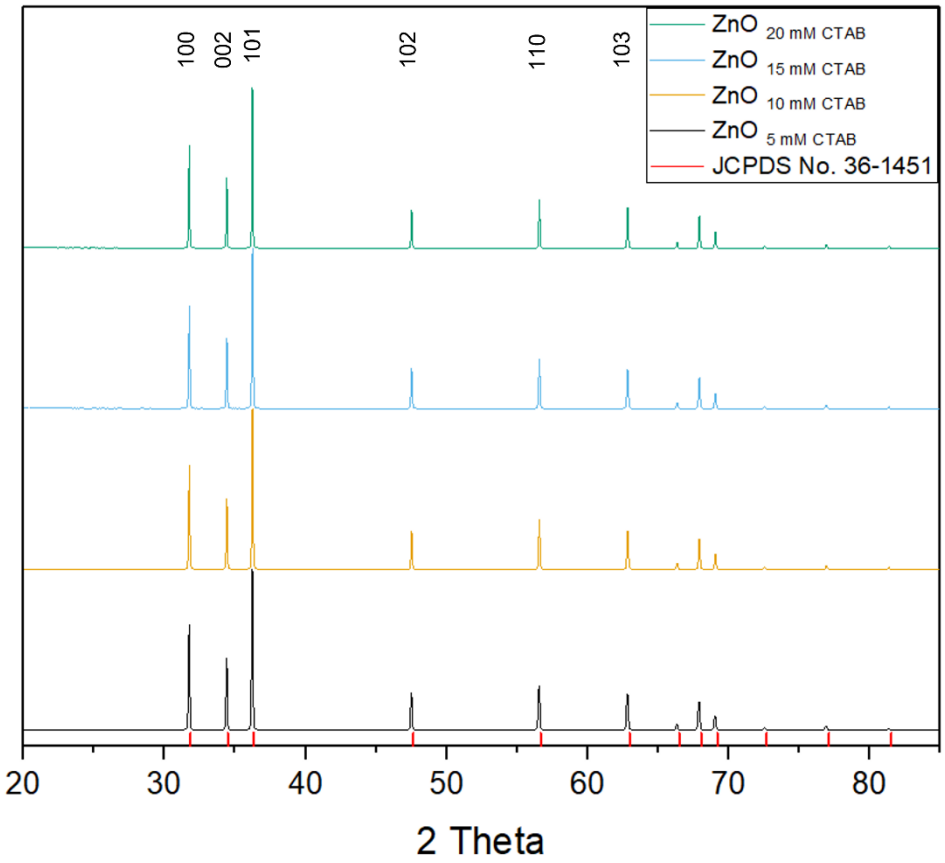

Figure S4.4: XRD pattern of ZnO MolFoams synthesised using different CTAB concentrations. Tick marks correspond to peaks reported from JCPDS No. 36-1451 [1]

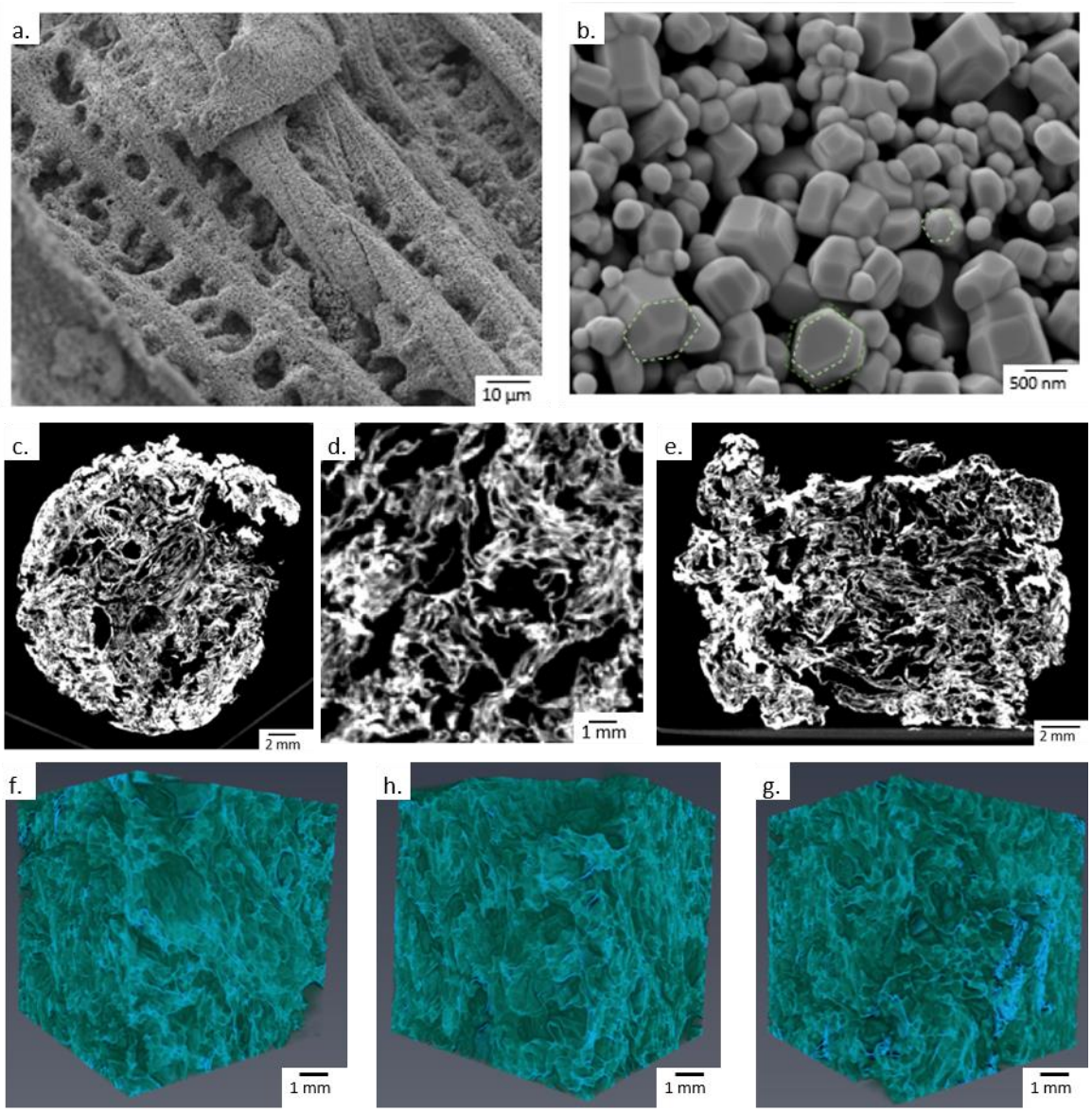

Figure S4.5 Various characterisations of ZnO MolFoams synthesised using 5 mM CTAB solutions a,b) FESEM c-e) MicroCT slices and f-g) 3D reconstructions based on MicroCT.

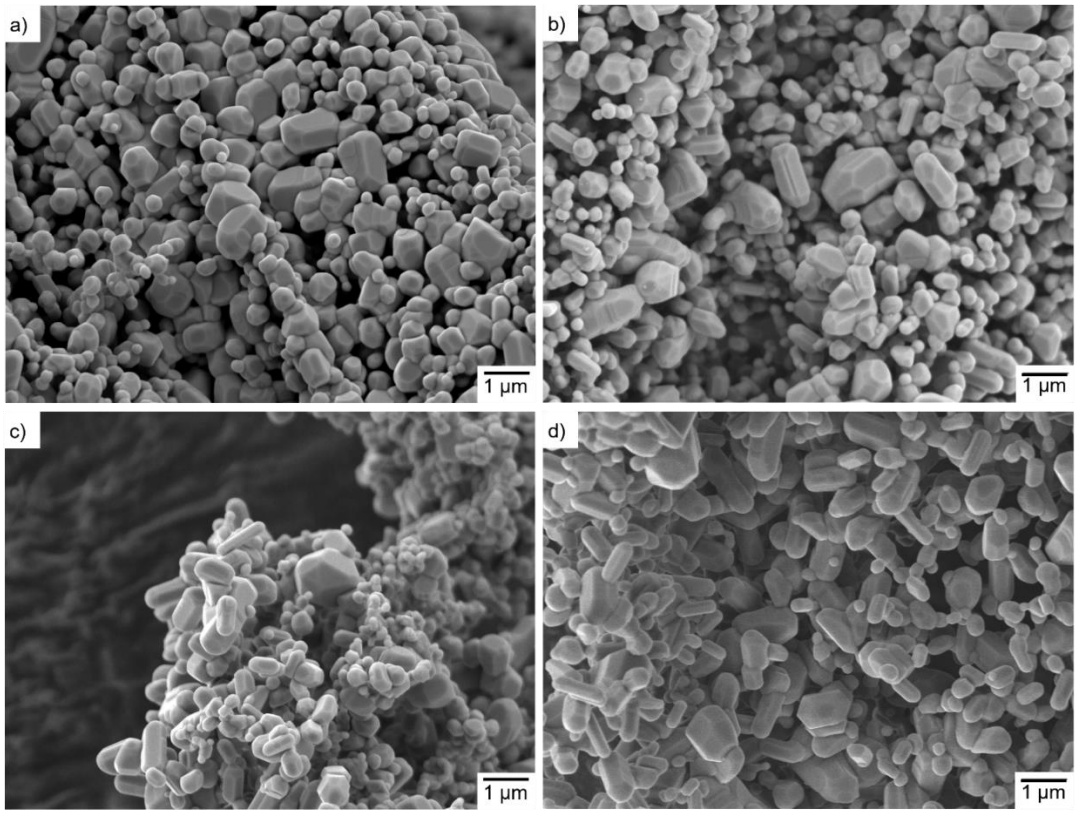

Figure S4.6: FE-SEM micrographs of ZnO MolFoams synthesised using a) 5mM, b) 10 mM, c) 15 mM and d) 20 mM CTAB solutions.

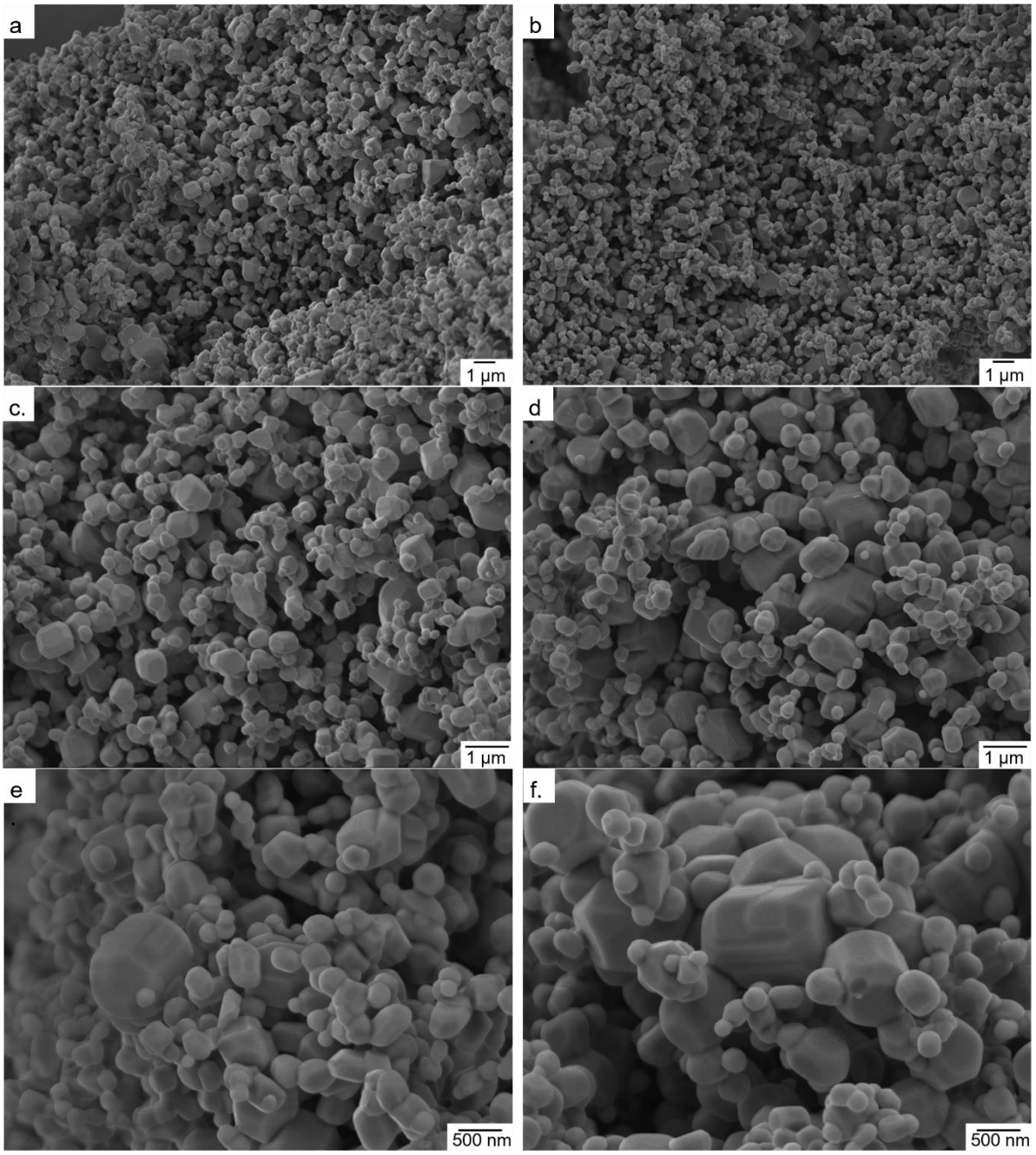

Figure S4.7: FE-SEM micrographs of ZnO MolFoams(a, c,e) before and (b,d,f) after application within reactor for photocatalytic CBZ degradation

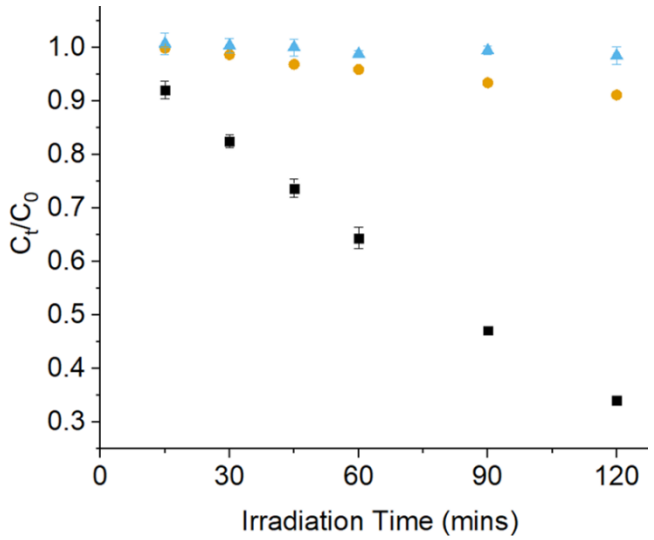

Figure S4.8: Removal of CBZ using MolFoams synthesised using 10 mM CTAB within a recirculating reactor operated at flow rate of 250 mL min^{-1} [■ Photocatalysis , ● Photolysis , ▲ Adsorption.

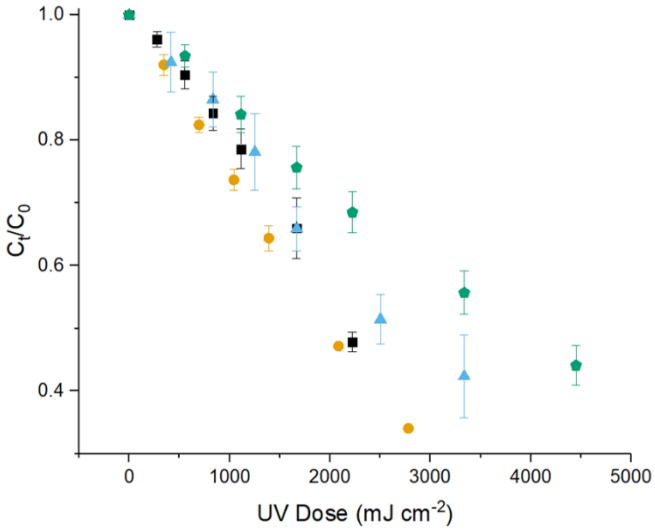

Figure S4.9: Photocatalytic degradation of CBZ using MolFoams synthesised using 10 mM CTAB within a recirculating reactor operated at various flow rates [■ 200 mL min^{-1} , ● 250 mL min^{-1} , ▲ 300 mL min^{-1} , ⬟ 400 mL min^{-1}]

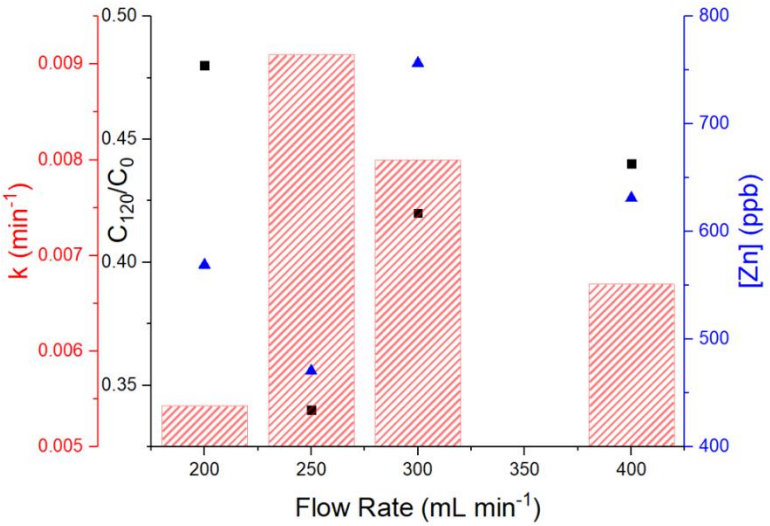

Figure S4.10: Comparison between n photocatalytic CBZ degredation after 120 mins, pseudo first order reaction kinetics (bar) and ◢ zinc concentration post PCA of MolFoam reactors operating at various flow rates.

Text S1. UV dose and quantum efficiency calculations

Within a recirculating reactor, the entire solution volume is not irradiated at any one time as with a batch reactor. The UV dose was calculated in equation 1 and the light attenuation calculated as shown in equation S4.1.[2]

$$UV\ Dose\ [\,mJ\ cm^{-2}] = \ Irradiation\ time\ [s] * I_{0\lambda} * (\tau * \frac{V_r}{V_0})\ [mW\ cm^{-2}]$$

$$I_{\alpha\lambda} = \ I_{0\lambda}(1 - 10^{((\epsilon H_2O*[H_2O]+\epsilon CBZ*[CBZ])L)}$$

Equation S4.1: UV dose calculations

Where $I_{0\lambda}$ is the incident light emitted by the UV lamps (mW cm^{-2}), τ is total residence time within the foam (s), V_r is the volume receiving UV dose within the foam per second (mL s^{-1}) and V_0 is the total volume of the reservoir (mL).

The measured light intensity was 10.4 mW cm^{-2}, τ was 4.5 seconds, V_r was dependent of flow rate and tabulated below, and V_0 was 500 mL. These conditions are exclusive to wavelengths of 254 nm only.

Table S4.2: Tabulation of V_r for corresponding flow rates.

Flowrate (mL min^{-1})	Volume of liquid exposed to UV within the foam per second (mL s^{-1})
100	1.67
200	3.33
300	5.00
400	6.67
500	8.33

Table S4.3: Tabulation of UV dose for recirculating reactors at various flow rates.

Time (s)	**UV Dose (100 mL min^{-1}) (mJ cm^{-2})**	**UV Dose (200 mL min^{-1}) (mJ cm^{-2})**	**UV Dose (250 mL min^{-1}) (mJ cm^{-2})**	**UV Dose (300 mL min^{-1}) (mJ cm^{-2})**	**UV Dose (400 mL min^{-1}) (mJ cm^{-2})**	**UV Dose (500 mL min^{-1}) (mJ cm^{-2})**
0	0	0	0	0	0	0
900	139	278	348	417	556	695
1800	278	556	695	834	1112	1391
2700	417	834	1043	1251	1669	2086
3600	556	1112	1391	1669	2225	2781
5400	834	1669	2086	2503	3337	4172
7200	1112	2225	2781	3337	4450	5562

The quantum efficiency allows for an assessment of the photon efficiency, assessing the number of pollutant molecules undergoing degradation relative to the number of photons reaching the catalyst surface. Based on the definitions contained in the IUPAC glossary, the following equations are proposed to calculate the quantum efficiency of photocatalytic foams:

$$k' = (k)(C_0)(V_{Illuminated}) \ (mol\ s^{-1})$$

$$N_P = \frac{I_{0\lambda} * S * t}{E_P} (-)$$

$$q_{n,p} = \left(\frac{N_P}{t}\right)\frac{1}{N_A} \ (mol\ s^{-1})$$

$$QE = \frac{k'}{q_{n,p}} \ (-)$$

Equation S4.2: Quantum efficiency calculations

where, k' is the rate of pollutant degradation (mol s^{-1}), k is the kinetic constant (s^{-1}), C_o is the initial pollutant concentration (mol L^{-1}), $V_{Illuminated}$ is the total volume of pollutant irradiated.

The number of photons can be calculated using Equation 4.2, where $I_{0\lambda}$ is the incident irradiance of the light source (W m^{-2}), S is the surface of the sample onto which the light impinges (m^2) and t is the time under irradiation.

$E_p = \frac{h*c}{\lambda} (J)$ is the photon energy at the wavelength emitted by the lamps, where h is Planck's constant, c is the speed of light and λ is the wavelength of light (m) from the lamps. The photon flux is the numbers of photons during irradiation of a mol of photons, where N_A is Avogadro's number (equation 4.2) . Finally, the quantum efficiency (QE) is calculated using equation 4.2.

Text S2. Photocatalytic reactor energy consumption calculations.

To assess the viability of scaling up of the system, the energy consumption of the reactor was accounted for by using the electrical energy per order (E_{EO}), defined as the kilowatt hours of electrical energy needed to decrease the concentration of a pollutant by an order of magnitude (90%) in one cubic metre of solution. [4]

$$E_{EO} = \frac{P * t * I * 1{,}000}{V(log^{C_0}/_{C_t})}$$

Equation S4.3 E_{EO}

Where: P is the power used to operate the lamps (kW), t is the irradiation time (hrs) , I is the irradiation factor (Length of catalyst irradiated/Length of tube irradiated) in cm cm^{-1} ,V is the volume of reservoir (L) and C_0 and C_t are the initial and final concentrations of pollutants respectively.

For the recirculating MolFoam reactors, three 5 W lamps were used, giving a P value of 15 X 10^{-3} kW, irradiation time was 120 minutes, volume of solution was 0.5 L, I is the irradiation factor, the ratio between the lengths of catalyst and the tube that are exposed to UV irradiation to better represent the recirculating nature of the reactor when compared to a batch reactor, wherein the entire reservoir would be irradiated.

Table S4.4: Degradation, pseudo-first order kinetics, quantum efficiency and E_{EO} data for MolFoams synthesised using 5 mM CTAB

Flow Rate (mL min^{-1})	C_{120}/C_0	k (X10^{-3}) (min^{-1})	QE	E_{EO} (KWh m^{-3})
100	0.64	4.18	1.21 X 10^{-3}	49.84
200	0.54	4.45	1.30 X 10^{-3}	39.71
300	0.54	5.77	1.67 X 10^{-3}	37.37
400	0.43	6.24	1.79 X 10^{-3}	27.28

Table S4.5: Degradation, pseudo-first order kinetics, quantum efficiency, zinc concentration and E_{EO} data for MolFoams synthesised using 10 mM CTAB

Flow Rate /mL min^{-1}	C_{120}/C_0	k (x10^{-3}) /min^{-1}	QE	[Zn] [ppb]	E_{EO} /KWh m^{-3} $order^{-1}$
200	0.48 ± 0.02	5.43 ± 0.36	1.56 X 10^{-3}	569	31.37 ± 1.85
250	0.34 ± 0.01	9.08 ± 0.44	2.63 X 10^{-3}	471	21.34 ± 0.59
300	0.42 ± 0.06	8.01 ± 0.41	2.31 X 10^{-3}	757	26.54 ± 4.83
400	0.44 ± 0.03	6.74 ± 0.12	1.93 X 10^{-3}	631	28.05 ± 2.45

Text S3. Hydrodynamics calculations.

Table S4.6: Hydrodynamic data and calculations for 5 mM CTAB foams

flow rate	flow rate	flow velocity	Re_{Dh}	Pe	Sc	Sh
(mL min^{-1})	(m^3 s^{-1})	(m s^{-1})				
100	1.67×10^{-6}	4.39×10^{-3}	3	4913		5
200	3.33×10^{-6}	8.77×10^{-3}	5	9826		7
250	4.17×10^{-6}	1.10×10^{-2}	7	12283	1.75×10^{3}	8
300	5.00×10^{-6}	1.32×10^{-2}	8	14739		9
400	6.67×10^{-6}	1.75×10^{-2}	11	19652		11
500	8.33×10^{-6}	2.19×10^{-2}	15	24565		12

Table S4.7: Hydrodynamic data and calculations for 10 mM CTAB foams

flow rate	flow rate	flow velocity	Re_{Dh}	Pe	Sc	Sh
(mL min^{-1})	(m^3 s^{-1})	(m s^{-1})				
100	1.67×10^{-6}	4.39×10^{-3}	2	4036		4
200	3.33×10^{-6}	8.77×10^{-3}	4	8071		6
250	4.17×10^{-6}	1.10×10^{-2}	5	10089		7
300	5.00×10^{-6}	1.32×10^{-2}	7	12107	1.75×10^{3}	7
400	6.67×10^{-6}	1.75×10^{-2}	9	16143		9
500	8.33×10^{-6}	2.19×10^{-2}	12	20179		10

$$Re_D = \frac{\rho Q D_p}{\mu A \varepsilon}$$

$$Pe = \frac{u D_p}{D}$$

$$Sc = \frac{\mu}{\rho D}$$

$$Sh = 1.029 * Sc^{0.33} * Re_{D_h}^{0.55} * \left(\frac{L}{D_p}\right)^{-0.472}$$

Equation S4.4 Hydrodynamic Calculations

Where Q is the volumetric flow rate of the fluid, D_p is the macropore size of the foams, μ is the dynamic viscosity of the fluid, A is the cross-sectional area of the foam, ε is the porosity of the foam, u is the mean velocity of the fluid, D is the diffusion coefficient of Carbamazepine, [5, 6] ρ is the density of the fluid and L is the length of the foam. Re, Pe, Sc and Sh are the dimensionless numbers, Reynolds, Peclet, Schmidt and Sherwood.

Reynolds number for the foam system (Eq 8) was calculated as reported by Mohsen Karimian et al. [7]

Text S4. Comparison with literature.

Table S4.8: CBZ photocatalytic degradation kinetics for slurries and immobilised systems reported from literature.

Material	Photocatalyst	Degradation conditions	$[CBZ]_0$	Kinetics	Eeo	QE	Ref
ZnO	0.1 g L^{-1} NP suspension	Batch reactor 100 mL volume Temperature: 25 °C Xenon Lamp, (5 KW, 5.5 W cm^{-2}, 6000 K, 483 nm)	50 mg L^{-1}	3.7 X 10^{-3}	46.48	3.55 X 10^{-4}	[8]
$ZnFe_2O_4$				36.7 X 10^{-3}	4.69	3.52 X 10^{-3}	
TiO_2	1.0 g L^{-1} NP suspension	Batch reactor 60 mL volume LED lamp (λ_{max} 417 nm, 450 W cm^{-2})	0.75 mg L^{-1}	4.7 X 10^{-3}			[9]
$g\text{-}C_3N_4$				566.8 X 10^{-3}			
$g\text{-}C_3N_4/TiO_2$ composites	1.0 g L^{-1} NP suspension	Batch reactor 100 mL volume LED lamp (50 W, 475 nm)	10.0 mg L^{-1}	5.5 X 10^{-3}	187.09		[10]
N-doped TiO_2-SiO_2-Fe_3O_4	1.0 g L^{-1} NP suspension	Batch reactor 250 mL reactor Compact fluorescent lamp (9 W, 320 µW cm^{-2}, 365 nm)	2.0 mg L^{-1}	2.2 X 10^{-3}	188.24		[11]
TiO_2	57 mg L^{-1} NP supported on PVDF dual layer hollow fibre membrane	Recirculating reactor, flow rate 100 mL min^{-1}, 500 mL volume Hg lamp (40 W, 45.0 W cm^{-2}, 254 nm)	0.4 mg L^{-1}	22.1 X 10^{-3}	153.00		[12]
TiO_2	P25 commercial NPs dispersed in MeOH before electrospray onto steel mesh (2.5-X 5.0 cm)	Batch reactor 50 mL volume Six 4-W blacklight blue lamps (4 W, Sankyo Denki F10T8, Japan) 365 nm	2.4 mg L^{-1}	32.2 X 10^{-3}	395.48		[13]
TiO_2	TiO_2 films obtained through plasma electrolytic oxidation of Ti meshes (geometric area 327.5 cm^2)	Batch reactor 1,000 mL volume Lamp (30 W low-pressure Hg vapor UV-C, 254 nm.)	0.1 mg L^{-1}	17.9 X 10^{-3}	37.01		[14]
TiO_2	0.5 g L^{-1} NP suspension (P25)	Recirculating reactor, flow rate 83.3 mL min^{-1}, 1,000 mL volume A blacklight-blue lamp (HQPower Lamp15TBL, nominal power 15 W, 365 nm)	5.0 mg L^{-1}	23.4 X 10^{-3}	4.05		[15]
TiO_2	TiO_2 drop coated onto $\alpha\text{-}Al_2O_3$ microfiltration membranes	Flow photocatalytic membrane reactor Volume 200 mL Xenon lamp(300 W, 76.7 mW cm^{-2})	1.0 mg L^{-1}	4.0 X 10^{-3}	2994.01	3.32 X 10^{-5}	[16]
$N\text{-}TiO_2$				8.5 X 10^{-3}	1000.00	7.06 X 10^{-5}	
TiO_2	1.0 g L^{-1} NP suspension	Batch reactor 50 mL volume Hg Lamps (6 X 8 W, 1.6mW cm^{-2}, 365 nm)	12.0 mg L^{-1}	15.4 X 10^{-3}	191.01	4.66 X 10^{-5}	[17]
ZnO				30.1 X 10^{-3}	624.49	9.98 X 10^{-5}	
$C\text{-}TiO_2$	0.1 g L^{-1} NP suspension	Batch reactor 400 mL volume Tungsten lamp (150 W, 6.3mW cm^{-2}, 400 nm)	0.05 mg L^{-1}	2.3 X 10^{-3}	166.39	4.64 X 10^{-8}	[18]
TiO_2	12.5 g L^{-1} NP supported on sand	Batch reactor 500 mL volume Xe high intensity lamp (55 W, 1.26 mW cm^{-2}, 475 nm)	5 mg L^{-1}	0.5 X 10^{-3}	12902.72	3.84 X 10^{-7}	[19]
ZnO	1.5 g L^{-1} foam	Recirculating reactor, flow rate 250 mL min^{-1}, 500 mL volume Lamps (3 X 5 W, 10.3 mW cm^{-2}, 254 nm)	2.4 mg L^{-1}	9.1 X 10^{-3}	21.34	2.63 X 10^{-3}	This work

References

1. R. Boppella, K. Anjaneyulu, P. Basak and S. V. Manorama, *The Journal of Physical Chemistry C*, 2013, **117**, 4597-4605.

2. C. M. Taylor, A. Ramirez-Canon, J. Wenk and D. Mattia, *J Hazard Mater*, 2019, **378**, 120799.

3. S. W. da Silva, J. P. Bortolozzi, E. D. Banús, A. M. Bernardes and M. A. Ulla, *Chemical Engineering Journal*, 2016, **283**, 1264-1272.

4. J. R. Bolton, K. G. Bircher, W. Tumas and C. A. Tolman, *Pure and Applied Chemistry*, 2001, **73**, 627-637.

5. J. R. Crison, V. P. Shah, J. P. Skelly and G. L. Amidon, *J Pharm Sci*, 1996, **85**, 1005-1011.

6. Y. Lu and M. Li, *J Pharm Sci*, 2016, **105**, 131-138.

7. S. A. M. Karimian and A. G. Straatman, *International Journal of Heat and Fluid Flow*, 2008, **29**, 292-305.

8. H. Mohan, V. Ramalingam, A. Adithan, K. Natesan, K. K. Seralathan and T. Shin, *J Hazard Mater*, 2021, **416**, 126209.

9. N. F. F. Moreira, M. J. Sampaio, A. R. Ribeiro, C. G. Silva, J. L. Faria and A. M. T. Silva, *Applied Catalysis B: Environmental*, 2019, **248**, 184-192.

10. Z. Hu, X. Cai, Z. Wang, S. Li, Z. Wang and X. Xie, *J Hazard Mater*, 2019, **380**, 120812.

11. A. Kumar, M. Khan, L. Fang and I. M. C. Lo, *J Hazard Mater*, 2019, **370**, 108-116.

12. L. Paredes, S. Murgolo, H. Dzinun, M. H. Dzarfan Othman, A. F. Ismail, M. Carballa and G. Mascolo, *Applied Catalysis B: Environmental*, 2019, **240**, 9-18.

13. S. Ramasundaram, M. G. Seid, H. E. Kim, A. Son, C. Lee, E. J. Kim and S. W. Hong, *J Hazard Mater*, 2018, **360**, 62-70.

14. S. Murgolo, S. Franz, H. Arab, M. Bestetti, E. Falletta and G. Mascolo, *Water Res*, 2019, **164**, 114920.

15. E. Mena, A. Rey and F. J. Beltrán, *Chemical Engineering Journal*, 2018, **339**, 369-380.

16. I. Horovitz, D. Avisar, M. A. Baker, R. Grilli, L. Lozzi, D. Di Camillo and H. Mamane, *J Hazard Mater*, 2016, **310**, 98-107.

17. S. Teixeira, R. Gurke, H. Eckert, K. Kühn, J. Fauler and G. Cuniberti, *Journal of Environmental Chemical Engineering*, 2016, **4**, 287-292.

18. A. Surenjan, B. Sambandam, T. Pradeep and L. Philip, *Journal of Environmental Chemical Engineering*, 2017, **5**, 757-767.

19. Y. He, N. B. Sutton, H. H. H. Rijnaarts and A. A. M. Langenhoff, *Applied Catalysis B: Environmental*, 2016, **182**, 132-141.

Chapter 5

Increased Photocorrosion Resistance of ZnO foams Through Transition Metal Doping.

The work presented in this chapter has been published to Royal Society of Chemistry Advances in January 2023

Warren, Z., et al. (2023). "Increased photocorrosion resistance of ZnO foams via transition metal doping." RSC Advances **13**(4): 2438-2450.

Chapter 5: Increased Photocorrosion Resistance of ZnO foams Through Transition Metal Doping.

This declaration concerns the article entitled:			
Increased Photocorrosion Resistance of ZnO foams Through Transition Metal Doping			
Publication status (tick one) **Draft manuscript** [ ] **Submitted** [ ] **In review** [ ] **Accepted** [ ] **Published** [X]			
Publication details (reference)	Warren, Z., et al. (2023). "Increased photocorrosion resistance of ZnO foams via transition metal doping." RSC Advances **13**(4): 2438-2450.		
Copyright status (tick the appropriate statement) The material has been published with a CC-BY license [ ] The publisher has granted permission to replicate the material included here [ ]			
Candidate's contribution to the paper (provide details, and also indicate as a percentage)	The candidate contributed to… Formulation of ideas: 90% The candidate conceived the research ideas and objectives under the supervision of DM and JW. Design of methodology: 90% The candidate designed the synthetic methodology for the manuscript under the supervision of DM and JW. Experimental work: 90% The candidate conducted all experimental procedures including synthesis, characterisation and analysis. ICP-MS and XPS experiments performed externally but analysed by the candidate and external input was acknowledged. Presentation of data in journal format: 90% The candidate wrote the manuscript and prepared graphs and tables under the supervision of DM and JW.		
Statement from Candidate	This paper reports on original research I conducted during the period of my Higher Degree by Research candidature.		
Signed	Zachary Warren	**Date**	21/09/2022

Increased Photocorrosion Resistance of ZnO foams Through Transition Metal Doping.

Zachary Warren,[a] Jannis Wenk,[a] and Davide Mattia*[a]

Graphical Abstract

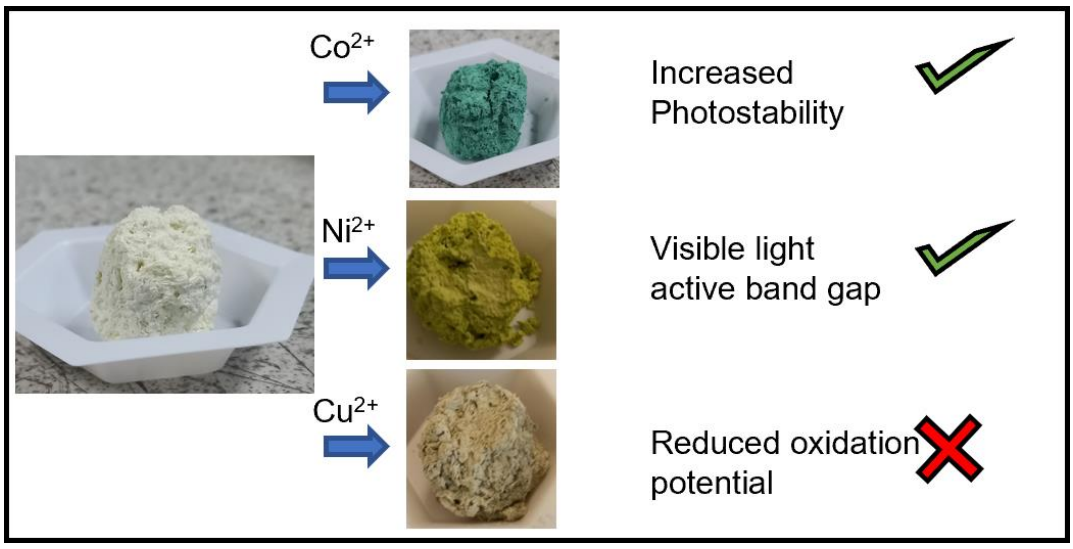

Abstract

ZnO is a widely studied photocatalyst, but practical use is hindered by its low resistance to photocorrosion in water, which leads to metal leaching and loss of performance over time. In this work, highly porous and mechanically stable ZnO foams, called MolFoams, were doped by adding 1% or 2% Co, Ni or Cu salts to the starting Zn salt, followed air insufflation during a sol-gel rection and sintering. The resulting doped foams showed a major increase in stability, with a 60-85% reduction in Zn^{2+} leaching after irradiation, albeit with a reduction in photocatalytic activity. A systematic analysis using XRD, Raman, XPS and XANES allowed for the identification of dopant species in the foams revealing the presence of Co_3O_4 , NiO and Cu_2O within the ZnO lattice with doping leading to a reduced band gap and significant increases in the resistance to photocorrosion of ZnO while identifying the cause of the reduction in photocatalytic activity to be shifting of the band edge positions.

These results provide a pathway to significantly reducing the photocorrosion of ZnO in water, with further work required to maintain the photocatalytic activity of undoped ZnO.

Increased Photocorrosion Resistance of ZnO foams Through Transition Metal Doping.

5.1. Published Manuscript

Introduction

ZnO is well reported for its use as a photocatalytic material in water treatment. [1] Its beneficial properties include high electron mobility and low toxicity, while also absorbing over a wider range of wavelengths of light than widely used TiO_2, allowing for greater utilisation of light. [2]

However a significant drawback of ZnO is its susceptibility to photocorrosion under UV irradiation in an aquatic environment, [3] leading to the dissolution and formation of Zn^{2+} ions in solution as shown in Eq 5.1. [4]

$$ZnO + h\nu \xrightarrow{Photocatalysis} ZnO + e^- + h^+$$
$$ZnO + h^+ \xrightarrow{Photocorrosion} Zn^{2+}_{(aq)} + \frac{1}{2}O_2$$

Equation 5.1: Photocorrosion of ZnO

Given the UV-induced production of photogenerated holes, higher intensities of incident light impinging on the photocatalyst lead to increased photocorrosion of ZnO. [3] Dissolved oxygen content also plays a role in the photocorrosion of ZnO, as in oxygen deficient conditions, the progress of photocorrosion leads to the generation of oxygen from the ZnO structure. [5] While it has been shown that operation under oxygen saturated conditions can reduce the impact of photocorrosion, [4] considerations still need to be made regarding its use in water treatment as the World Health Organisation limits the maximum concentration of Zn^{2+} in water to 3.0 ppm. [6]

Additionally, ZnO is a wide band gap semiconductor, with a band gap of 3.2 eV, meaning that only short wavelength, ultra-violet irradiation can be utilised for the degradation of organic pollutants. Furthermore ZnO suffers from a relatively high surface recombination of charge carriers (e^-/h^+) further reducing its photocatalytic activity.[7]

Doping of semiconductors is a long-established method for adapting and improving photocatalyst materials. Doping with both metals and nonmetals leads to red-shifted band gaps and visible light active photocatalysts.[8] Metal doping introduces shallow or deep level states, above the valence band or below the conduction band, allowing for the absorption of longer wavelengths of light, or the formation of heterojunctions due to the coupling of semiconductors with different bandgaps, leading to greater charge separation and e^-/h^+ lifetimes due to a reduction in recombination rates.[9] However, it has been reported that the presence of the mid-gap level states show the potential to act as recombination centres, particularly when care is not taken to avoid the formation of metal clusters.[10]

ZnO is a promising candidate for doping to further improve the photocatalytic activity under visible light irradiation. As an intrinsic n-type semiconductor, the presence of p-type dopants, often transition metals, leads to the formation of an acceptor level below the original conduction band of ZnO, narrowing the band gap. [10] Furthermore, through selective use of transition metals that form oxides with a valence band higher in energy than ZnO, e^-/h^+ charge pair separation can be achieved, with the holes moving to the valence band of the dopant metal from the ZnO. [11] This leads to a twofold benefit, increased charge separation, which is key to improving efficiency of photocatalytic systems, [12] and the removal of h^+ from the ZnO surface, which reduces the photocorrosion and dissolution of Zn^{2+} into solution. [3]

The state of the art for ZnO doping shows a wide range of potential dopants, from non-metals such as C, N, or S, [13-15] to a wide range of metals including, transition metals, [16] and rare earth metals. [17] However these procedures have only been applied to films or particles of ZnO and as such are still hindered by the low surface areas and the need for downstream removal when applied in water treatment. [18, 19]

MolFoams, or Molecular Foams, is the term used to describe foams produced using the synthetic method herein and developed previously. [20] Through the use of a sol-gel synthesis with controlled incorporation of air to produce a porous structure which is then sintered to produce a singular interconnected foam structure made of metal oxide without the presence of discrete particles.

In this work doping of ZnO foams was achieved via addition of dopant metal salts to an aerated sol-gel solution. The photocorrosion resistance was based on dissolved Zn content in solution after photocatalysis and assessed using ICP-MS while photocatalytic activity measured through analysis of the degradation of carbamazepine, an anticonvulsant and target micropollutant. [21]

This work was conducted to apply the improvements in photocatalytic activity and stability seen only in doped ZnO films and particles to foams, to be used in a system that shows promise for wide-scale adoption due to overcoming the limitations of slurry and immobilised catalysts.

Experimental

Materials

Zinc acetylacetonate (Zn(AcAc)2; ≥95.0 %), Cobalt acetylacetonate (Co(AcAc)2; ≥99.0 %), Nickel acetylacetonate (Ni(AcAc)2; ≥99.0 %), Copper acetylacetonate (Cu(AcAc)2; ≥99.0 %), Oxalic acid anhydrous (≥99.9 %), Hexadecyltrimethylammonium bromide (CTAB; ≥99.9 %), Polyethylene glycol (PEG; 10,000), Carbamazepine and Ethanol (Absolute) were all purchased from Sigma Aldrich and used as provided. Jacketed, fritted funnels were purchased from Chemglass Lifesciences and fitted with PTFE sheets (Zwanzer). Desiccant from a Drierite™ gas-drying unit (Sigma Aldrich) was used as provided by the manufacturer but transferred to a smaller tube.

Synthesis of doped foams $Zn_{1-x}M_xO$

Doped ZnO foams were synthesised using a modified method from previous work. [20] Briefly, $M^{2+}(AcAc)_2$ (15.0 mmol) was added to a 25 mL Pyrex beaker with $M^{2+}(AcAc)_2$ being a combination of $Zn(AcAc)_2$ and the acetylacetonate salt of the dopant metal (Co, Ni, Cu), such that the total molarity of metal salt in the reaction solution was kept constant at 15 mmol. Exact masses and molar quantities are shown in Table 5.. Subsequently, 15 mL of a 10 mM CTAB solution was made up in ethanol and added to the beaker. Oxalic acid (15.0 mmol) and 40 µmol PEG10000 with 10 mL EtOH were mixed in a separate beaker. Both solutions were stirred at 60 °C for 60 minutes in an oil bath until homogenous solutions were obtained. The metal acetylacetonate

solution was added to a PTFE-lined, temperature controlled jacketed filter funnel at 60 °C, followed immediately by the oxalic acid solution. The reaction mixture was aerated with compressed air with an upward flow rate of 0.1 Standard Litres per Minute (sL min^{-1}) using a rotameter.

Table 5.1: Molarities and masses of metal salts used in synthesis of doped ZnO MolFoams.

Dopant		Metal Salt				
Dopant % (x)	mmol Dopant	$Co(AcAc)_2$	$Ni(AcAc)_2$	$Cu(AcAc)_2$	$Zn(AcAc)_2$	
		Dopant Mass /g			mmol	Mass /g
0.5	0.075	0.0193	0.0193	0.0196	14.925	3.9344
1	0.150	0.0386	0.0385	0.0393	14.850	3.9147
2	0.300	0.0771	0.0771	0.0785	14.700	3.8751

The reaction mixture of the zinc/dopant and acid solutions was aerated for 3 hours leading to the formation of a coloured gel, red/pink for cobalt-doped, light green for nickel-doped and blue for copper-doped samples. The gel was then transferred to a pre-weighed ceramic crucible and placed in a preheated muffle furnace (Carbolite CWF 1100) at 80 °C and dried for 12 hours to remove any remaining ethanol, resulting in a dry doped zinc oxalate foam which was stored under ambient conditions.

Conversion of doped zinc oxalate foams into doped zinc oxide foams and removal of remaining organic components was achieved using a two-step thermal sintering process: The zinc oxalate foam was sintered using a furnace, heated to 1,000 °C with a ramp rate of 5 °C min^{-1} and held at temperature for 0.5 hours, and then 900 °C with a ramp rate of 5 °C min^{-1} and held at temperature for 20 hours. This resulted in the formation of a mechanically stable doped ZnO foam. The high temperature sintering was also used to remove any remaining organic components. After sintering, the foams were cylindrical in shape, with an average diameter of 20 ± 1 mm and height of 19 ± 1 mm.

Characterisation of doped foams $Zn_{1-x}M_xO$

The surface morphology of the doped foams was studied using a JEOL JSM-7900F FESEM. Prior to imaging, samples were coated with 20 nm Cr. The crystal structure of the foams was investigated using a STOE STADI P dual powder transmission x-ray diffractometer using a scanning range of 2θ = 20 – 90 degrees and a scan time of 20 minutes. The chemical stability of the MolFoams was analysed using inductively coupled plasma mass spectrometry (ICP-MS) in a Thermo Fisher Scientific X-Series II instrument. All samples, standards, and blanks were spiked with internal standard elements Be, In, and Re. The Zn, Co, Ni and Cu concentrations were calibrated using six synthetic standards prepared from a 1000 ppm Inorganic Ventures (VA, USA) standard. The associated error was typically lower than 1.0%.

The porosity and internal structure of the MolFoam were determined using a combination of different characterisation methods. First, gravimetric porosity measurements were conducted using the Archimedes principle: [22]

$$\varepsilon = \frac{\frac{\omega_1 - \omega_2}{D_u}}{\frac{\omega_1 - \omega_2}{D_u} + \frac{\omega_2}{D_f}}$$

Equation 5.2: Gravimetric Porosity calculation

where ε is the porosity of the foam, ω_1 is the mass of the wet foam, ω_2 is the mass of the dry foam, D_u is the density of water (deionised, ultrapure) and D_f is the density of ZnO.

UV-Vis spectroscopy for surface characterisation was conducted using a PerkinElmer LAMBDA 650s series spectrometer. The reflectance of the doped and undoped ZnO produced in this work and the data gathered to conduct the band gap analysis was collected using a UV/Vis/NIR spectrometer with an integrating sphere.

Raman spectra used in this work were collected using a Renishaw InVia Confocal Raman microscope, excitation laser wavelength 532nm, 100% laser power at 74 mW on the sample with 2.6 s exposure time, and a diffraction grating of size 1,800 l/mm with slit opening of 65 µm. Detector used was a 1040 x 256 pixel CCD camera.

XPS and UPS data was acquired using a Kratos Axis SUPRA using monochromated Al kα (1486.69 eV) X-rays at 15 mA emission and 12 kV HT (180W) and a spot

size/analysis area of 700 x 300 µm and a He(I) UV lamp running at 20 mA emission. The instrument was calibrated to gold metal Au 4f (83.95 eV) and dispersion adjusted give a BE of 932.6 eV for the Cu 2p3/2 line of metallic copper. Ag 3d5/2 line FWHM at 10 eV pass energy was 0.544 eV. Source resolution for monochromatic Al Kα X-rays is ~0.3 eV. The instrumental resolution was determined to be 0.29 eV at 10 eV pass energy using the Fermi edge of the valence band for metallic silver.

XANES analysis was performed on an easyXAFS 300+ spectrometer, with Ag or Mo X-rays operating at 40 mA and 15 kV emission and silicon spherical bent crystal analysers.

Photocatalytic reactor setup

The photocatalytic activity of the doped MolFoams was analysed using a bespoke recirculating reactor, reported previously.[20] Reactor cartridges were made up of a quartz tube (h = 250 mm, OD = 25 mm , ID = 22 mm) with a 3D printed plastic buffer designed to hold the foams in place and prevent loss of the foam into the tubing and pump, positioned to avoid interference with the light source.

MolFoams of known mass (0.7 g) were placed inside the cartridge and secured using subaseal fittings, connected to a gear pump (Ismatec, MCP-Z with a pump head Model GBS.P23.JVS.A-B1, Cole Parmer) and to a jacketed beaker of 500 mL (acting as the reservoir) with a magnetic stirrer, where the temperature was maintained using a water-cooled bath (RC-10 Digital Chiller, VWR). Three UV lamps (Aquatix pond UV lamp, λ = 254 nm, 5W), positioned equidistant around the quartz tube reactor at a distance of 3 cm, served as the light source.

Photocatalytic activity (PCA) experiments

PCA experiments were conducted using 10 µM solutions of carbamazepine (CBZ) in 500 mL unbuffered ultrapure water at 10 ± 1 °C. CBZ was selected as a model organic micropollutant for photocatalytic activity (PCA) studies, due to its high UV stability, [23] known degradation pathways [24] as well as allowing for comparison with prior work conducted on MolFoams. [20] To minimize photocorrosion of ZnO, [4] CBZ solutions were saturated with O_2 for 40 minutes prior to experiments. The recirculating reactors

were operated at flow rate of 250 mL min^{-1}. Control experiments were conducted in the absence of MolFoams in the reactor both under irradiation and in the dark.

For all photocatalysis experiments, CBZ removal was monitored from 1 mL aliquots collected during sampling every 15 minutes for the first hour and every 30 minutes thereafter, such that the total volume removed was less than 10% of the starting reservoir volume, using high performance liquid chromatography (HPLC).

HPLC analysis of CBZ was performed on a Thermo Scientific Ultimate 3000 liquid chromatograph with a UV detector. CBZ analysis used a Thermo Scientific Acclaim 120 C18 column (3.0 X 75.0 mm, particle size 3.0 µm) and a Thermo Scientific Acclaim 120 C18 guard column (R) 120 C18 (3.0 X 10.0 mm, particle size 5.0 µm) The mobile phase was 5.0 mM phosphoric acid and acetonitrile 70:30 (v:v) with a flow rate of 0.8 mL min^{-1}, injection volume of 20 µL and detection wavelength of 285 nm. Degradation of carbamazepine was measured via plotting (C_t/C_0) Vs time where C_0 is the initial concentration of CBZ and C_t is the concentration of CBZ at a given time. The pseudo first order degradation kinetics (k) was calculated via linear regression of a plot of Ln(C_t/C_0) Vs time.

Photocatalyst quantum efficiencies

The quantum efficiency (QE) of a photocatalytic system is defined as the number of molecules of pollutant (carbamazepine) undergoing degradation relative to the number of photons reaching the catalyst surface. [25] The photon flux (E_{qf}) arriving at the surface of the photocatalyst along with the kinetic constant (k) allows calculating the quantum efficiency, assuming negligible photon loss due to scattering and all photons are absorbed by the photocatalyst. Details of the calculations are provided in the SI.

Electrical Energy Per Order (EEO)

To assess the scale-up potential of the system, the energy consumption of the reactor was estimated via the electrical energy per order (EEO), defined as the kilowatt hours of electrical energy needed to decrease the concentration of a pollutant by an order of magnitude (90%) in one cubic metre of solution: [26]

$$E_{EO} = \frac{P}{(F)(log\ {}^{C_0}/_{C_t})}$$

Equation 5.2 Electrical Energy Per Order

where: P is the power output of the lamps and F is the volumetric flow rate of solution. Details of the calculations are provided in the SI.

Results and discussion

Characterisation of doped MolFoams

Once removed from the funnel, the doped zinc oxalate monoliths were free standing and plastic under gentle compression and coloured according to the dopant metal: cobalt-doped foams were red/pink, nickel-doped foams were light green, and copper-doped foams were blue. The dried monoliths were 28 mm in diameter and 30 mm in height on average. This decreased to 20 ± 1 mm diameter and 19 ± 1 mm height post sintering and the foams were robust enough to be handled and subjected to flow experiments. Furthermore, in all cases a colour change occurred during the sintering of the doped foams, with the cobalt-doped turning to a deep green, the nickel-doped foams becoming yellow, and the copper doped turning grey, indicating the formation of the respective metal oxides, [27-29] as seen in Figure 5.1. The gravimetric porosity of the foams was calculated using the Archimedes principle [22] and found to be 95 ± 2%, comparable with aero- or xero-gels without the need for supercritical solvent extraction nor volatile foaming agents. [30, 31]

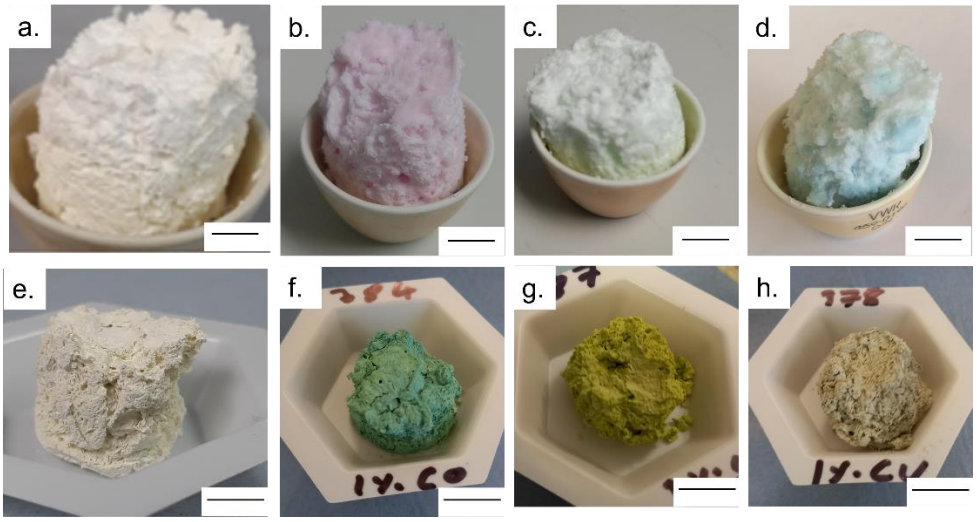

Figure 5.1: a,b,c,d) images of dried $Zn_{1-x}M_xO$ foams were M is Zn, Co, Ni or Cu, respectively; e,f,g,h) images of sintered $Zn_{1-x}M_xO$ foams were M is Zn, Co, Ni or Cu, respectively. Scale bar is 1 cm in all images.

The photocatalytic activity of the MolFoams was investigated by analysing the degradation of carbamazepine in a recirculating flow reactor operated at a previously optimized flowrate of 250 mL min^{-1}. [20] In the absence of irradiation, removal of carbamazepine via adsorption was found to be negligible. When the reactors were operated without MolFoam, the degradation due to photolysis was found to be minimal (9%) after 2 hours of irradiation. Undoped ZnO MolFoams provided strong photocatalytic activity and increased the degradation of carbamazepine to 66% (Figure 5.2). The incorporation of dopant into the ZnO structure led to significant decreases in photocatalytic activity with foams doped with 2% Ni showing the lowest decline, at 25% removal of carbamazepine over the same irradiation time. Comparing dopant metals at 1% concentration shows there is no significant difference in photocatalytic activity when using different metal dopants, while when doping increases to 2%, the Ni doped foams show greater photocatalytic activity than those doped with Co or Cu, but still significantly lower than the pure ZnO foams. Figure S5.1 provides an alternative data presentation arranged by dopant metal. Co-doped foams showed reduced activity at higher dopant %, Ni-doped foams showed an increase in activity with dopant concentration, while Cu-doped foams showed no significant difference in activity. This is in contrast to reported findings for doped ZnO slurries in the literature, which in the case of Co, Ni and Cu, show increasing the

dopant concentration leads to an increase in photocatalytic activity, up to around 5% at which point activity plateaus or decreases. [32-34]

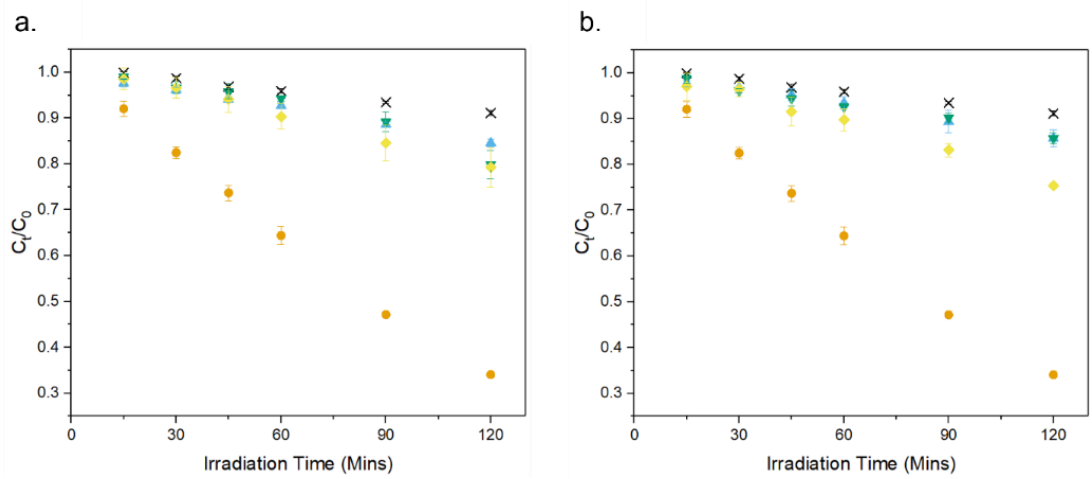

Figure 5.2: Photocatalytic degradation of CBZ using ZnO doped with a) 1% and b) 2% of various transition metals: × photolysis, ● undoped, ◤ Co, ◆ Ni, ◢ Cu. Numerical values provided in Table 5.2.

As expected by the reduced photocatalytic activity, the doped foams had significantly lower quantum efficiency and higher electrical energy per order (E_{EO}) values, both indicating the foams were less efficient in terms of electrical energy and photon usage, as shown in Table 5.2.

However, doping foams with different metals led to 60-85% less photocorrosion of ZnO compared to the undoped samples, as indicated by the lower Zn^{2+} concentrations measured in solution after irradiation experiments (Table 5.2), far in excess of reported findings on coupled photocatalyst films.[35] One potential explanation for this reduction in photocorrosion, and why it decreases at increased dopant concentration irrespective of dopant, is that the presence of the dopant metals leads to changes in the crystal structure of ZnO, leading to decreases in the surface energy. This, in turn, would reduce the possibility of hole attack, resulting in less photocorrosion of ZnO.[36] An alternative mechanism for the reduction in photocorrosion is charge separation of holes onto dopant atoms, thus reducing the attack of ZnO by holes, with higher dopant concentrations leading to a greater number of dopant atoms to allow for the greater charge separation.[37] Additionally, the ICP-MS analysis of the solution post-photocatalysis, for the specific metal used (i.e. for the [Co] for the Co doped foams) can be seen in Table 5.2. In all cases the

concentration of metals were significantly lower than the WHO limits for drinking water. [6]

Table 5.2 CBZ removal for pure and doped ZnO MolFoams, pseudo first order degradation kinetics (k) and Zn concentration post photocatalytic degradation. Also tabulated are quantum efficiency (QE) and EEO for each condition.

Sample	C_{120}/C_0	k (x10^{-3}) /min^{-1}	[Zn^{2+}] /ppb	[Co] /ppb	[Ni] /ppb	[Cu] /ppb	E_{EO} /KWh m^{-3}	QE	Ref
ZnO	0.34 ± 0.01	9.08 ± 0.44	482	/	/	/	21	2.63 X10^{-3}	[20]
1 % Co	0.80 ± 0.03	1.70 ± 0.12	193	13	/	/	105	4.91 X10^{-4}	This Work
2 % Co	0.85 ± 0.01	1.30 ± 0.05	99	16	/	/	145	3.75 X10^{-4}	
1 % Ni	0.79 ± 0.04	2.02 ± 0.11	112	/	8	/	100	5.77 X10^{-4}	
2 % Ni	0.75 ± 0.01	2.04 ± 0.11	80	/	5	/	82	5.77 X10^{-4}	
1 % Cu	0.85 ± 0.01	1.36 ± 0.04	102	/	/	2	145	4.04 X10^{-4}	
2 % Cu	0.85 ± 0.02	1.27 ± 0.05	71	/	/	2	145	3.46 X10^{-5}	

The XRD patterns (Figure S5.2) in all cases showed the formation of hexagonal wurtzite ZnO with lattice parameters of a = b = 3.25 Å and c = 5.21 Å, with the strongest intensity for the peaks associated with the (100), (002) and (101) crystal phases, and with sharp peaks indicative of a highly crystalline structure. All peaks are in agreement with those reported from JCPDS no. 36-1451, [38] as well as previously reported work on MolFoams. For all dopants and different dopant concentrations, these peaks showed slight broadening with an average increase in full width at height maximum (FWHM) of 5%, indicating a decrease in crystallinity of the samples. In all cases, XRD analysis showed single phase hexagonal wurtzite structure, indicative of doping through the crystal lattice. [39] Furthermore, the absence of crystal phases of Co, Ni or Cu, nor mixed metal oxides, should be noted, indicating that no dopant metal or metal oxide clusters were observed in the samples. The three most intense peaks of the XRD pattern show peak shifting towards higher angles for both Ni and Cu doping, while only the (101) peak shows higher angle shifting with Co doping, indicating a reduction in the unit cell. This is consistent with the fact that the atomic radii of the dopant metals are all smaller than that of Zn^{2+}.[40] However, due to the low dopant concentrations and small peak shift, doping had no impact on the lattice parameters of the crystal. In the case of all dopants, the intensity of the (100), (002), and (101) peaks decreased as did the relative intensities of the (100)/(101) and (002)/(101) ratios with average reductions of 0.02 and 0.03 respectively. This is

indicative of the increased presence of (1011) facets in the crystal lattice which have shown to be highly reactive and beneficial for photocatalysis. [41] The decrease in crystallinity caused by doping of metal ions into the lattice, as observed by the broadening of the peaks, has been shown to lead to a decrease in the surface energy of the ZnO lattice. [42] This decrease in surface energy has a stabilising effect on the ZnO, and reduces the susceptibility to attack from holes, thus leading to the observed increase in resistance to photocorrosion.

The FE-SEM micrographs show the presence of irregular pores surrounded by an interconnected network of crystallites, along with morphological features unique to each dopant: Undoped ZnO shows the presence of faceted rod-like crystals, reported previously for MolFoams synthesised using 10 mM CTAB solutions. MolFoams doped with Co show larger, jagged crystals with clear facets along their length, while foams doped with Ni form faceted spheroidal crystals, and Cu doping forms smooth spheroidal crystals (Figure 5.3).

It is well-known that highly faceted crystal structures tend to be more photocatalytically active. [20] As such, the smooth crystals obtained with copper doping (Figure 5.3d) could explain the lower photocatalytic activity of these samples. However, the reduction in activity is too high to be attributed solely to the crystal morphology, [43] and, in any case, this does not apply to Ni- and Co-doped foams due to the presence of faceted crystals seen in Figure 5.3 b and c. It is of note, the presence of faceted crystals in the doped samples is significantly reduced compared with the pure ZnO. While the XRD reports a slight decrease in the (100)/(101) and (002)/(101) ratios due to the presence of (1011) facets, the FESEM micrographs show the morphology to be smoother in all cases, particularly the Cu doped samples. This is of import, as the photocatalytically active facets also possess high surface energies, allowing for photocorrosion to occur as holes react at the surface. [44] The reduction in the number of these faceted crystals leads to lower surface energies and as such, increased resistance to photocorrosion.

Additionally, elemental mapping confirmed uniform dispersion of dopant metal throughout the structure of the crystal lattice as shown in Figure S5.3.

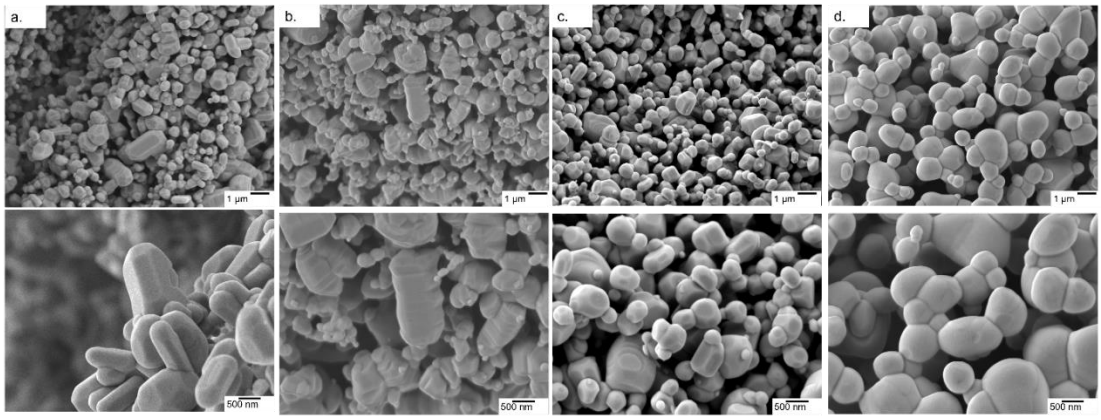

Figure 5.3 FE-SEM micrographs of a) pure ZnO and ZnO doped with b) Co, c) Ni and d) Cu at two different magnifications.

Raman scattering spectra were collected on both pure and doped ZnO samples to study the crystal lattice, particularly looking for phases of dopant metal oxide, present in potentially too low concentrations to be detected by XRD. Figure 5.4 shows the Raman spectra from pure and doped ZnO samples collected with green excitation wavelength (532 nm). In all cases, the predominant peak corresponds to the non-polar optical phonon mode of ZnO, the high frequency E_2 mode, associated with the vibrations pf oxygen atoms within the ZnO lattice. [45] The spectra of the pure ZnO also shows the A_1 and E_1 Raman peaks at shifts of 379.6 and 583.9 cm^{-1} respectively. Peaks marked with an asterisk (*) are due to multi-phonon features present in the spectra and are caused by interaction between the E_2^{low} peak, that can be detected at wavenumbers > 100 cm^{-1}, and the E_2^{high} peak at 432.5 cm^{-1}. Upon doping the ZnO, noticeable changes can be seen in the spectra. Firstly, downshifts occur for the E_2^{high} and E_1 peaks, which are attributed to increasing bond lengths between the zinc (or dopant) atom and oxygen atom in the lattice structure. [46] Secondly, broadening of these peaks for all metal dopants, associated with surface disorder caused by incorporation of dopants into the lattice structure.[39] As discussed earlier, this surface disorder and the reduced crystallinity lead to a reduction in photocorrosion.

The broad peak present around 550 cm^{-1} in the Co and Ni doped samples is attributed to peak overlap between the weak ZnO peak, as seen in the pure sample, and a peak associated with either Co_3O_4, [47] or NiO [48]. CoO reports Raman peaks at around 675 and 455 cm^{-1},with the former being absent from the spectra, meanwhile

Co_3O_4 exhibits Raman peaks in around 482, 519, 621 and 690 cm^{-1} with the peak at 519 cm^{-1} being clearly prominent in the spectra and increasing in intensity as doping concentration increases (Figure S5.4), while the peak at 482 cm^{-1} overlaps with the ZnO E_2^{high} peak at 432.5 cm^{-1} leading to the peak broadening. The peak at 620 cm^{-1} can be seen in the doped samples and is absent from the pure, while the dopant concentration is too low to observe the peak at 690 cm^{-1}. This suggests that the cobalt present in the doped foams is in the form of Co_3O_4 rather than CoO.

CuO exhibits an intense peak around 600 cm^{-1}, which is absent from the spectra collected from the Cu doped foams. These samples instead exhibit a weak peak around 525 cm^{-1} which is used to characterise Cu_2O rather than CuO,[49] suggesting that the Cu within the doped foams is Cu(I) rather than the desired Cu(II). The presence of Cu(I) only within the foams is also shown and corroborated by the XPS analysis, (Figure 5.6) and XANES analysis (Figure S5.6).

These effects are relative to the dopant concentration, with the higher dopant concentrations leading to greater peak shifting and broadening as well as the peaks associated with Co_3O_4 and NiO becoming more intense (Figure S5.4).

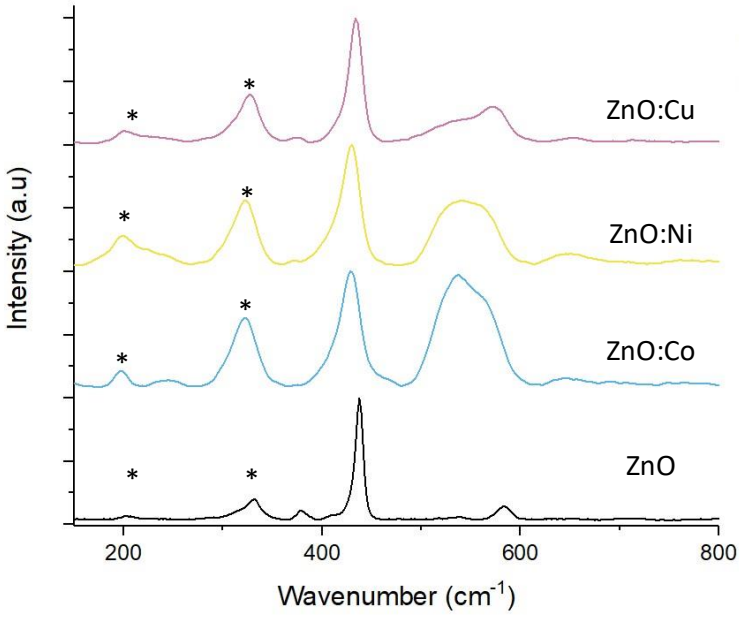

*Figure 5.4: Raman spectra of pure and doped ZnO molfoams. * correspond to multi-phonon features*

UV-Vis spectroscopy was used to evaluate the impact of doping transition metals on the optical properties of ZnO. Figure 5.5 shows that pure ZnO exhibits strong absorption at 380 nm, corresponding to a band gap of 3.2 eV, further shown in the Tauc plots. For all dopant metals and concentrations, this absorption edge is red-shifted, corresponding to enhanced visible light response and a narrowing of the band gap. This is due to the formation of dopant levels in the band structure of ZnO, acting as acceptor levels below the conduction band, thus requiring lower energy photons to promote electrons from the valence band. [10] Furthermore, all doped samples show greater absorbance across in the range of 400 – 800 nm compared to the pure samples, with cobalt and nickel doped samples exhibiting an increase in absorbance between 550 and 700 nm and the nickel exhibiting a broad absorption centred around 500 nm. These absorbances of specific wavelengths are responsible for the colour of the samples. By absorbing strongly in the region of ~700 nm, associated with red light, the cobalt samples appear the complimentary colour of green. The same is true of the nickel doped samples, the absorption around ~500 nm corresponds to violet light and as such the samples appear the complimentary yellow colour. The copper doped samples show no strong absorbance at a specific wavelength, instead absorbing over the entire visible range, leading to the grey colouration. These changes were clearly observable by eye, as all the doped samples were of darker colour than the white of the pure ZnO (Figure 5.1).

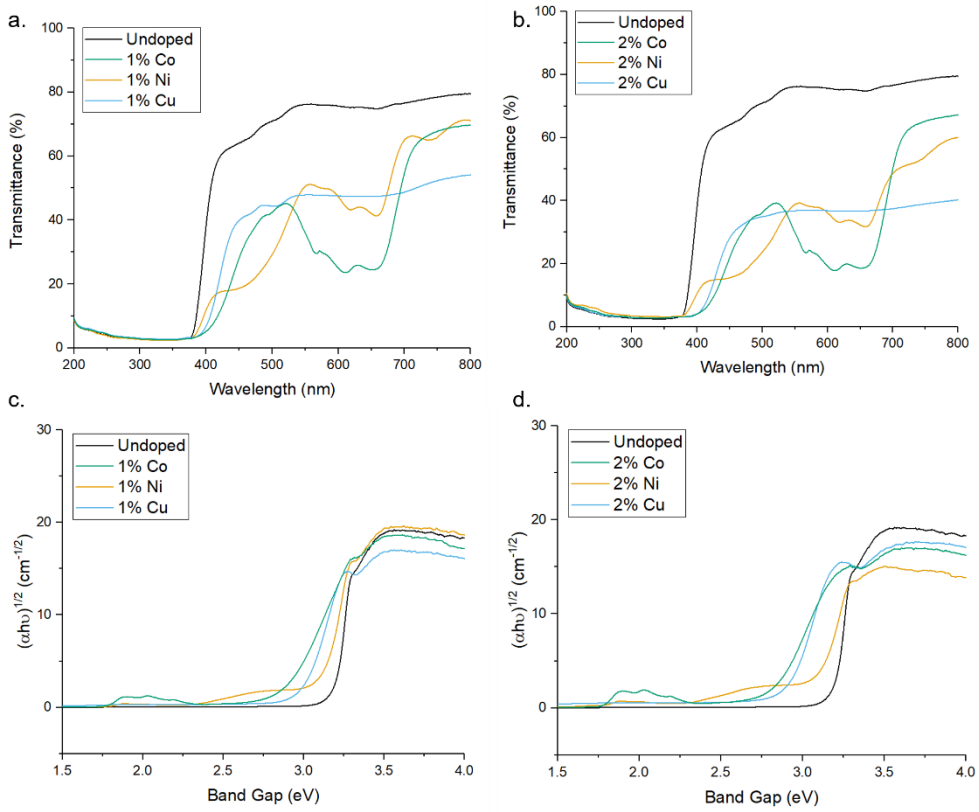

Figure 5.5 a,b) UV-Vis transmittance spectra of pure and doped ZnO MolFoams. C,d) show corresponding Tauc plots.

The chemical states of compounds of the MolFoams were identified using the binding energies of the XPS spectra. The XPS provides further evidence for the incorporation of dopant into the ZnO lattice. Figure 5.6 shows the XPS spectra of b) Zn 2p, c) O 1s and d), e) and f) show the 2p spectra of Co, Ni, and Cu, respectively. In the Zn spectra, the two intense peaks at 1021.0 and 1043.9 eV are in agreement with the binding energies of Zn $2p_{3/2}$ and Zn $2p_{1/2}$ as well as the peak splitting of 23.1 eV confirming the Zn was present as Zn^{2+}. [50] This is further corroborated by the modified auger parameter (the sum of the kinetic energy of Zn auger peak and the binding energy of the Zn $2p_{3/2}$ peak) value of ~2010 eV confirming the presence of ZnO rather than Zn metal.

The oxygen 1s peak was fitted by three components centred at 529.8, 531.0 and 532.0 eV. The low energy peak corresponds to O^{2-} ions in the wurtzite structure of ZnO, surrounded by Zn atoms with a full complement of nearest neighbour O^{2-} ions, such that the oxygen is in a fully oxidised stoichiometric environment. [51] The highest

energy peak is attributed to loosely bound oxygen species, often physisorbed water, at the surface of the sample. [39] The medium binding energy component is attributed to O^{2-} in oxygen deficient regions of the ZnO lattice and is associated with oxygen vacancies within the crystal structure. [52]

In the Co-doped foams, despite the low doping concentrations, the two peaks corresponding to the Co $2p_{3/2}$ and Co $2p_{1/2}$ peaks at 779.9- and 795.6 eV respectively, in agreement with values reported elsewhere. [53, 54] Additionally the peaks show a spin-orbital splitting of 15.7 eV indicative of Co^{2+} and providing confirmation that no Co metal clusters are present in the samples as in this case the difference in peaks would be 15.0 eV. [39]

Furthermore, the region around the Co $2p_{3/2}$ peak shows a number of small peaks within the range of 779.9- to 785.5 eV including a broad peak centred around 780 eV. These peaks are attributed to Co_3O_4 which reports a number of peaks in this range, in particular peaks at 779.9- and 781.2 eV. [55] Given the low concentration of dopant leading to low resolution, it is not possible to resolve these as separate peaks, and as such the spectra shows a single broad peak. This spectrum shows that while the dopant cobalt is only present within the lattice, with the absence of metal clusters at the surface, the cobalt exists in a mixed oxidation state as Co_3O_4 which is in agreement with the Raman (Figure 5.4) and XANES (Figure S5.6).

Analysis of the Ni 2p XPS spectra main peak, associated with the $2p_{3/2}$ peak shows a doublet structure with peak splitting of ~ 5 eV, likely caused by a metallic Ni 3d interaction with ligand oxygen 2p level in the valence band. [56] Additionally, the position of the $2p_{3/2}$ peak and the $2p_{1/2}$ peak at 854.5- and 872.2 eV, respectively, are in good agreement with literature values reported for NiO. [57]

The XPS analysis of the Cu-doped foams clearly shows the presence of only Cu(I) species within the lattice, given the absence of satellite peaks in the Cu 2p spectra which would indicate the presence of Cu(II). [50] The presence of Cu(I) over Cu(0) is corroborated by the modified auger value as well as the shoulder region of the $2p_{3/2}$ peak, as Cu metal exhibits a sharp $2p_{3/2}$ peak while a shoulder region is reported in

Cu(I), caused by trace amounts of Cu(II) formed through self-oxidation. [58] The presence of Cu (I) is further corroborated by the Raman spectroscopy.

These results are further corroborated by the XANES spectra (Figure S5.6) which confirm the presence of Co_3O_4, [59] NiO, [60] and Cu_2O [61] with the insets of Figure S5.6 a and c showing the distinctive pre-edge features indicative of Co_3O_4, and Cu_2O respectively.

These results further show that the substitution of cobalt, nickel and copper into the ZnO lattice can be achieved via simple modification of the previously reported MolFoam synthesis, leading to the formation of Co_3O_4, NiO and Cu_2O respectively. Co_3O_4 has a visible light active band gap of 2.6 eV and has been shown to form a heterojunction with ZnO,[62] and along with NiO, [63] have been used as a photocatalyst, co-catalyst and a p type dopant and, as such, the presence of Co^{2+} and Ni^{2+} in the XPS spectra is desirable as these will lead to an increased charge separation of the holes, thus removing them from the ZnO surface, limiting the photocorrosion of ZnO. On the other hand, the presence of metal clusters could act as recombination centres, leading to a reduction in charge species lifetime and a subsequent reduction in photocatalytic activity. [64]

In the case of Cu doping, the presence of the Cu(I) rather than leading to increased charge separation, thus preventing photocorrosion of the ZnO, the Cu (I) acts as a species to be preferentially oxidised, as Cu (I) is highly susceptible to photocorrosion and oxidation to Cu(II).[58] The intent of the dopant was to reduce the photocorrosion of ZnO, without itself undergoing photocorrosion as overtime this will lead to the need to replace the photocatalyst, along with additional production of the foams. This is before consideration is placed on any potential reduction in activity caused by the formation of mixed oxide structures within the ZnO crystal lattice due to the irregular orientation and position within the lattice acting as recombination centres. Furthermore, if it is found that the CuO provides greater beneficial effects on photocatalytic activity and reduction of photocorrosion, it is of interest that CuO be formed during the synthesis of the foams, rather than through gradual oxidation of Cu_2O during the use of the photocatalyst.

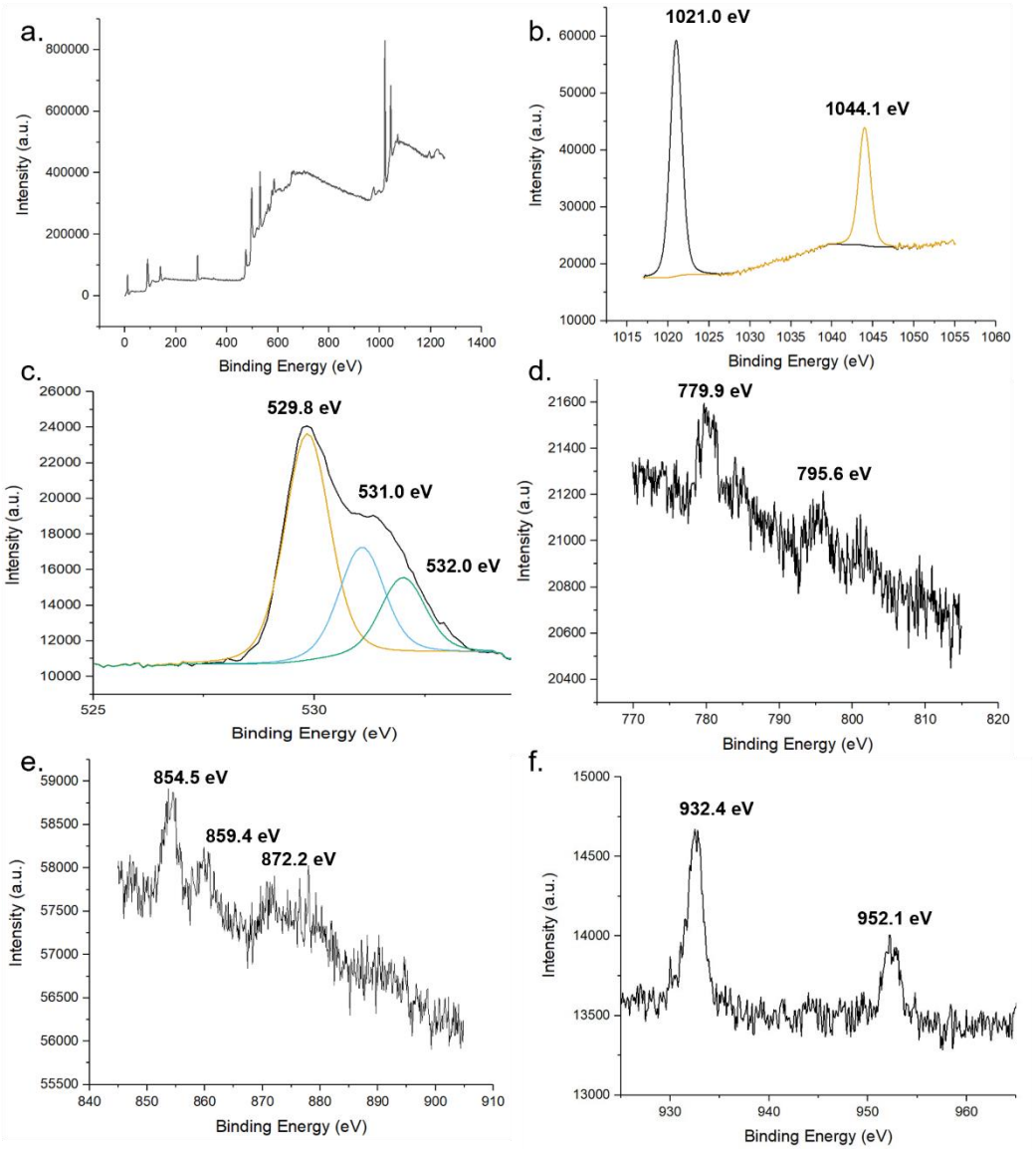

Figure 5.6: XPS spectra of pure and doped ZnO foams. a) global, b) Zn and c) O of undoped foams. XPS spectra of 2p regions of TM dopant d) Co, e) Ni and f) Cu.

The impact of doping on the electronic structure was further elucidated using ultra-violet photoelectron spectroscopy (UPS), allowing for determination of the work function (W) and valence band maxima (VB_{max}) of the materials which, when combined with the band gap, allows for the calculation of the conduction band minima (CB_{min}) and study of the band edge positions of the photocatalyst. [65] Figure 5.5 show the UPS spectra, along with valence band and cut-off regions of the spectra. The cut-off region allows for calculation of the work function (W) of the material, or the energy required to remove one electron from the material. [66] Calculations and graphs of UPS spectra, including cut off and valence band regions can be found in the SI. From this value, and the intercept of the valence band region, the energy level of

VB_{max} was calculated and, using the band gap derived from the Tauc plots in Figure 5.5, a complete diagram of the band edge positions was constructed (Figure 5.7). These calculations can be found in the SI. Inclusion of dopant metals at all concentrations leads to a lower binding energy in the valence bands of the material. This is caused by the formation of additional energy levels near or above the valence band due to the dopant metals being more electron deficient relative to Zn. [67] Furthermore, the reduction in the band gap, as calculated through the Tauc plots, has a lesser impact on the band structure than the valence band edge, as the conduction band edge of the doped samples show less deviation from that of the pure sample, when compared to the valence band edges. The key information provided by the UPS is the band edge positions relative to the redox potentials for the reduction of oxygen into superoxide radicals. The oxidation of water into hydroxyl radicals are -0.28 V vs. Standard Hydrogen Electrode (SHE) and +2.27 V v.s SHE respectively. [68]

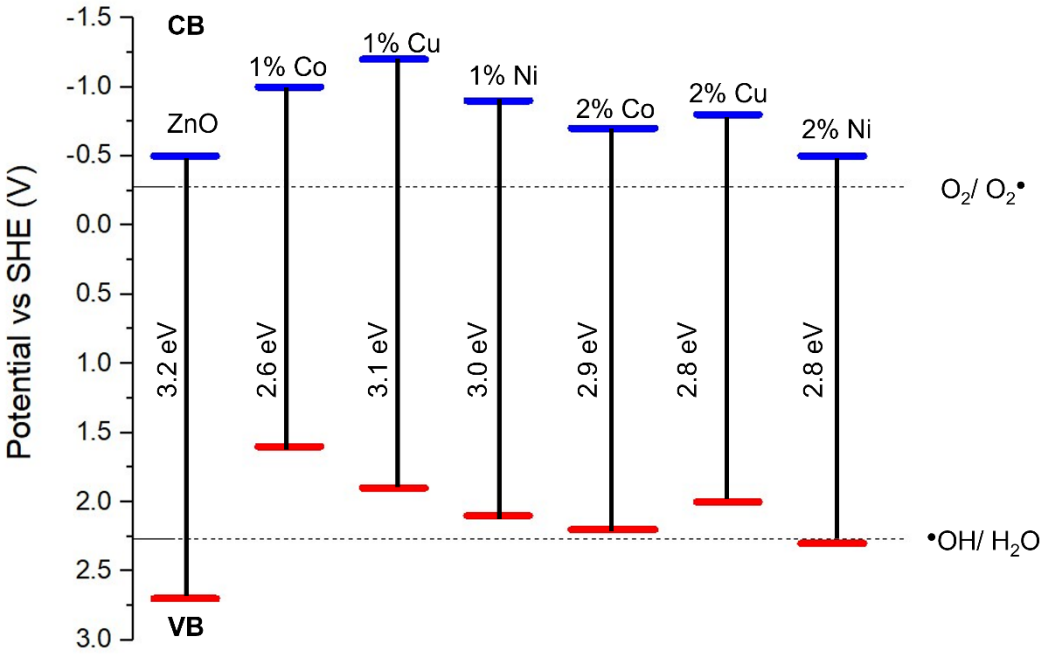

Figure 5.7: Band diagram of pure and doped ZnO based on UPS and Tauc plot calculations.

For a photocatalyst to facilitate these redox reactions, the band edge positions must straddle the redox potential of both redox reactions to take place. [69] As shown in Figure 5.7, in all cases except the ZnO doped with 2% Ni, the valence band edge is

significantly lower that the redox potential for the $^{\bullet}OH/ H_2O$ couple and, as such, lacks the oxidation capability required for the production of the hydroxyl radical from water, a key component in the photocatalytic degradation of organic compounds. [70] The reduction in photocatalytic activity in the doped samples is likely caused by the increase in the valence band edge, reducing the oxidising potential of the foams and as such preventing the production of hydroxyl radicals for the degradation of carbamazepine. Given that the position of the 2% Ni doped foam band edge is only +0.03 V relative to the redox potential for the $^{\bullet}OH/ H_2O$ couple, this provides an explanation as for why the activity of these samples were the highest among all doped foams but still significantly lower than pure ZnO which has a band edge position +0.43 V compared to the hydroxyl couple.

The inhibition of hydroxyl radical production of Co-, Ni and Cu-doped ZnO nanoparticles has been reported previously using the terephthalic acid photoluminescence technique along with a reduction in the photocatalytic activity of these samples relative to pure ZnO. [19] Similar reductions in photocatalytic activity have been reported for Co- and Mn-doped ZnO nanoparticles with the reduction attributed to recombination centres. [71] The dopant-induced shift in valence band edge position is highly significant and provides the best explanation for the low photocatalytic activities reported herein and within the literature.

Conclusions

Building upon previous work on ZnO MolFoams, dopant metals were introduced into the foams to reduce the photocorrosion of ZnO, thus overcoming one of the key hinderances in its widespread application as a method for removal of recalcitrant organic micropollutants from water. Three different transition metals Co, Ni, and Cu, were doped into ZnO foams at concentrations of 1 and 2 %, resulting in foams of a range of colours and crystal morphologies. Photocorrosion, as assessed by dissolved Zn content post degradation was reduced 60-85% in all doped foams and was attributed to increased charge separation induced by doping transition metals, leading to the formation of heterojunctions, as well as the doping induced disorder

of the crystal structure reducing the surface energy of the material, reducing the susceptibility to attack from holes.

Analysis of the structure of the doped foams was conducted to ascertain the impact of doping on the structure of ZnO as well as to identify the nature of the dopant species within the crystal structure. XRD, EDX, raman and XPS were conducted and found that doping was successful and uniform throughout the structure with the cobalt doping leading to the formation of Co_3O_4, nickel doping forming NiO and copper-doped foams led to the formation of Cu_2O species within the lattice. The cobalt and nickel doping lead to reduced photocorrosion through charge separation of holes, while the copper doping formed Cu_2O which were preferentially oxidised to CuO by photocorrosion, rather than ZnO. In addition to specific effects caused by the individual dopants, all dopants lead to a decrease in crystallinity and a reduction in the surface energy of ZnO, further increasing the photocorrosion resistance.

However, doping of the foams lead to a decrease in photocatalytic activity. Advanced analytical methods were used to understand the cause of this loss in activity, with UPS and UV-Vis allowing for construction of a band edge diagram. This revealed that the doping of transition metal into the foams leads to a shift in the band edge positions, such that the foam no longer shows the required oxidation potential for the formation of the hydroxyl radicals necessary for the degradation of organic pollutants.

As such, further investigation is required into the impact of doping on the photocatalytic activity of ZnO, as the resistance to photocorrosion exhibited by the foams discussed here show promise for overcoming one of the key drawbacks of ZnO, as long as the photocatalytic activity is not hindered.

CRediT authorship contribution statement

Zachary Warren: Conceptualisation, Investigation, Methodology, Validation, Visualisation, Writing – original draft. **Jannis Wenk:** Supervision, Writing – review & editing. **Davide Mattia:** Funding acquisition, Project administration, Resources, Supervision, Writing – review & editing.

Conflicts of interest

There are no conflicts to declare

Acknowledgements

The authors would like to acknowledge the EPSRC for funding (EP/P031382/1). ZW acknowledges The University of Bath for funding his PhD. ZW would also like to acknowledge P. Fletcher, D. Lednitzky and S. Reeksting of MC^2 University of Bath analytical facilities, G. Kociok-Köhn of Department of Chemistry, J.A. Milton of The National Oceanography Centre Southampton and M. Isaacs of Harwell research facility for support and assistance in collection of the data presented here.

Data supporting this work is freely accessible in the Bath research data archive system at DOI: 10.15125/BATH-XXXX

References

1. C. Sushma and S. Girish Kumar, *Chemical Papers*, 2017, **71**, 2023-2042.
2. R. Qiu, D. Zhang, Y. Mo, L. Song, E. Brewer, X. Huang and Y. Xiong, *J Hazard Mater*, 2008, **156**, 80-85.
3. J. Han, W. Qiu and W. Gao, *J Hazard Mater*, 2010, **178**, 115-122.
4. C. M. Taylor, A. Ramirez-Canon, J. Wenk and D. Mattia, *J Hazard Mater*, 2019, **378**, 120799.
5. A. M. Ali, E. A. C. Emanuelsson and D. A. Patterson, *Applied Catalysis B: Environmental*, 2010, **97**, 168-181.
6. W. a. UNICEF, WHOUNICEF-Joint-Monitoring-Program-for-Water-Supply-Sanitation-and-Hygiene-JMP, https://www.unwater.org/publications/whounicef-joint-monitoring-program-water-supply-sanitation-hygiene-jmp-2017-update-sdg-baselines/).
7. Q. X. Zhao, L. L. Yang, M. Willander, B. E. Sernelius and P. O. Holtz, *Journal of Applied Physics*, 2008, **104**.
8. X. Chen, S. Shen, L. Guo and S. S. Mao, *Chem Rev*, 2010, **110**, 6503-6570.
9. S. G. Kumar and K. S. R. K. Rao, *RSC Advances*, 2015, **5**, 3306-3351.

10. M. Samadi, M. Zirak, A. Naseri, E. Khorashadizade and A. Z. Moshfegh, *Thin Solid Films*, 2016, **605**, 2-19.
11. F. Rasouli, A. Rouhollahi and F. Ghahramanifard, *Superlattices and Microstructures*, 2019, **125**, 177-189.
12. S. Wang, C.-Y. Huang, L. Pan, Y. Chen, X. Zhang, A. Fazal e and J.-J. Zou, *Catalysis Today*, 2019, **335**, 151-159.
13. M. Samadi, H. A. Shivaee, A. Pourjavadi and A. Z. Moshfegh, *Applied Catalysis A: General*, 2013, **466**, 153-160.
14. B. M. Rajbongshi, A. Ramchiary and S. K. Samdarshi, *Materials Letters*, 2014, **134**, 111-114.
15. G. Poongodi, R. Mohan Kumar and R. Jayavel, *Ceramics International*, 2014, **40**, 14733-14740.
16. G. Murugadoss, *Journal of Materials Science & Technology*, 2012, **28**, 587-593.
17. J. Iqbal, X. Liu, H. Zhu, Z. B. Wu, Y. Zhang, D. Yu and R. Yu, *Acta Materialia*, 2009, **57**, 4790-4796.
18. E. S. Tuzemen, K. Kara, S. Elagoz, D. K. Takci, I. Altuntas and R. Esen, *Applied Surface Science*, 2014, **318**, 157-163.
19. J. Kaur and S. Singhal, *Ceramics International*, 2014, **40**, 7417-7424.
20. Z. Warren, T. T. Guaraldo, J. Wenk and D. Mattia, *Journal of Materials Chemistry A*, 2022, **10**, 11542-11552.
21. J. L. Wilkinson, A. B. A. Boxall, D. W. Kolpin, K. M. Y. Leung, *Proc Natl Acad Sci U S A*, 2022, **119**.
22. Y. Liao, R. Wang, M. Tian, C. Qiu and A. G. Fane, *Journal of Membrane Science*, 2013, **425-426**, 30-39.
23. F. Ali, J. A. Khan, N. S. Shah, M. Sayed and H. M. Khan, *Process Safety and Environmental Protection*, 2018, **117**, 307-314.
24. J. Zhai, Q. Wang, Q. Li, B. Shang, M. H. Rahaman, J. Liang, J. Ji and W. Liu, *Sci Total Environ*, 2018, **640-641**, 981-988.
25. N. Serpone and A. Salinaro, *Pure and Applied Chemistry*, 1999, **71**, 303-320.
26. J. R. Bolton, K. G. Bircher, W. Tumas and C. A. Tolman, *Pure and Applied Chemistry*, 2001, **73**, 627-637.

27. A. S. Zoolfakar, R. A. Rani, A. J. Morfa, A. P. O'Mullane and K. Kalantar-zadeh, *J. Mater. Chem. C*, 2014, **2**, 5247-5270.

28. S. J. Teichner and J. A. Morrison, *Transactions of the Faraday Society*, 1955, **51**.

29. P. M. S. Monk, S. L. Chester, D. S. Higham and R. D. Partridge, *Electrochimica Acta*, 1994, **39**, 2277-2284.

30. A. Benad, F. Jürries, B. Vetter, B. Klemmed, R. Hübner, C. Leyens and A. Eychmüller, *Chemistry of Materials*, 2017, **30**, 145-152.

31. B. Chen, X. Wang, S. Zhang, C. Wei and L. Zhang, *Journal of Porous Materials*, 2014, **21**, 1035-1039.

32. M. Fu, Y. Li, S. wu, P. Lu, J. Liu and F. Dong, *Applied Surface Science*, 2011, **258**, 1587-1591.

33. C. Xu, L. Cao, G. Su, W. Liu, X. Qu and Y. Yu, *Journal of Alloys and Compounds*, 2010, **497**, 373-376.

34. J. Zhao, L. Wang, X. Yan, Y. Yang, Y. Lei, J. Zhou, Y. Huang, Y. Gu and Y. Zhang, *Materials Research Bulletin*, 2011, **46**, 1207-1210.

35. R. T. Sapkal, S. S. Shinde, T. R. Waghmode, S. P. Govindwar, K. Y. Rajpure and C. H. Bhosale, *J Photochem Photobiol B*, 2012, **110**, 15-21.

36. B. Weng, M.-Y. Qi, C. Han, Z.-R. Tang and Y.-J. Xu, *ACS Catalysis*, 2019, **9**, 4642-4687.

37. C. Yu, K. Yang, Q. Shu, J. C. Yu, F. Cao, X. Li and X. Zhou, *Science China Chemistry*, 2012, **55**, 1802-1810.

38. R. Boppella, K. Anjaneyulu, P. Basak and S. V. Manorama, *The Journal of Physical Chemistry C*, 2013, **117**, 4597-4605.

39. B. Panigrahy, M. Aslam and D. Bahadur, *The Journal of Physical Chemistry C*, 2010, **114**, 11758-11763.

40. M. Dhiman, S. Bhukal, B. Chudasama and S. Singhal, *Journal of Sol-Gel Science and Technology*, 2016, **81**, 831-843.

41. J. Chang and E. R. Waclawik, *CrystEngComm*, 2012, **14**.

42. X. Zhang, P. Fan, Y. Han and J. Yu, *Energy Technology*, 2019, **7**, 263-268.

43. J. Luo, S. Zhang, M. Sun, L. Yang, S. Luo and J. C. Crittenden, *ACS Nano*, 2019, **13**, 9811-9840.

44. G. Liu, J. C. Yu, G. Q. Lu and H. M. Cheng, *Chem Commun (Camb)*, 2011, **47**, 6763-6783.

45. V. Russo, M. Ghidelli, P. Gondoni, C. S. Casari and A. Li Bassi, *Journal of Applied Physics*, 2014, **115**.

46. F. Hardcastle and I. Wachs, *Solid State Ionics*, 1991, **45**, 201-213.

47. C.-W. Tang, C.-B. Wang and S.-H. Chien, *Thermochimica Acta*, 2008, **473**, 68-73.

48. A. J. Deotale, U. Singh, M. Golani, K. Hajela and R. V. Nandedkar, presented in part at the National Conference on Physics and Chemistry of Materials: Ncpcm2020, 2021.

49. Y. Deng, A. D. Handoko, Y. Du, S. Xi and B. S. Yeo, *ACS Catalysis*, 2016, **6**, 2473-2481.

50. M. C. Biesinger, L. W. M. Lau, A. R. Gerson and R. S. C. Smart, *Applied Surface Science*, 2010, **257**, 887-898.

51. M. Chen, X. Wang, Y. H. Yu, Z. L. Pei, X. D. Bai, C. Sun, R. F. Huang and L. S. Wen, *Applied Surface Science*, 2000, **158**, 134-140.

52. D. Chen, F. Li and A. K. Ray, *AIChE Journal*, 2000, **46**, 1034-1045.

53. C. V. Schenck, J. G. Dillard and J. W. Murray, *Journal of Colloid and Interface Science*, 1983, **95**, 398-409.

54. M. S. Hegde, A. Srinivasan, K. Jagannathan and G. C. Chaturvedi, *Journal of Chemical Sciences*, 1980, **89**, 145-151.

55. J. Yang, H. Liu, W. N. Martens and R. L. Frost, *The Journal of Physical Chemistry C*, 2009, **114**, 111-119.

56. H. W. Nesbitt, D. Legrand and G. M. Bancroft, *Physics and Chemistry of Minerals*, 2000, **27**, 357-366.

57. G. Ertl, R. Hierl, H. Knözinger, N. Thiele and H. P. Urbach, *Applications of Surface Science*, 1980, **5**, 49-64.

58. C. Y. Toe, Z. Zheng, H. Wu, J. Scott, R. Amal and Y. H. Ng, *Angew Chem Int Ed Engl*, 2018, **57**, 13613-13617.

59. A. Saib, A. Borgna, J. Vandeloosdrecht, P. Vanberge and J. Niemantsverdriet, *Applied Catalysis A: General*, 2006, **312**, 12-19.

60. T. Sakamoto, H. Kishi, S. Yamaguchi, D. Matsumura, K. Tamura, A. Hori, Y. Horiuchi, A. Serov, K. Artyushkova, P. Atanassov and H. Tanaka, *Journal of The Electrochemical Society*, 2016, **163**, H951-H957.

61. A. Sharma, M. Varshney, J. Park, T.-K. Ha, K.-H. Chae and H.-J. Shin, *RSC Advances*, 2015, **5**, 21762-21771.

62. G. Mohamed Reda, H. Fan and H. Tian, *Advanced Powder Technology*, 2017, **28**, 953-963.

63. N. Park, K. Sun, Z. Sun, Y. Jing and D. Wang, *Journal of Materials Chemistry C*, 2013, **1**.

64. A. Šuligoj, I. Arčon, M. Mazaj, G. Dražić, D. Arčon, P. Cool, U. L. Štangar and N. N. Tušar, *Journal of Materials Chemistry A*, 2018, **6**, 9882-9892.

65. J. M. Lee, J. H. Baek, T. M. Gill, X. Shi, S. Lee, I. S. Cho, H. S. Jung and X. Zheng, *Journal of Materials Chemistry A*, 2019, **7**, 9019-9024.

66. J. Hölzl and F. K. Schulte, in *Solid Surface Physics*, eds. J. Hölzl, F. K. Schulte and H. Wagner, Springer Berlin Heidelberg, Berlin, Heidelberg, 1979, pp. 1-150.

67. N. Kamarulzaman, M. F. Kasim and N. F. Chayed, *Results in Physics*, 2016, **6**, 217-230.

68. A. Fujishima and X. Zhang, *Comptes Rendus Chimie*, 2006, **9**, 750-760.

69. L. I. Bendavid and E. A. Carter, *J Phys Chem B*, 2013, **117**, 15750-15760.

70. M. Cheng, G. Zeng, D. Huang, C. Lai, P. Xu, C. Zhang and Y. Liu, *Chemical Engineering Journal*, 2016, **284**, 582-598.

71. R. He, R. K. Hocking and T. Tsuzuki, *Journal of Materials Science*, 2011, **47**, 3150-3158.

Supplementary Information for

Increased Photocorrosion Resistance of ZnO foams Through Transition Metal Doping.

Zachary Warren,[a] Jannis Wenk [a] and Davide Mattia*[a]

5.2. Supplementary Information

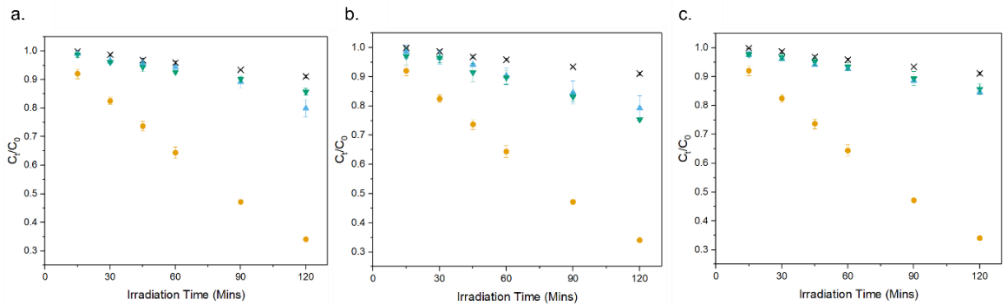

Figure S5.1: Photocatalytic degradation of CBZ using ZnO doped with various concentrations of a) Co, b) Ni and c) Cu: ✕ photolysis, ● undoped, p 1%, and ◤ 2%.

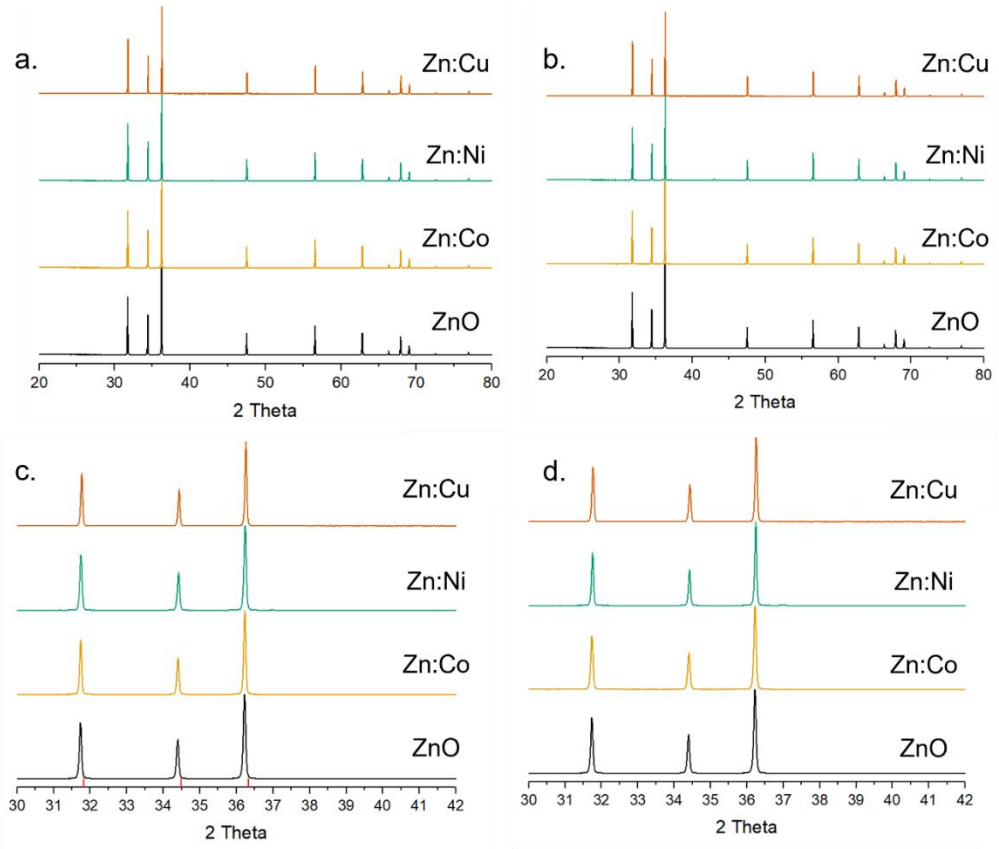

Figure S5.2: XRD spectra of a,c) 1% and b,d) 2% transition metal doped ZnO molfoams. Tick marks correspond to peaks reported from JCPDS No. 36-1451 [1]

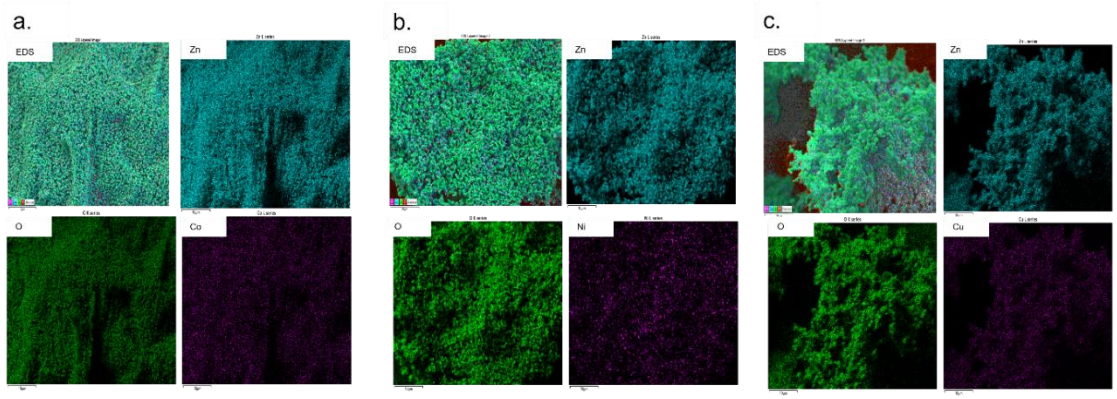

Figure S5.3: EDX elemental mapping for ZnO doped with a) Co, b) Ni and c) Cu.

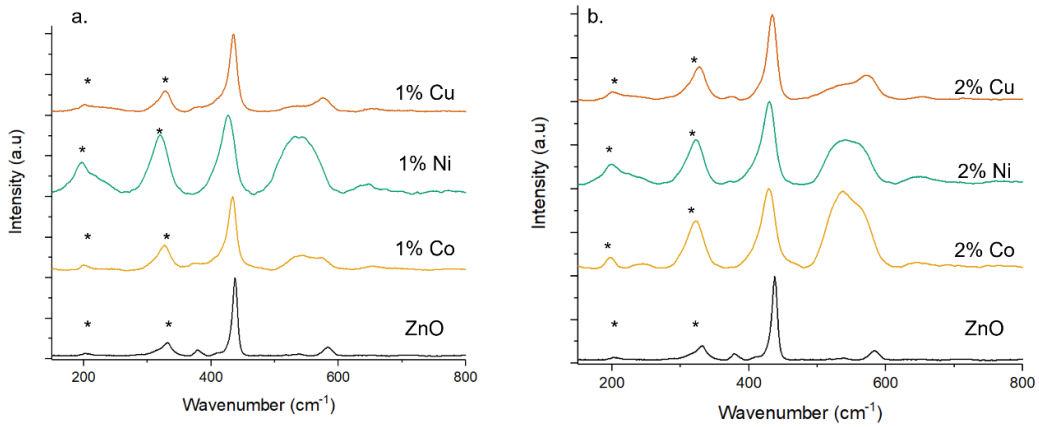

*Figure S5.4: Raman spectra of pure and doped ZnO molfoams at dopant concentrations of a) 1% and b) 2%. * correspond to multi-phonon features.*

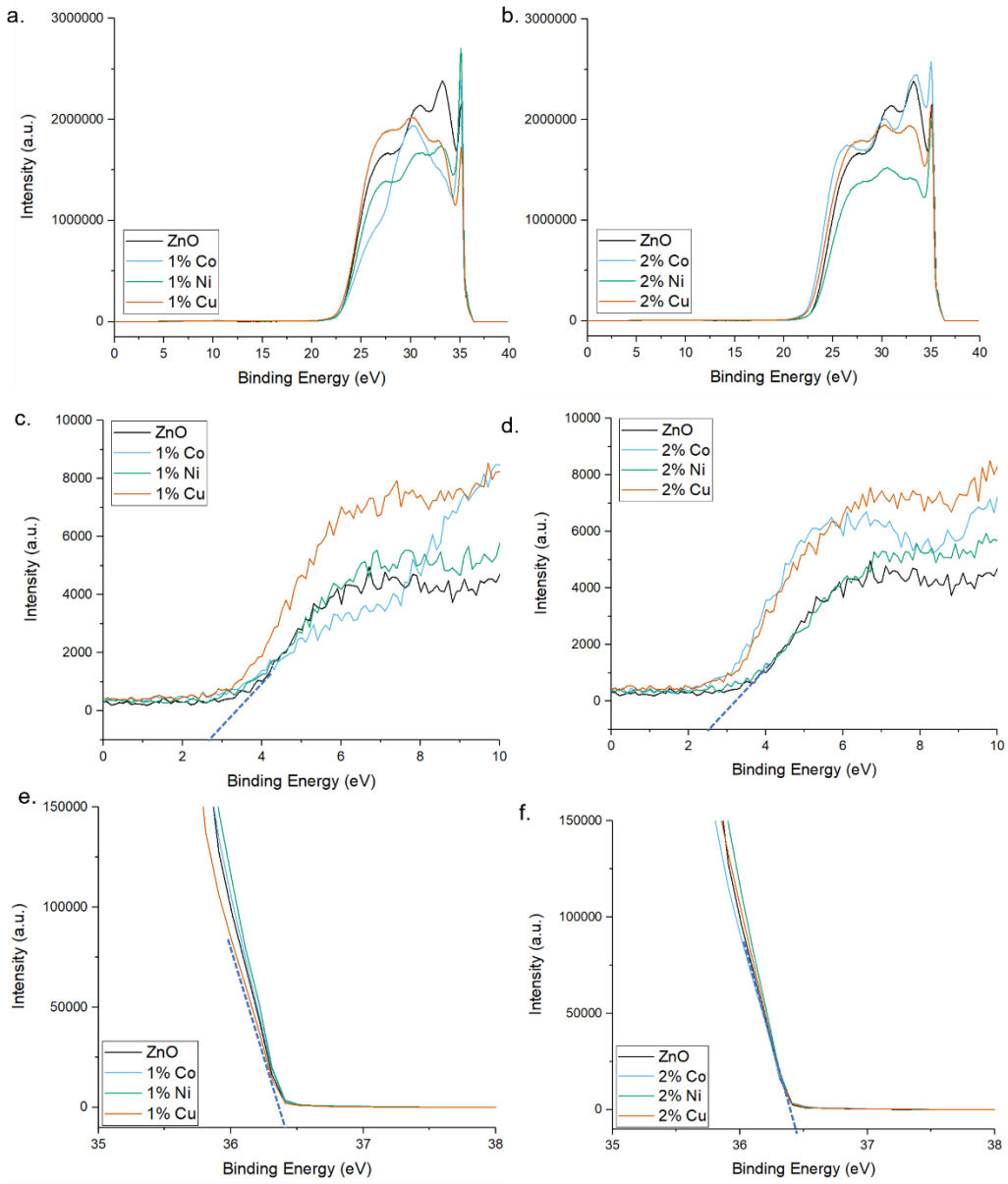

Figure S5.5: UPS spectra of doped and pure ZnO showing a,d) full spectra, b,e) valence band region and c,f) cut off region.

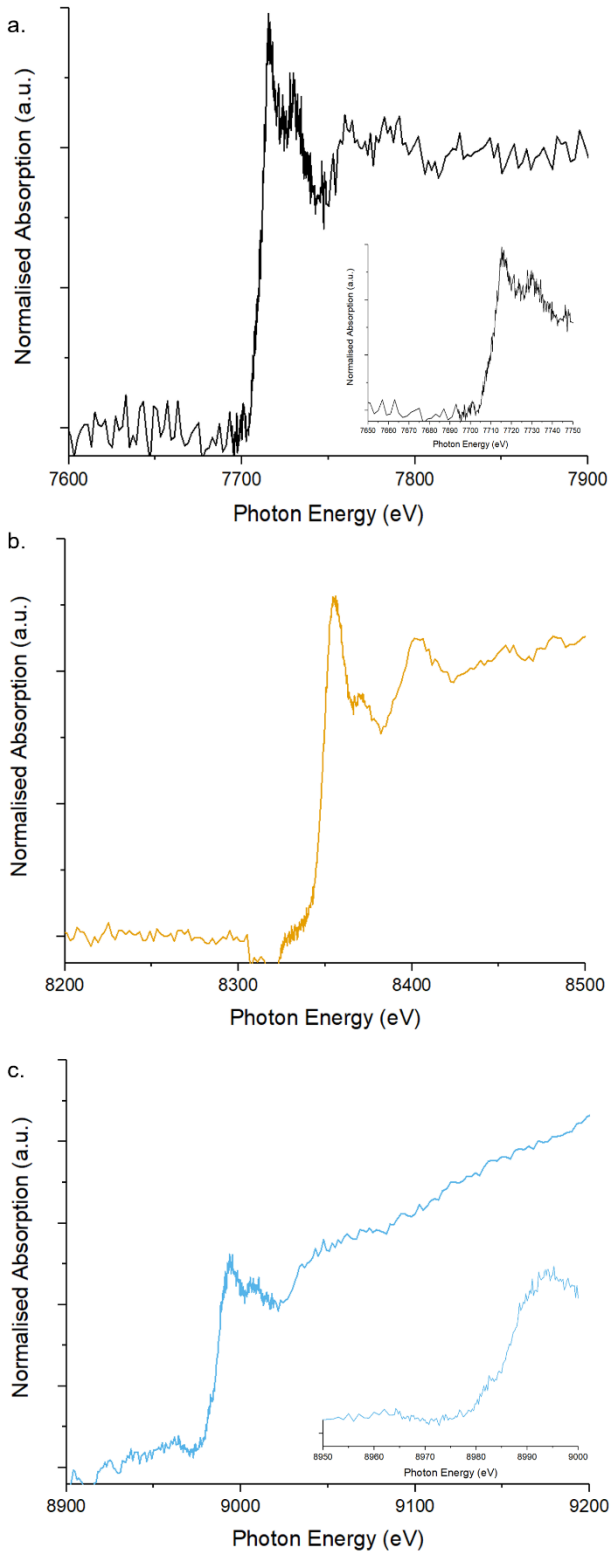

Figure S5.6: Xanes spectra of a) Co, b) Ni and c) Cu within doped ZnO foams. The insets of a and c show clearer the pre-edge features.

Text S1. Quantum efficiency calculations

The quantum efficiency allows for an assessment of the photon efficiency, assessing the number of pollutant molecules undergoing degradation relative to the number of photons reaching the catalyst surface [2]. Based on the definitions contained in the IUPAC glossary, the following equations are proposed to calculate the quantum efficiency of photocatalytic foams:

$$k' = (k)(C_0)(V_{Illuminated}) \ (mol\ s^{-1})$$

$$N_P = \frac{I_{0\lambda} * S * t}{E_P} (-)$$

$$q_{n,p} = \left(\frac{N_P}{t}\right)\frac{1}{N_A} \ (mol\ s^{-1})$$

$$QE = \frac{k'}{q_{n,p}} \ (-)$$

Equation S5.1 Quantum Efficiency Calculations

where, k' is the rate of pollutant degradation (mol s^{-1}), k is the kinetic constant (s^{-1}), C_o is the initial pollutant concentration (mol L^{-1}), $V_{Illuminated}$ is the total volume of pollutant irradiated.

The number of photons can be calculated using Equation S5.1, where $I_{0\lambda}$ is the incident irradiance of the light source (W m^{-2}), S is the surface of the sample onto which the light impinges (m^2) and t is the time under irradiation.

$E_p = \frac{h*c}{\lambda} (J)$ is the photon energy at the wavelength emitted by the lamps, where h is Planck's constant, c is the speed of light and λ is the wavelength of light (m) from the lamps. The photon flux is the numbers of photons during irradiation of a mol of photons, where N_A is Avogadro's number (equation S5.1) . Finally, the quantum efficiency (QE) is calculated using equation S5.1.

Text S2. Photocatalytic reactor energy consumption calculations.

To assess the viability of scaling up of the system, the energy consumption of the reactor was accounted for by using the electrical energy per order (E_{EO}), defined as

the kilowatt hours of electrical energy needed to decrease the concentration of a pollutant by an order of magnitude (90%) in one cubic metre of solution. [3]

$$E_{EO} = \frac{P*t*I*1{,}000}{V(log^{C_0}/_{C_t})}$$

Equation S5.2 E_{EO} calculation

Where: P is the total power output of the 3 lamps onto the 12 cm long quartz tube (kW), t is the irradiation time (hrs) V is the volume of reservoir (L) and C_0 and C_t are the initial and final concentrations of pollutants respectively. As the foam occupied only a fraction of the quartz tube, the total power of the lamps, which act on the whole quartz tube, was multiplied by the volumetric fraction occupied by the foam (i.e. foam volume/quartz tube volume), to provide the effective power used for photocatalysis, considering that the contribution of photolysis is negligible. This is rendered necessary by the recirculating nature of the reactor, unlike a simple batch reactor, where the entire reservoir would be irradiated. In the present work, the external diameter of the foam corresponds to the internal diameter of the tube, so that the volumetric fraction is equivalent to the ratio of the foam's length to the total length of the quartz tube: 2 cm/12 cm = 0.17. For the recirculating MolFoam reactors, three 5 W lamps were used, giving a P value of 15 X 10^{-3} kW, irradiation time was 120 minutes, volume of solution was 0.5 L, and the volumetric fraction 0.17.

Text S3. Calculations used in band edge diagram construction.

In order to construct the band edge diagram, the energies of the valence and conduction bands had to be calculated using a combination of ultraviolet photoelectron spectroscopy (UPS) and UV-Vis spectroscopy.

The UPS measurements determined the work function (W) of the samples (Equation S5.2)

Where W is the work function of the material, 40.8 eV corresponds to the characteristic energy of He (II), and cut off region intercept is the extrapolation of where the higher energy portion of the spectra crosses the x axis as shown in Figure S5.2 c and f.

From this, the energy level of the valence band maximum can be calculated (Equation 5.3.2) using the work function of the sample and the x intercept of the valence band region in the low binding energy region of the spectra as shown in Figure S5.2 b and e.

$$W\ (eV) = 40.8\ eV\ He(II) - cut\ off\ region\ intercept$$

$$VB_{max}\ (eV) = W + x\ intercept\ of\ valence\ band\ region$$

$$CB_{min}\ (eV) = \ VB_{max}\ (eV) - Band\ Gap$$

$$E\ vs\ SHE\ (V) = E\ vs\ vac.\ (eV) - 4.5$$

Equation S5.3 UPS measurement calculation

In order to compare energy values with the redox potentials of the $^{\bullet}OH/\ H_2O$ and $O_2{}^{\bullet}/O_2$ couples, energies were converted to the scale of the Standard Hydrogen Electrode (SHE) by subtracting 4.5 V, (i.e. 0 V vs Vac = -4.5 V vs SHE) (Equation 5.3)

1. R. Boppella, K. Anjaneyulu, P. Basak and S. V. Manorama, *The Journal of Physical Chemistry C*, 2013, **117**, 4597-4605.
2. N. Serpone and A. Salinaro, *Pure and Applied Chemistry*, 1999, **71**, 303-320.
3. J. R. Bolton, K. G. Bircher, W. Tumas and C. A. Tolman, *Pure and Applied Chemistry*, 2001, **73**, 627-637.

Chapter 6

Conclusions

Conclusions

6.1. Context

This thesis has investigated the synthesis of highly porous ZnO monoliths designed for use in wastewater treatment for the removal of organic micropollutants. The work has focused on ZnO foams, free from nanoparticles and without the need for a supporting substrate, such that the final foam is wholly photocatalytic. This involved the development of a novel synthetic method for the production ZnO foams (section 6.2), using direct air incorporation into a sol-gel reaction. These foams were characterised, and the photocatalytic activity assessed via degradation of carbamazepine, a known and widely used pharmaceutical micropollutant (section 6.3). The synthetic method was adapted to allow for incorporation of dopant metals into the ZnO foams to improve the photocorrosion resistance of the foams (section 6.4). Finally, a meta-review of the literature surrounding the use of foams as photocatalysts was conducted, using a semi-quantitative approach allowing for comparison of disparate systems and conclusions drawn based on foam materials and type (section 6.5).

6.2. MolFoam Synthetic Method

Most methods for the production of ZnO focuses on nanoparticles, films and wires, with some recent publications expanding on this and immobilising particulate ZnO onto inert foams. This immobilisation builds upon particles and films, but still suffers from the risk of particulate leaching. To build upon this development, a novel method of production was developed, the formation of ZnO foams via direct air incorporation into a sol-gel mixture. Changes in CTAB concentration led to minor macroscopic changes and significant changes to the crystal morphology and pore size of the foams. 10 mM CTAB was found to be the optimum concentration, resulting in highly faceted rod like crystals and smaller macropores both of which were found to be beneficial for photocatalytic degradation of carbamazepine. These foams where characterised with a range of analytical techniques including FE-SEM, MicroCT and HPLC.

6.3. Photocatalytic Activity

The photocatalytic activity of the materials was investigated by monitoring the degradation rate of carbamazepine under UV irradiation. A recirculating batch reactor was developed to apply the foams under simulated conditions while also taking advantage of the highly porous and hierarchical structure of the foams. This reactor allowed for increased mass transfer of carbamazepine to the surface of the catalyst. Furthermore, altering the flow rate of pollutant to the catalyst was shown to lead to an increase in photocatalytic activity.

6.4. Doping of ZnO Molfoams

One key drawback of ZnO is its susceptibility to photocorrosion leading to instability. To counter this, metal dopants were introduced into the crystal structure of the foams, to increase charge separation and separate holes from the ZnO structure. Three different metals, Co, Ni and Cu were doped into the foams at concentrations of 1 and 2% leading to changes in the colour and crystal morphologies of the foams. In all cases, photocorrosion was reduced, relative to undoped foams, as was photocatalytic activity. As such advanced analytical methods such as XPS and UPS were conducted in order to identify the cause for the loss of activity, investigation and a discussion often lacking in published literature.

6.5. Expansion of Current Nomenclature

This thesis also includes a review and meta-analysis of the available literature surrounding photocatalytic foams showed they have the potential to address the limitations of slurries and immobilised catalysts (need for downstream removal and low activities, respectively), for use in the removal of organic pollutants from water. This review set out a set of definitions to characterise foams based on their synthesis as well as expanding the IUPAC classification of porosity to account for the larger pores found throughout foams. It also highlights fundamental gaps in the field, particularly surrounding the application of recirculating and flow reactors, while prioritising key challenges facing the field and research community. Finally, it

proposed a list of best practices to be followed in order to allow for better standardisation across experiments, allowing for easier comparison between systems and improving the quality of research.

This thesis has demonstrated the viability and effectiveness of photocatalytic foams for degradation of organic pollutants in water. It has shown that ZnO foams can be produced using a novel synthetic method, with the foams showing very high porosities comparable to xero-and aerogels within the literature without the need for foaming agents or supercritical solvents. This synthetic method allowed for the tuning of the pore sizes of the foam through use of a surfactant and allows for dopant incorporation into the foam via control of reagents.